



HAL
open science

Développement d'un bassin à houle numérique pour l'étude des efforts hydrodynamiques en éolien flottant

Constance Clement

► To cite this version:

Constance Clement. Développement d'un bassin à houle numérique pour l'étude des efforts hydrodynamiques en éolien flottant. Mécanique des fluides [physics.class-ph]. Normandie Université, 2021. Français. NNT : 2021NORMR028 . tel-03331232

HAL Id: tel-03331232

<https://theses.hal.science/tel-03331232>

Submitted on 1 Sep 2021

HAL is a multi-disciplinary open access archive for the deposit and dissemination of scientific research documents, whether they are published or not. The documents may come from teaching and research institutions in France or abroad, or from public or private research centers.

L'archive ouverte pluridisciplinaire **HAL**, est destinée au dépôt et à la diffusion de documents scientifiques de niveau recherche, publiés ou non, émanant des établissements d'enseignement et de recherche français ou étrangers, des laboratoires publics ou privés.



Normandie Université

THÈSE

Pour obtenir le diplôme de doctorat

Spécialité MECANIQUE DES FLUIDES, ENERGETIQUE, THERMIQUE, COMBUSTION,
ACOUSTIQUE

Préparée au sein de l'Université de Rouen Normandie

Investigation of Floating Offshore Wind Turbine Hydrodynamics with Computational Fluid Dynamics

Présentée et soutenue par
Constance CLEMENT

Thèse soutenue publiquement le 23/06/2021
devant le jury composé de

Michel BENOIT	EDF	Rapporteur
Pierre LUBIN	Bordeaux INP	Rapporteur
Amy ROBERTSON	National Renewable Energy Laboratory (NREL), USA	Examinatrice
François-Xavier DEMOULIN	ESITech de Rouen	Examineur
Julien REVEILLON	Université de Rouen Normandie	Directeur de thèse
Pauline BOZONNET	IFP Energies nouvelles	Encadrante

Thèse dirigée par Julien REVEILLON, Complexe de Recherche Interprofessionnel en Aérothermochimie (CORIA)



To my grandparents and Philippe

A mes grands-parents et Philippe

Remerciements

Je tiens tout d'abord à remercier l'IFP Energies nouvelles pour cette opportunité de thèse dans ce domaine passionnant et en pleine expansion qu'est l'éolien flottant. Merci au CORIA (Rouen) d'avoir accepté de suivre académiquement cette thèse et à l'Université Rouen Normandie de m'avoir attribué le titre de docteur.

Je remercie sincèrement les deux correcteurs de la thèse Michel Benoit et Pierre Lubin avec qui j'ai pu avoir une discussion très enrichissante lors de la soutenance de thèse. Merci également à Amy Robertson, experte en éolien offshore, d'avoir accepté de faire partie du jury de la thèse. Je remercie aussi François-Xavier Demoulin d'avoir présidé le jury.

Cette thèse n'aurait pu aboutir sans l'aide précieuse de mes encadrants de thèse : Pauline Bozonnet, Guillaume Vinay et Philippe Pagnier. Merci Pauline pour ta confiance durant ces trois années et ta rigueur lors des corrections d'articles et du manuscrit. Merci Guillaume pour tes conseils, ton expertise CFD et toute l'aide que tu m'as apportée lors des multiples problèmes rencontrés. Philippe, je suis si honorée d'avoir pu croiser ton chemin. Je retiendrai ta bienveillance, ta profonde gentillesse et ton soutien moral lors des derniers mois de rédaction avant que tu nous quittes brutalement. Merci également à Adrià Borràs Nadal, fidèle compagnon OpenFOAM en éolien flottant, toujours attentif à mon bien-être. J'ai énormément appris à vos côtés, techniquement sans aucun doute mais également humainement. Je n'ai aucun regret si ce n'est celui de ne pas avoir pu plus vous voir « physiquement » à cause de cette satanée pandémie.

Je remercie également Julien Réveillon du CORIA qui a dirigé ma thèse. J'ai apprécié nos échanges, toujours faciles et très utiles pour prendre du recul et mener à bien ce projet de thèse.

Je remercie aussi sincèrement Lionel Gamet, expert OpenFOAM à l'IFPEN, toujours enclin à m'aider et me proposer des solutions lorsque je me heurtais à des problèmes numériques.

Merci aussi aux développeurs des codes opensource utilisés durant cette thèse, qui ont toujours répondu à mes mails avec précision: Niels Jacobsen, Pablo Higuera and Johan Roenby. Je remercie également les nombreux chercheurs de la plateforme d'aide en ligne cfdonline, véritable mine d'informations pour monter le modèle numérique de la thèse.

Enfin je remercie mes parents, ma famille et mes amis qui m'ont encouragée tout au long de ces années. Merci François d'avoir été quotidiennement à mes côtés,

Constance
Juillet 2021

Contents

1	Introduction	17
1.1	A short history and advantages of Floating Offshore Wind Turbines . . .	17
1.2	Bottom fixed offshore wind structures	21
1.3	Floating Offshore Wind Turbines (FOWT)	22
1.3.1	Degrees of freedom for floater motion	22
1.3.2	Mooring system	23
1.3.3	Stability strategies	23
1.4	Design of a FOWT	24
1.4.1	Coupled engineering tools	24
1.4.2	Limitations of the standard O&G hydrodynamic practices when applied to FOWT design	25
1.4.3	High fidelity simulations to model the hydrodynamic of a FOWT floater	26
1.5	The thesis objective	26
1.5.1	Numerical Wave Tank implementation	27
1.5.2	Surface piercing cylinder in regular waves	27
1.5.3	SBM Offshore/IPPEN Tension Leg Platform in regular waves	27
1.6	Outline of the thesis	28
I	State of the Art	29
2	Hydrodynamics of offshore floating structures	30
2.1	Wave theory	30
2.1.1	Regular wave characteristics	30
2.1.2	Potential theory	31
2.1.3	Airy waves	33
2.1.4	Stokes 2 nd order waves	35
2.1.5	Stokes 3 rd order waves	36
2.2	Cylinder in an oscillating flow	36
2.2.1	Fixed cylinder in an oscillating flow	37
2.2.2	Moving cylinder in a flow at rest	37

2.2.3	Generalisation to a moving cylinder	38
2.3	Morison force approach	38
2.3.1	Determination of the inertia and drag coefficients in Morison empirical formula	40
2.3.2	Application of Morison empirical formula in engineering tools	47
2.3.3	Wave loads classification according to Chakrabarti [2005]	47
2.4	Sea-keeping theory for FOWT	49
2.4.1	Float motion in waves: 2 nd Newton law	49
2.4.2	Potential flow theory for hydrodynamic load determination	50
2.4.3	Resolution of the motion equation in the frequency domain	51
2.4.4	Second order loads: Quadratic Transfer Function (QTF)	52
2.4.5	Combination of Morison equation to sea-keeping theory	52
3	CFD modelling in OpenFOAM for the study of FOWT Hydrodynamics	54
3.1	Fluid Mechanics equations	55
3.1.1	Navier-Stokes equations	55
3.1.2	Turbulence modelling	55
3.1.3	Free surface modelling	55
3.2	Numerical implementation in OpenFOAM	56
3.2.1	Finite Volume Method in OpenFOAM	56
3.2.2	Free surface resolution	57
3.3	Wave generation solvers	58
3.3.1	waveFoam: a passive wave generation and absorption solver	58
3.3.2	olaFlow: an active wave generation and absorption solver	59
4	Hydrodynamics for FOWT: limitations of current models and CFD investigation	62
4.1	Hydrodynamic modelling of FOWT with engineering solvers	62
4.1.1	Combination of Morison empirical formula and potential linear theory to predict wave loads on FOWT	63
4.1.2	Calibration of Morison hydrodynamic coefficients for FOWT	63
4.1.3	Non-linear loads on FOWT	64
4.2	Numerical Wave Tank	67
4.2.1	Wave generation and absorption in OpenFOAM	67
4.2.2	Numerical Wave Tank examples	67
4.2.3	VOF resolution limitation	68
4.3	Fluid-structure interaction in CFD	69
4.3.1	CFD modelling of vertical piercing cylinders in waves	69
4.3.2	CFD studies of FOWT	71

II	Results	79
5	A two-step methodology to investigate wave loads on a floater	80
5.1	How to set up a Numerical Wave Tank	80
5.1.1	Characteristics of the four waves retained for the study	81
5.1.2	CFD post-treatment specifics	85
5.1.3	Geometry and boundary conditions of the NWT	86
5.1.4	Relaxation zone lengths	87
5.1.5	Grid refinement	88
5.1.6	Time step	92
5.1.7	General guidelines to setup a NWT	94
5.1.8	Results for the four waves	94
5.2	Development of a slice methodology on a complex floater for determining Morison coefficients	98
5.2.1	The floater configuration	98
5.2.2	Definition of the local frames of the braces	99
5.2.3	Main steps of the numerical slice methodology	101
6	Wave loads on a surface-piercing cylinder subjected to waves	105
6.1	Setup and validation of the CFD model	105
6.1.1	Physical case description	105
6.1.2	CFD Numerical model	107
6.2	Application of the slice methodology	109
6.2.1	Calculation of the wave velocity at the center of each slice	109
6.2.2	Determination of Morison coefficients	111
6.2.3	Analysis of CFD and Morison loads along the cylinder	112
6.2.4	Analysis of CFD and Morison loads for the entire cylinder	117
6.3	Physical analysis of the influence of the interface on the wave loads	118
6.3.1	Nonlinear diffraction load on the surface-piercing cylinder	118
6.3.2	Physical analysis of the influence of the interface on two slices	121
6.4	Conclusion	126
7	Investigation of FOWT hydrodynamics	128
7.1	Captive test description and simulation	129
7.1.1	Experiments	129
7.1.2	Modelling of the captive test in DeepLinesWind™	130
7.1.3	Setup and validation of the CFD model	131
7.2	Distribution of the forces on the floater	136
7.3	Two methods to determine Morison coefficients for brace load prediction	139
7.4	Impact of the structure	140
7.4.1	Impact of the TLP floater on all the braces	140

7.4.2	Impact of the floater presence on a horizontal and deeply submerged brace, intercepted by other braces, Brac1	142
7.4.3	Impact of the floater presence on a horizontal and deeply submerged brace, between two large buoys, Brac12	148
7.5	Impact of the air/water interface vicinity	153
7.5.1	Impact of the interface vicinity on a vertical surface-piercing brace at the centre of the floater, Cent1	153
7.5.2	Impact of the interface vicinity on an inclined vertical surface-piercing cylinder at the upstream of the floater, Trans2	157
7.6	Impact of the structure and the free-surface at the brace group level . . .	163
7.6.1	Analysis for the small wave w1	163
7.6.2	Analysis for the higher wave w2	166
7.6.3	Analysis for the design wave for turbine park conditions w3	167
7.7	Impact of the brace orientations varying the wave characteristics	170
7.7.1	Impact of the brace orientation on the loads for an oriented horizontal submerged brace, Brac1	170
7.7.2	Impact of the brace orientation on the loads determined on a slice within an oriented vertical surface-piercing brace, Trans2	174
7.7.3	A attempt to consider brace orientation in the determination of Morison coefficients used for design purposes	177
7.8	Distribution of the coefficients through the TLP floater	180
7.9	Towards a few advice to improve Morison formula predictions	181
8	Conclusion and perspectives	183
9	Annexes	198
9.1	Froude scale	198
9.2	Numerical Wave Tank with olaFlow	199
9.2.1	Physical problem	199
9.2.2	Set up of OpenFOAM model	201
9.2.3	Numerical results	202
9.3	Scalability study for OpenFOAM	208
9.4	Numerical schemes used in the CFD simulations	209

List of Figures

1.1	Evolution of the total installed capacity of offshore wind in Europe (Ramírez et al. [2020]).	17
1.2	Annual gross offshore wind capacity installations per country in 2020 in Europe (MW) (Ramírez et al. [2020]).	17
1.3	Floating wind global outlook by Equinor.	18
1.4	Hywind floating wind park (Source: Equinor website).	19
1.5	Hywind floating roadmap (Source: IOWTC2021 Equinor presentation).	19
1.6	WindFloat FOWTs (Source: WindFloat website).	20
1.7	Different types of offshore wind turbines (Source: Principle Power website).	21
1.8	Typical fixed offshore wind turbine foundations (Source: EAWE website).	22
1.9	Translation	23
1.10	Rotation	23
1.11	Degrees of freedom definition of the floating body.	23
1.12	Potential theory and Morison empirical formula.	25
2.1	Regular wave main characteristics.	31
2.2	Validity of several theories for periodic water waves, according to Méhauté [1976].	33
2.3	Velocity field (left side) and velocity orbitals (right side) in deep, intermediate and shallow water (Susbielles et al. [1981]).	34
2.4	Cylinder scheme and reference frames.	37
2.5	Frame of the brace.	39
2.6	Cylinder in a oscillating flow. Inertia coefficient C_M as a function of K_C for different values of β (Sarpkaya [1977]).	41
2.7	Cylinder in a oscillating flow. Drag coefficient C_D as a function of K_C for different values of β (Sarpkaya [1977]).	42
2.8	Hydrodynamic coefficients derived by Chakrabarti from two 1-ft sections force data on a vertical cylinder for different wave periods.	43
2.9	Free surface effect as shown by the ratio of predicted to measured forces as a function of free-surface proximity (Dean et al. [1981]).	44

2.10	Total force and moment on a 4-ft diameter pile in the region of the crest -with and without free surface modifications, wave travelling from left to right, near breaking wave (Dean et al. [1981]).	45
2.11	Distribution forces on a 4-ft diameter pile at crest phase - with and without free surface modifications, near breaking waves (Dean et al. [1981]). . . .	46
2.12	Determination of wave loads according to H,D, and λ by Chakrabarti [2005].	48
2.13	Coordinate systems.	49
2.14	Linear decomposition of hydrodynamic loads (Massie and Journée [2001]).	51
3.1	Edges of the Numerical Wave Tank.	58
3.2	Relaxation zones.	59
3.3	Active wave absorption experiments.	60
4.1	CFD modelling of the OO-star floater: schematic of the computational domain and boundary conditions (left side), snapshot of the floater in the numerical wave tank (right side) (Sarlak et al. [2018]).	72
4.2	Mesh of the semisubmersible floater (Pan and Ishihara [2019]).	74
4.3	Free surface representation with radiated waves from the floater for the surge decay simulation (Burmester et al. [2018]).	75
4.4	Free surface elevation surrounding the OC5-DeepCWind semisubmersible in free motion in waves (Rivera Arreba [2017]).	76
5.1	Modelled waves reported in Le Méhauté [1976] classification.	82
5.2	Wave elevation time series for Stansberg wave derived with Stokes 2 nd and Stokes 3 rd order theories.	83
5.3	Velocity profile along water depth derived with Stokes 2 nd and Stokes 3 rd order theories.	83
5.4	Wave/structure interaction case reported in Le Chakrabarti [2005] classification.	85
5.5	Numerical Wave Tank sketch.	87
5.6	Wave height for three different absorption zone lengths (Stansberg wave).	88
5.7	Numerical Wave Tank mesh (wave w2).	89
5.8	Free surface refinement (wave w2).	89
5.9	Influence of the number of cells per wave height (nz) on the wave height variation (wave w2).	90
5.10	Influence of the ratio r ($dz/dx = r * H/\lambda$) on the wave height variation (wave w2).	91
5.11	Wave height along the tank for the time step convergence study (wave w3).	92
5.12	Visualisation of air crest velocities along (Ox) (wave w3) (zoom $x3$ on (Oz)).	93
5.13	Wave height variation along the tank for the four waves.	96
	(a) Stansberg	96

(b) w1	96
(c) w2	96
(d) w3	96
5.14 Wave elevation time series for the four waves, at the position corresponding to the location where will be placed the floater.	97
(a) Stansberg	97
(b) w1	97
(c) w2	97
(d) w3	97
5.15 Typical groups of braces.	99
5.16 Braces sliced in the floater.	99
5.17 Local frames of the braces.	101
6.1 Cylinder test configuration from Stansberg [1997].	106
6.2 Wave elevation time series from Stansberg experiments.	107
6.3 Horizontal wave loads (F_x) on the fixed cylinder.	108
6.4 Velocity profile along water depth. CFD (—), Stokes 2 nd order (—.), Vertical stretching (— —), Wheeler stretching (...), Stokes 2 nd order extrapolated (— —), A_{max} (—).	110
6.5 Velocity profile along water depth. CFD (—), Stokes 2 nd order wave theory extrapolated (— —), Standard deviation of CFD velocity (■), $A_{min}:A_{max}$ (— —).	111
6.6 Morison drag and inertia coefficients for each slice along the cylinder. C_M (●), C_D (× :), $A_{min}:A_{max}$ (— —).	112
6.7 Location of the four cylinder slices. $A_{min}:A_{max}$ (— —).	113
6.8 Loads on the slice centred at $z = -0.95$ m. CFD loads (—), Morison loads determined with the specific slice coefficient (—.), Morison loads determined with the coefficients averaged over the water depth (— —). . .	114
6.9 Loads on the slice centred at $z = -0.35$ m. CFD loads (—), Morison loads determined with the specific slice coefficient (—.), Morison loads determined with the coefficients averaged over the water depth (— —). . .	114
6.10 Loads on the slice centred at $z = -0.025$ m. CFD loads (—), Morison loads determined with the specific slice coefficient (—.), Morison loads determined with the coefficients averaged over the water depth (— —). . .	115
6.11 Loads on the slice centred at $z = 0.025$ m. CFD loads (—), Morison loads determined with the specific slice coefficient (—.), Morison loads determined with the coefficients averaged over the water depth (— —).	116
6.12 Maximum force profile along the cylinder length. CFD (—), Morison force with average coefficients determined in CFD (—.).	116

6.13	Total loads on the cylinder. Morison load (—.), Inertia term (---), Drag term (...).	117
6.14	Total load on the cylinder. CFD (—), Morison formula with averaged coefficients (—.), Experiments (—).	118
6.15	Time histories of the inline force on a vertical cylinder (Paulsen et al. [2012]).	119
6.16	Inline force on a vertical cylinder. 2 nd harmonic (Top left), 3 rd harmonic (Top right), 4 th harmonic (Bottom left) and 5 th harmonic (Bottom right). Comparison between the values obtained experimentally by Huseby and Grue [2000] and numerically by Ferrant [1998].	120
6.17	Slice split into an upstream and a downstream part.	121
6.18	Wave loads on the slice centred at $z=-0.225$ m.	122
6.19	Visualisation of the air/water interface at four key moments for slice $z = -0.225m$.	123
	(a) t1	123
	(b) t2	123
	(c) t3	123
	(d) t4	123
6.20	Wave loads on the slice centred at $z=-0.025$ m.	124
6.21	Visualisation of the air/water interface at height key moments for slice $z = -0.025m$.	125
	(a) t1	125
	(b) t2	125
	(c) t3	125
	(d) t4	125
	(e) t5	125
	(f) t6	125
	(g) t7	125
	(h) t8	125
7.1	Photos of the captive tests performed at MARIN (the Netherlands).	129
7.2	Experimental loads on the TLP (wave w1).	130
7.3	Calibration of DeepLinesWind™ on experiments (wave w1).	131
7.4	Inclusion of the TLP floater in the NWT mesh.	132
7.5	Inclusion of the TLP floater in the NWT mesh (zoom).	132
7.6	Surge (F_x) and heave (F_z) forces for the convergence study in CFL number (wave w2).	133
7.7	Surge (F_x), sway (F_y) and heave (F_z) forces from CFD and experiments (wave w1).	134
7.8	Typical groups of braces and buoys.	136
7.9	Surge (F_x) and heave (F_z) force distribution from CFD (wave w1).	136

7.10	Surge (F_x) and heave (F_z) force distribution from CFD (wave w2).	137
7.11	Surge (F_x) and heave (F_z) force distribution from CFD (wave w3).	137
7.12	Surge, sway and heave force distribution for the groups of braces for the three waves.	138
7.13	Detail of the brace names in the TLP floater.	139
7.14	Visualisation of the two configurations of Brac1 in the NWT (the free surface is coloured with the dynamics pressure field)	140
	(a) Brac1 alone	140
	(b) Brac1 in the TLP	140
7.15	Brac1 in TLP	142
7.16	Surge, sway and heave forces for Brac1 alone and in the TLP.	142
7.17	Visualisation of the pierced slices and two not-pierced slices on both sides for Brac1.	143
7.18	Forces on the not-pierced slices of Brac1 alone and in the TLP.	143
7.19	Morison coefficients derived from CFD for Brac1 in TLP.	144
7.20	F_X and F_Z CFD forces on a whole slice and a pierced slice in the brace local frame.	144
7.21	F_X and F_Z forces from CFD and Morison for a whole slice ($C_{D_X} = 2.9$, $C_{M_X} = 1.85$, $C_{D_Z} = 2.05$ and $C_{M_Z} = 1.97$) and for a pierced slice ($C_{D_X} = 82$, $C_{M_X} = 2.23$, $C_{D_Z} = 3.7$ and $C_{M_Z} = -1.38$).	145
7.22	Morison prediction for a pierced slice.	145
7.23	Morison coefficients derived from CFD for Brac1 in TLP without the pierced slices.	146
7.24	Inertia Morison coefficients derived from CFD for Brac1 in TLP without the pierced slices.	146
7.25	Morison prediction with variable coefficients for Brac1.	147
7.26	Morison prediction with constant averaged coefficients for Brac1.	147
7.27	Morison prediction with constant coefficients averaged over not-pierced slices for Brac1.	148
7.28	Brac12 in TLP	149
7.29	Surge, sway and heave forces for Brac12 isolated or in the TLP.	149
7.30	Morison C_{M_X} and C_{M_Z} derived from CFD loads on Brac12 alone and in the TLP.	150
7.31	Morison prediction with variable coefficients for Brac12.	151
7.32	Morison prediction with constant averaged coefficients for Brac12.	151
7.33	Cent1 in TLP	153
7.34	Influence of the interface on Cent1 at the brace level.	154
7.35	Morison coefficients derived from CFD for Cent1 (C_{D_X} on the left, C_{M_X} on the right).	154

7.36	Morison and CFD loads for a submerged slice (on the left) and a slice in the interface (on the right).	155
	(a) $z = 2.31m \simeq -2.3H$ ($C_{D_X} = 0.13$ and $C_{M_X} = 1.93$)	155
	(b) $z = -0.84m \simeq -0.1H$ ($C_{D_X} = 2.82$ and $C_{M_X} = 1.14$)	155
7.37	Morison prediction with variable coefficients for Cent1.	155
7.38	Morison and CFD loads for a not-pierced slice (on the left) and for a pierced slice (on the right).	156
	(a) $z = -5.59m \simeq -5.6H$ ($C_{D_X} = 0.13$ and $C_{M_X} = 1.94$)	156
	(b) $z = -6.71m \simeq -6.7H$ ($C_{D_X} = 44.8$ and $C_{M_X} = 1.87$)	156
7.39	Morison prediction with constant averaged coefficients for Cent1.	156
7.40	Morison prediction with constant averaged coefficients (including the slices in the interface) for Cent1.	157
7.41	Trans2 in TLP	158
7.42	Influence of the interface on Trans2 at the brace level.	158
7.43	Morison coefficients derived from CFD for Trans2 (C_{D_X} on the left, C_{M_X} on the right).	159
7.44	CFD and Morison F_X forces for the three slices in the interface for the oriented vertical surface-piercing brace Trans2.	159
	(a) $z = 1.3H$ ($C_{D_X} = -0.68$ and $C_{M_X} = 1.46$)	159
	(b) $z = -0.4H$ ($C_{D_X} = -21.88$ and $C_{M_X} = -4.72$)	159
	(c) $z = -0.6H$ ($C_{D_X} = -20.24$ and $C_{M_X} = -6.14$)	159
7.45	Morison prediction with variable coefficients for Trans2.	160
7.46	Morison prediction with constant averaged coefficients for Trans2.	161
7.47	Morison prediction with constant averaged coefficients (including the slices in the interface) for Trans2.	161
7.48	Morison prediction with constant averaged coefficients for Trans3.	162
7.49	Morison and CFD forces at the brace group level (wave w1).	164
7.50	Morison and CFD forces at the brace group level (wave w2).	166
7.51	Morison and CFD forces at the brace group level (wave w3).	168
7.52	Slice 3 in Brac1 in TLP	171
7.53	C_{D_Z} (left side) and C_{M_Z} (right side) for the horizontal and submerged Brac12 added on Boccotti's plots.	172
7.54	C_{D_X} , C_{D_Z} (left side), C_{M_X} and C_{M_Z} (right side) for slice 3 in the oriented horizontal submerged Brac1 added on Boccotti's plots.	172
7.55	CFD and Morison loads on slice 3 in Brac1 (wave w2).	173
7.56	F_X force on slice 3 in Brac1 (wave w3).	174
7.57	F_Z force on slice 3 in Brac1 (wave w3).	174
7.58	Slice 5 in Trans2 in TLP	175
7.59	C_{M_X} (at the top) and C_{D_X} (at the bottom) derived from CFD loads on slice 5 in Trans2 reported in Chakrabarti et al. [1976].	176

7.60	F_X derived from Morison ($C_{D_X} = 0.51$ and $C_{M_X} = 2.32$) and CFD for slice 5 in Trans2 (wave w3).	176
7.61	Morison prediction with C_D and C_M determined with the three methods for Brac1 (wave w1).	178
	(a) Directional coefficients	178
	(b) Simple average	178
	(c) Magnitude	178
	(d) Weighted average	178
7.62	Morison prediction with C_D and C_M determined with the three methods for Brac1 (wave w2).	179
	(a) Directional coefficients	179
	(b) Simple average	179
	(c) Magnitude	179
	(d) Weighted average	179
7.63	Morison prediction with C_D and C_M determined with the three methods for Brac1 (wave w3).	179
	(a) Directional coefficients	179
	(b) Simple average	179
	(c) Magnitude	179
	(d) Weighted average	179
7.64	Directional coefficients for each brace derived from the CFD modelling of the TLP subjected to the three different waves w1, w2 and w3.	180
	(a) C_{D_X}	180
	(b) C_{D_Z}	180
	(c) C_{M_X}	180
	(d) C_{M_Z}	180
9.1	Cases run with olaFlow solver.	200
9.2	Wave elevation time series at the center of the tank (waveA).	202
9.3	Amplitude envelop during one period (waveA).	203
9.4	Wave elevation time series at 5 probes (waveB).	203
9.5	Amplitude envelop at t=80s over one period along the tank (waveB).	204
9.6	Wave elevation time series (waveC).	205
9.7	Amplitude envelop at t=80s over one period along the tank (waveC).	205
9.8	Free surface elevation time series at the center of the tank (x=4 m).	206
9.9	SW-AWA library for 2 nd order and deep water waves.	206
9.10	ER-AWA library for 2 nd order and deep water waves.	207
9.11	Wave height along the NWT obtained with olaFlow and waveFoam runs.	208
9.12	Scalability study with interFoam solver.	209

Acronyms

CAE Computer-Aided Engineering

CFD Computational Fluid Dynamics

CFL Courant–Friedrichs–Lewy

CPU Central Processing Unit

DLC Design Load Cases

DOF Degree Of Freedom

FOWT Floating Offshore Wind Turbine

FSE Free Surface Elevation

IOWTC International Offshore Wind Technical Conference

MULES Multidimensional Universal Limiter with Explicit Solver

MSL Mean Sea water Level

n.a. not available

NWT Numerical Wave Tank

PDE Partial Differential Equation

ppwh Point Per Wave Height

ppwl Point Per Wave Length

PV Photovoltaic

SST Shear Stress Transport

TLP Tension Leg Platform

VOF Volume-of-Fluid

Chapter 1

Introduction

1.1 A short history and advantages of Floating Offshore Wind Turbines

The concept of offshore wind turbines was first invented in 1972 by Heronemus [1972] but it took twenty years to generate electricity with the first fixed offshore park "Windeby" built in 1991. Since then, many offshore wind farms have been built resulting in a total net installed capacity of 35.3 GW at the end of 2020 for a total wind energy capacity of 743 GW (GWEC [2021]). 2.9 GW of offshore wind gross power capacity was installed in 2020 in Europe, UK, Germany, Netherlands, Belgium and Denmark being the major players as shown in Fig. 1.1 and 1.2.

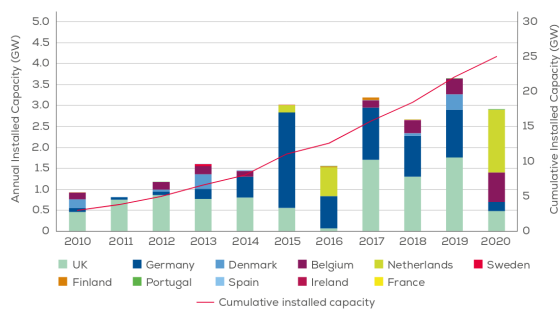


Figure 1.1: Evolution of the total installed capacity of offshore wind in Europe (Ramírez et al. [2020]).

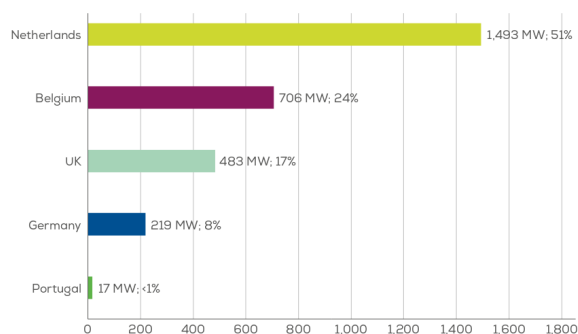


Figure 1.2: Annual gross offshore wind capacity installations per country in 2020 in Europe (MW) (Ramírez et al. [2020]).

Currently, the most common offshore wind turbine type is bottom-founded. However, Floating Offshore Wind Turbines (FOWTs) are developing and their part in the offshore energy market is forecasted to increase quickly as detailed by Equinor in Fig. 1.3, which predicts a total FOWT installed capacity of 180 GW by 2050.

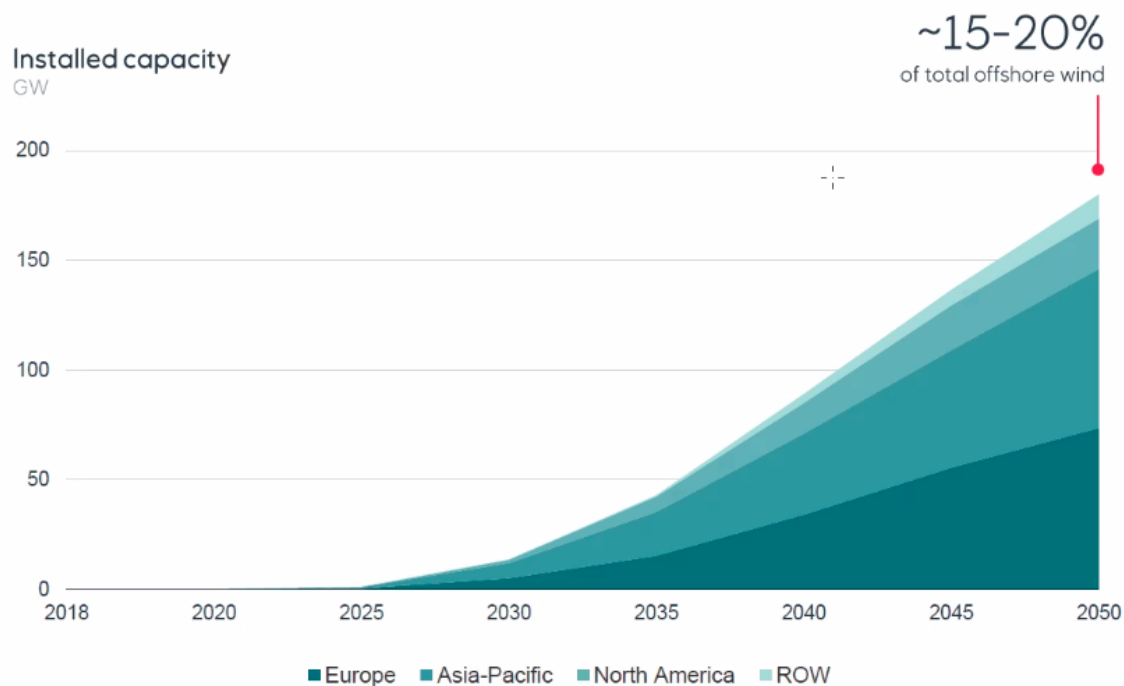


Figure 1.3: Floating wind global outlook by Equinor.

In 2021, FOWTs are still at pre-commercial development stage. FLOAT was the first model test realised in 1993 to prove FOWT concept, as detailed by Quarton [2004]. It consisted in a spar floater with catenary mooring lines. A lot of projects have been proposed over the past few years. In 2009, the world's first full-scale floating wind turbine "Hywind" (developed by Equinor and Siemens) was installed in Karmoy, Norway. This 2.3 MW floating wind turbine produced more than 40 GWh of electricity in eight years of operation. The success of Equinor's demo wind turbine led to the construction of the first floating wind farm composed of 5 turbines (5 x 6 MW) off the coast of Aberdeen, Scotland (Fig. 1.4) followed by other projects (Fig. 1.5). Equinor's FOWT farm has been producing electricity since October 2017 with a 65% capacity factor (the capacity factor of onshore wind turbines being around 30%, offshore wind: 40%, hydro-power: 50% and photo-voltaic: 18%, based on IEA data). In 2011, Principle Power Inc. installed its first 2 MW FOWT prototype WindFloat off the coast of Aguçadoura, Portugal. The FOWT was dismantled in 2016 after 5 years of deployment, to let place to the new generation of WindFloat units as illustrated in Fig. 1.6: a farm of 3 turbines was installed in 2019 off the coast of Viana de Castelo, Portugal.

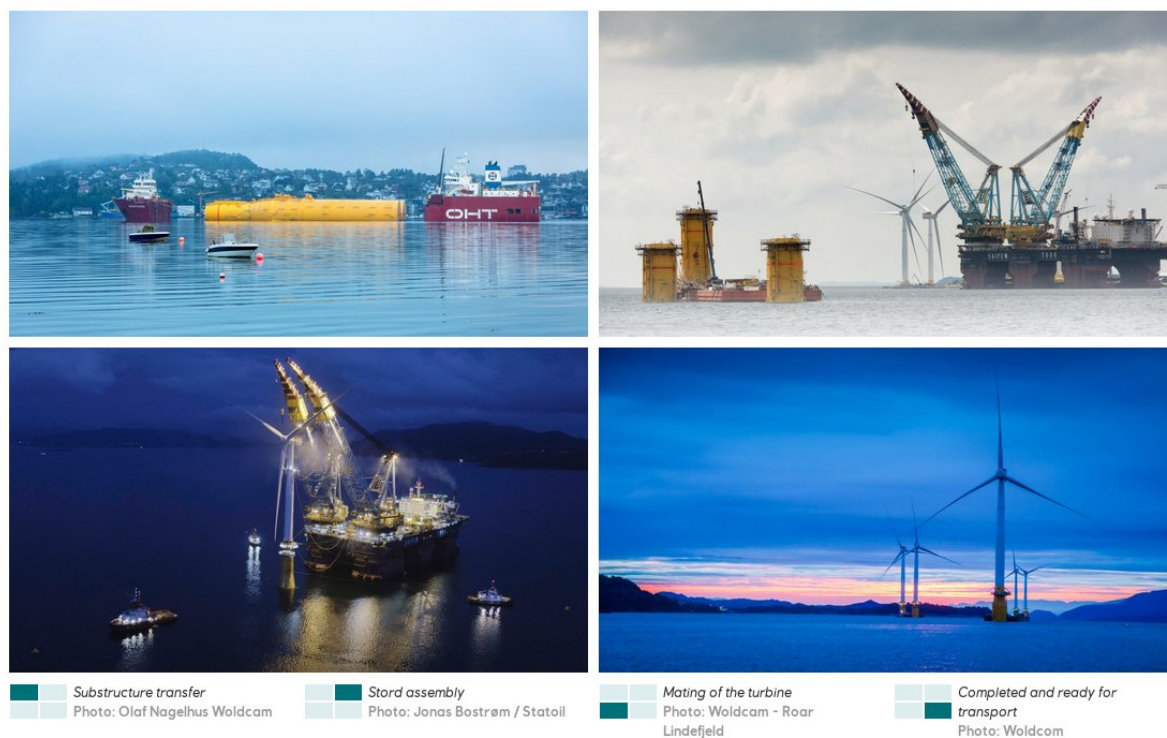


Figure 1.4: Hywind floating wind park (Source: Equinor website).

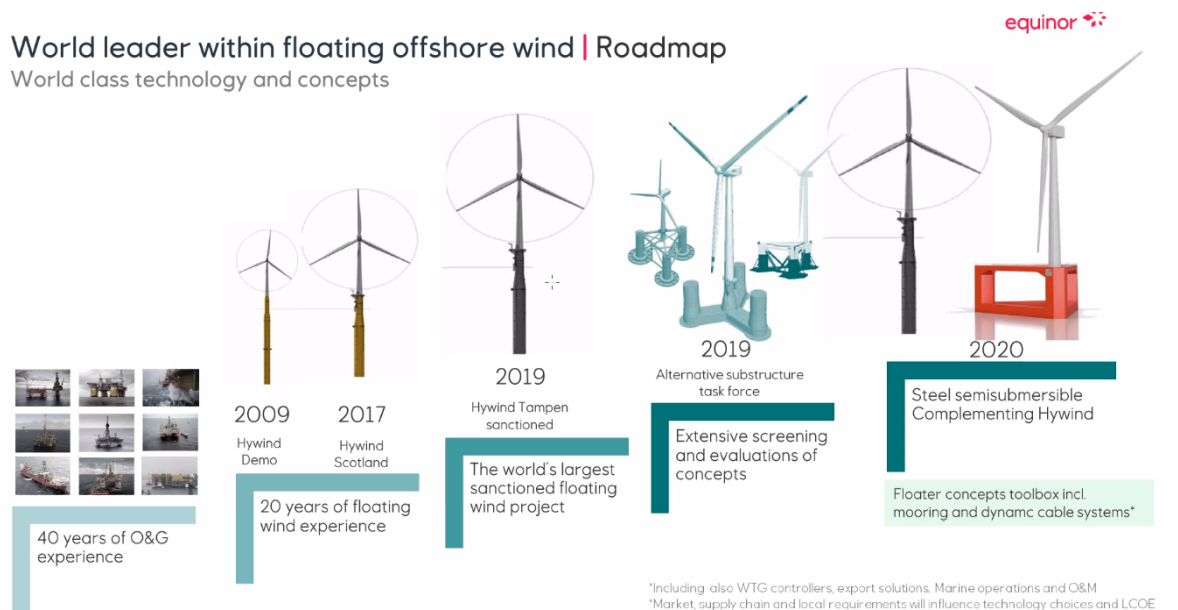


Figure 1.5: Hywind floating roadmap (Source: IOWTC2021 Equinor presentation).

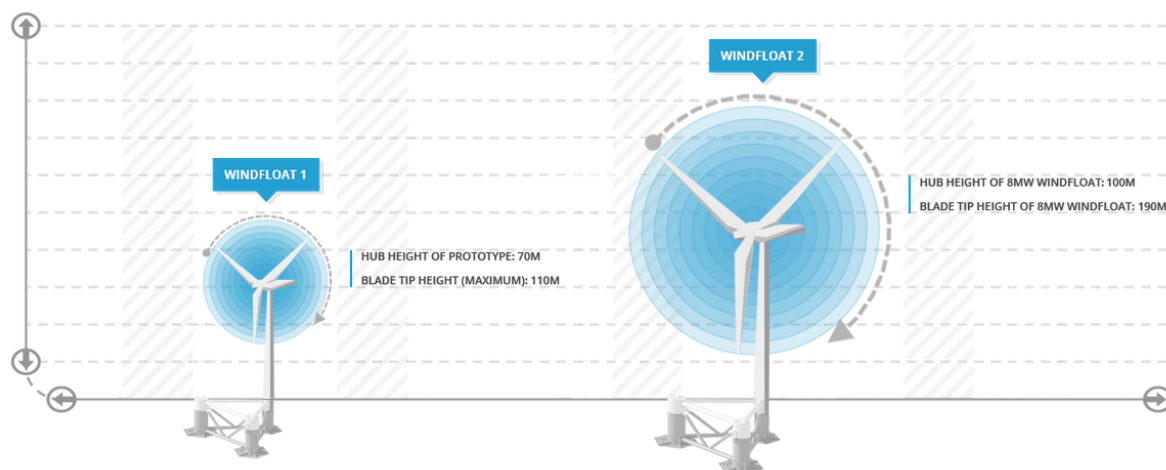


Figure 1.6: WindFloat FOWTs (Source: WindFloat website).

More and more research is done to support the development of FOWT and new projects are often announced at dedicated international events such as Floating Offshore Wind Turbine Conference or the International Offshore Wind Technical Conference.

Floating wind turbines have many advantages compared to their fixed counterpart, as detailed by Sarmiento J. [2018]:

- They are less sensitive to water depth than bottom-fixed turbines (limited to shallow waters $\simeq 20\text{-}50$ m). This increases the number of possible installation sites (in France, UK, Japan, Norway or USA).
- The wind is more stable and higher far from the coast and can be more easily predicted. This leads to a better control of electricity generation and eases grid management.
- Installation emits less noise thus decreasing the environmental impact. Heavy and intrusive foundations required for bottom-fixed foundations are not used for floaters and replaced by anchoring system. The turbine can be assembled at quayside and then towed to the location with standard vessels, which decreases the time of installation compared to bottom-fixed offshore wind turbines.

In Fig. 1.7 below, different kinds of offshore wind structures are depicted:

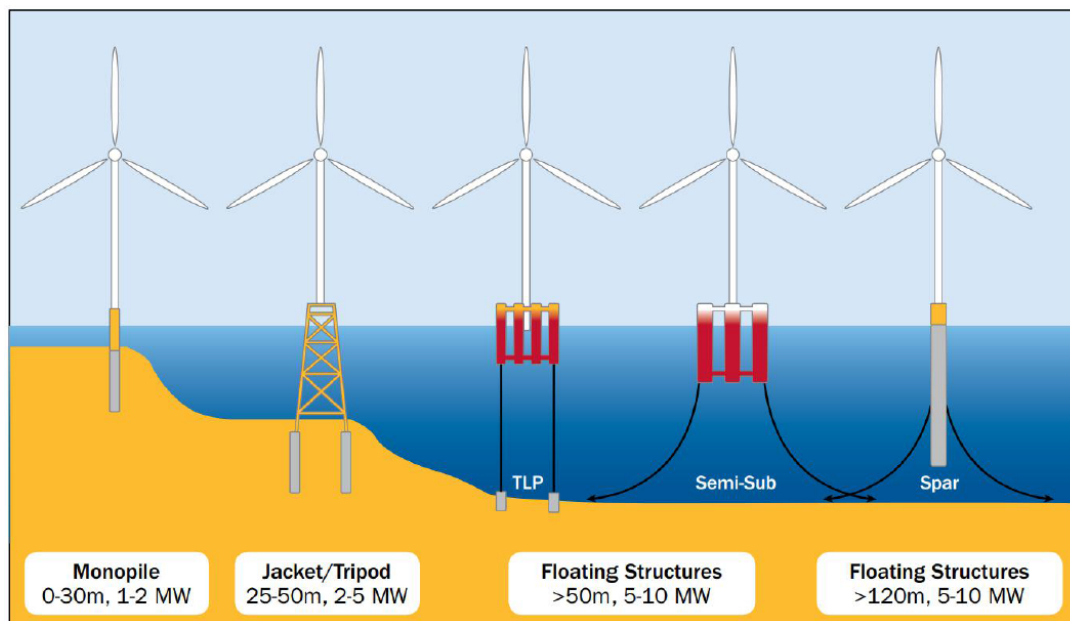


Figure 1.7: Different types of offshore wind turbines (Source: Principle Power website).

In the next sections, bottom-fixed foundations are presented followed by the various floating structures.

1.2 Bottom fixed offshore wind structures

Different structures co-exist as it can be seen in Fig. 1.8. The most common, because of its rather easy manufacturing and installation, is the monopile. It is suited for shallow waters with a depth between 0 and 30 m. Jacket structures also exist and are suited for larger water depth (20 m-50 m). Wave loads on these structures are smaller than for monopiles: no wave vibration is induced and the turbine behaves quite like an onshore one. However, jackets are more expensive and maintenance costs are larger than for monopiles. Gravity based structures (GBS) that can also be used to support offshore fixed turbines, are limited to moderate wave loads but the manufacturing cost remains rather low due to the use of concrete.

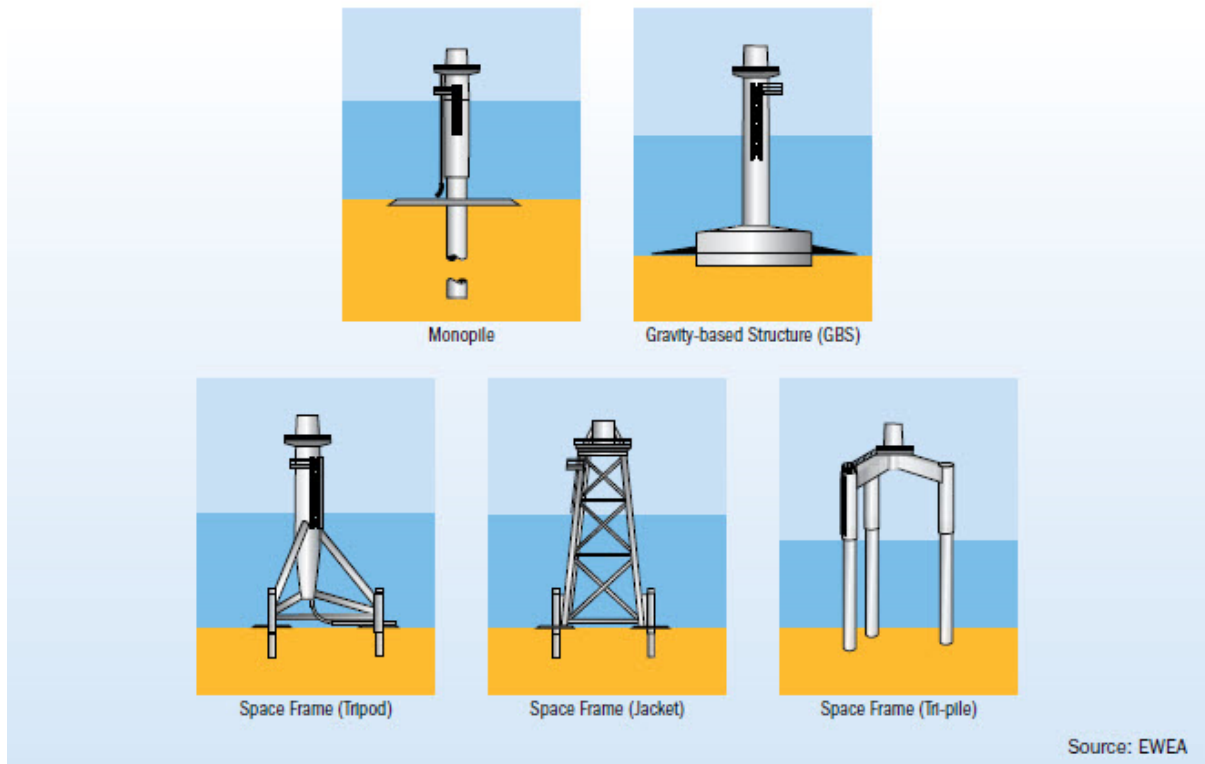


Figure 1.8: Typical fixed offshore wind turbine foundations (Source: EWEA website).

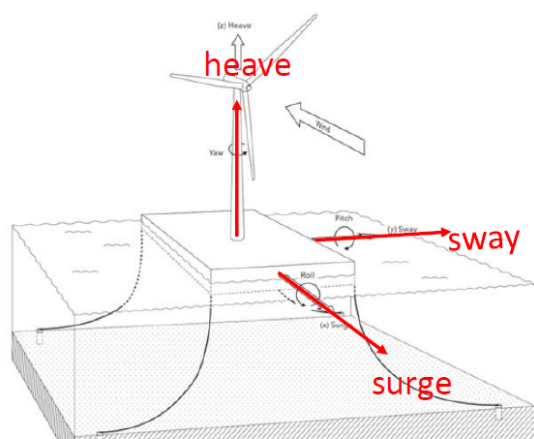
1.3 Floating Offshore Wind Turbines (FOWT)

A FOWT is made of three components: the wind turbine, the floater and its mooring system.

1.3.1 Degrees of freedom for floater motion

In waves, large motions of the floater occur and can be decomposed in 6 rigid body modes: surge, sway, heave, roll, pitch and yaw.

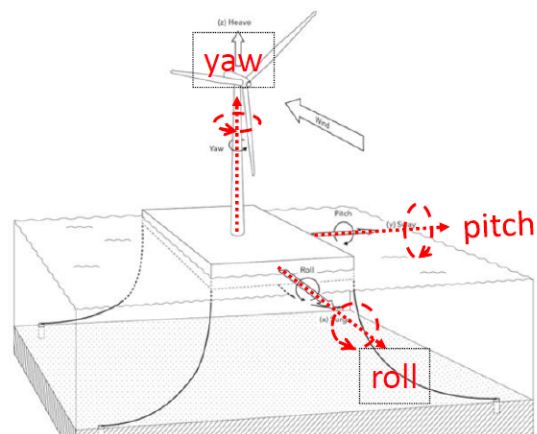
They correspond to three translations and three rotations around the main axes of the structure under study, in an orthogonal coordinate system as explained in MARINeT2 courses by Gueydon S. [2018] and as represented in Fig. 1.9 and 1.10.



Source: DNVGL RP 0286

14

Figure 1.9: Translation



Source: DNVGL RP 0286

15

Figure 1.10: Rotation

Figure 1.11: Degrees of freedom definition of the floating body.

1.3.2 Mooring system

Station-keeping solutions avoid the drift of the floater (limited surge and sway offset represented in Fig. 1.9). FOWT are anchored to the seabed by different means, depending on the soil characteristics and mechanical constraints: dead weight anchors, drag embedment anchors, anchor piles or vertical load anchors. The station keeping solutions put at stake catenary mooring line or tension leg solutions. In the case of Tension Leg Platform (TLP), the mooring system also aims at stabilising the floater and minimising its motion.

1.3.3 Stability strategies

Floating wind turbines are usually categorised according to the floater stability strategy as shown in Fig. 1.7.

- Ballast stabilized: the center of gravity is far below the mean sea level. Spar-type floaters consist in long cylindrical platforms with ballast weight at the bottom to lower the gravity center.
Ex: Hywind Scotland wind farm, Equinor.
- Mooring line stabilised: the stability is provided by the station-keeping system which consists in tensioned lines. The mooring system keeps the platform at a draft that is larger than its natural equilibrium value. The resulting excess in buoyancy maintains the tension in the moorings, which in turn preserves the stability of the platform.
Ex: Pelastar TLP (Nordstrom, 2013), Iberdrola TLP, SBM Offshore/IFPEN TLP.
- Buoyancy stabilized: the restoring effect from a large water-plane area ensures stability. Semi-submersible floaters consist of large-diameter hulls that are connected

with slender braces. This configuration limits the wave loads compared to a barge.
Ex: WindFloat 1 (2 MW) installed off the Portuguese coast (2011-2015).

1.4 Design of a FOWT

1.4.1 Coupled engineering tools

Specific engineering tools are used to design FOWT. These so-called aero-hydro-servo-elastic solvers simulate the coupled behaviour of the turbine subject to wind and the floater motion due to waves, including elasticity of the whole structure. The modelling of coupled interactions such as the aerodynamic impact on mooring-line fatigue or conversely the impact of the platform motion on aerodynamic loads. Thousands of Design Load Cases (DLC) are run to test the behaviour of the FOWT in different conditions, including fatigue and extreme events. The design of the system is thus validated or modified according to modelling results, to verify design criteria on the motion, acceleration, tension in mooring lines, structural forces and moments, ...

IFPEN with Principia has developed a tool marketed since 2011 under the name of DeepLinesWind™. This aero-servo-hydro-elastic solver is used to simulate wind turbines in their environment, aiming at optimising their design and reducing costs. Coupled simulations with aerodynamic loads, turbine and floater structural dynamics, active controller, hydrodynamic loads and mooring line dynamics can be performed. As detailed by Le Cunff et al. [2013], a non linear beam finite element formulation is included to model the structural component flexibility - blades, drivetrain, tower, floater, mooring lines and umbilicals - for both horizontal and vertical axis wind turbines. The floating supports are defined with hydrodynamic database computed with seakeeping program such as DIODORE or WAMIT, including added mass and radiation damping matrices, 1st order and 2nd wave loads (Chapter 2.4). Wave loads can also be computed based on Morison empirical formulation (Chapter 2.3).

OpenFAST is another engineering tool, opensource, able to simulate the coupled dynamic response of wind turbine. This aeroelastic computer-aided engineering (CAE) code is developed by Jonkman et al. [2005] from NREL. As DeepLinesWind™, aero-hydro-servo-elastic simulations of wind turbines are run to analyse a range of wind turbine configurations.

Aerodynamics for onshore wind (rating below 5 MW) and hydrodynamics for O&G offshore structures have been developed for many years. However, their application to design FOWT raises new research questions. In particular, the use of hydrodynamic theories inherited from the O&G sector to predict wave loads on FOWT can reveal some limitations.

1.4.2 Limitations of the standard O&G hydrodynamic practices when applied to FOWT design

Two theories, extensively used for offshore O&G systems, are implemented in design solvers to model the hydrodynamic load and behaviour of FOWT. The choice of the theory applied to describe wave loads on the floater mainly depends on the diameter of the system (D) and of the wave amplitude (A) as presented in Fig. 1.12 and detailed in Molin [2002]:

- **Potential flow theory** (large body, $A \ll D$)

The oscillating flow is not fast enough for the detachment of the boundary layer. Hydrodynamic forces on the floater can be calculated thanks to linear potential theory detailed in the section 2.4.2.

- **Morison empirical formula** (small body, $A \gg D$)

The oscillating flow is detached from the surface of the body. Morison force requires empirical coefficients as detailed in the section 2.3.

A more detailed classification is presented in the section 2.3.3.

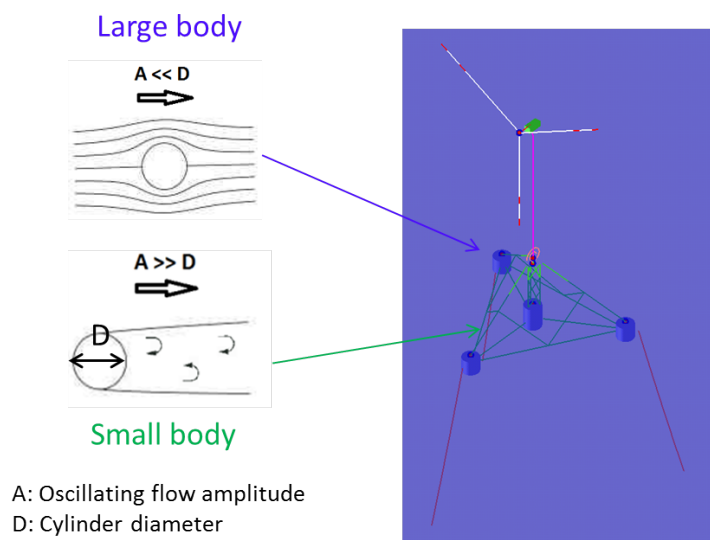


Figure 1.12: Potential theory and Morison empirical formula.

Historically developed for the design of offshore O&G systems, using these theories for FOWT design with the same standard practices, may not lead to an optimised design:

- Under specific wave characteristics and structure dimensions, the FOWT can be at the limit of the validity range of these theories and combination of both theories require to be considered as explained in the section 2.3.3.
- Regarding Morison formula, database of hydrodynamic coefficients were obtained with various test campaigns (section 2.3.1) and were extensively used for the design

of offshore platform. Some assumptions or simplifications are commonly considered for sake of simplicity and robustness, such as using one set of coefficients whatever the sea state and identical for all the braces. One can wonder if such databases and their standard implementation are sufficiently accurate in the context of FOWT design (higher economic constraints, lower safety constraints). Morison coefficients depend on the braces and the buoys dimensions (diameter and length), the proximity of the considered part of the floater with the free surface, the interaction between the braces, the braces orientation and the motion of the floater or the wave characteristics (amplitude, frequency). Including this complexity in the design process could lead to design optimisation.

- Irregular waves are responsible for second-order wave loads that are known not to be accurately predicted with engineering tools compared to experimental results (section 4.1.3). They appear to be under-estimated applying potential flow theory and on the contrary over-estimated when using Morison formula.
- Some limits of the experimental tests extensively used to validate and calibrate the design models can also be highlighted: they are expensive and their number is limited. Also, scaling relative problems exist. Keeping relevant all non-dimensional similarity parameters between the scaled model and the full-scale prototype remain difficult. A choice has to be made between Froude and Reynolds similarities detailed in Annexes 9.1.

1.4.3 High fidelity simulations to model the hydrodynamic of a FOWT floater

The above mentioned limitations justify the study of FOWT hydrodynamics with an alternative tool: the Computational Fluid Dynamics (CFD). CFD is a recent solution to model the hydrodynamic behaviour of a FOWT in waves. Navier-Stokes equations are resolved for the fluid and Newton law is applied to determine the floater motion. CFD simulations provide comprehensive information about pressure and velocity fields, as well as load distributions on specific part of the float. Different wave characteristics and structure dimensions can be modelled in CFD simulations. However, it often comes with high computation costs and numerical uncertainties. The latter has to be evaluated with validation studies.

1.5 The thesis objective

In such a context, this thesis is proposed to contribute to the following problematic: How can we evaluate, improve and adapt the commonly used hydrodynamic theories to FOWT design, thanks to CFD modelling?

To address this research question, a three-stage methodology is followed in the thesis:

1.5.1 Numerical Wave Tank implementation

A Numerical Wave Tank (NWT) is implemented in the open-source CFD tool OpenFOAM, in which waves are generated, propagated and absorbed. Different CFD libraries are tested to generate waves, in order to select the most appropriate library to then run fluid-structure interaction cases. The numerical model is validated against experiments (Stansberg [1997]). The waves at stake are regular, deep-water and non breaking type. A rigorous methodology is developed in order to ascertain the accuracy of the wave-only model. Once it is ensured that waves can be generated and propagated in a controlled way, minimising any reflection or damping phenomena, the structure is included into the simulation. This first step dealing with the validation of the Numerical Wave Tank is crucial since the hydrodynamic analyses proposed in the thesis rely on the CFD results.

1.5.2 Surface piercing cylinder in regular waves

Secondly, the interaction of a fixed surface-piercing cylinder with regular waves is modelled. The CFD case is validated against experiments Stansberg [1997]. It consists in a vertical piercing cylinder in deep water waves, similar sea conditions in which FOWTs usually operate. This simple case enables us to validate a first wave-structure interaction CFD case before focusing on a more complex structure: the TLP. A first comparison between CFD results and Morison approach is led on this case. We propose the so-called slice methodology to determine Morison coefficients from CFD loads along the cylinder. The impact of the interface on the loads, not taken into account in Morison empirical formula, is also investigated. This methodology can then be extended to more complex structures and realistic floating offshore wind turbines.

1.5.3 SBM Offshore/IFPEN Tension Leg Platform in regular waves

The Tension Leg Platform developed by SBM Offshore/IFPEN is modelled in deep water waves. CFD results are validated against experiments performed at MARIN Offshore wave tank, Netherlands and presented by Caillé et al. [2017]. As a first stage, the structure is set fixed. This simplifies the CFD model, comparing experimental and numerical excitation loads only and easing the analysis of the results. The motion of the floater using a 6 degrees of freedom (DOF) solver is simulated separately, see for example Borràs Nadal and Bozonnet [2020], and both features (wave and motion) will be combined in a future work. Once the CFD model has been validated against experimental data, an analysis is performed to evaluate the commonly used Morison empirical formula based on CFD simulations. First, Morison coefficients are determined from CFD loads, adapting the above-mentioned slice methodology to the FOWT platform. The coefficient values are compared to those commonly used in DeepLinesWind™ (based on standards or experimental comparison). The Morison theory assumptions (infinite cylinder, undisturbed flow, submerged cylinder) are checked by comparing CFD loads to theoretical

loads derived from design tool simulations. The load and Morison coefficient variation throughout the structure is assessed. Finally, this work is extended to other wave characteristics (height, period). Combined with the other structure characteristics (length, orientation, vicinity with other braces or free surface), a database of Morison coefficients adapted to FOWT is thus obtained.

1.6 Outline of the thesis

This report is constructed as follows:

The context and the problematic of the thesis were described in Chapter 1.

Part I is devoted to the state of the art of the thesis. Chapter 2 is devoted to the commonly used hydrodynamic theories for FOWT design and potential limitations.

In Chapter 3, OpenFOAM software and the specifics at stake to implement a NWT are presented.

The state of the art dealing with the hydrodynamic modelling of FOWT studies to improve theoretical and empirical formulations is conducted in Chapter 4.

Part II presents the main results of the thesis, articulated in three chapters.

Chapter 5 presents the two-step methodology proposed in the PhD thesis to investigate wave loads on a floater. The first section deals with the set up of a Numerical Wave Tank. We propose some guidelines to generate, propagate and absorb waves in a controlled way along space and time. The numerical slice methodology for determining Morison coefficients from CFD loads on the complex FOWT floater is developed in the second section.

In Chapter 6, the case of a surface-piercing cylinder in regular waves is presented. The CFD model implementation and validation is presented. Then the wave loads on the structure are studied and the agreement between Morison approach and CFD results is investigated. The last section focuses on the physical analysis of the influence of the interface on the wave loads.

In Chapter 7, we investigate FOWT hydrodynamics. The SBM Offshore/IFPEN TLP floater is modelled in a constrained configuration subjected to regular waves. The CFD case is validated against experiments. Three different waves are modelled. The applicability of Morison formula for FOWT load prediction is evaluated. The impact of the structure, the interface and the brace orientation on the wave loads, not taken into account when applying Morison approach in design tools, is investigated. To conduct this analysis, Morison coefficients are notably derived from CFD loads applying the numerical slice methodology. Some advice to improve Morison formula for FOWT load prediction are proposed at the end of the chapter.

Finally, conclusions, main findings and perspectives are summarised in Chapter 8.

Part I

State of the Art

Chapter 2

Hydrodynamics of offshore floating structures

This part describes the theoretical background to study the motion of floating structures in waves, referred as hydrodynamic or sea-keeping theories. Though the thesis aims at evaluating the hydrodynamic loads on a complex and realistic FOWT platform, in this chapter, hydrodynamic background for a cylinder is presented. Indeed, a major part of hydrodynamics for offshore structures deals with circular cylinders and can be extended to more complex offshore systems, with some assumptions and modifications, since these structures mostly consist of cylinders assembly.

2.1 Wave theory

Most of this part focusing on waves is based on the book of Molin [2002] entitled "Hydrodynamique des structures offshore". First, the potential theory applied to determine regular wave velocity and elevation is detailed. Then, Airy waves (1st order), Stokes 2nd and Stokes 3rd order wave formulations are presented.

2.1.1 Regular wave characteristics

Only regular waves are considered in this report. Irregular waves are commonly defined as a sum of regular waves but are not detailed here. A regular wave is progressive if it propagates in one direction. Regular wave consists in harmonic wave characterised by several parameters depicted in Fig. 2.1:

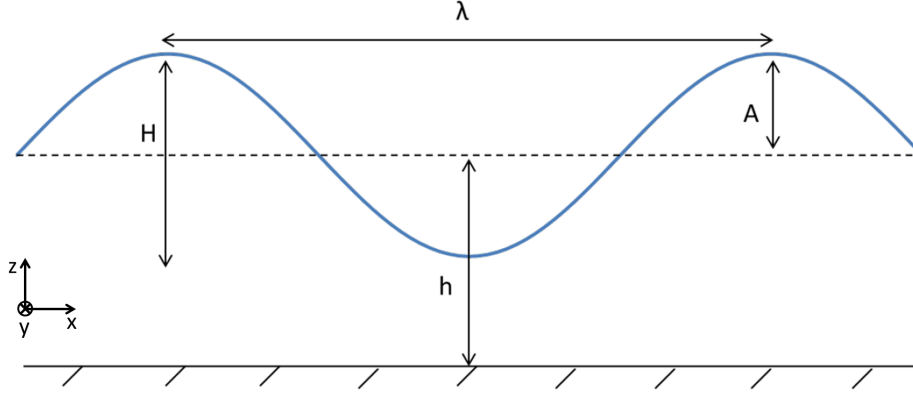


Figure 2.1: Regular wave main characteristics.

- H: Wave height (crest to trough) [m]
- A: Wave amplitude [m]
- h: Mean water depth [m]
- T: Wave period [s]
- g: Gravitational acceleration [$\text{m}\cdot\text{s}^{-2}$]
- λ : Wavelength [m]

2.1.2 Potential theory

In the orthonormal basis $(Oxyz)$, the velocity potential Φ is defined as:

$$\vec{V}(x, y, z, t) = \nabla\Phi(x, y, z, t) \quad (2.1)$$

Considering u , v and w the velocity components of the flow along (Ox) , (Oy) and (Oz) axes, the potential difference between two points A and B in the fluid is introduced by Massie and Journée [2001] as:

$$\begin{aligned} \Delta\Phi_{A \rightarrow B} &= \int_A^B \vec{V} \cdot d\vec{s} = \int_A^B (u \cdot dx + v \cdot dy + w \cdot dz) \\ &= \int_A^B \left(\frac{\partial\Phi}{\partial x} dx + \frac{\partial\Phi}{\partial y} dy + \frac{\partial\Phi}{\partial z} dz \right) = \int_A^B d\Phi = \Phi(B) - \Phi(A) \end{aligned} \quad (2.2)$$

The potential function Φ can thus be defined by the three following equalities:

$$u = \frac{\partial\Phi}{\partial x} \quad v = \frac{\partial\Phi}{\partial y} \quad w = \frac{\partial\Phi}{\partial z} \quad (2.3)$$

Considering an infinite ocean of water filled by an incompressible, non-viscous, irrotational (i.e. null velocity gradient) flow, the four conditions below have to be verified:

1. **Laplace equation** (mass conservation):

$$\Delta \Phi = 0 \quad (2.4)$$

2. **No-leak boundary condition:** The vertical velocity of a water particle at the seabed is zero.

$$\frac{\partial \Phi}{\partial z} = \Phi_z = 0 \quad z = -h \quad (2.5)$$

3. **Free surface dynamic boundary condition**

The pressure p of the fluid at the free surface ($z = \eta(x, y, t)$) is equal to the atmospheric pressure p_0 . This leads to:

$$\Phi_t + \frac{1}{2}(\nabla \Phi)^2 + gz = 0 \quad \text{at } z = \eta(x, y, t) \quad (2.6)$$

4. **Free surface kinematic boundary condition**

The vertical velocity of a particle at the free surface is equal to the vertical velocity of the free surface itself. This means that the free surface is considered as a material surface.

$$\eta_t + \Phi_x \eta_x + \Phi_y \eta_y = \Phi_z \quad \text{at } z = \eta(x, y, t) \quad (2.7)$$

Φ can also be developed in a Taylor series for z along water depth as:

$$\Phi(x, y, z, t) = \Phi(x, y, 0, t) + z\Phi_z(x, y, 0, t) + \dots \quad 0 \leq z \leq \eta(x, y, t) \quad (2.8)$$

The resolution of the system formed by 2.4, 2.5, 2.6 and 2.7 for the potential, with Taylor development leads to Stokes wave theory. Stokes order depends on the order of the Taylor development realised. In Fig. 2.2, Le Méhauté diagram details the wave theories and the order of Taylor development that should be selected to correctly model a wave depending on the wave height, wave period (noted τ in the graph) and water depth.

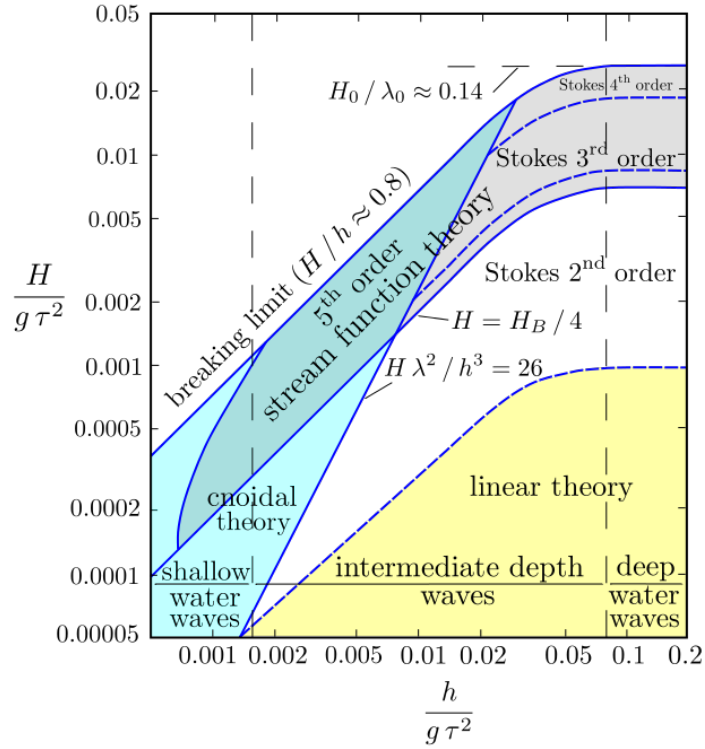


Figure 2.2: Validity of several theories for periodic water waves, according to Méhauté [1976].

2.1.3 Airy waves

First the wave is assumed periodic in time and in space. The flow is restrained to the (Oxz) vertical plane. The resolution of the system above using first order Taylor development for the velocity potential leads to the following expression of the free surface elevation:

$$\eta^{(1)} = A \cos(kx - \omega t) \quad (2.9)$$

The first order velocity potential is expressed as:

$$\Phi^{(1)} = \frac{Ag}{w} \frac{\cosh k(z+h)}{\cosh kh} \sin(kx - \omega t) \quad (2.10)$$

The free surface kinematic boundary condition leads to the dispersion relation valid only for regular waves:

$$\omega^2 = gk \tanh kh \quad (2.11)$$

The wavelength $\lambda = \frac{2\pi}{k}$ can then be expressed as:

$$\lambda = \frac{gT^2}{2\pi} \tanh \frac{2\pi h}{\lambda} \quad (2.12)$$

This relation can be solved iteratively. For infinite depth (i.e. $\tanh \frac{2\pi h}{\lambda} \simeq 1$), it can be

simplified as:

$$\lambda = \frac{gT^2}{2\pi} = 1.56T^2 \quad (2.13)$$

From the velocity potential 2.10 and the dispersion relation, the kinematics of water particle can be expressed by the orbital velocities expressed below:

$$u = \frac{\partial\Phi}{\partial x} = \frac{\partial x}{\partial t} = \frac{Agk \cosh k(z+h)}{\omega \sinh kh} \sin(kx - \omega t) \quad (2.14)$$

$$w = \frac{\partial\Phi}{\partial z} = \frac{\partial z}{\partial t} = \frac{Agk \sinh k(z+h)}{\omega \sinh kh} \sin(kx - \omega t) \quad (2.15)$$

Depending on water depth, velocity fields will be different as shown below:

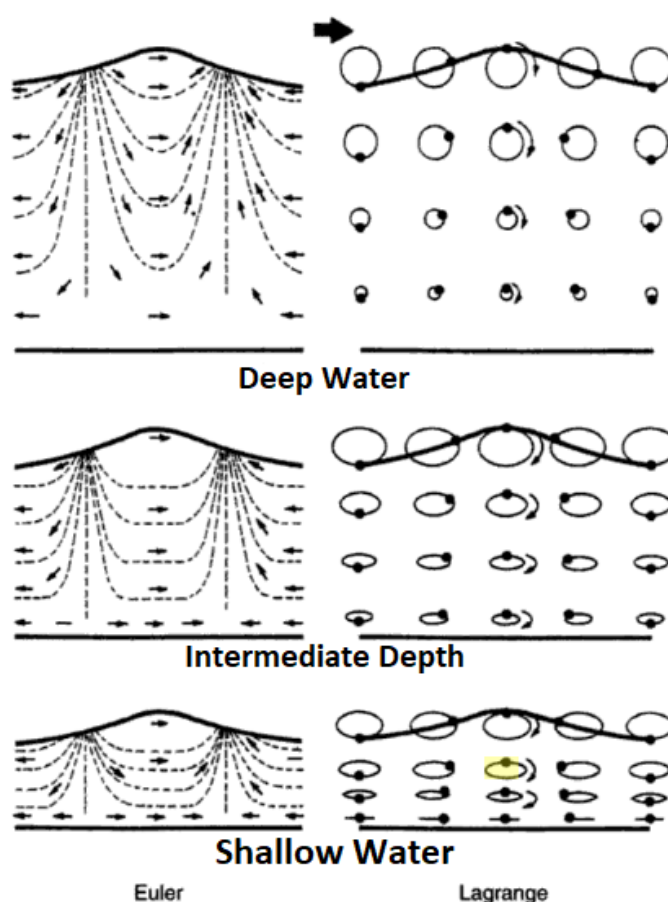


Figure 2.3: Velocity field (left side) and velocity orbitals (right side) in deep, intermediate and shallow water (Susbielles et al. [1981]).

Also, with the dispersion relation, the phase velocity (velocity of peaks) $c = \omega/k$ can be determined as:

$$c = \sqrt{\frac{g}{k} \tanh kh} \quad (2.16)$$

In deep water, $\tanh kh = 1$ leads to $c = g/\omega$.

In shallow water, $\tan kh = kh$ leads to $c = \sqrt{gh}$

2.1.3.1 Pressure field for Airy waves

The pressure and velocity are key variables in hydrodynamics. For Airy waves, the pressure field can be obtained by solving Bernoulli equation with the expression of the velocity potential given in 2.10.

As detailed by Massie and Journée [2001], for an unsteady and irrotational flow, the Bernoulli equation leads to:

$$\frac{\partial\Phi}{\partial t} + \frac{1}{2}(u^2 + v^2 + w^2) + \frac{p}{\rho} + gz = Constant \quad (2.17)$$

In two dimensions ($v = 0$) and assuming the waves have a small steepness (u and w are small), this equation becomes:

$$p = -\rho gz - \rho \frac{\partial\Phi}{\partial t} \quad (2.18)$$

From the wave velocity potential 2.10, the following expression of the linearised pressure at first order is obtained:

$$p = -\rho gz + \rho g A \frac{\cosh k(h+z)}{\cosh kh} \cos(kx - \omega t) \quad (2.19)$$

The first term of this expression is the hydrostatic pressure. The second one is the dynamic pressure, associated to waves.

In deep water ($kh \geq 3$), the linearised pressure is:

$$p = -\rho gz + \rho g A e^{kz} \cos(kx - \omega t) \quad (2.20)$$

In shallow water ($kh \ll 1$), the pressure becomes:

$$p = -\rho gz + \rho g A \cos(kx - \omega t) \quad (2.21)$$

2.1.4 Stokes 2nd order waves

In operation conditions, FOWT are usually subjected to waves belonging to the second order Stokes category according to Le Méhauté classification (Fig. 2.2). The wave elevation expression is notably used to compare the CFD wave elevation obtained at one location in the NWT to the corresponding theoretical signal. Velocity and acceleration expressions are crucial in the numerical slice method proposed to derive Morison coefficients from the CFD loads on the floater.

Stokes second order wave potential is the sum of the velocity potential $\Phi^{(1)}$, derived in the previous paragraph, and the second order potential $\Phi^{(2)}$. The three boundary conditions (2.5, 2.6 and 2.7) combined with Laplace Eq. 2.4 leads to the following expression:

$$\Phi^{(2)}(x, z, t) = \frac{3}{8} \frac{A^2 w}{\sinh^2 kh} \cosh 2k(z+h) \sin 2(kx - \omega t) \quad (2.22)$$

The free surface elevation is obtained as:

$$\eta(x, t) = \eta^{(1)}(x, t) + \eta^{(2)}(x, t) \quad (2.23)$$

in which $\eta^{(2)}(x, t)$ is the second order component of the free surface elevation defined as as:

$$\eta^{(2)}(x, t) = \frac{A^2 k}{4} (3 \coth^3 kh - \coth kh) \cos 2(kx - \omega t) \quad (2.24)$$

If one deals with deep water waves (i.e $kh \geq 3$), $\Phi^{(2)}$ is null and the second order free surface elevation component becomes:

$$\eta^2(x, t) = \frac{1}{2} A^2 k \cos 2(kx - \omega t) \quad (2.25)$$

2.1.5 Stokes 3rd order waves

In this section, the waves are assumed infinite. The velocity potential developed to the third order is defined in Eq. 2.26 as:

$$\Phi(x, z, t) = \frac{Ag}{\omega} e^{k'z} \sin(k'x - \omega t) \quad (2.26)$$

where $k' = (1 - A^2 k^2)k$.

The free surface elevation is defined in Eq. 2.27 as:

$$\eta(x, t) = (1 - \frac{3}{8} A^2 k^2) A \cos \theta + \frac{1}{2} A^2 k \cos(2\theta) + \frac{3}{8} A^3 k^2 \cos 3\theta \quad (2.27)$$

where $\theta = (k'x - \omega t)$.

The development of the velocity potential to the third order does not impact the prediction of the peak-to-peak amplitude but can lead to a difference on the predicted value of the wavelength compared to Airy and Stokes 2nd order theories.

More complex methods exist, to notably to take into account wave nonlinearities such as Dean [1976] stream function, but are not used in this PhD thesis.

The velocity potential, free surface elevation and pressure field describing waves were detailed in this section. The following section focuses on hydrodynamic loads on a cylinder in an oscillating flow. Finally, hydrodynamic loads on offshore floating structures will be described in the last section.

2.2 Cylinder in an oscillating flow

This section aims at describing the hydrodynamic loads on a cylinder in an oscillating flow representing wave effects. It focuses on the dynamic loads obtained due to the oscillating flow. In this case, the hydrostatic load is the buoyancy. First, the potential

theory is applied to describe dynamic loads on the cylinder referring to Molin [2002]. Then, Morison experimental formula is introduced.

As for wave theory described previously in the section 2.1, the following fluid hypotheses have to be respected in order to be in potential flow condition: incompressible, non viscous, continuous and homogeneous fluid.

The inline flow on a given cylinder, represented in Fig. 2.4 ((R, θ) the cylinder frame), is considered.

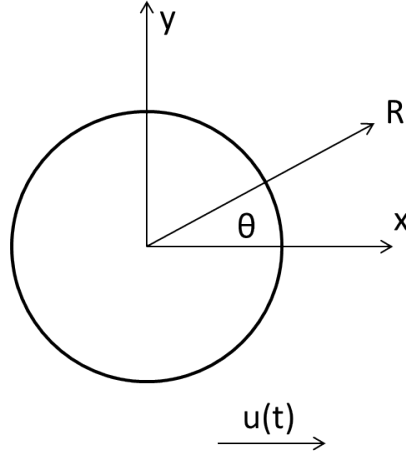


Figure 2.4: Cylinder scheme and reference frames.

The flow is supposed oriented along (Ox) and $u(t)$ is the velocity along this axis. This leads to the incident potential Φ_I respecting the following Eq. 2.28:

$$\Phi_I = u(t)x = u(t)R \cos \theta \quad (2.28)$$

The cylinder is considered as infinite and loads on the cylinder are given per cylinder length in the following subsections.

2.2.1 Fixed cylinder in an oscillating flow

The cylinder is considered fixed. The resulting forces on the cylinder in (Ox) direction is given by:

$$F_x(t) = \int_S p(R, \theta, t) \vec{dr} \cdot \vec{n} = \int_0^{2\pi} p(R, \theta, t) R \cos \theta d\theta = 2\rho\pi R^2 \dot{u}(t) \quad (2.29)$$

where p is the dynamic pressure defined in Eq. 2.19.

F_x is also known as Froude-Krilov force: the force resulting of the integration of pressure over the surface of the cylinder in an undisturbed flow.

2.2.2 Moving cylinder in a flow at rest

Considering a moving cylinder in a flow at rest, $\ddot{X}(t)$ its acceleration in (Ox) direction, the hydrodynamic force is given by:

$$F_x = -\rho\pi R^2 \ddot{X}(t) \quad (2.30)$$

2.2.3 Generalisation to a moving cylinder

Finally, hydrodynamic loads on a moving cylinder in an oscillating flow applying potential theory are expressed by:

$$F_x = (1 + C_{axx})\rho S\dot{u}(t) - C_{axx}\rho S\ddot{X}(t) \quad (2.31)$$

$$F_y = (1 + C_{ayy})\rho S\dot{v}(t) - C_{ayy}\rho S\ddot{Y}(t) \quad (2.32)$$

where S is the cylinder section in (Oxy) plan, $u(t)$ and $v(t)$ the flow velocity component in (Ox) and (Oy) directions, $X(t)$ and $Y(t)$ the position of the cylinder in (Oxy) coordinate system. C_{axx} and C_{ayy} are the added mass coefficient for radiation in each direction (equal to 1 for a circular section in potential flow theory).

In equations 2.31 and 2.32, due to the assumption of a perfect flow, no viscosity is taken into account. To include viscous loads and detached flow on the cylinder, a specific empirical formula was derived for oscillating viscous flows on a cylinder: Morison formula.

2.3 Morison force approach

When one deals with small structures ($D/\lambda < 0.1$), viscous effects become important and have to be included to derive hydrodynamic loads in motion equation. In 1950, Morison et al. [1950] introduced the famous empirical formula for the wave force on a constrained vertical cylinder (infinite cylinder, ignoring end effect), as the sum of an inertia and a drag term. The consideration of an infinite cylinder combined with the restriction to slender cylinders implies that the surrounding flow around the cylinder is the same at any instant t . The flow can thus be characterized at a single point: the center of the cylinder.

$$F_x(t) = \rho C_M \frac{\pi D^2}{4} \dot{u}_x(t) + \frac{1}{2} \rho C_D D u_x(t) |u_x(t)| \quad (2.33)$$

In which:

- x : the component in the direction of wave propagation
- C_D : the dimensionless drag coefficient
- $C_M = 1 + C_a$: the dimensionless inertia coefficient
- $u_x(t)$ and $\dot{u}_x(t)$ are respectively the wave orbital velocity and acceleration in the direction of the force x at the center of the cylinder. $|u_x(t)|$ the magnitude of the velocity.

More precisely, the inertia term expression was demonstrated by Morison to be the sum of the Froude-Khrilov force (2.29) and an additional force to model the impact of the structure on the flow expressed by:

$$C_A \rho S \dot{u}(t) \quad (2.34)$$

C_A is often known as the hydrodynamic mass. Thus the total inertia force is:

$$F_I = (1 + C_A) \rho S \dot{u}(t) = C_M \rho S \dot{u}(t) \quad (2.35)$$

If C_A is equal to one, then C_M is 2 and one deals with a potential flow (Eq. 2.31).

This formula was then generalised by Borgman [1958] and other researchers (Chakrabarti et al. [1977], Sumer et al. [2006] and Massie and Journée [2001]) to arbitrarily oriented cylinders. We propose the following notation for the generalisation of Morison formula, as represented in Fig. 2.5.

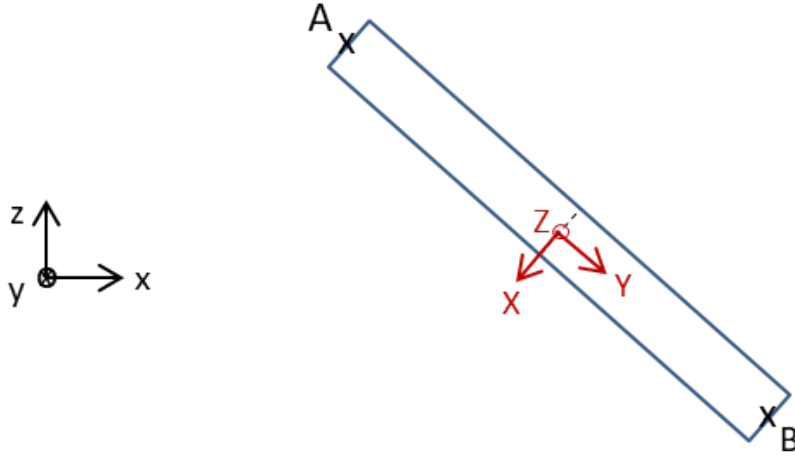


Figure 2.5: Frame of the brace.

A local orthonormal frame is defined as follows: \mathbf{Y} is the vector along the axis oriented from A to B, \mathbf{X} and \mathbf{Z} the normal vectors to the cylinder axis. The axial force component (parallel to the cylinder axis along \mathbf{Y}) is considered as negligible and so the force vector is included in the plan perpendicular to the cylinder axis containing \mathbf{X} and \mathbf{Z} , its components defined as:

$$F_X(t) = \frac{1}{2} \rho C_D D U(t) \|\mathbf{V}_n(t)\| + \frac{\rho \pi D^2}{4} C_M \dot{U}(t) \quad (2.36)$$

$$F_Y(t) = 0 \quad (2.37)$$

$$F_Z(t) = \frac{1}{2} \rho C_D D W(t) \|\mathbf{V}_n(t)\| + \frac{\rho \pi D^2}{4} C_M \dot{W}(t) \quad (2.38)$$

In which:

- $U(t)$ and $\dot{U}(t)$ are respectively the wave orbital velocity and acceleration in the direction X.
- $W(t)$ and $\dot{W}(t)$ are respectively the wave orbital velocity and acceleration in the direction Z
- $\|\mathbf{V}_n(t)\|$ is the magnitude of the normal orbital velocity to the cylinder defined as $\sqrt{U(t)^2 + W(t)^2}$

Venugopal et al. [2006] used directional coefficients replacing, in each direction X and Z in Eq. 2.36, C_D by C_{D_X} and C_{D_Z} and C_M by C_{M_X} and C_{M_Z}

Morison empirical formula was also extended to describe hydrodynamic loads on a moving cylinder ($\dot{X}(t)$ and $\dot{Z}(t)$ the cylinder velocity in the local frame):

$$F_X(t) = \frac{1}{2}\rho C_D D(U(t) - \dot{X}(t))\sqrt{(U(t) - \dot{X}(t))^2 + (W(t) - \dot{Z}(t))^2} + \frac{\rho\pi D^2}{4}C_M\dot{U}(t) - \frac{\rho\pi D^2}{4}(C_M - 1)\ddot{X}(t) \quad (2.39)$$

$$F_Z(t) = \frac{1}{2}\rho C_D D(W(t) - \dot{Z}(t))\sqrt{(U(t) - \dot{X}(t))^2 + (W(t) - \dot{Z}(t))^2} + \frac{\rho\pi D^2}{4}C_M\dot{W}(t) - \frac{\rho\pi D^2}{4}(C_M - 1)\ddot{Z}(t) \quad (2.40)$$

Morison inertia and drag coefficients have been determined experimentally as explained in the following subsection.

2.3.1 Determination of the inertia and drag coefficients in Morison empirical formula

In this section, only smooth-surfaced cylinders are considered. Nevertheless, the accumulation of marine growth on the surface that modifies the hydrodynamic forces can be accounted imposing a cylinder roughness.

Many experiments have been carried out in the 80's to derive C_D and C_M in the context of the design of O&G platforms. The experiments consisted either in placing a constrained tube in a oscillating flow or submitting the tube to forced oscillations in still water. The coefficients were derived from the measured inline force on a section of the cylinder or on the entire cylinder, applying Fourier series or least squares methods resolution to identify the coefficient values as detailed in the section 5.2.

One of the first experiment was led by Keulegan et al. [1958]. It consisted in a horizontal tube at the node of a standing wave in a tank (one-dimensional flow). They demonstrated that C_M and C_D depends on the Keulegan-Carpenter number KC defined as:

$$KC = \frac{u_m \cdot T}{D} \quad (2.41)$$

in which u_m is the maximum velocity and T is the period of the oscillatory flow. Considering the flow velocity given at first order by:

$$u = u_m \sin(\omega t) \quad (2.42)$$

The maximum orbital particle velocity is defined as:

$$u_m = A\omega = \frac{2\pi A}{T} \quad (2.43)$$

where ω is the angular frequency and A is the amplitude of the motion.

From 2.41 and 2.43, the expression of KC number for an oscillating flow is thus:

$$KC = 2\pi \frac{A}{D} \quad (2.44)$$

The Reynolds number is thus defined as:

$$Re = \frac{u_m D}{\nu} \quad (2.45)$$

Another study by Sarpkaya [1977] dealt with horizontal cylinder in a vertical U-tube in which the water oscillates harmonically back and forth the cylinder. He also found a dependence between the inertia and drag coefficients and the Keulegan-Carpenter number testing different values of the ratio β , see Fig. 2.6 and Fig. 2.7.

β , which characterizes the oscillation frequency, is the ratio of Reynolds and Keulegan-Carpenter numbers defined as:

$$\beta = \frac{Re}{KC} = \frac{u_m D}{\nu} \cdot \frac{D}{u_m T} = \frac{D^2}{\nu T} \quad (2.46)$$

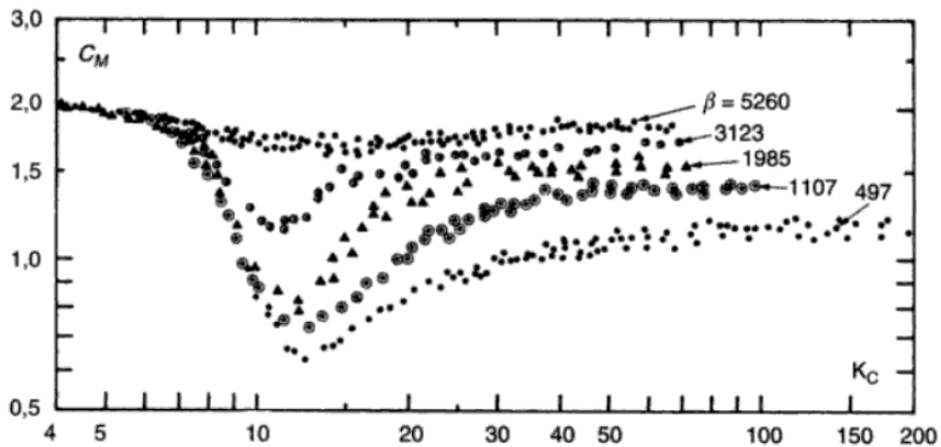


Figure 2.6: Cylinder in a oscillating flow. Inertia coefficient C_M as a function of K_C for different values of β (Sarpkaya [1977]).

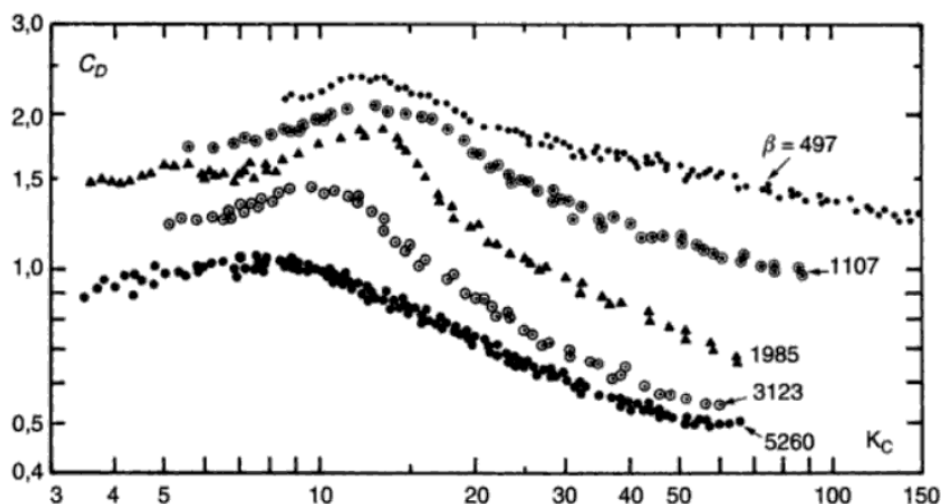


Figure 2.7: Cylinder in a oscillating flow. Drag coefficient C_D as a function of K_C for different values of β (Sarpkaya [1977]).

It must be kept in mind that Sarpkaya results were obtained with an oscillating flow perpendicular to the cylinder, there is only one velocity component. However, considering a vertical/horizontal cylinder in waves, at least two directions for the velocity field have to be taken into account because of the so-called orbital velocities typical of wave velocity field (Fig. 2.3).

Chakrabarti's studies deal with the investigation of Morison coefficients on vertical cylinder(s) in waves in experimental tanks. He performed different experimental tests: one vertical tube (Chakrabarti et al. [1976]), several vertical tubes (Chakrabarti [1979]), one tube with different orientations (Chakrabarti et al. [1975]). He plotted the variation of coefficients in function of K_C , based on experimental values. The derivations are very often done on the total force measured experimentally on the whole cylinder or on one or two specific sections. The coefficients are plotted in function of $u_m T/D$ in Fig. 2.8 where u_m is the horizontal maximal velocity from Airy theory at the point where the force is considered.

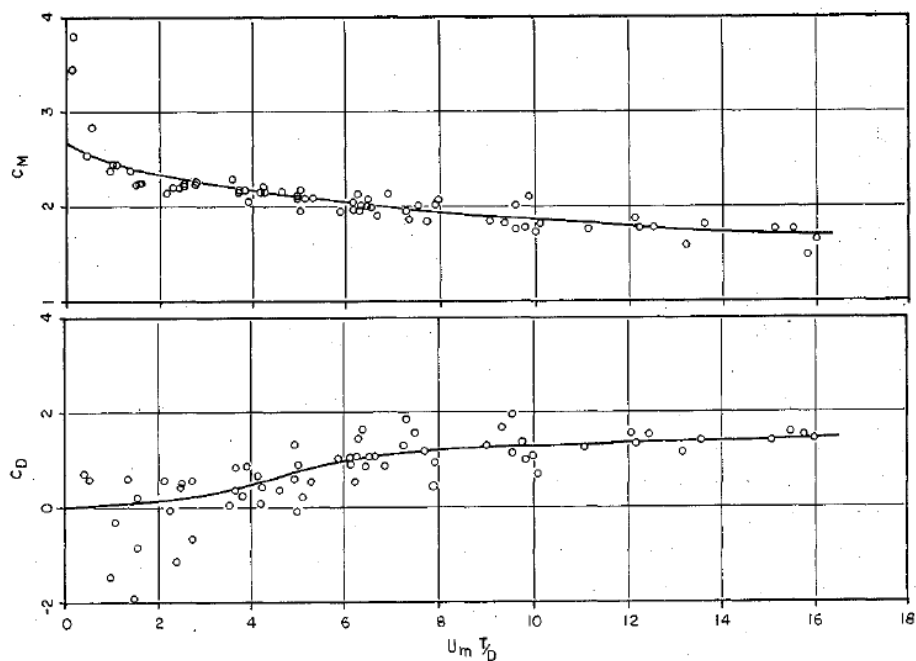


Figure 2.8: Hydrodynamic coefficients derived by Chakrabarti from two 1-ft sections force data on a vertical cylinder for different wave periods.

In Morison empirical formula, the cylinder is totally submerged by water. However, the FOWT floater is crossed by the air/water interface. One can wonder if Morison load prediction is still enough accurate for surface-piercing braces. The effect of the free surface on wave load prediction has been investigated by Dean et al. [1981]. The wave loads were obtained on an instrumented platform in the Gulf of Mexico. Four vertical piles were instrumented by seven or height force transducers above their bottom. Dean et al. [1981] observed that, for experimental waves of Reynolds number higher than 2×10^6 , the average predicted forces are greater than the measured in the range $-1.5 < s' < 0$ but higher for $-4 < s' < -1.5$ where $s' = \frac{-s}{u^2/2g}$ (Fig. 2.9) with s the distance below the undisturbed free surface. A "bow wave" effect caused by the pilling may be responsible for the additional drag on the measured force.

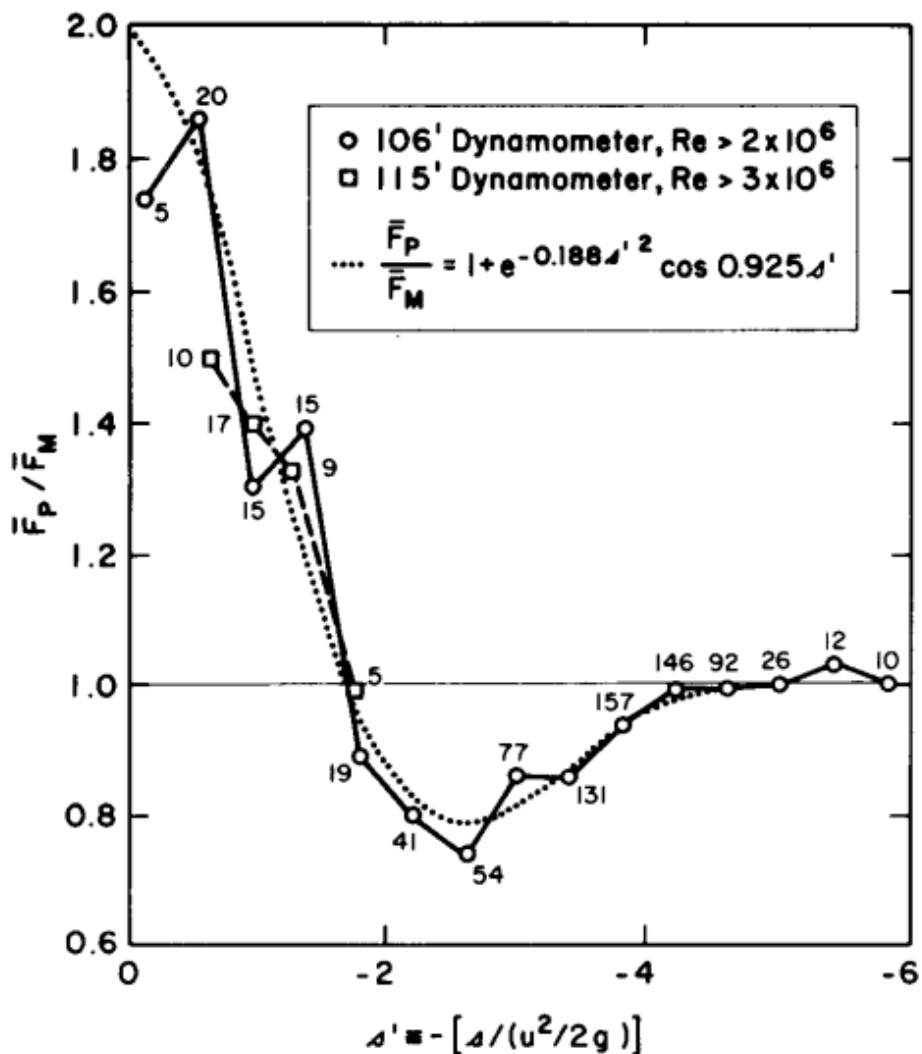


Figure 2.9: Free surface effect as shown by the ratio of predicted to measured forces as a function of free-surface proximity (Dean et al. [1981]).

Based on the fitting of the measured force with Morison prediction, the Morison formula was adapted to take into account the free surface effects as:

$$F = VC_D \frac{\rho}{2} u|u| + C_M \frac{\rho \pi D}{4} \dot{u} \quad (2.47)$$

in which

$$V^{-1} = 1 + e^{-0.188s'} \cos 0.925s' \quad \text{if } s' \leq -1 \quad (2.48)$$

$$V^{-1} = -1.37 + \frac{6.37}{(1-s')^{1.15}} \quad \text{if } -1 \leq s' < 1 \quad (2.49)$$

$$(2.50)$$

Dean et al. [1981] applied their empirical recommendations on a design example (the

wave characteristics being $H = 17.4$ m, $T = 12$ s, $h = 24.4$ m and $D = 1.22$ m). The resulting predicted forces and moments, applying Morison formula or the adapted free surface formula (Eq. 2.47) vs. position of the wave crest from the piling are plotted in Fig. 2.10. The ratio of maximum forces and moments with and without free surface effects accounted are respectively 0.833 and 0.817. The force distribution along the depth obtained with the two different prediction ways is plotted in Fig. 2.11. The "bow wave" effect may be responsible for the feature at approximately 95 ft.

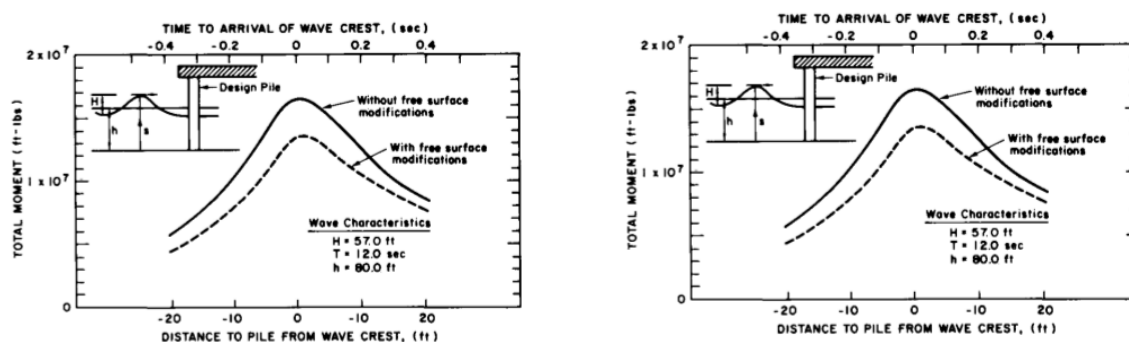


Figure 2.10: Total force and moment on a 4-ft diameter pile in the region of the crest -with and without free surface modifications, wave travelling from left to right, near breaking wave (Dean et al. [1981]).

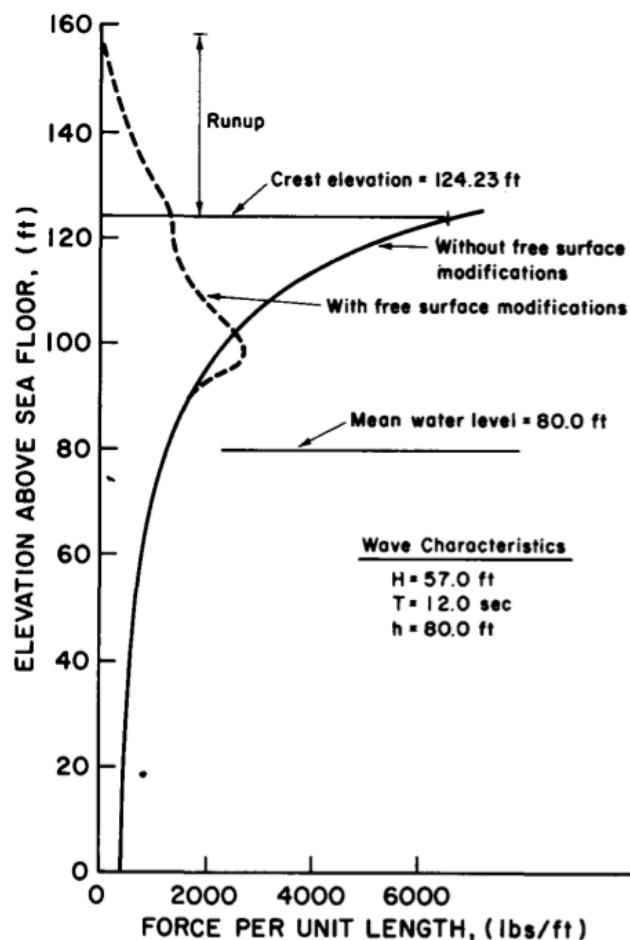


Figure 2.11: Distribution forces on a 4-ft diameter pile at crest phase - with and without free surface modifications, near breaking waves (Dean et al. [1981]).

The CFD load distribution along the braces crossing the interface will be compared to Dean's load predictions. Nevertheless, it is important to underline the specificity of Dean's results: obtained experimentally from loads on the piles of an O&G platform for a few waves ($Re > 2 \times 10^6$) with 7 force transducers.

Rainey [1989, 1995] modified the Morison inertia term calculating the potential flow wave-load accurate to second order in wave height. In that way, Rainey slender-body theory considers the axial divergence, the surface intersection and surface distortion components. Rainey dealt thus with complex cylinders such as cylinder of arbitrary cross sections and formed into a partially immersed lattice with joints.

These different campaigns show large scatter in the coefficient values derived from experimental loads according to the cylinder orientation, the diameter, the wave amplitude and the period. Several studies also modified Morison formula to better handle the load prediction on oriented and surface-piercing cylinders. CFD is an alternative way to determine Morison coefficients with CFD loads as it was done with experimental loads. With CFD, the applicability of Morison formula itself can also be investigated. This will be deeply investigated in the thesis.

A transverse force can also exist but is not defined in Morison formula. It consists in a lift force due to the separation of the flow and the formation of eddies: $F_L(z, t) = 0.5C_L\rho Du(z, t)^2$. Sarpkaya [1977] derived the lift coefficient values for different periods. Chakrabarti et al. [1976] concluded that for $u_m T/D < 5$ this lift force was negligible but should be taken into account for $u_m T/D > 15$. In the PhD, we will verify if the transverse force is negligible or should be considered compared to the inline forces when analysing the CFD wave loads.

2.3.2 Application of Morison empirical formula in engineering tools

In engineering design tools using Morison empirical formula, the cylinder is commonly discretized in slices (or strips) on which the Morison load are determined. The same set of Morison coefficient is applied for all the slices. The coefficient values are given by norms (DNV Veritas [2010], API, SNAME) and are adapted according to the wave/structure interaction case studied characterised by the Keulegan-Carpenter number, the Reynolds number and the cylinder roughness. Some corrections are given for wall interaction and free surface effects, based on experiments. The acceleration and velocity of the flow impacting each slice are also computed based on wave theory (cf. section 2.1). This enables to compute a specific value of Morison force on each slice of the cylinder.

The following subsection sums up the method proposed by Chakrabarti [2005] to choose between the potential theory (section 2.2) and Morison formula (section 2.3) to predict wave loads on a cylinder. Chakrabarti's classification identifies the dominance of inertia over drag loads and the possible presence of diffraction loads.

2.3.3 Wave loads classification according to Chakrabarti [2005]

The ratio of Morison drag term over inertia term gives the following expression:

$$\frac{F_{drag}}{F_{inertia}} = \frac{1}{\pi^2} \cdot \frac{C_D}{C_M} \cdot KC \quad (2.51)$$

Considering $C_D \simeq 1$ and $C_M \simeq 2$, the last relation can be expressed as:

$$\frac{F_{drag}}{F_{inertia}} \simeq 0.043 \cdot KC \quad (2.52)$$

Fig. 2.12 represents the regions where diffraction/inertia/drag effects are predominant; the y-axis H/D is equivalent to the Keulegan-Carpenter number whereas the x-axis is the diffraction parameter $\pi D/L$.

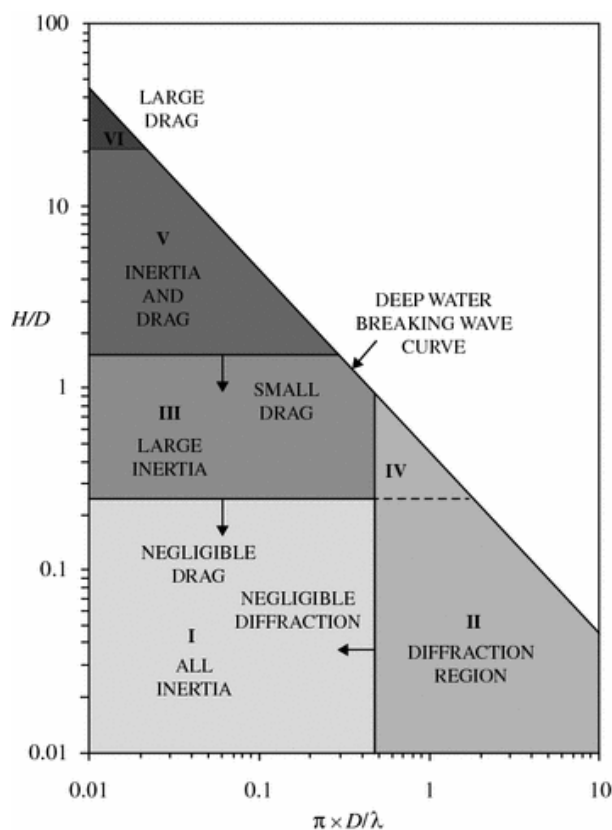


Figure 2.12: Determination of wave loads according to H/D , and λ by Chakrabarti [2005].

If the diameter of the cylinder has the same order of magnitude than the wavelength, the potential flow theory has to be applied in order to consider diffraction effects (zone II, IV). This corresponds to the right part on the x-axis. On the contrary, for small diameters compared to the wavelength, Morison empirical formula can be used to predict wave loads on the cylinder (zone I, III, V and VI):

- For $KC < 3$ (zone I), the inertia term is dominant and drag loads are negligible. Thus both the potential flow theory and Morison formulation are applicable.
- For $3 < KC < 15$ (zone III), drag load becomes significant, the drag term can be linearised.
- For $15 < KC < 45$ (zone V), Morison expression is applied to describe loads on the structure.
- For $KC > 45$ (zone VI), the drag force is dominant.

The hydrodynamic theories to describe loads due to an oscillating flow on a moving cylinder has been described, including potential flow theory and Morison empirical formula. The potential flow theory can be advantageously extended to more complex geometries. The so-called sea-keeping theory determining wave loads on offshore moving structures is detailed in the following section.

2.4 Sea-keeping theory for FOWT

2.4.1 Float motion in waves: 2nd Newton law

The system considered in this section is a floater, as represented in Fig. 1.9. The motion of the rigid floater is defined by three translations of the gravity centre G and three rotations around G , as detailed in the section 1.3.1.

As written by Massie and Journée [2001], three main systems exist to describe the motion of a floating structure:

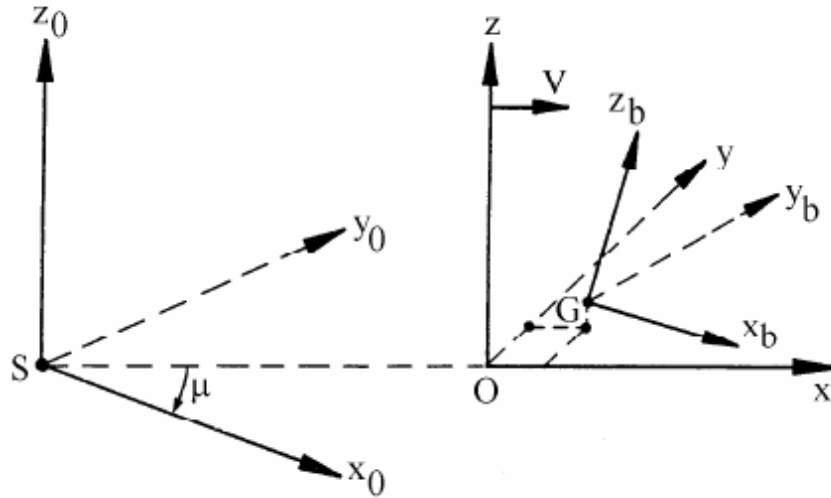


Figure 2.13: Coordinate systems.

- The earth-bound coordinate system $S(x_0, y_0, z_0)$: defined by (x_0, y_0) plan lying in the still water surface. (Ox_0) is the positive axis in the direction of wave propagation. (Oz_0) is directed upwards.
- The body-bound coordinate system $G(x_b, y_b, z_b)$: the origin of this system is the floater centre of gravity G . (Gx_b) is the direction in the longitudinal forward direction, (Gy_b) in the lateral port side direction and (Gz_b) in the upward direction.
- The steadily translating coordinate system $O(x, y, z)$: this system moves with a ship velocity V . For a stationary floater, the body-bound and steadily coordinate systems have the same axes.

The position of the floater is given by the vector $\mathbf{x}(x, y, z, \phi, \theta, \psi, t)$ in $(Oxyz)$ system. Applying Newton 2nd law to the floater constrained to the seabed with a mooring system, the following motion equation is obtained:

$$\mathbf{W} + \mathbf{\Pi} + \mathbf{F}_{\text{mooring}} + \mathbf{F}_{\text{hydrodynamic}} = M\mathbf{a} \quad (2.53)$$

- \mathbf{a} is the acceleration of the floater

- \mathbf{W} is the weight of the structure and $\mathbf{\Pi}$ is the Archimedes' buoyant force. The sum of both forces is often simplified as the hydrostatic force expressed as $K_{stiff} \cdot \mathbf{x}$, where K_{stiff} is the linear hydrostatic stiffness matrix.
- $\mathbf{F}_{\text{mooring}}$ is the mooring force often expressed as $K_{anchor} \cdot \mathbf{x}$, with K_{anchor} the linear mooring stiffness matrix.
- $\mathbf{F}_{\text{hydrodynamic}}$ is the hydrodynamic force due to waves and current. In this thesis, only waves are considered.

2.4.2 Potential flow theory for hydrodynamic load determination

To determine hydrodynamic loads on the structure, the method detailed below is followed.

Assuming the flow is constant, incompressible, non viscous, irrotational and homogeneous, the potential flow theory described in the section 2.2 is applied. These hypotheses imply that the floater is considered as a large structure, meaning that the wavelength is negligible compared to the floater diameter (zone II in Fig. 2.12). Two conditions are added to the four conditions previously detailed in Eq. 2.4, 2.5, 2.6 and 2.7 to determine hydrodynamic loads on the float:

1. No leak condition on the float:

The wall of the structure is considered as impermeable and water can not come into the float. At any given position on the floater wall, the following equation is verified:

$$\nabla\Phi \cdot \mathbf{n} = \mathbf{u} \cdot \mathbf{n} \quad (2.54)$$

where \mathbf{n} is the local normal vector to the surface and \mathbf{u} the local velocity of the floater wall.

2. No perturbation at infinity condition:

The radiated waves are completely dissipated far from the float.

The wave velocity potential, which is assumed linear, is decomposed as follows:

$$\Phi(x, y, z, t) = \Phi_0 + \Phi_7 + \Phi_{1-6} \quad (2.55)$$

- Φ_0 : The incident wave potential: determined without the structure, focusing only on the non-disturbed incoming wave.
- Φ_7 : The diffracted wave potential: resulting from the action of waves around the structure considered as fixed. This is represented by the "restrained in waves" term on scheme 2.14.
- Φ_{1-6} : The radiated wave potential: resulting from the motion of a body in water without incoming waves. This corresponds to the "oscillation in still water" term on scheme 2.14.

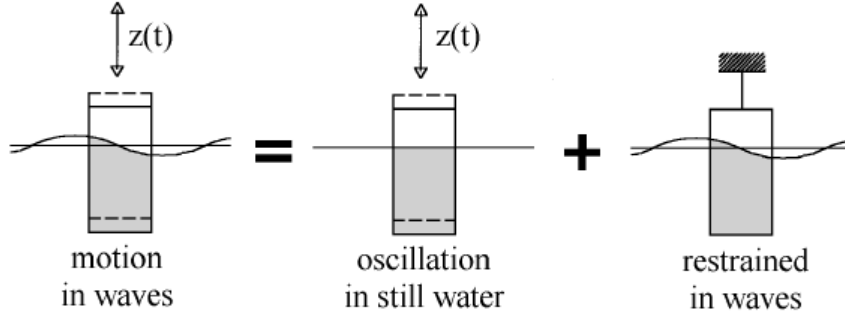


Figure 2.14: Linear decomposition of hydrodynamic loads (Massie and Journée [2001]).

In the potential flow theory, the hydrodynamic force $F_{hydrodynamic}$ is thus decomposed following the previous decomposition of the velocity potential.

$$\mathbf{F}_{hydrodynamic} = \mathbf{F}_{incoming\ wave} + \mathbf{F}_{diffracted} + \mathbf{F}_{radiation} \quad (2.56)$$

in which:

- $\mathbf{F}_{incoming\ wave} + \mathbf{F}_{diffracted}$. This force is obtained considering a fixed floater submitted to waves. The incoming force is known as the Froude-Krilov force resulting from the integration of pressure on the surface of the body in the undisturbed waves. The diffracted term corrects Froude-Krilov term to take into account the impact of the floater on wave field. The sum of these two forces is known as the 1st order wave excitation force $\mathbf{F}_{excitation}$.
- $\mathbf{F}_{radiation} = M_a \mathbf{a} + B_{radiation} \mathbf{v}$. M_a is the added mass matrix and $B_{radiation}$ the radiation damping matrix, both obtained by considering a moving floater in still water.

Thus the **motion equation** 2.53 becomes:

$$(M + M_a) \mathbf{a} + (B_{radiation}) \mathbf{v} + (K_{stiff} + K_{anchor}) \mathbf{x} = \mathbf{F}_{excitation} \quad (2.57)$$

The equation of motion 2.57 is resolved in the frequency domain.

2.4.3 Resolution of the motion equation in the frequency domain

The resolution in the frequency domain aims at getting information about the motion of the floater in waves, with strong linearity assumptions. Eq. 2.57 can be solved for each degree of freedom.

Here, to provide an example and for the sake of simplicity, one degree of freedom is considered: the heave response. The heave motion response to a regular wave is described resolving Eq. 2.57 in the frequency domain. The incoming wave elevation is defined by $\eta = |\eta|e^{-i\omega t}$. z is the coordinate of the system along (Oz) axis and defined by

$z = |z|e^{-i\omega t}$. Knowing that the excitation force is proportional to the incoming wave, the following equation is obtained:

$$-\omega^2(M + M_a(\omega))z - \omega(B_{rad}(\omega))z + Kz = F_0\eta \quad (2.58)$$

where $K_{stiff} + K_{anchor} = K$ and F_0 is the linear excitation force complex amplitude per wave height.

The motion Response Amplitude Operator (RAO) can then be introduced as the ratio between z and η :

$$RAO = \frac{z}{\eta} = \frac{F_0}{-(M + M_a(\omega)) - (B_{rad}(\omega)) + K} \quad (2.59)$$

This relation is verified in the frequency domain.

2.4.4 Second order loads: Quadratic Transfer Function (QTF)

In the case of irregular waves (often modelled as the sum of regular Airy waves), various wave frequencies can interact. As detailed by Faltinsen [1990] and Roald et al. [2013], their difference or sum leads to low frequency or high frequency loads, the so-called second order wave loads. These second order loads are also computed in the framework of the potential flow theory. Quadratic-transfer-functions, so-called QTF, are derived. $\mathbf{F}_{excitation}$ in Eq. 2.57 becomes the sum of first order and second order wave loads.

2.4.5 Combination of Morison equation to sea-keeping theory

In engineering software, such as DeepLinesWind™, the FOWT floater behaviour in waves can be simulated combining different hydrodynamic models. For the SBM Offshore/IF-PEN TLP floater for example, the potential linear flow theory is used to predict wave loads on the large side buoys whereas Morison empirical theory is applied on thin braces as depicted in Fig. 1.12. To take into account the fluid viscosity and flow separation, that could also occur when dealing with "large body", for example in the axis of a large buoy (vortex shedding occurs on the edges), Morison drag forces can also be superimposed to the potential flow loads previously detailed.

In this chapter, regular wave theory is described. Another part is dedicated to loads on a cylinder submitted to an oscillating flow: loads can be calculated based on potential flow theory or thanks to empirical Morison formula. The choice between the two theories is based on cylinder dimension and wave characteristics. Finally the last part focuses on the sea-keeping theory for FOWT implemented in the engineering tools.

To investigate the behaviour of a floater in waves and compare it to loads provided by

either potential flow theory or Morison formula, Computational Fluid Dynamics (CFD) is used in the present PhD thesis. The following chapter aims at presenting this numerical method to solve Fluid Mechanics equations and its application to offshore hydrodynamics.

Chapter 3

CFD modelling in OpenFOAM for the study of FOWT Hydrodynamics

This part focuses on CFD modelling, using OpenFOAM software (Greenshields [2020]), in order to study wave-structure interaction. CFD is used in this study to mimic wave basin experiments. A Numerical Wave Tank (NWT) is implemented: waves are generated at the inlet, propagated along a given distance and absorbed at the end of the tank. A structure, constrained or mobile, can then be added in the NWT where the interactions between the structure and the waves are calculated.

Experiments are commonly used to validate CFD models. Once this validation obtained, CFD can fruitfully complete experimental studies: a multitude of cases with various wave conditions and different structures can be led, extreme events can be tested without damaging any experimental facilities. The velocity and pressure fields are fully determined and can provide access to detailed information on flow characteristics and structural loads. Full scale simulations can be run and give access to "measurements" not available so far.

However, many simulations have to be run and analysed to get an accurate NWT, where generated waves are well controlled. Also, since different numerical models able to simulate such flows are implemented in OpenFOAM, we need to choose the most appropriate for each study. Notably, different solvers exist to generate and absorb waves, to track the air/water interface and to model turbulent flow.

The first section is dedicated to Fluid Mechanics equations solved in the CFD framework. Then, a description of the finite volume method is presented explaining how fluid mechanics equations are resolved in OpenFOAM. The last section focuses on wave generation, propagation and absorption in OpenFOAM.

3.1 Fluid Mechanics equations

3.1.1 Navier-Stokes equations

The governing equations of fluid flow are the continuity and momentum equations known as Navier-Stokes equations, as detailed by Jacobsen [2017].

$$\nabla \cdot \mathbf{u} = 0 \quad (3.1)$$

$$\frac{\partial(\rho\mathbf{u})}{\partial t} + \nabla\rho\mathbf{u} \cdot \mathbf{u} = -\nabla p^* + \nabla \cdot (\mu_{tot}\nabla\mathbf{u}) + g \cdot (\mathbf{x} - \mathbf{x}_r)\nabla\rho + f_\sigma \quad (3.2)$$

where:

- \mathbf{u} is the velocity field in Cartesian coordinates [m.s⁻¹]
- \mathbf{x} is the Cartesian coordinate position vector and \mathbf{x}_r a reference location (defined as sea level at rest) [m]
- OpenFoam does not solve directly the pressure p but instead a pseudo-dynamic pressure defined as $p^* = p - \rho\mathbf{g} \cdot \mathbf{x}$. This pressure consists in the dynamic pressure only if the free surface at rest is located at $z = 0$ as detailed by Higuera [2015]. Near the waterline, ρ may change between the water density and the air density depending on whether the probe location is. If one needs to determine the dynamic pressure near the interface, it is advised to derive it as $p_{dym} = p - \rho_{water}\mathbf{g} \cdot \min(\mathbf{x}, 0)$ [Pa]
- ρ : fluid density [kg.m⁻³]
- μ_{tot} : fluid dynamic viscosity [Pa.s]
- f_σ : surface tension, null in the CFD simulations run and described in this report [N]

3.1.2 Turbulence modelling

The Reynolds number (Eq. 2.45) of the wave/structure cases modelled during the thesis are high ($Re \simeq 10^5 - 10^6$) so the flow must be considered as turbulent. To model the turbulence of the flow, a specific Reynolds Averaged Navier-Stokes (RANS) model is available in OpenFOAM. It is based on Osborne Reynolds assumption: an instantaneous quantity can be seen as the sum of a time-averaged and a fluctuating quantity. Menter [1994] developed the k-omega SST turbulence model tested during the thesis and commonly used in CFD for offshore application. However, this model induces a high damping of wave elevation, as noted by Larsen and Fuhrman [2018], Larsen et al. [2019] who proposed a modified version, k-omega SST stabRAS, to improve the air/water interface resolution.

3.1.3 Free surface modelling

Wave propagation is a two-phase problem where we need to describe the interface between the air and the water. In OpenFOAM, a Volume of Fluid method (VOF) is used to track

the air/water interface, as explained in OpenFOAM user guide by Greenshields [2020]. VOF methods consists in introducing a variable α (phase fraction), defined as $\alpha = 1$ in cells filled by water, $\alpha = 0$ in cells filled by air and α in the range $[0:1]$ in the air/water interface area. The local density and the viscosity are defined as:

$$\rho = \alpha\rho_{water} + (1 - \alpha)\rho_{air} \quad (3.3)$$

$$\mu = \alpha\mu_{water} + (1 - \alpha)\mu_{air} \quad (3.4)$$

and α is governed by the advection Eq. 3.5 expressed as:

$$\frac{\partial\alpha}{\partial t} + \nabla \cdot (\alpha\mathbf{u}) = 0 \quad (3.5)$$

The wave elevation is obtained by integrating the alpha field over the height.

Equations 3.1, 3.2 and 3.5 are discretised using Finite Volume method as explained in the next section.

3.2 Numerical implementation in OpenFOAM

3.2.1 Finite Volume Method in OpenFOAM

OpenFOAM applies the co-located finite volume method to solve the fluid mechanics equations presented above. The equations are discretised to derive the value of the unknown quantity (the pressure, velocity or phase fraction) at the center of each cell of the mesh. Different numerical schemes exist to discretise each term of the governing equations. These schemes are precisely detailed by Greenshields [2015]. Tab.9.4 in Annexe 9.4 indicates the discretisation schemes chosen in our CFD model.

The governing equations are resolved applying a combination of the MULES and the PIMPLE algorithms at each time step. The interFoam solver, dedicated to two-phase incompressible flow, solves the advection Eq. 3.5 determining the phase fraction field with MULES (Multidimensional Universal Limiter with Explicit Solver) detailed by Deshpande et al. [2012]. Once the phase fraction field is known, the momentum and continuity equations are resolved via the PIMPLE loop calculating the velocity-pressure coupling. PIMPLE comes from the mix of PISO (Pressure Implicit with Splitting of Operators) and SIMPLE (semi-implicit method for pressure linked equations), a comprehensive explanation of this algorithm is drawn by Jasak [1996]. Each resolution step is notably controlled by a looping parameter that imposes the maximal error on pressure, velocity and phase fraction fields.

In OpenFOAM, we can impose a fixed time step (\maxDt) or impose a maximum Courant Number (\maxCo) to ensure the numerical stability. The Courant-Friedrichs-Lewis (CFL) is defined by Lewy et al. [1928] as:

$$Co = \frac{|u_i|\Delta t}{\Delta x_i} \quad (3.6)$$

where $|u_i|$ is the magnitude of the velocity in (O_i) direction and Δx_i the cell size in (O_i) direction. For any explicit convection problem, the Courant number must be equal or smaller than 1. For implicit scheme, this CFD condition is not obligatory. Larsen et al. [2019] investigated the performances of interFoam with the library waves2Foam and demonstrated that the CFL should be smaller than 0.15 to correctly propagate waves. This condition will be investigated throughout the thesis, notably when performing convergence studies to define a valid Numerical Wave Tank in the section 5.

3.2.2 Free surface resolution

3.2.2.1 interFoam

The most common solver in OpenFOAM to solve the advection equation of the interface (Eq. 3.5) is the algebraic one known as interFoam. It solves interface for 2 incompressible, isothermal and immiscible fluids. Density and viscosity are assumed constant in each phase. In each cell, the velocity field \mathbf{u} , pressure p and volume fraction α are determined.

To get a sharp interface, interface compression is introduced in interFoam with MULES limiter for boundness (Multi-dimensional Universal Limiter for Explicit Solution) adding an artificial interface compression term in the advection equation to keep α bounded. The phase fraction value in a given cell is thus determined as follows:

$$\frac{\partial \alpha}{\partial t} = -\nabla \cdot (\alpha \mathbf{u}) - \nabla \cdot (\alpha(1 - \alpha) \mathbf{u}_c) \quad (3.7)$$

The second term of the right hand side is known as the compression flux in which \mathbf{u}_c is defined as:

$$\mathbf{u}_c = \min(c_\alpha |\mathbf{u}|, \max(|\mathbf{u}|)) \frac{\nabla \alpha}{|\nabla \alpha|} \quad (3.8)$$

Where c_α is typically equal to 1. This method is precisely detailed by Deshpande et al. [2012].

Another approach to solve the interface is the geometric resolution with isoAdVector solver.

3.2.2.2 isoAdVector

Roenby et al. [2016] developed a new VOF approach called isoAdVector based on geometrical interface reconstruction for a two-phase incompressible flow. The interface resolution follows two steps.

First, the isosurface concept is used to reconstruct geometrically the interface inside each cell. Phase fraction is not interpolated from cell center to faces as in interFoam, but

to vertices. Then for each edge, a cutting point is found by linear interpolation and these points are connected to form the isosurface.

Secondly, the motion of the face-intersection line for a general polygonal face is modelled to describe the time evolution of the submerged face area during a time step.

⇒ We did not have enough time to test precisely isoAdVector solver coupled recently with the waves2Foam library. Nevertheless, it will be tested in the work following the thesis.

3.3 Wave generation solvers

Numerical Wave Tank (NWT) are basins in which waves are generated, propagated and absorbed. Specific boundary conditions for the velocity, pressure and phase fraction fields are imposed on edges of the tank, as illustrated in Fig. 3.1.

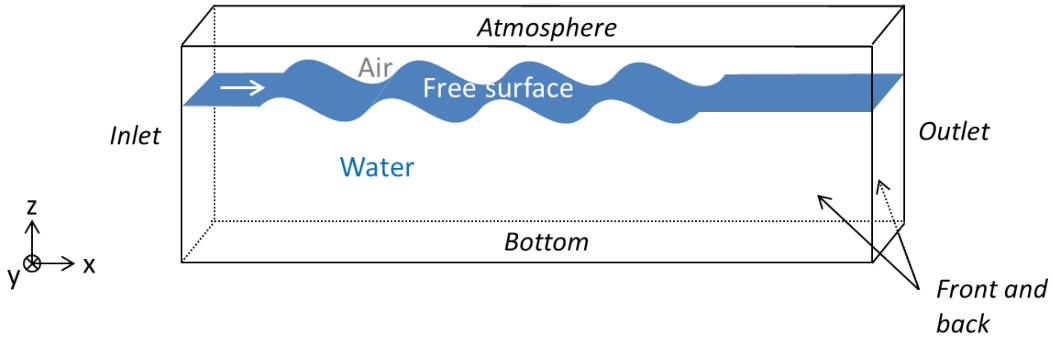


Figure 3.1: Edges of the Numerical Wave Tank.

To accurately model a regular wave in a NWT and control the wave propagation, one has to ensure minimal damping along the tank and reflection at the outlet and walls. olaFlow and waveFoam are two solvers available in OpenFOAM to generate and absorb waves applying different methods. CFD studies achieved with both solvers are presented in 4.2.

3.3.1 waveFoam: a passive wave generation and absorption solver

The wavesFoam library, implemented by Jacobsen [2017], applies relaxation zone method at the inlet and at the outlet of the domain. The generation zone at the inlet is responsible for the creation of waves. The absorption zone at the outlet of the NWT controls the wave absorption to avoid reflection. This method is considered as passive due to the use of relaxation zones. In each zone, the velocity and alpha field are updated at each time step based on a chosen weighted function χ defined below and represented in scheme 3.2.

$$\mathbf{u} = \chi \mathbf{u}_{\text{computed}} + (1 - \chi) \mathbf{u}_{\text{target}} \quad (3.9)$$

$$\alpha = \chi \alpha_{\text{computed}} + (1 - \chi) \alpha_{\text{target}} \quad (3.10)$$

$\mathbf{u}_{\text{target}}$ and α_{target} represent the target values of velocity and alpha fields which are defined using a selected wave theory (as detailed in Chapter 2) at the inlet and a null velocity and free surface at rest at the outlet. The computed values ($\mathbf{u}_{\text{computed}}$ and α_{computed}) are the numerical values based on Navier Stokes and VOF equation resolution.

Three weighted functions can be defined as explained by Jacobsen [2017]. The most common one is the default one: the exponential weight χ .

$$\chi(\xi) = 1 - \frac{\exp(\xi^\beta) - 1}{\exp(1) - 1} \quad (3.11)$$

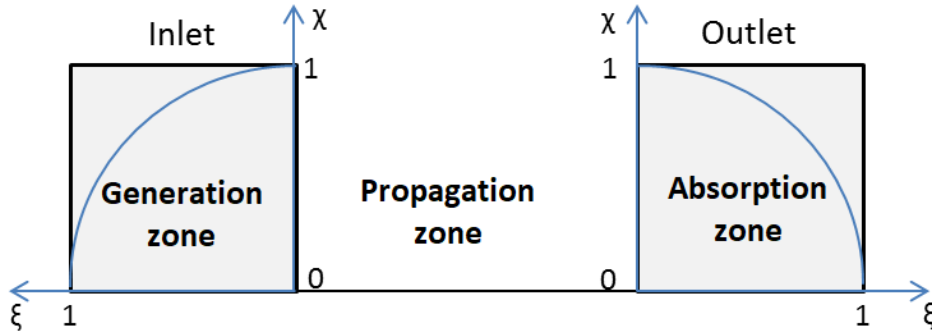


Figure 3.2: Relaxation zones.

ξ represents the local coordinate system for relaxation zones. χ is assigned such that the target value ($\mathbf{u}_{\text{target}}$ or α_{target}) gains more weight near the boundary wall (inlet or outlet) away from the propagation zone. Thus the boundary conditions at the wall are not affected by the computed field between the two relaxation zones.

3.3.2 olaFlow: an active wave generation and absorption solver

The solver olaFlow developed by Higuera et al. [2015] applies active wave generation and absorption method. The wave is generated at the boundary imposing directly a specific velocity and surface elevation.

3.3.2.1 Background: experimental method

This method was first described experimentally by Schäffer and Klopman [2000] with piston-type wave maker. They simply explained that if waves are generated in x-positive direction with time growing, they can be absorbed for time decreasing in x-negative direction.

In the Fig. 3.3, the experimental closed-loop system used to generate waves and absorb waves in order to avoid reflection is detailed (FSE: Free Surface Elevation).

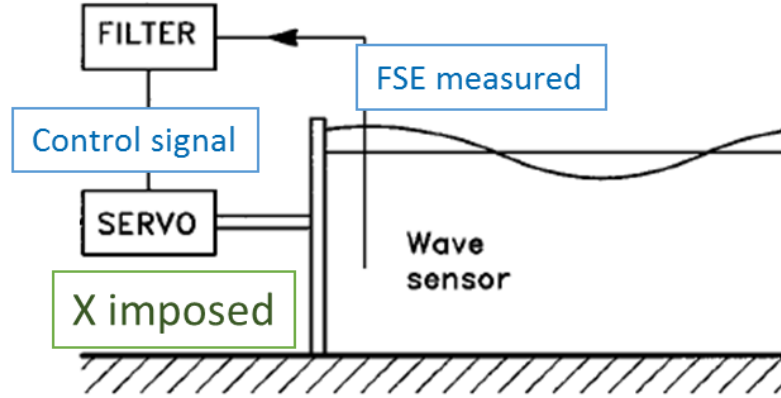


Figure 3.3: Active wave absorption experiments.

The motion of the paddle is imposed after measuring the free surface elevation at the inlet of the tank and comparing with the initially prescribed wave. Thus a specific wave is generated and then corrected with the servo system.

3.3.2.2 olaFlow library

To generate waves, Higuera uses this active absorption principle by implementing new boundary conditions at the inlet and outlet for wave velocity and phase fraction.

More precisely, the elevation calculated in the first cells along the boundary is compared with the theoretical value imposed by the user-defined wave parameters. According to the results of this comparison, a specific face patch velocity and alpha field is then imposed. The formulation is detailed below.

Shallow-Water Active Wave Absorption (SW-AWA)

The code was firstly implemented with SW-AWA strategy. A correction velocity is defined and aims at absorbing reflected waves at the patch. It is determined assuming two important hypotheses: the waves are in **shallow water** range and **linear**.

The shallow water hypothesis induces that the velocity is constant along the water column, i.e. it does not depend on the depth. The horizontal correction velocity u_c can thus be written as:

$$u_c h = c \eta \quad (3.12)$$

with:

- h : the water depth of the NWT
- c : wave celerity (defined by Eq. 2.16)
- η : the surface elevation measured at the inlet of the patch

In shallow water regime, $c = \sqrt{gh}$ (as seen in Eq. 2.16). The correction velocity at the boundary is given by:

$$u_c = -\sqrt{\frac{g}{h}}\eta_R \quad (3.13)$$

with η_R the reflected wave elevation corresponding to the difference between the measured wave elevation and the target wave at the patch. If this boundary condition is imposed at the inlet patch, the target wave corresponds to the theoretical wave. The wave theory has been detailed in Chapter 2.

At the outlet, the aim is to absorb wave applying active absorption like at the inlet. The boundary condition simply imposes the velocity to be equal to the sum of the theoretical velocity wanted (null velocity for total absorption) and the correction velocity 3.13, the target state being the mean sea water level at rest.

Extended-Range Active Wave Absorption (ER-AWA)

According to Higuera [2020], ER-AWA overcomes the initial shallow water limitation by re-deriving Eq. 3.12. The velocity correction (cf. Eq. 3.13) is modified to take into account the variation of the wave horizontal velocity profile along the depth. Higuera implemented a new velocity correction defined as follows:

$$u_c = -2\eta_R \frac{\cosh[k(h+z)]}{\sinh[kh]} \quad (3.14)$$

⇒ olaFlow and waveFoam solvers will be tested at the beginning of the thesis to get a proper comparison and analysis of their performance for wave modelling in deep water and second order waves conditions (cf. section 2.1.4).

This Chapter 3 focused on the CFD implementation of a Numerical Wave Tank in the open-source software OpenFOAM. The resolution of Fluid Mechanics and advection equations to derive the pressure, velocity and alpha phase fraction fields was presented. Two main wave generation and absorption methods were introduced, detailing olaFlow and waveFoam libraries.

Having presented the theories underlying hydrodynamics of offshore floating structures in Chapter 2 and the CFD model of a Numerical Wave Tank in Chapter 3, the limitations of the commonly used hydrodynamic theories when applied to FOWT and their study thanks to CFD simulations as described in the literature will be summed-up in the following chapter.

Chapter 4

Hydrodynamics for FOWT: limitations of current models and CFD investigation

This state-of-the-art chapter is organised in three sections.

The first part is dedicated to the hydrodynamic modelling of FOWT platform with engineering software, commonly used for the FOWT design. The limitations that have been identified by the scientific community in this context will be detailed. To investigate these limitations and propose improved hydrodynamic formulations, this PhD thesis aims at studying FOWT hydrodynamics with a NWT.

Thus, the second section focuses on the implementation of Numerical Wave Tanks in CFD with OpenFOAM software. This section intends to summarise what are the existing solvers to generate and absorb waves and what are the limits of CFD models that have been revealed so far.

Finally, the third section focuses on wave-structure interaction in OpenFOAM, first focusing on cylinders and then on FOWT platforms. A review of numerical studies putting at stake the simulations of decay tests and forced oscillations, fixed floater in waves and free motion in waves having been led so far is proposed. The few studies dealing with the analysis of CFD results to specify the hydrodynamic behaviour of a floater will be presented.

4.1 Hydrodynamic modelling of FOWT with engineering solvers

As explained in the section 1.4.1, aero-hydro-servo-elastic solvers are used to design FOWT. The principle limitations of the hydrodynamic theories applied in the engineering tools to predict wave loads on the floater are listed in the section 1.4.2. This the section 4.1 details the studies achieved so far that illustrate such limitations. Each subsection focuses on one limitation: the complex combination of potential theory and Morison formula for FOWT design, the important uncertainties when calibrate Morison coefficients

for FOWT and the inaccurate prediction of second-order loads with the hydrodynamic theories applied in the design tools.

4.1.1 Combination of Morison empirical formula and potential linear theory to predict wave loads on FOWT

Most of the different engineering software used for floater design were benchmarked in the Offshore Code Comparison Collaboration Continuation (OC4) project managed under the framework of IEA Wind and presented by Robertson et al. [2014]. This code-to-code comparison project studied the OC4-DeepCWind semisubmersible platform equipped with a 5 MW NREL wind turbine. One of OC4 aims was to better understand the influence of the hydrodynamic modelling on the FOWT response. The aforementioned tools are all based on the use of the potential flow theory or the Morison empirical formula or a combination of both (explained in the section 2.4 and 2.3).

The potential flow theory resolution requires hydrodynamic database that provides Froude-Khrilov and diffraction loads, radiation and added mass matrices. They are obtained with CAE preprocessor software, such as WAMIT or Diodore, that solve the potential flow problem presented in the section 2.4. For some elements of the floater such as slender buoys, Morison formula is applied to take into account the viscosity for the prediction of wave loads. Morison drag and inertia coefficients are obtained with empirical databases or standards, such as the DNV-RP-C205 by Veritas [2010].

Using such complex combinations of these theories coming from O&G is very recent and specific to FOWT studies.

OC4 code-to-code comparison aimed to highlight the impact of different modelling assumptions and choices, as well as various coefficient calibration on simulations results. The results (motion, line tension, bending moment at tower bottom) were rather similar at wave frequencies but some differences on low and high frequency ranges were highlighted and are detailed in the section 4.1.3.

→ Many combinations of potential flow theory and Morison formulation are possible to predict wave loads on FOWT floater. OC4 benchmark was performed by different participants with an important range of open-source and commercial software, exploring a wide range of Morison / potential flow theory combinations. Defining the validity range of each theory during the PhD thesis will thus bring more precision to these current studies and more generally to the prediction of loads on FOWT float.

4.1.2 Calibration of Morison hydrodynamic coefficients for FOWT

In OC4, hydrodynamic models were not validated against experiments and it was not possible to assess the accuracy of one method over another one. Following the OC4 project, Robertson et al. [2017] launched the OC5 project: the Offshore Code Comparison Collaboration Continuation with Correlation project complements the code-to-code

comparison with validation against wave tank experiments. Phase I of OC5 focused on the calibration of hydrodynamic coefficients on a constrained cylinder applying Morison formula. Different methods exist to derive Morison drag (C_D) and inertia (C_M) coefficients from load data (numerically or experimentally generated): Fourier analysis, least squares methods. Look-up table approaches based on sea-state and structure diameter are also available and commonly used in the design process, as suggested by norms and standards. Values of C_D and C_M obtained by the participants according to the method of their choice were rather dispersed and so the predicted loads.

OC5 phase II focused on a code comparison with experiments for a more complex structure: the OC5-DeepCwind semisubmersible platform, for which basin tests were led at MARIN. In OC5 Phase II, for each test (decay test / forced oscillations/ free motion in waves), different set of coefficients were defined for the same float. Coefficients thus depend on the structure but also on wave characteristics. The same conclusions were obtained in Rivera-Arreba et al. [2019] work; the author adjusted drag coefficients for decay tests of a FOWT floater and concluded that hydrodynamic coefficients should be adjusted for any kind of wave regime.

In VALEF project, led by several French research laboratories, C_D and C_M are calibrated for each buoy and brace of a semisubmersible float. Though the same standard was applied, very different results were obtained, highlighting the fact that uncertainties exist in the prediction of wave loads on a FOWT floater.

→ From these projects and research works, it appears there is no clear standard process, neither consensus on coefficient choices in the research and industry community. Practically the coefficient choices heavily depend on the user expertise, available data (for example is there a dedicated experimental campaign), and practical requirements. CFD will be used in this PhD thesis in order to re-determine Morison coefficients on a real offshore structure dedicated to floating wind. Variation of Morison coefficients through the structure, due to cylinder diameters, orientations and vicinity with the free surface, will be investigated. The effect of wave characteristics and scale (model-scale versus full-scale) will also be examined. Coefficient comparison with standard values will be discussed in Chapter 7.

4.1.3 Non-linear loads on FOWT

If the wave-structure interaction problem is considered as linear, incoming wave and wave loads have the same frequency due to the linearity of the problem. In the case of irregular waves, the various wave frequencies can interact. As detailed by Faltinsen [1990] and Roald et al. [2013], their difference or sum leads respectively to low frequency or high frequency excitation and thus the floater motion response. In the low frequency region, according to the type of the platform, the natural motion frequency of the floater can be excited. For high frequencies, mooring lines, tower and the turbine natural frequencies can be excited resulting in vibrations and possible structure damages, related to fatigue.

Wave tank tests also suggest that second-order effects might be crucial for FOWT. Several papers focus on non-linear loads modelling of FOWT as detailed below.

4.1.3.1 Low frequencies

According to Coulling et al. [2013], it might be reasonable to neglect second-order loads when modelling wind and wave loading on a FOWT in FAST. But, for specific turbine condition (parked rotor), response driven by wave loads (similar to wave-only condition case), second-order difference-frequency loads can not be neglected. The authors used the quadratic damping model in low frequency region to capture the response near the surge natural frequency. However, for low frequencies, some discrepancies on amplitudes and phases between tank tests and simulations were observed. Bayati et al. [2014] worked on second-order hydrodynamic effects on the OC4-DeepCWind semisubmersible platform using FAST and WAMIT, applying the same method as Roald et al. [2013]. Hydrodynamic second-order loads were modelled with sum and difference QTF. Results showed that second-order low frequency hydrodynamic loads excite the floater at its natural frequency. This response was overestimated compared to experimental data because WAMIT does not include elements to model viscous drag. Azcona et al. [2019] and Pegalajar-Jurado and Bredmose [2019] highlighted similar under-prediction of the low-frequency response.

4.1.3.2 High frequencies

For Roald et al. [2013], offshore structures are designed to have their eigen frequencies out of the wave excitation range. However second-order loads may excite the structure eigen-frequencies. High frequency vibrations can be generated if the damping of the excited eigen modes is small. A TLP and a spar were modelled with FAST and WAMIT, including first and second-order hydrodynamic loads (both sum and difference). The TLP response in heave was dominated by sum frequency effects (with or without exciting any eigen frequency). For the spar modelling, second-order forces were less important and the motion due to aerodynamic loads dominates the global motion.

4.1.3.3 OCx projects

The IEA Wind project, OC5 phase II, notably dealt with non-linear loads on the OC5-DeepCwind semisubmersible platform. If Morison formula is applied, low frequency loads are well predicted but high-order effects are overestimated resulting in large motion of the tower-top. On the contrary, models based on potential flow theory, including quadratic transfer function (QTF) to consider non-linear loads, result in an underestimation of ultimate and fatigue loads in low frequency region (about 20%) whereas tower-top motion is well predicted. To address this particular issue dealing with the under-prediction of low-frequency hydrodynamic loads and responses of a FOWT floater, the investigations were pursued within the OC6 Phase I project, as presented by Robertson et al. [2020].

Participants built two configurations (fixed and floating floater) in their engineering tools and their simulations were confronted to experimental data obtained at MARIN concept basin. Different combinations of the hydrodynamic theories were used. Also, some participants used a second-order solution including the quadratic transfer functions (QTF) to derive the radiation/diffraction matrices. Due to important discrepancies on low frequency load prediction, it was concluded that an improvement of the formulation of the engineering models themselves should be considered more than tuning engineering-level models. To investigate this low-frequency prediction issue, the OC6 project sets up CFD simulations, as detailed in the section 4.3.2.1.

Bachynski and Moan [2014] modelled four baseline TLP (of different diameters, drafts and pontoon radius/heights) in severe conditions, which can induce ringing response, according to Faltinsen criteria. The model matches well with experimental data when using second-order sum-QTF and third-order long wave Faltinsen, Newman, Vinje formulation with a Morison drag term added. The authors also observe that viscous damping coefficient has very small effect on ringing loads. This is in agreement with the results from OC5 Phase I project, where some of the participants underestimate third harmonic loads that are crucial in the prediction of ringing loads.

→ Second-order loads modelling is a hot research topic. Morison formulation and potential flow theory lead to different results both at high- and low-frequencies. When comparing to experiments, Morison formulation overestimates the response in a given frequency range while underestimating the response in another frequency range, and vice-versa for the potential flow theory.

→ The above mentioned uncertainties in the modelling of FOWT hydrodynamics highlight the interest of implementing a Numerical Wave Tank. Some limitations of the mid-fidelity engineering tools, such as the combination of the potential flow theory with Morison formula and the calibration of Morison coefficients for FOWT design will be investigated during the thesis with high-fidelity numerical modelling. The thesis work will also set the basis for the study of second-order wave loads on the FOWT floaters.

Computational Fluid Dynamic is a solution to investigate the issues previously detailed. With CFD simulation of the float, hydrodynamic loads on the structure can be determined with a limited number of hypotheses. These simulations are expected to be more accurate than the models previously described and to advantageously complement the experimental data sets. Calibration of hydrodynamic coefficients and the validity range of potential flow theory and Morison empirical formula can be investigated based on this type of numerical simulations.

CFD modelling of wave-structure interaction imposes to master:

- Wave generation, propagation and absorption along a NWT (the section 4.2)
- Fluid interaction with a constrained (and moving in a second step) solid structure

(section 4.3)

4.2 Numerical Wave Tank

This bibliographic review mainly relies on paper using OpenFOAM CFD software. This code has many advantages: it is open source, a large growing community of users exist and the code has been developed and improved over the past twenty years. That is why OpenFOAM is used for this thesis. Other software exist such as StarCCM (developed by CD-adapco and bought by Siemens in 2016), also known to be powerful for hydrodynamic applications, but not open-source and thus implying high license costs.

4.2.1 Wave generation and absorption in OpenFOAM

Different solvers exist in OpenFOAM to generate and absorb waves. They rely on relaxation zone method or active absorption method as explained in 3.3. Most of the solvers were tested and compared by Windt et al. [2019] and Miquel et al. [2018].

Windt et al. [2019], compared five wave generation and absorption methods for deep, shallow water waves and polychromatic waves. They consisted in: a relaxation zone method waveFoam (RZM, cf. section 3.3.1), a static boundary method olaFlow (SBM ola, cf. section 3.3.2), a static boundary method directly implemented in OpenFOAM v6 (SBM OF), a dynamic boundary method (DBM) and an impulse source method proposed by Schmitt et al. [2019]. For deep water waves, the RZM suggested to be the most interesting method with a low damping of amplitude along the tank (0.5%) and the weakest reflection coefficient (5%) compared to SBM ola where its reflection coefficient is about 25% due to its absorption method developed for shallow waters only. For shallow waters, RZM and SBM ola showed similar results but active absorption came at lower computational cost due to the smaller mesh size required.

Miquel et al. [2018] analysed the efficiency of a combination of relaxation method and active absorption for intermediate water depth compared to relaxation zone or active absorption boundary only. They concluded that the use of relaxation at the outlet provide the lowest reflection in the tank for both short and long waves, with either relaxation or active generation at the inlet. Active absorption at the outlet resulted in higher reflection coefficient for long waves than short waves. As Windt et al. [2019], they insisted on the fact that RZM comes at higher computational costs.

4.2.2 Numerical Wave Tank examples

Several Master theses present the implementation of a NWT in OpenFOAM.

Bruinsma [2016] from TU Delft modelled the propagation of a regular wave in intermediate water depth in 2D with waves2Foam library. He proceeds to a grid convergence study checking the diffusive error (the difference between the numerical wave elevation and the analytical signal) over time. Based on Paulsen et al. [2012] convergence method,

Bruinsma carried out the convergence study in a rectangular domain where cyclic boundary conditions were applied. The domain was only one wave length and so the computational time was lower compared to a model including relaxation zones. He insisted on the importance of performing a grid convergence study for each new wave modelled.

Davidson et al. [2015] also used waves2Foam library to implement a NWT. They detailed the structure of the CFD case and the tools available to post-treat the results. However, no information about mesh characteristics were given.

Afshar [2010] implemented a NWT with tailored boundary conditions to generate a fifth order Stokes deep water wave in OpenFOAM. He applied relaxation zones at the inlet and outlet of the NWT. He focused on the calculation of the error with analytical solution, but no validation against experiment was led.

Diz-Lois Palomares [2015] modelled different waves from literature in 2D with IH-FOAM solver, an active wave absorption solver developed at IHCantabria (Higuera et al. [2015]). He observed that wave profiles for steep waves are very unstable, partially due to the compression term in Eq. 3.8. As outlined by Windt et al. [2019], the use of active absorption for the propagation of deep water waves led to high reflection occurring in the tank.

→ From the above mentioned studies, passive solver using relaxation zones seem more appropriate to propagate deep-water waves but come at higher computational cost than active ones. A proper grid refinement and time step convergence study seems to be necessary for each new wave generated. To our knowledge, no consensus about a general set of dimensionless characteristics has been achieved so far.

4.2.3 VOF resolution limitation

Another point highlighted by Afshar [2010], Paterson [2008] and Pedersen et al. [2017] is the unwanted high air velocity on the crest of waves obtained with VOF MULES method available in interFoam solver. They are often called spurious air velocities though no surface tension is imposed in the CFD models. According to Afshar, high air velocities (5 to 8 times the maximum wave velocity) at interface induce premature wave breaking. To solve this issue, Afshar proposed a relaxation of the velocities just above the water surface.

Paterson [2008] also tried to minimize these high air velocities modifying the interface transport equation: he multiplied the convective term by the phase fraction value to get a null convective term in air and a reduced term in partially filled cells.

Larsen et al. [2019] investigated the performance of interFoam solver and how to minimize these air velocities on wave crests. Using diffusive convective schemes for the VOF transport equation (upwind) decreased air velocities but caused wave height damping along the NWT and along time. Larsen et al. [2019] also tested to resolve the convective term of the momentum equation with an upwind scheme but it induced a damping of wave height (smaller than the damping obtained with upwind scheme for transport

equation convective term).

Finally, Roenby et al. [2016] developed a new solver, called isoAdVector, applying geometric reconstruction of the free surface. The interface is less smeared and sharper than with interFoam solver.

⇒ In this PhD thesis, one first objective is to implement a proper Numerical Wave Tank. waveFoam and olaFlow (coupled with the VOF MULES interFoam method) will be tested and challenged for different sea conditions (results are presented in Appendix 9.2). According to the bibliography, both have advantages but also some limitations. One solver will be chosen to then perform wave-structure interaction modelling. Also, the resolution of the air/water interface, based on the VOF method, seems to be tricky and will be handled with care. The final objective is to determine a set of numerical parameters to generate, propagate and absorb waves in a controlled way, minimizing any reflection or damping phenomenon, while keeping achievable computational time. The reflection will be investigated analyzing wave elevation over time but also the spatial variation of the wave height along the tank, the last one being rarely quantified in the literature.

4.3 Fluid-structure interaction in CFD

To investigate fluid-floater interaction with CFD during the present thesis, it was decided to begin with a simple structure, namely a cylinder, and then include the complex IF-PEN/SBM Offshore TLP platform in the NWT. That is why this bibliographic review is divided into two subsections: first a review of the CFD modelling of a vertical piercing cylinder in waves is presented and secondly papers dealing with CFD simulation of FOWT floaters are discussed.

4.3.1 CFD modelling of vertical piercing cylinders in waves

4.3.1.1 Constrained vertical cylinder

Miquel et al. [2018] propagated waves on a constrained cylinder with a diameter larger than the incident waves amplitude. They concluded that the reflection in the tank does not impact significantly the forces (peak-to-trough) on the cylinder comparing two wave generation solvers, putting at stake passive and active absorption. Still, wave force crests with active absorption were 7% lower than with passive method.

Kristiansen and Faltinsen [2008] focused on wave loads on a constrained cylinder. A null velocity was imposed on the cylinder wall to consider the adherence of the flow on the wall. No turbulence model was implemented and viscous loads are captured thanks to a mesh refinement able to directly simulate the viscous layer, as achieved by Chen et al. [2019]. Paulsen et al. [2014] and Rivera Arreba [2017] did not consider the viscous layer imposing a null velocity gradient on the cylinder. They justified this choice explaining

that the flow is mainly inertial and viscous effects negligible for the regular wave they model.

Turbulence models exist in OpenFOAM to take into account the turbulence of the flow. Larsen and Fuhrman [2018] and Devolder et al. [2017] highlighted the fact that the commonly used offshore turbulence model k-omega SST gives incorrect results when combined with VOF resolution in OpenFOAM. In fact, an increase of kinetic turbulent energy and eddy viscosity on wave crest is observed leading to a drastic damping of amplitude in time and space. Larsen and Fuhrman [2018] implemented a modified version of k-omega SST method called k-omegaSST stabRAS which “stabilizes the model in nearly potential flow regions with modification remaining passive in sheared flow regions”.

→ From this part, it seems important during the thesis to check the reflection occurring in the NWT and the possible impact on wave loads. Boundary conditions for velocity and pressure on the cylinder/floater wall will also be examined to reproduce reality the most accurately. Turbulence models for fluid-structure simulations, implying VOF resolution and wave generation/absorption solvers, will also be investigated.

4.3.1.2 Cylinder in motion

To model the cylinder motion in waves, specific mesh techniques have to be used for allowing floater motion: dynamic mesh (moving and compliant) is usually used, overset-mesh is another promising technique. The CFD Fluid Mechanics equations have to be coupled with 6-DOF equations of motion to compute the floater motion, including mass and inertia effects as well as mooring stiffness. Dunbar et al. [2015] modelled the free heave decay test of a circular cylinder and evidenced some instabilities when applying the coupled CFD/6-DOF model. Rivera Arreba [2017] in her master thesis simulated Palm et al. [2016] moored cylinder experiments with waveFoam solver. Rivera Arreba [2017] used the CFD/6-DOF coupling adding the finite element method for mooring cables. They highlighted the strong dependence of the cylinder motion on the wave height. Also, heave and pitch responses show low error when compared to experiments ($< 10\%$). Surge motion differs due to the higher experimental front mooring line force and the restoring response.

→ Simulating the motion of a floating structure seems rather complex, some numerical difficulties exist when applying coupled CFD/6-DOF solvers. It has been chosen for the thesis to only model fixed floater in waves. The motion of the floater in waves will be modelled in a work following the thesis.

4.3.1.3 Hydrodynamic study of wave loads on a cylinder, based on CFD results

Paulsen [2013] in his thesis demonstrated the dependency to water depth, wave height and structure diameter of wave loads on a bottom mounted surface piercing circular cylinder for intermediate water depths. He performed an harmonic analysis of forces

to check the evolution of each harmonic component depending on wave characteristics. Paulsen also compared numerical loads to theoretical formula such as Morison empirical formula and third-order perturbation theories to predict ringing, as presented by Faltinsen et al. [1995] and š. Malenica and Molin [1995]. He notably checked the validity of these theories, originally developed for waves of small steepness, to predict wave loads on cylinder subjected to steep waves. He also studied the wave impact on the surface piercing cylinder, focusing on the creation of a secondary load cycle, a phenomenon that has already been discussed in Chaplin et al. [1997], Grue [2002], Rainey [2007].

Yan et al. [2020] investigated numerically the wave interaction with a fixed suspending payload (cubic shape) for offshore lifting, performing the simulations with waves2Foam library. He analysed the effects of the cuboid's position and size and wave characteristics on the loads and moments in order to identify the best posture of the payload, that would minimize the wave loads and the change of moment around a given axis. Though the study dealt with a suspended cuboid, it detailed a parametric study that can be valued in the thesis analyzing the wave loads on the braces of the floater characterized by different orientations, diameters, positions in the floater and under different wave conditions.

Benitz et al. [2015] modelled a vertical surface piercing cylinder in a steady current. They also modelled the slanted member of the semi submersible floater crossing the interface in different orientations. The cylinder was divided in slices to determine the loads on each slice. The author thus analyzed the variation of the inline force along the cylinder length and derive a drag coefficient for each slice. Up to now, this is the only CFD study that has sliced a cylinder along its axis to derive coefficients. However, no waves were modelled, that would complicate the derivation of the coefficients.

⇒ Many papers present the implementation and the validation of CFD models of a cylinder in waves. Few studies deal with the hydrodynamic investigation of the wave loads derived from CFD and the comparison with the existing theories. This thesis will notably study the wave loads on a surface-piercing cylinder and then on the FOWT platform checking notably the load dependency on the wave characteristics (period, height, depth), the structure dimension (diameter and length) and the orientation.

The study of extreme loads, occurring notably in steep water waves conditions or when the wave frequency is close to the natural frequency of the floater, will not be carried out. The purpose of the thesis is to set up a CFD model of a floater subjected to linear and operational waves.

4.3.2 CFD studies of FOWT

Over the ten past years, many CFD studies of FOWT hydrodynamics have been reported in the literature. Due to the complexity of modelling the free motion of the floater in waves, different simplified configurations of the floater are usually performed: constrained floater in waves, forced oscillations of the floater and decay tests. Most of the CFD studies mentioned in this subsection are performed with OpenFOAM software. However,

if a different software is used to derive hydrodynamic loads on a floater, its name is systematically mentioned.

4.3.2.1 Constrained floater in waves

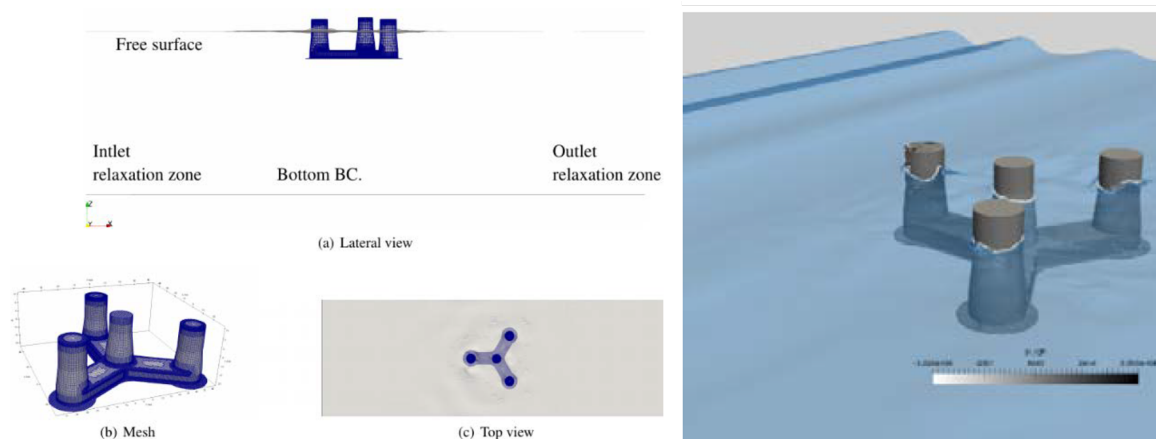


Figure 4.1: CFD modelling of the OO-star floater: schematic of the computational domain and boundary conditions (left side), snapshot of the floater in the numerical wave tank (right side) (Sarlak et al. [2018]).

Sarlak et al. [2018] investigated the prediction of wave excitation loads on the OO-Star semisubmersible platform, designed within the European project Life50+ for a 10 MW wind turbine (Fig. 4.1). The platform behaviour, in a constrained configuration and subjected to waves of increasing height, was simulated in OpenFOAM with library. The influence of the mesh refinement on loads was also investigated, notably varying the grid base resolution and the mesh refinement near the structure. They observed that the steeper the wave is, the higher harmonics of heave and surge forces are.

A part of the OC6 project, still ongoing, aims at studying the under-prediction of the low frequency response (cf. section 4.1) using CFD modelling. In Phase I of the project, CFD simulations of the constrained OC5-DeepCWind semisubmersible platform in bichromatic waves were performed but no experimental data was available to validate the numerical results. Nevertheless, Wang et al. [2020a] proposed an intensive evaluation of the numerical uncertainties to assess the accuracy of the CFD results. This estimation is crucial, notably because of the smallness of the non-linear loads compared to the linear loads (from direct wave excitation), which can be twice higher than non-linear loads. Wang proposed a systematic uncertainty analysis, based on an iterative, a discretization and a statistical source of uncertainty, to evaluate the different CFD models among them and with future experimental data. The determination of the numerical uncertainty was also detailed by Eça and Hoekstra [2009, 2014], Eça et al. [2019]. Wang et al. [2021] also pointed out that all CFD models are responsible for higher nonlinear load prediction than potential flow engineering solvers for the bichromatic wave case studied, up to twelve times higher for the surge force. The differences between CFD and engineering tools strongly exceed the numerical uncertainty estimated for the CFD results. The author

mentioned that this result does not imply that the potential flow solver is not able to capture resonance effect but it has to be adjusted. The transfer function dependence on wave height could be implemented in the linear potential flow theory. The author concluded that for preliminary design stages, potential solvers are essential because they correctly predict motion and loads on the structure in operational sea conditions. CFD provides an added-value for detailed design, focusing for instance on local effects such as the wave run-up around buoys or on extreme nonlinear effects, such as ringing and slamming phenomena.

Benitz et al. [2015] modelled the OC5-semisubmersible platform in regular waves. Under the wave conditions imposed in the model, the loads contribution from Morison formula are negligible compared to the one from the diffraction theory. No information about the meshing strategy was given.

→ Defining a set of numerical parameters, such as mesh refinement, time step or CFL, numerical schemes, to get an accurate CFD model is rather complex and specific to the understudy case, even for simple cases with constrained structure. An intensive numerical study will be achieved during the thesis to ascertain the accuracy of the CFD model. The numerical uncertainty of the CFD model will be evaluated. Also, the CFD loads will be compared to the loads derived with the mid-fidelity engineering solver DeepLinesWindTM. No study has been found yet conducting the derivation of Morison coefficients from CFD loads on a floater subjected to waves. In this work, we will propose a numerical method to determine the hydrodynamic coefficients of each brace of the constrained floater in waves (cf. section 5.2).

4.3.2.2 Forced oscillations

Contrary to the lack of studies dealing with the determination of Morison coefficients for a constrained floater subjected to waves, some studies have been carried out to determine the hydrodynamic coefficients on a structure subjected to forced oscillations.

Bozonnet et al. [2015] modelled a heave plate in OpenFOAM with the $k - \omega$ SST model, imposing forced oscillations to the floater in still water. They determined drag coefficients and added mass matrices with a Fourier analysis of the CFD signal. Dynamic or overset mesh strategies have to be implemented to model the motion of the float. This adds a new difficulty compared to the fixed floater case. Tao et al. [2004], Tao and Cai [2004], Tao et al. [2007] also studied the hydrodynamic loads on an heave plate (cylinder + disk) in forced oscillation conditions. They precisely analysed the influence of vortex shedding on the hydrodynamic coefficient values.

Zhang and Ishihara [2018], Zhang and Ishihara [2019] investigated the hydrodynamic load prediction on multiple heave plates, thanks to large eddy simulations in the CFD Ansys software, validated against experimental data. Predicting the added mass and drag coefficients on such a floater compared to a simple heave plate is very challenging; the interaction between elements and the complexity of the structure has to be taken into

account.

Pan and Ishihara [2019] investigated the hydrodynamic coefficients for a semisubmersible floater used for the Fukushima Forward Project (Fig. 4.2). The author insists on the importance of a validation step of the CFD simulation in order to conduct a coherent load analysis. The effect of KC number on the numerically-predicted hydrodynamic coefficients is detailed. The interaction between buoys themselves reduces the hydrodynamic coefficients. The effect of the interface can be neglecting for coefficients in the vertical direction obtained for CFD simulations of vertically forced oscillations. However, the free surface strongly impacts the horizontal coefficients obtained for CFD simulations of horizontally forced vibrations.

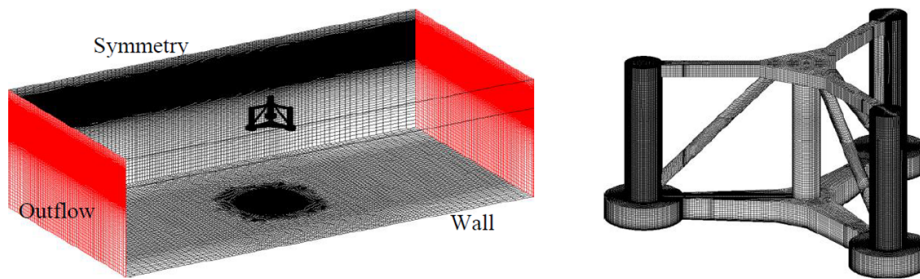


Figure 4.2: Mesh of the semisubmersible floater (Pan and Ishihara [2019]).

4.3.2.3 Decay tests

Sarlak et al. [2018] performed free decay tests simulations of the OO-Star floating platform with dynamic meshing only allowing to move in heave. They obtained similar results than with FAST simulations concerning damping magnitude and the trend of damping for large motion amplitudes. They underline that the numerical stability strongly depends on the choice of released degrees or freedom, the mesh and the floater mass.

Borràs Nadal and Bozonnet [2020] simulated surge decay tests of the SBM Offshore/IF-PEN TLP floater and validated the CFD results against experiments. The simulations run with the k-omega SST and the k-omega SST stabRAS (developed by Larsen and Fuhrman [2018]) turbulence models show critical differences on the dynamic pressure and the turbulent viscosity at the interface.

Bruinsma [2016] and then Rivera-Arreba et al. [2019], both from DTU Wind Energy section, model the free and moored decay tests of the OC5-semisubmersible platform with waveDyMFoam solver available in OpenFOAM. The heave, pitch and roll motions were validated against experiments. Rivera-Arreba et al. [2019] compared results obtained with potential-diffraction tools adding Morison elements (WADAM and SIMO-REFLEX) with CFD simulations (OpenFOAM with waves2Foam library). No information about the Morison coefficient values imposed in the design tool is given. For heave and pitch decay tests, both numerical models give rather similar results.

Burmester et al. [2017] and Wang et al. [2019] also modelled the free decay test of the OC5-semisubmersible platform but using ReFRESCO with the KSKL turbulent model (Menter and Egorov [2010]). They applied the PQ analysis (Van der Vegt [1984]) to compute the damping coefficients from CFD loads.

Burmester et al. [2017] modelled the damping in surge motion (Fig. 4.3). Results showed that the linear damping obtained in CFD is close to the experimental one. The quadratic damping computed in CFD is lower than experimental value, maybe due to the lack of mooring, turbine and power cable in the CFD model. Another aspect investigated by Burmester et al. [2017] was the scaling effect on viscous damping. The damping at model scale is larger than the damping at full scale, and the damping difference between both models increases in time. The author explained this increase in damping by the larger boundary layer at model scale than at full scale. A more recent study was proposed by Burmester et al. [2018] to follow-up on the first linear/quadratic damping analysis detailed in Burmester et al. [2017]. According to Burmester et al. [2018], the free surface (radiation) has a major influence on linear damping whereas quadratic damping is mostly due to viscous effects. Using non-linear model for the mooring lines does not improve the difference on damping between CFD and experimental results. Burmester et al. [2018] underlined the importance of CFD to determine the damping coefficients in order to improve inputs for engineering models.

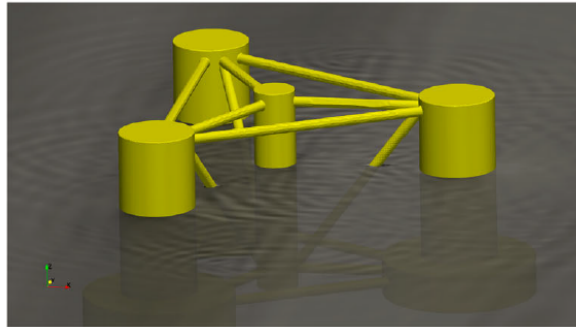


Figure 4.3: Free surface representation with radiated waves from the floater for the surge decay simulation (Burmester et al. [2018]).

For Wang et al. [2019], the pitch period of the OC5-semisubmersible platform was accurately predicted by the CFD model (ReFRESCO). They also highlighted that the heave damping plates are responsible for a major hydrodynamic damping and an important generated turbulent flow.

→ Forced oscillations and decay tests studies of FOWT floater in CFD highlight the strong influence of the mesh, the turbulence model and the motion solver on the numerical stability of the simulation. The damping seems also very sensitive to the modelling of the free surface and the scale chosen. Some authors derive the linear/quadratic damping coefficient from CFD results to improve mid-fidelity solvers.

4.3.2.4 Free motion in waves

All the studies detailed in this section were performed with the OC5-DeepCWind semisubmersible platform.

Rivera-Arreba et al. [2019] modelled the free motion of the floater in nonsteep wave and obtained good agreement between experiments and CFD for the pitch and heave response (Fig. 4.4, wave steepness = 0.60). Rivera-Arreba et al. [2019] also analyzed the response in heave resonance conditions propagating swell waves and comparing CFD results with a second-order potential flow model (SIMO-RIFLEX). The potential flow solver response is 40% lower than the CFD response.



Figure 4.4: Free surface elevation surrounding the OC5-DeepCWind semisubmersible in free motion in waves (Rivera Arreba [2017]).

Like Rivera-Arreba et al. [2019], Pinguet et al. [2021] modelled the free motion of the floater in regular waves with the waves2Foam library but coupled with the overset mesh module recently available in OpenFOAM.

Wang et al. [2020b] modelled the motion of the floater under two regular waves using ReFRESECO code the sea conditions are the ones imposed in the OC6 project. They derive the Response Amplitude Operators from the CFD results of the heave, surge and pitch motions and show acceptable agreement between numerical results and experiments with moderate discrepancies in surge and pitch (20 – 30%).

Tran and Kim [2015] also compared engineering tools to CFD (Star CCM) for the floater in free motion. A dynamic overlapping grid technique was applied to account for the dynamic motion of the FOWT. Regarding turbulence models, k-epsilon model is responsible for an excessive damping as the k-omega SST model. The authors explain that CFD simulations are run at full scale and compared to model scale experiments, scaled down based on the Froude similitude. However, as already underlined before, this similitude does not conserve the Reynolds number and might be responsible, in part, for the differences between experiments and CFD results, especially as regards the viscous damping.

→ All the above studies show the complexity of modelling the free motion of a floater in waves. Like the forced oscillations/decay test, the choice of an accurate turbulence model and a motion solver is uncertain. Also, waves must be generated, propagated and absorbed in a control way. The CFD models are validated against experimental data and results determined with design tool simulations.

4.3.2.5 Aero-hydro coupled behaviour modelling

A few people tried to model the complete behaviour of the entire floating wind turbine in CFD. The turbine motion is simulated with aerodynamic model while the motion of the floating part and the mooring system are modelled as detailed in the last section.

Liu et al. [2017] modelled the coupled behaviour of the OC5-DeepCwind semisubmersible platform in CFD. They focused on the action of the platform motion on the aerodynamic behaviour of the wind turbine and on the effect of the turbine on the platform motion and cable tensions. Good agreement with experiments was obtained in heave and pitch motion. The use of static mooring systems to model the dynamic mooring lines induces an under-prediction of line tensions compared to experiments. According to the authors, CFD brings precision to engineering studies about the aerodynamic flow field and hydrodynamic loads description close to structure walls. The continuation of this project was presented by Zhou et al. [2020], implementing a turbulent wind field with a time-varying spectrum. They conclude that despite the creation of fluctuations of the rotor thrust, the FOWT motion remains not influenced by the wind turbulence. Ren et al. [2014] also modelled the coupled simulation in CFD with Fluent software of the OC5-semisubmersible floater.

→ Modelling the response of a FOWT subjected to waves and wind in CFD is particularly complex and computationally expensive. It seems preferable to model separately the hydrodynamic and the aerodynamic behaviour to precisely describe the associated phenomena to the two different fluids. That is why in the thesis, we decided to only focus on the hydrodynamic part of the FOWT.

Summary

A major part of the above mentioned CFD studies deals with the OC5-DeepCWind semisubmersible platform that is modelled in the OC6 project and for which experimental database are publicly available and continuously extended. The CFD studies of a TLP-type floater are very limited. Here we will model the hydrodynamic behaviour of the SBM/IFPEN TLP floater in waves.

A few simulations of the fixed platform in waves have been achieved so far, contrary to decay tests/forced oscillations more often reproduced with CFD. Hydrodynamic analysis of loads on a constrained platform subjected to waves are also limited. This justifies the interest of this work that notably aims at investigating the wave loads on the TLP floater. We will restrain the study to the constrained configuration subjected to waves. This enables to simplify the problem understudy and investigate the influence of the wave characteristics/ structure dimensions on total loads (floater and braces separately) without taking into account the floater motion.

Hydrodynamic coefficients are often computed from CFD loads such as the drag coefficient/added mass matrices for forced oscillations and the damping coefficients for decay

tests. However, Morison coefficients are rarely derived from CFD loads on a floater subjected to waves, maybe partially due to the complexity of estimating the wave velocity field along each braces of the floater compared to a free surface at rest or a current only conditions. In this work, we will develop a methodology, inspired from the 80's experiments, to derive the Morison coefficients from the wave loads calculated with CFD approach for each braces. The influence on the coefficients values, of the buoys interactions, orientations, dimensions, distances to the interface, and the flow characteristics will be analysed.

Part II

Results

Chapter 5

A two-step methodology to investigate wave loads on a floater

In this work, we define a two-step methodology to investigate wave loads on a floater.

The first step consists of a precise practice to validate the accuracy of the Numerical Wave Tank. This methodology has been improved all along the thesis with the modeling of regular waves with different characteristics. The ultimate purpose is to provide dimensionless criteria to set-up a NWT for a large range of waves.

The second step is a methodology to derive Morison coefficients from CFD loads on a FOWT floater, inspired from the 80s experimental techniques (Chakrabarti [1981], Wolfram and Naghipour [1999]) initially used to determine the hydrodynamic coefficients on a cylinder subjected to waves.

5.1 How to set up a Numerical Wave Tank

In this section, we assess the validity of the NWT and propose criteria to set up a valid NWT based on four different regular waves with waves2Foam library (cf. section 3.3.1).

Many grid and time step sensitivity studies are carried out comparing the CFD wave elevation to the experimental and/or theoretical ones. The influence of the relaxation zone lengths on the wave height is also investigated.

We always analyse two outputs:

- The wave elevation time series at the future position of the floater centre. The objective is to obtain a CFD signal as close as possible to the corresponding theoretical/experimental wave elevation.
- The wave height variation along the tank. We check the wave damping along the tank and the possible reflection occurring along the tank. The objective is to minimise both phenomena.

Also, the velocity profiles derived from the CFD results at a given position in the NWT are compared to theoretical ones (cf. section 6.2.1).

Some dimensionless criteria are defined, and should be applied to correctly model the wave imposed in the simulation. Nevertheless, even if these advice are followed, a few extra simulations should be performed to ensure the quality of results and obtain a negligible level of errors.

The set up of the NWT for Stansberg wave (cf. Tab. 5.1) is also detailed in a paper submitted at the ASME 2020 39th International Conference on Ocean, Offshore and Arctic (Clément et al. [2020]).

5.1.1 Characteristics of the four waves retained for the study

The four waves characteristics are detailed in Tab. 5.1. H is the wave height, T the wave period, h the water depth, λ the wavelength, KC the Keulegan-Carpenter number defined in Eq. 2.44 as $u_m * T/D$ where u_m is the maximum velocity of the flow and D the diameter of the considered cylinder.

For Stansberg vertical surface-piercing cylinder (cf. Chapter 6), the maximum velocity considered in the formula is the maximum of the velocity time series under the wave crest. For the TLP floater (cf. Chapter 7), the KC varies according to the considered brace since u_m is taken equal to the non-disturbed velocity at the brace. In Tab. 5.1 we give the minimum and maximum of the KC number for each case. The minimum corresponds to the KC obtained for the deepest brace (lowest velocity) whereas the maximum corresponds to the KC derived for the surface-piercing braces (highest velocity).

Case	H [m]	T [s]	h [m]	λ [m]	kA (steepness)	KC
Stansberg	0.33	1.5354	10	3.68	0.28	5.2
w1	0.0246	1.271	2.2	2.52	0.031	0.63-2.20
w2	0.123	1.271	2.5	2.52	0.155	3.17-11.01
w3	0.225	2.214	2.5	7.43	0.095	15.16-22.74

Table 5.1: Wave characteristics.

The four waves are reported in Le Méhauté [1976] classification in Fig. 5.1:

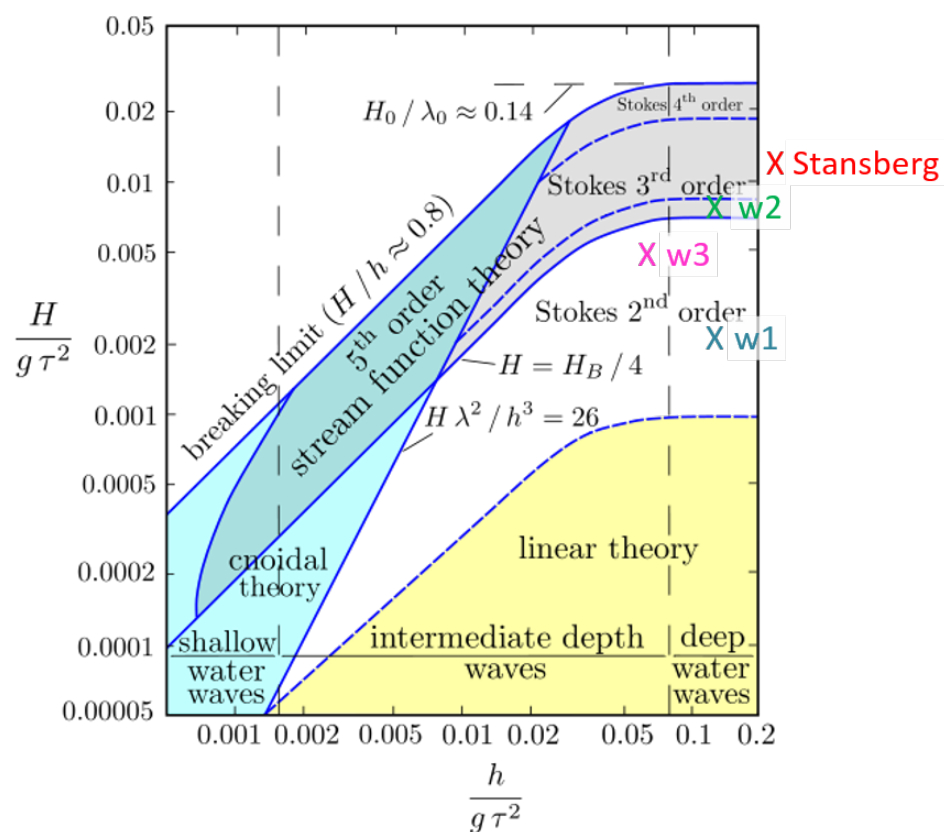


Figure 5.1: Modelled waves reported in Le Méhauté [1976] classification.

Fig. 5.1 shows that all the waves modelled belong to the deep water wave range.

Stansberg wave, chosen from Stansberg [1997] experiments, is Stokes 3rd order. Fig. 5.2 reveals a very weak difference between the wave elevation time series derived with 2nd and 3rd order theories (cf. sections 2.1.4 and 2.1.5).

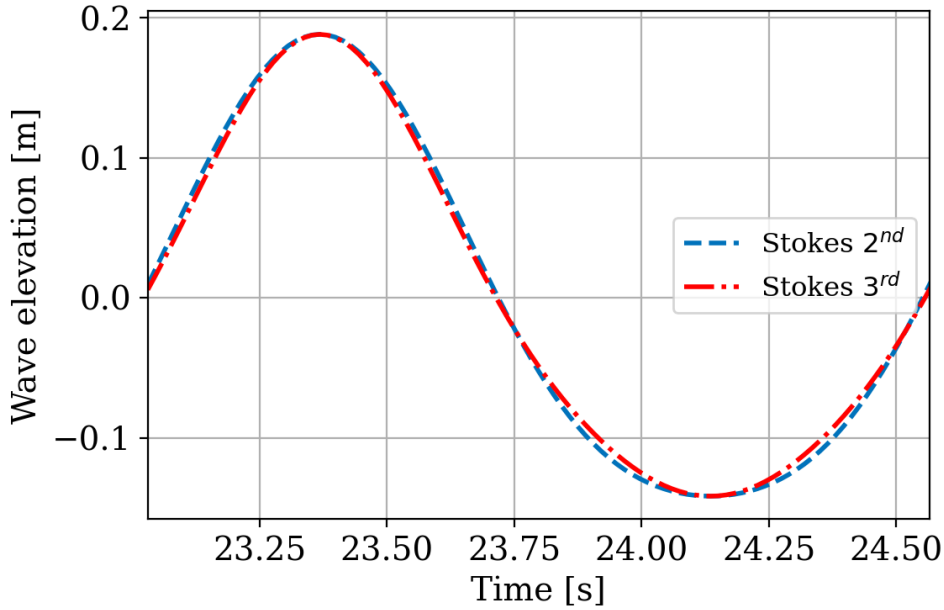


Figure 5.2: Wave elevation time series for Stansberg wave derived with Stokes 2^{nd} and Stokes 3^{rd} order theories.

The profiles of the maximum velocity along the water depth determined with the two theories extrapolated upper the mean sea level (cf. section 6.2.1) are rather similar as shown in Fig. 5.3.

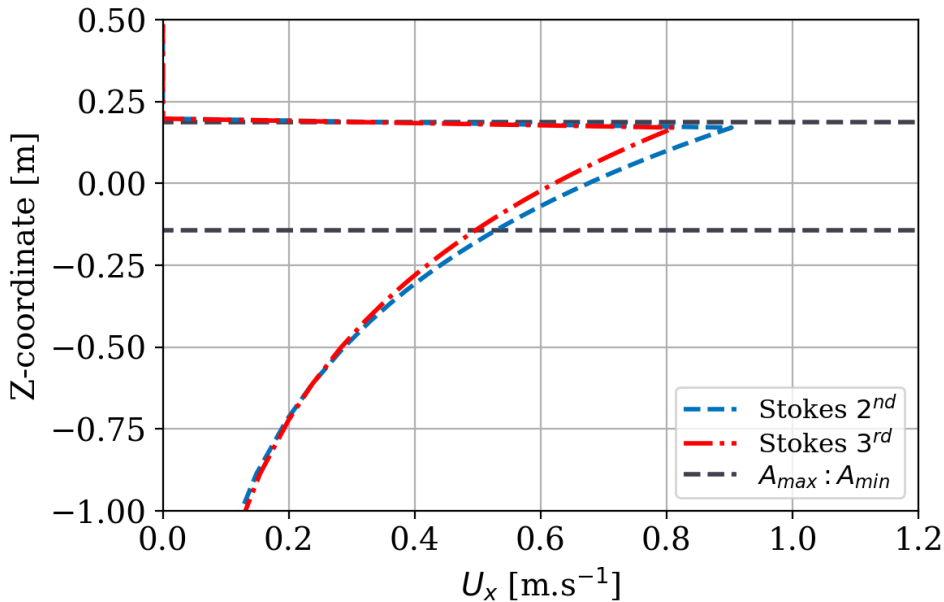


Figure 5.3: Velocity profile along water depth derived with Stokes 2^{nd} and Stokes 3^{rd} order theories.

That is why we decided to use Stokes 2^{nd} order theory for the analyses performed with Stansberg wave.

The TLP waves are second order, similar to sea conditions in which FOWTs are usually installed. The purpose is to scan the range of waves that can be encountered by FOWT

floater installed in open sea (with the limitation that in this study only regular waves are considered).

Wave w1 is a typical wave encountered by the FOWT in operating conditions. The wave w1 was performed at MARIN Offshore wave tank, Netherlands (Caillé et al. [2017]).

Wave w2 is an intermediate wave between w1 and w3. This wave was not performed at MARIN, it is chosen to have the same period as the wave w1 but the height is five times larger.

Wave w3 is an extreme wave barely encountered by the floater but used for the design in extreme conditions. The turbine is not operating because the wind is above the cut-out wind speed in this condition. This wave was performed as an irregular wave at MARIN. Due to the complexity of modelling irregular wave in CFD, we simplify w3 as a regular wave whose period and height are taken from the Jonswap spectra characteristics of the irregular wave w3.

The wave elevation and velocities time series determined with the CFD model will thus be compared to Stokes 2^{nd} order analytical formula detailed in the section 2.1.4 or experimental signals.

The waves are chosen to review different Morison contribution ranges as illustrated in Chakrabarti classification in Fig. 5.4. Indeed, with these waves and the structure diameter (the Stansberg cylinder or the FOWT braces), the structure can be considered as a slender cylinder ($D/\lambda < 0.1$). The wave loads can be predicted applying Morison empirical formula (Eq. 2.33).

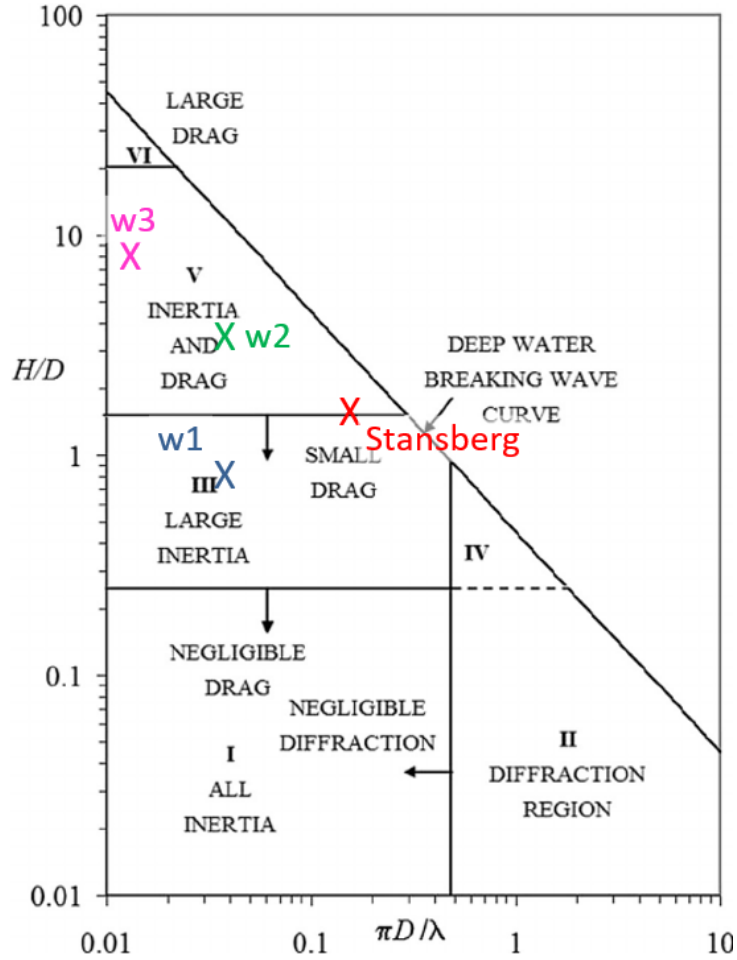


Figure 5.4: Wave/structure interaction case reported in Le Chakrabarti [2005] classification.

Fig. 5.4 shows that the wave/structure cases belong to different inertia/drag ratio ranges.

Thus we will test our numerical slice methodology deriving Morison coefficients from the CFD loads and investigate FOWT loads for different validity ranges of Morison formula.

5.1.2 CFD post-treatment specifics

In the global frame ($Oxyz$) represented in Fig. 5.5, the wave elevation time series $\eta(t, x, y)$ at one given position (x, y) is determined by integrating the water phase fraction field on a column of height $2H$ passing by M , the point of coordinate ($x, y, 0$). This post-treatment is based on the python code implemented by Higuera [2015] in the olaFlow code.

Signal dispersion

The dispersion of the signal is determined by the standard deviation σ_{max} of the series of the maxima of the temporal signal. The signal is considered as stabilised over time if the maxima evolve in a $\pm 2\sigma_{max}$ band around the mean of maxima (95% confidence interval). The same analysis is performed with the series of minima.

Wave height

In the global frame ($Oxyz$), the wave height at one location (x,y) in the tank is determined from $\eta(t, x, y)$ as (Eq. 5.1):

$$H_{calc}(x, y) = 2\sqrt{2\text{var}(\eta(t, x, y))} \quad (5.1)$$

where

$$\text{var}(\eta(t, x, y)) = \sigma_{max}^2 = \frac{1}{n} \sum_{i=1}^n (\eta(t_i, x, y) - \bar{\eta}(x, y))^2 \quad (5.2)$$

Error quantification on wave height

To quantify the differences between the wave elevation time series derived from the CFD simulations and the reference (experimental or theoretical signal), the error in the percentage between the height derived from both signals is determined as:

$$\text{Error}(H_{CFD}, H_{ref}) = \frac{H_{CFD} - H_{ref}}{H_{ref}} * 100 \quad (5.3)$$

Error quantification on time series

The Normalised Root Mean Square Error (NRMSE) defined in Eq. 5.4 is also used to precisely compare two signals over time:

$$\text{NRMSE} = \frac{\sqrt{(\frac{1}{n}) \sum_{i=1}^n (\eta_{Model}(t_i, x, y) - \eta_{Reference}(t_i, x, y))^2}}{H_{Reference}}, \quad (5.4)$$

where η_{Model} is the wave elevation at time t_i derived from the CFD simulation or from the analytical formula, $\eta_{Reference}$ is derived from the experimental model, and n the total number of time steps.

To complement those statistics, plots are presented but only a few periods are shown for the sake of clarity.

All the above mentioned formula are also used to validate CFD wave loads on the structure against experimental data or theoretical formula, that will be detailed in Chapter 6 and Chapter 7.

5.1.3 Geometry and boundary conditions of the NWT

The NWT implemented with the relaxation zone solver waveFoam is sketched in Fig. 5.5.

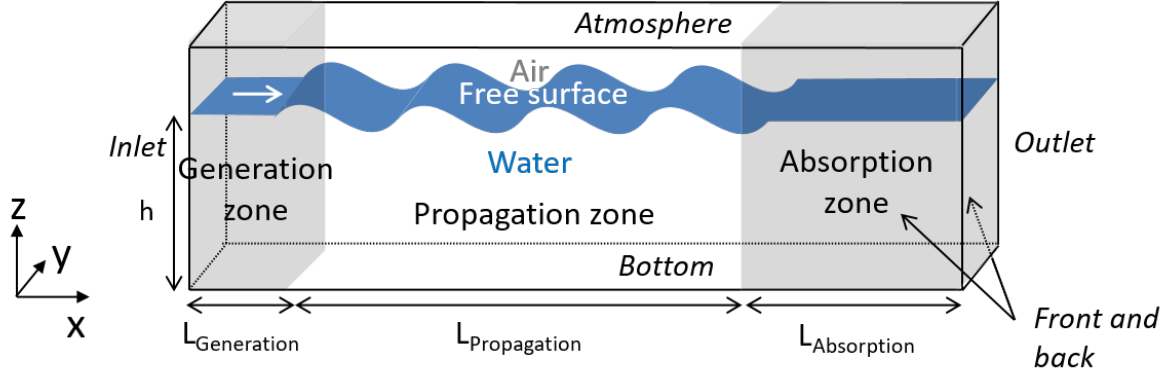


Figure 5.5: Numerical Wave Tank sketch.

The NWT is composed of three zones: the generation zone, the propagation zone and the absorption zone of respective lengths $L_{Generation}$, $L_{Propagation}$ and $L_{Absorption}$. The width of the tank is 10 times the diameter of the structure to avoid side wall effects. The boundaries of the NWT are indicated in italic on the sketch and the boundary conditions on each boundary are presented in Tab. 5.2.

Boundary patch	Velocity	Pressure	Phase fraction
Inlet	waveVelocity	zeroGradient	waveAlpha 0
Outlet	fixedValue 0	zeroGradient	zeroGradient
Bottom	fixedValue 0	zeroGradient	zeroGradient
Atmosphere	pressureInletOutletVelocity	totalPressure	inletOutlet
Front	slip	zeroGradient	slip
Back	slip	zeroGradient	slip

Table 5.2: Boundary conditions for the NWT.

Boundary conditions at the inlet for the velocity and phase fraction are specific to waves2Foam generation library (see section 3.3.1). For the four waves, Stokes 2nd order wave theory is imposed at the inlet of the NWT. Other boundary conditions are standards. The atmosphere behaves like an open face. The front and back walls are similar to symmetry walls to represent the flow as infinite in (Oy) direction.

No turbulence model is activated for the simulations unless mentioned.

In the following sections, the key parameters to implement a NWT are detailed.

5.1.4 Relaxation zone lengths

The influence of the relaxation zone lengths on the wave reflection along the tank is investigated in this section.

For the CFD model of Stansberg wave, three different absorption zone lengths are

tested. We define $L_{Absorption}$ as a multiple of the wavelength λ ; $L_{Absorption} = 3\lambda$, $L_{Absorption} = 6\lambda$ and $L_{Absorption} = 9\lambda$ are referenced as 3 w.l., 6 w.l. and 9 w.l. respectively, in Fig. 5.6.

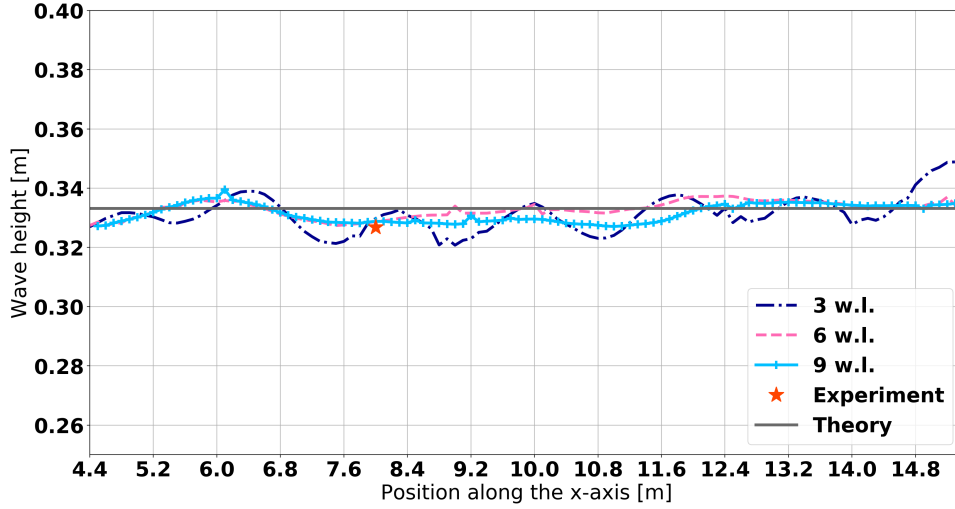


Figure 5.6: Wave height for three different absorption zone lengths (Stansberg wave).

We observe that oscillations due to reflection decrease with increasing absorption zone length.

It is more common in literature (Paulsen [2013], Rivera Arreba [2017]) to absorb second order deep water waves with an absorption zone length equal to 3λ . However, the mesh with a 6λ absorption zone length being only 8% bigger than the 3λ mesh, we decided to carry on with a $L_{Absorption} = 6\lambda$ absorption zone length providing a good compromise between accuracy and computation time.

The generation zone length $L_{Generation}$ is defined such that $L_{Generation} = 1\lambda$. Contrary to the absorption zone length, the generation zone length has a small influence on the variation of the wave height along the tank, as demonstrated during the internship preceding this PhD thesis (Clément [2018]).

5.1.5 Grid refinement

The mesh convergence study is a crucial step to obtain a valid mesh and thus a correct generation, propagation and absorption of the waves along the tank.

The mesh is depicted in Fig. 5.7 and a cross-section by (Oxz) plane is shown in Fig. 5.8.

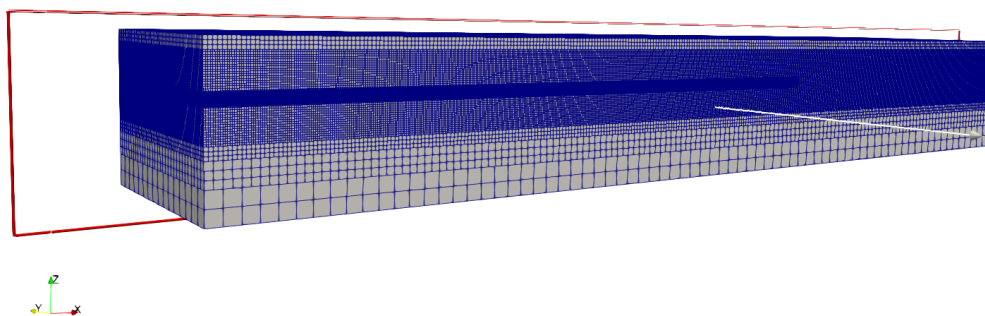


Figure 5.7: Numerical Wave Tank mesh (wave w2).

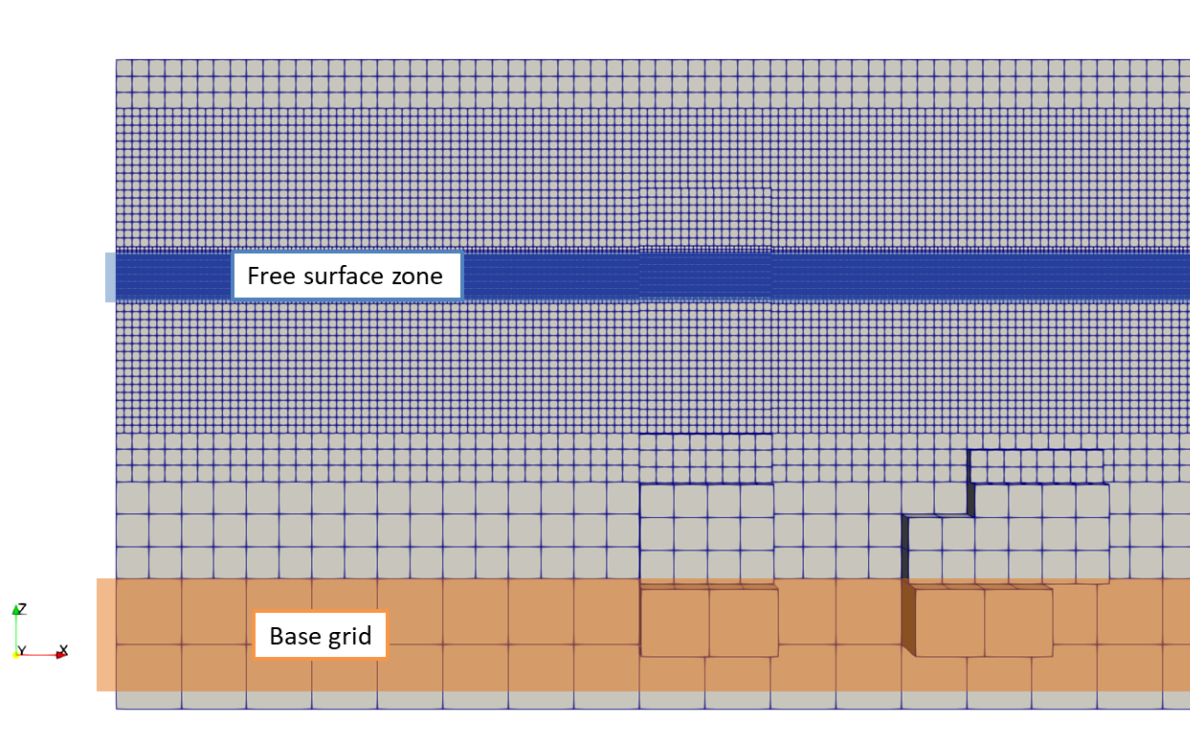


Figure 5.8: Free surface refinement (wave w2).

The base grid is generated with the blockMesh tool. An aspect ratio of $AR = 1$ is imposed. The zone in which the free surface evolves has to be intensively refined to correctly propagate the wave. This zone called "the free surface zone" has a height of $2H$ around the mean sea water level as represented in Fig. 5.8.

For wave w2, three levels of refinement are tested in the free surface zone: $nz = 10$, $nz = 20$ and $nz = 30$, nz is the number of cells per wave height in (Oz) direction. The influence of the number of points per wave height on the wave elevation variation along the tank is shown in Fig. 5.9. The larger nz is, the smaller the damping of wave height

along the tank is.

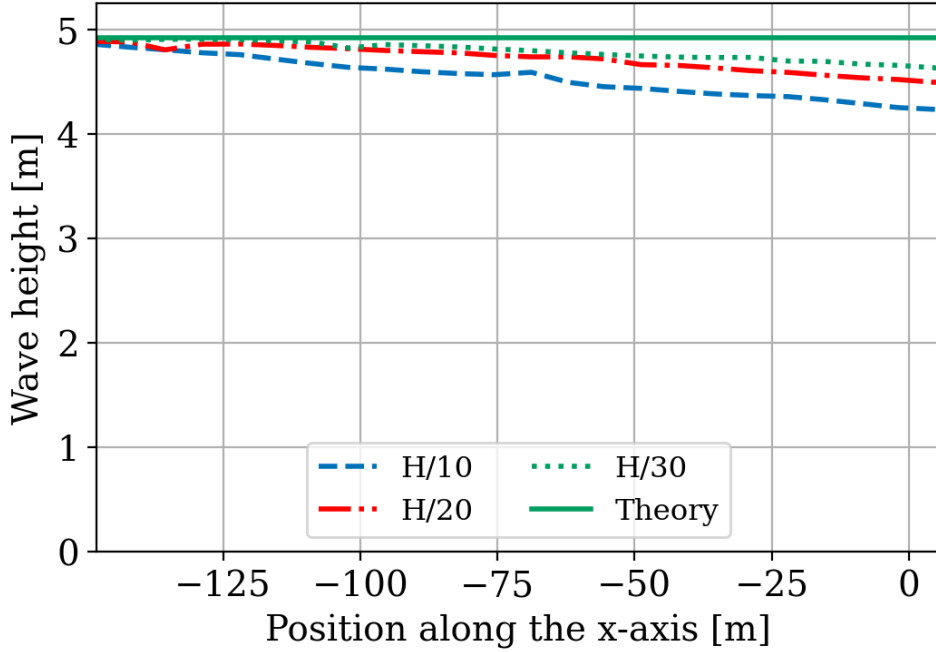


Figure 5.9: Influence of the number of cells per wave height (nz) on the wave height variation (wave w2).

In the simulations run to obtain the results plotted in Fig. 5.9, the number of points per wave length on (Ox) was set fixed to 100. We consider the damping as important even for the highest nz . That is why we then vary the cell size on (Ox) to check the influence on the wave height variation. Fig. 5.10 represents the wave height variation along the tank for two models with $nz = 20$ and different nx . A ratio r is defined in Eq. 5.5 to relate the vertical cell size dz and the horizontal one dx .

$$\frac{dz}{dx} = \frac{H/nz}{\lambda/nx} = \frac{H}{\lambda} * r \quad (5.5)$$

The ratios r for the two simulations are respectively 5 and 10.

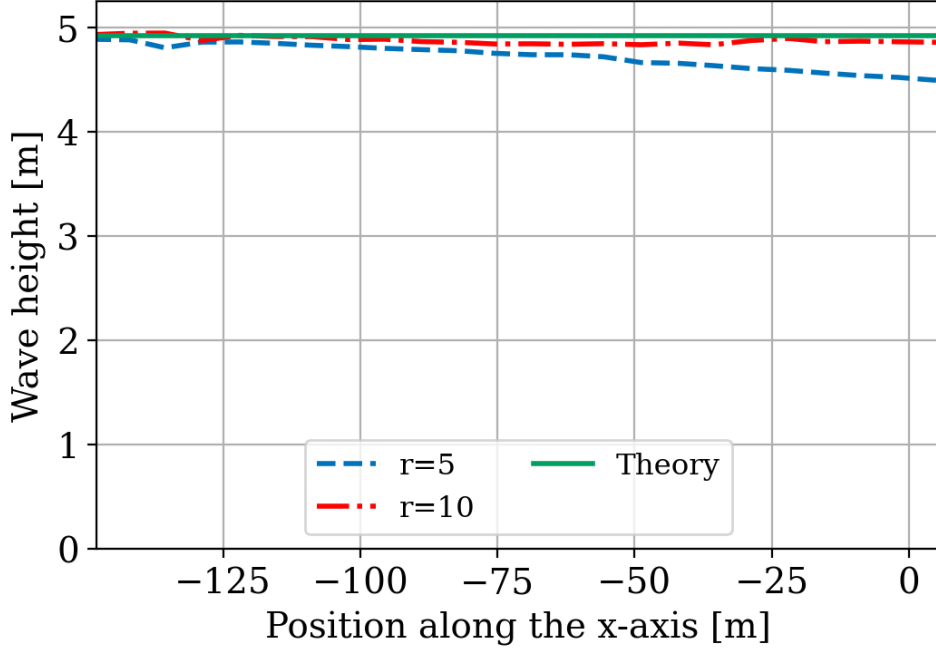


Figure 5.10: Influence of the ratio r ($dz/dx = r * H/\lambda$) on the wave height variation (wave w2).

For $r = 10$, we do not observe any damping so we keep this ratio as a reference.

Finally we define two refinement criteria that should be respected in the free surface zone to control the wave propagation along the NWT:

- A minimum number of points per wave height (nz) on (Oz) direction of 10-20. The cell size on (Oz) is defined as $dz = H/nz$.
- A ratio r that should be around 10. r is defined in Eq. 5.6 as:

$$r = \frac{nx}{nz} = \frac{H/dz}{\lambda/dx} \quad (5.6)$$

in which dz and dx are the cell sizes in (Oz) and (Ox) directions and nz and nx are the number of cells per wave height and wavelength.

Finally, we highlight that the refinements along (Ox) and (Oz) axes are not independent and this numerical ratio r should be taken as a reference rather than only nz as it is most of the time proposed in the literature.

Practically, the refinement of the mesh around the free surface is performed with refinement levels in one or several directions using the snappyHexMesh solver available in OpenFOAM.

The main characteristics of the meshes obtained with such refinement rules are detailed in Tab. 5.3 for each wave case.

5.1.6 Time step

In this time step convergence study, we vary the time step relating it with the period T ($dt = T/n$ where n is the number of time steps per wave period) while keeping the simulation CFL under a certain value. The NWT cases are run with fixed time steps.

A convergence study is performed in order to optimise the time step, in order to get results as close as possible from convergence while optimising the computational time.

With wave w3 and a mesh in agreement with the criteria previously mentioned, four time steps between $T/246$ and $T/1100$ are tested. The influence of the time step on the variation of the wave height along the tank is illustrated in Fig 5.11.

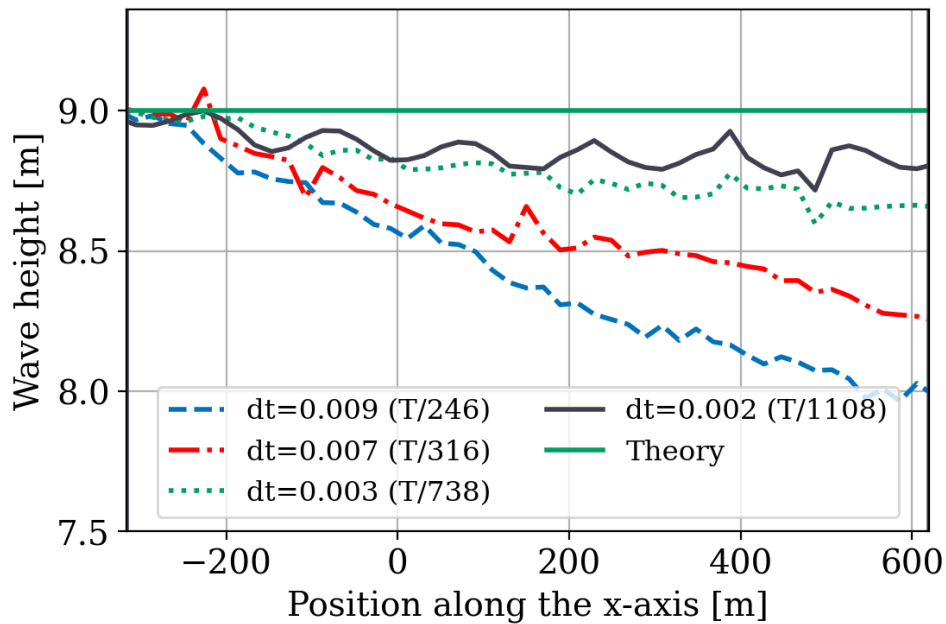


Figure 5.11: Wave height along the tank for the time step convergence study (wave w3).

The simulation performed with the largest time step ($dt = 0.009 \text{ s} = T/246$) does not reveal any instability but a strong damping of wave elevation along the tank is noticed. For this time step, the visualisation of the velocity field reveals high air crest velocities increasing along the NWT as shown in Fig. 5.12.

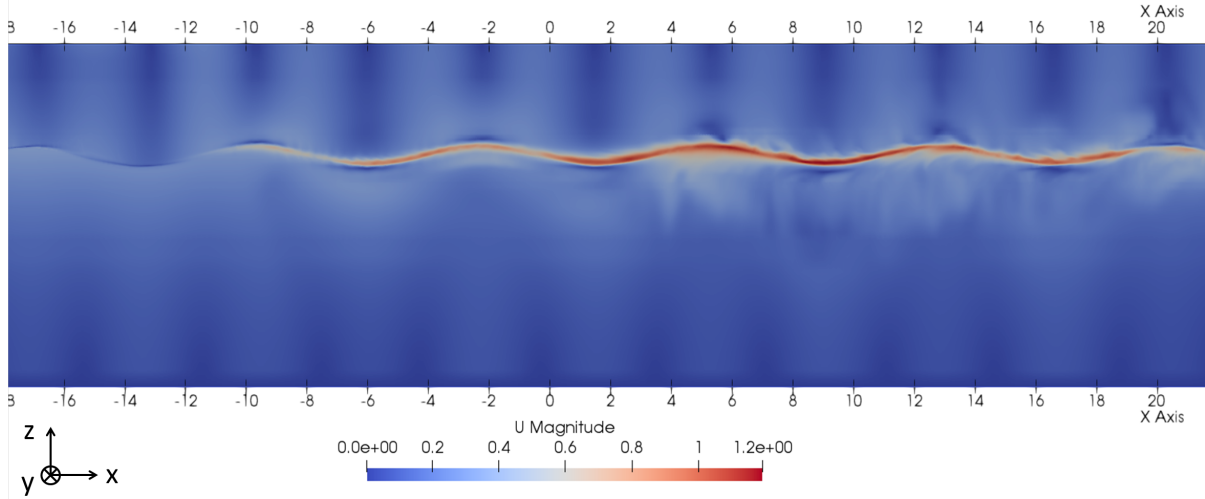


Figure 5.12: Visualisation of air crest velocities along (Ox) (wave w3) (zoom $\times 3$ on (Oz)).

These important velocities seem to be responsible for the wave amplitude damping. This phenomenon was also studied by Larsen et al. [2019]. For the authors, the resolution of the interface applying VOF MULES method with large CFL ($0.15 < CFL < 0.5$) leads to high crest velocities and wave height damping. They solved this problem by decreasing the CFL ($dz = H/12.5$ and $CFL < 0.05$). We also observe that the air crest velocities are reduced with smaller time steps.

However, wave height oscillations appear when the time step is reduced. This numerical instability can be reduced increasing the absorption zone length. Each signal does not have the same oscillation period though the same mesh and wave parameters are imposed. Therefore we cannot properly speak of a physical reflection phenomenon.

The wave height variation along the tank obtained imposing $dt = 0.003 \text{ s} = T/738$ slightly decreases along the tank so this choice of time step seems consistent.

The maximum CFL number obtained for these simulations in descending order of time steps are 0.72, 0.5, 0.2 and 0.14. Larsen and Fuhrman [2018] advised to keep a CFL number smaller than 0.05 for the numerical stability of the VOF MULES method. Satisfying this criteria would lead to critical computational time. With $dt = 0.003 \text{ s} = T/738$, the maximum CFL achieved is 0.2. So we keep 0.2 as the maximum value of the CFL number that should not be exceeded at the interface zone.

Finally, two main criteria drive the time step selection:

- The time step has to be smaller than $T/700$ to avoid numerical damping of the wave height along the tank explained by the existence of high air crest velocities for large time step. The time step has also to be higher than $T/900$ to limit the numerical reflection along the tank and maintain a reasonable computational time
- To ensure numerical stability of the VOF MULES method, the maximum CFL in the interface zone should not be higher than 0.2.

5.1.7 General guidelines to setup a NWT

To generate, propagate and absorb waves in a controlled way along space and time, we have the following suggestions:

- The generation zone length must be around 1λ
- The propagation zone length can not be too long along (Ox) to minimize the damping of the wave height along the tank, but not too short to let the wave propagate. That is why, we impose at least 1λ between the end of the generation zone and the upstream part of the structure and 2λ between the downstream part of the structure and the beginning of the absorption zone.
- An absorption zone of 6λ is necessary to correctly absorb the wave.
- The free surface must evolve in a $2H$ height refinement box, centered around the mean sea water level (free surface zone). Its dimensions on (Ox) and (Oy) are the same as the background grid ones. Still, the free surface box can be shorten 1λ after the beginning of the absorption zone along (Ox) to reduce the mesh size. The ratio r relating the cell size on (Oz) and (Ox) to the wave steepness ($dz/dx = r * H/L$) has to be around 10, while keeping the maximum number of points per wave height on (Oz) direction between 10 and 20. The mesh is coarsened from the free surface zone to the base grid with several levels of refinements.
- We advise aiming for an aspect ratio of 1 for the cells of the base grid and the first levels of refinement connecting this background grid to the free surface zone.
- The time step should be smaller than $T/700$ to minimize the wave height damping along the tank and higher than $T/900$ to avoid numerical reflection along the tank and maintain a reasonable computational time
- To ensure numerical stability of the VOF MULES method, the maximum CFL in the interface zone should not be higher than 0.2.

It is important to keep in mind that these guidelines were identified and validated only for the four regular waves considered in the PhD thesis, as detailed in the following section. These tips can be used as a starting point, but we recommend running a few more simulations to ensure the validity of the results. In any case, we strongly recommend checking the temporal evolution of the wave elevation at a position in the NWT and also the spacial variation of the wave height along the tank.

5.1.8 Results for the four waves

In this section, the results obtained with the final simulations for the four different waves are presented. The CFD models are implemented applying the guidelines previously detailed.

More precisely, the mesh characteristics for each wave are detailed in Tab. 5.3. FSZ stands for the Free Surface Zone, namely the box of height $2H$ centered on the mid-sea water level. The refinement levels are given along (Ox) , (Oy) and (Oz) directions, as a reference the base grid refinement level is 0.

Case	Base grid	Refinement level in the FSZ	nz in the FSZ	r in the FSZ
Recommandations	/	/	10-20	$\simeq 10$
Stansberg	2H/3	3 3 3	12	11
w1	6H	3 3 6	11	13
w2	3H	5 0 6	20	10
w3	4H/5	4 4 6	20	8

Table 5.3: Mesh characteristics.

For all the waves apart from the Stansberg one, the free surface refinement zone ends 1 w.l. after the beginning of the absorption zone along (Ox) direction to optimize the mesh size.

The time step imposed in the simulation as well as the maximum CFL obtained when running the simulation are presented in Tab. 5.4.

Case	Time step [s]	Max CFL
Recommandations	$T/700 - T/900$	< 0.2
Stansberg	0.002 ($T/768$)	0.08
w1	0.002 ($T/640$)	0.07
w2	0.002 ($T/640$)	0.19
w3	0.003 ($T/738$)	0.14

Table 5.4: Time step and maximum interface Courant number.

It can be noted that a time step of $T/640$ is sufficient for wave w1 (and for wave w2 that has the same period than w1) to keep the maximum CFL number lower than 0.2 and propagate the waves in a controlled way.

Finally, the variation of the wave height along the tank and the wave elevation time series at the center of the tank for the four waves are shown in Fig. 5.13 and Fig. 5.14.

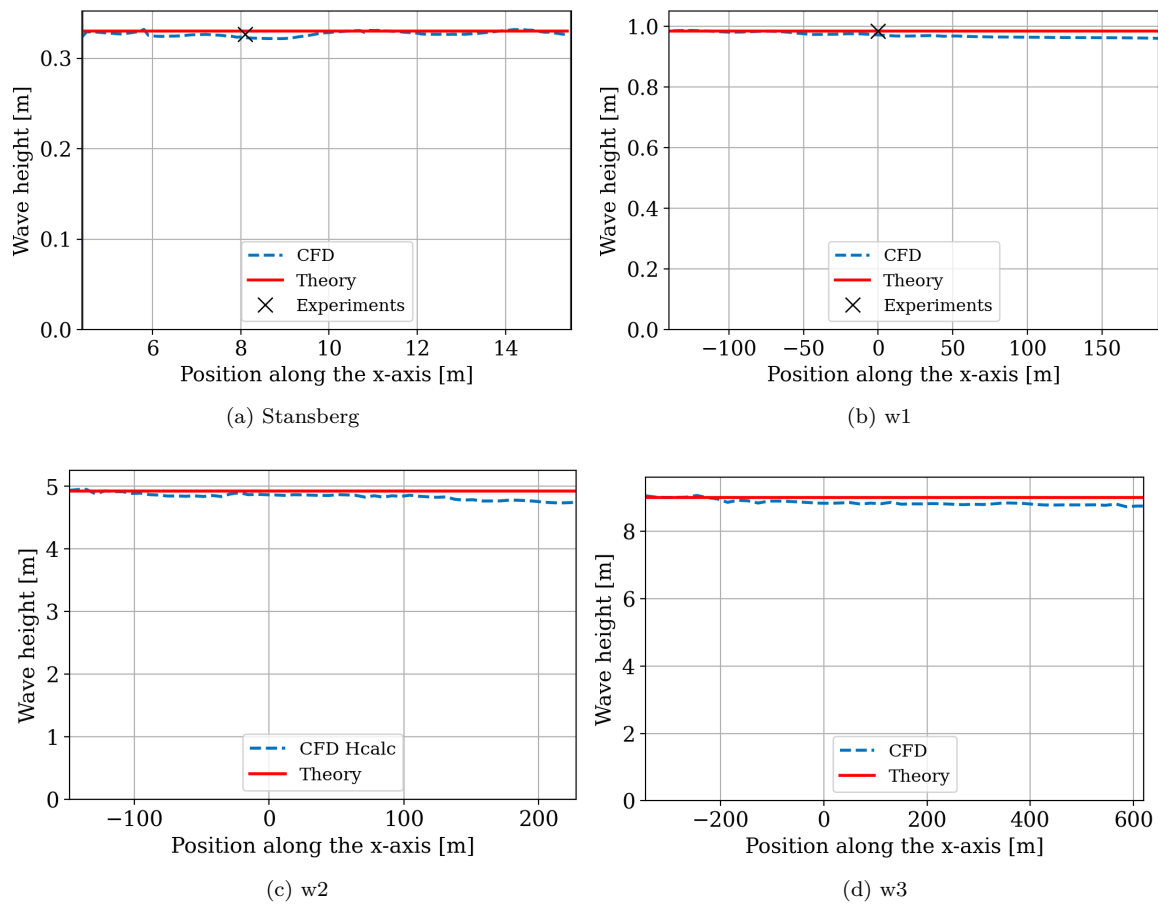


Figure 5.13: Wave height variation along the tank for the four waves.

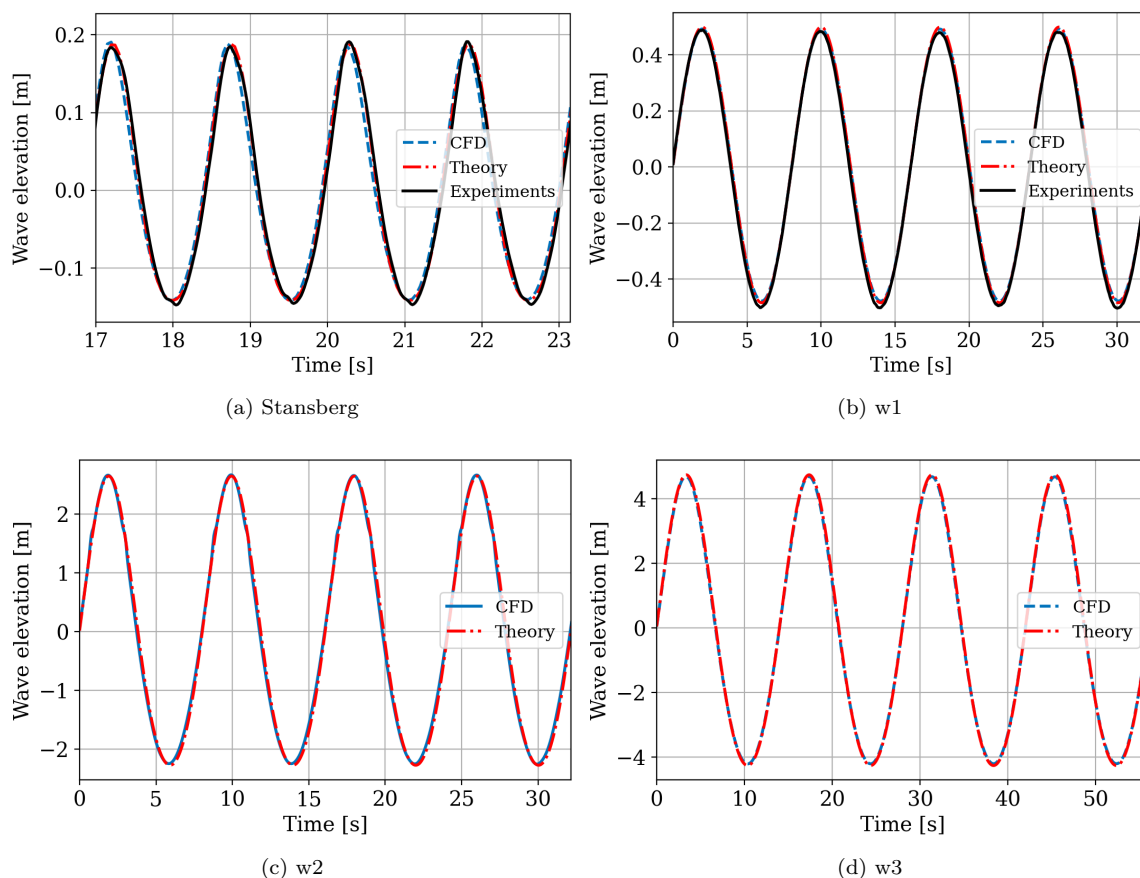


Figure 5.14: Wave elevation time series for the four waves, at the position corresponding to the location where will be placed the floater.

The wave height exhibits low variations along the tank and remains close to the theoretical value. The damping and the reflection along the NWT are negligible. We also observe that the CFD and theoretical (and experimental) wave elevation time series at the center of the tank are in excellent agreement.

The four NWT implemented are thus valid following the criteria detailed in this section. The methodology we propose to derive Morison coefficients from the wave loads determined once the structure is included in the NWT is described in the following section.

5.2 Development of a slice methodology on a complex floater for determining Morison coefficients

As explained in the section 2.3.1, various test campaigns were conducted in the 80s to determine database of hydrodynamic coefficients. The obtained standards were intensively used for the design of offshore O&G platforms, but reveal some limitations for FOWT design as detailed in the section 4.1.2. In this thesis, a method is proposed, inspired from the experimental one, to derive Morison coefficients from the CFD loads obtained on the braces of the floater.

In experiment, Morison coefficients are often derived from the total load on the cylinder. Very few studies take into account the load variation along the cylinder in the determination of the coefficients since it is complex to get this type of detailed information experimentally. Only Chakrabarti [1979] measured the inline force on two sections of a given cylinder in addition to the total load. Thank to CFD, we propose to go further and to determine Morison coefficients values along the cylinder by slicing the cylinder along its axis. This method can be applied to any type of cylinder and thus on a realistic and complex floater structure. The Morison coefficient values obtained for such a FOWT floater will thus take into account the cylinder orientation, the position in the structure, the distance to the interface and the interaction between the braces, as well as the wave characteristics imposed in the NWT. In this section, we detail this slice methodology for the complex SBM Offshore/IFPEN TLP floater.

5.2.1 The floater configuration

The braces of the floater are gathered in typical groups according to their diameter, length and orientation. They are represented in Fig. 5.15 and consist in:

- Braci: 3 longest horizontal braces connecting the three lateral buoys, at the bottom of the floater
- Brac1i: 3 shortest horizontal braces connecting the three lateral buoys to the central buoy, at the bottom of the floater
- Transi: 3 inclined braces piercing the interface connecting the three lateral buoys to the top of the platform
- Centi: 3 vertical braces piercing the interface connection the center buoy to the top of the platform
- Interi: 6 inclined braces connecting the middles of the braces Transi and Braci
- Renforti: 9 small braces connecting the three Centi braces

Height braces are selected from these groups to apply the numerical slice method. They consist in Brac1, Brac2, Brac12, Brac13, Cent1, Cent2, Trans2 and Trans3 as detailed

in Fig. 5.16. They all have the same diameter ($D = 1.24$ m). The brace is discretized in slices along its axis as illustrated in Fig. 5.16. All the braces are divided in 20 slices apart from the Transi braces that are divided in 30 slices. Morison coefficient values are determined for each slice.

The same slicing practice is applied for Stansberg [1997] cylinder. We divide the lateral patch i.e., the patch without the basis of the cylinder in slices along its axis.

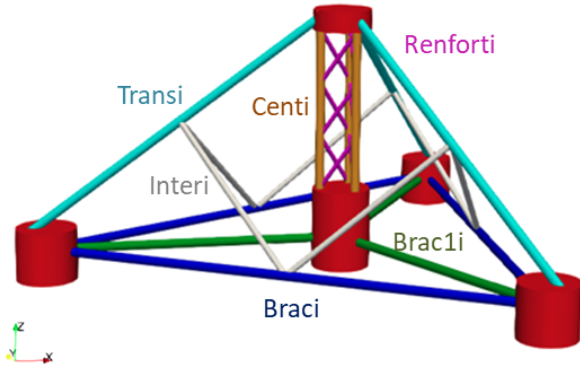


Figure 5.15: Typical groups of braces.

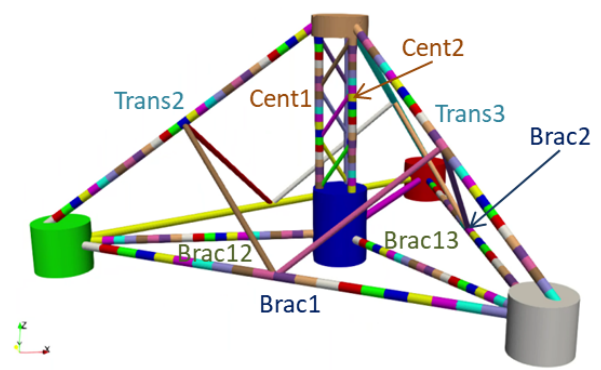


Figure 5.16: Braces sliced in the floater.

CFD loads on each slice are determined in the global frame ($Oxyz$). However, the generalization of the Morison empirical formula to oriented cylinders is obtained in the local frame of the cylinder (Eq. 2.36). That is why the local frame of each brace is rigorously defined in the following section. The CFD loads will be moved to this local frame before post-processing them.

5.2.2 Definition of the local frames of the braces

The local frame (ΩXYZ) of a brace is defined as represented in Fig. 2.5 for an oriented cylinder. Ω is the center of the brace.

\mathbf{Y} is always the vector parallel to the cylinder axis and so \mathbf{X} and \mathbf{Z} belong to the plane perpendicular to the cylinder axis. The local frame is obtained from the global frame with the combination of three successive rotations: one around (Ox) by the angle α , then around (Oy) by the angle β and finally around (Oz) by the angle γ . The rotation angles are given in Tab. 5.5 in the trigonometric direction of rotation.

Braces	α	β	γ
Brac1	0	0	$\frac{4\pi}{3}$
Brac2	0	0	0
Brac12	0	0	$\frac{3\pi}{2}$
Brac13	0	0	$\frac{7\pi}{6}$
Cent1	$\frac{\pi}{2}$	0	0
Cent2	$\frac{\pi}{2}$	0	$\frac{2\pi}{3}$
Trans2	$\frac{\pi}{2}$	1.57-0.6435	0
Trans3	$\frac{\pi}{2}$	1.57-0.6435	$\frac{2\pi}{3}$

Table 5.5: Rotation angles (in rad) for each brace in the global frame ($Oxyz$).

The components (X, Y, Z) of a given vector \mathbf{A} in the local frame are obtained using Eq. 5.7:

$$\mathbf{A}(X, Y, Z) = P(\text{Brac } i) * \mathbf{a}(x, y, z) \quad (5.7)$$

where (x, y, z) are the components of the vector \mathbf{a} in the global frame ($Oxyz$) and $P(\text{Brac } i)$ stands for the transfer matrix, defined by Eq. 5.8.

$$P(\text{Brac } i) = {}^t(R_z(\gamma)R_y(\beta)R_x(\alpha))$$

$$P(\text{Brac } i) = {}^t \left(\begin{pmatrix} \cos(\gamma) & -\sin(\gamma) & 0 \\ \sin(\gamma) & \cos(\gamma) & 0 \\ 0 & 0 & 1 \end{pmatrix} \begin{pmatrix} \cos(\beta) & 0 & \sin(\beta) \\ 0 & 1 & 0 \\ -\sin(\beta) & 0 & \cos(\beta) \end{pmatrix} \begin{pmatrix} 1 & 0 & 0 \\ 0 & \cos(\alpha) & -\sin(\alpha) \\ 0 & \sin(\alpha) & \cos(\alpha) \end{pmatrix} \right) \quad (5.8)$$

The three rows of $P(\text{Brac } i)$ correspond to the coordinates of \mathbf{X} , \mathbf{Y} and \mathbf{Z} in ($Oxyz$). The local frames obtained are represented in Fig. 5.17.

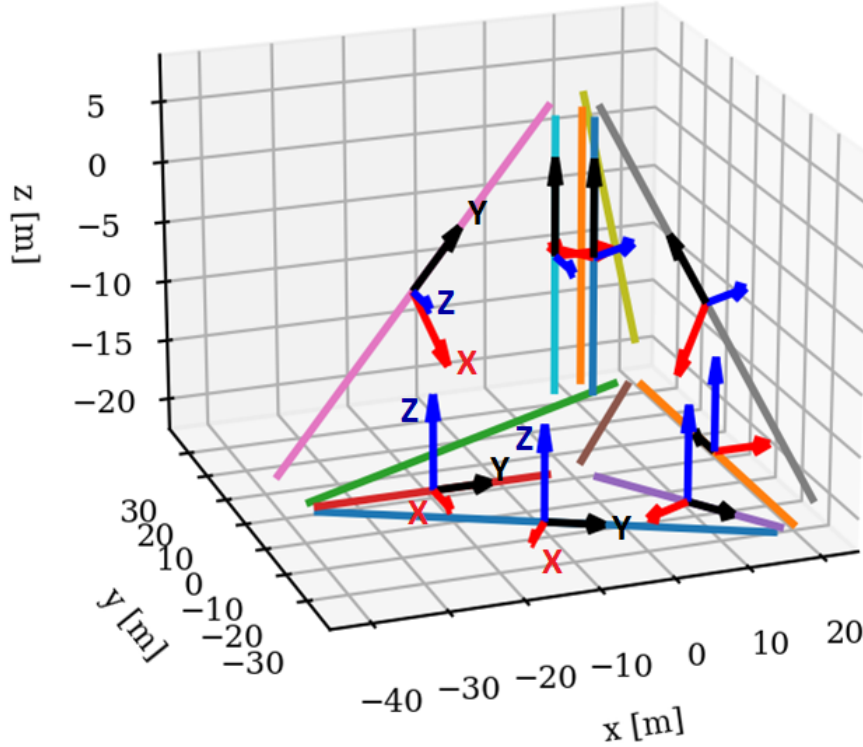


Figure 5.17: Local frames of the braces.

Having presented the definition of the local frames of the braces, the main steps of the numerical slice method are described in the following section.

5.2.3 Main steps of the numerical slice methodology

Here we present our numerical slice methodology to derive Morison coefficients from CFD loads for each brace.

For each slice, we proceed to the following steps:

1. The CFD load time series are calculated over 15-20 periods, referred as time interval T_{int} . The time interval T_{int} is composed of an exact number of periods, N_P (15 to 20). For each period k ($k = [0 : N_P]$), we output I time values of each component of the force in the global frame ($Oxyz$), defined as F_x^i , F_y^i and F_z^i , where i is the time index ($i = [0 : I]$). We eventually have $I \times N_P$ values of each component of the force to post-process for each slice.
2. We project the forces on the local frame: F_X^i , F_Y^i and F_Z^i are obtained thanks to Eq. 5.7.
3. We then calculate the theoretical fluid velocity (considered not disturbed by the structure in Morison approach) $\mathbf{V}_n^i(U, W)$ and acceleration $\mathbf{A}_n^i(\dot{U}, \dot{W})$ components

at the center of the slice in the local frame ($OXYZ$). The appropriate wave theory is used, here equation 6.1.

4. For each period k of T_{int} , we calculate the hydrodynamic coefficients $C_{D_X}^k$, $C_{M_X}^k$, $C_{D_Z}^k$ and $C_{M_Z}^k$ following the steps detailed below:

- (a) We extend the least square method introduced by Sumer et al. [2006] to both components of the force F_X^i and F_Z^i . To our knowledge, such a resolution has never been proposed so far; only the inline force is considered when deriving Morison coefficients. The forces predicted by Morison formulation in the local frame are expressed as:

$$\mathbf{F}_{Mor}^i = F_X^i \mathbf{X} + F_Z^i \mathbf{Z} \quad (5.9)$$

$$F_X^i = \frac{1}{2} \rho C_{D_X} D U^i \|\mathbf{V}_n^i\| + \frac{\rho \pi D^2}{4} C_{M_X} \dot{U}^i \quad (5.10)$$

$$F_Z^i = \frac{1}{2} \rho C_{D_Z} D W^i \|\mathbf{V}_n^i\| + \frac{\rho \pi D^2}{4} C_{M_Z} \dot{W}^i \quad (5.11)$$

$$(5.12)$$

- (b) The error (\mathbf{R}) between the CFD loads (\mathbf{F}_{CFD}^i) and the ones based on Morison theoretical expression (\mathbf{F}_{Mor}^i) in the local frame of the brace is minimized, cancelling its derivative in function of the drag and inertia constant term (\mathbf{f}_D^k and \mathbf{f}_I^k) as detailed below:

$$\mathbf{R}^{k,2} = \sum_{i=1}^I [\mathbf{F}_{Mor}^i - \mathbf{F}_{CFD}^i]^2$$

$$\mathbf{R}^{k,2} = \sum_{i=1}^I \left[\frac{1}{2} \rho D C_D^k U^i \|\mathbf{V}_n^i\| + \frac{\rho \pi D^2}{4} C_M^k \dot{U}^i - \mathbf{F}_{CFD}^i \right]^2$$

where $\mathbf{C}_D^k = C_{D_X}^k \mathbf{X} + C_{D_Z}^k \mathbf{Z}$

$$\mathbf{R}^{k,2} = \sum_{i=1}^I [\mathbf{f}_D^k U^i \|\mathbf{V}_n^i\| + \mathbf{f}_I^k \dot{U}^i - \mathbf{F}_{CFD}^i]^2$$

$$\frac{\partial \mathbf{R}^2}{\partial \mathbf{f}_D^k} = 0 \quad \text{and} \quad \frac{\partial \mathbf{R}^2}{\partial \mathbf{f}_I^k} = 0$$

- (c) For sake of brevity, we only consider F_X for the following equations. Similar equations are derived for F_Z . F_X and F_Z are the CFD force components in the local frame.

$$R^{k,2} = \sum_{i=1}^I \left[\frac{1}{2} \rho D C_{D_X}^k U^i \|\mathbf{V}_n^i\| + \frac{\rho \pi D^2}{4} C_{M_X}^k \dot{U}^i - F_X^i \right]^2$$

$$\frac{\partial R^{k,2}}{\partial f_{D_X}} = 0 \quad \text{and} \quad \frac{\partial R^{k,2}}{\partial f_{I_X}} = 0 \quad (5.13)$$

$$\text{where } f_{D_X} = \frac{1}{2} \rho D C_{D_X}^k \quad \text{and} \quad f_{I_X} = \frac{\rho \pi D^2}{4} C_{M_X}^k$$

- (d) We resolve the system of two equations Eq. 5.13 to obtain the Morison coefficients for a given period k . The sums in the equations are calculated over the I elements of the period k .

$$C_{D_X}^k = \frac{2}{\rho D} \frac{\sum_{i=1}^I F_X U \|\mathbf{U}_n\| \sum_{i=1}^I \dot{U}^2 - \sum_{i=1}^I F_X \dot{U} \sum_{i=1}^I U \|\mathbf{U}_n\| \dot{U}}{\sum_{i=1}^I U^2 \|\mathbf{U}_n\|^2 \sum_{i=1}^I \dot{U}^2 - (\sum_{i=1}^I U \dot{U} \|\mathbf{U}_n\|)^2}, \quad (5.14)$$

$$C_{M_X}^k = \frac{4}{\rho \pi D^2} \frac{\sum_{i=1}^I F_X \dot{U} \sum_{i=1}^I U^2 \|\mathbf{U}_n\| - \sum_{i=1}^I F_X U \|\mathbf{U}_n\| \sum_{i=1}^I U \|\mathbf{U}_n\| \dot{U}}{\sum_{i=1}^I \dot{U}^2 \sum_{i=1}^I U^2 \|\mathbf{U}_n\|^2 - (\sum_{i=1}^I U \dot{U} \|\mathbf{U}_n\|)^2} \quad (5.15)$$

Wolfram and Naghipour [1999] determined the drag and inertia coefficients expressions from experimental data for a vertical cylinder considering only the inline force. Wolfram and Naghipour [1999] formula are consistent with the ones derived in the present numerical slice methodology.

- (e) The same process is applied for F_Z and leads to:

$$C_{D_Z}^k = \frac{2}{\rho D} \frac{\sum_{i=1}^I F_Z W \|\mathbf{U}_n\| \sum_{i=1}^I \dot{W}^2 - \sum_{i=1}^I F_Z \dot{W} \sum_{i=1}^I W \|\mathbf{U}_n\| \dot{W}}{\sum_{i=1}^I W^2 \|\mathbf{U}_n\|^2 \sum_{i=1}^I \dot{W}^2 - (\sum_{i=1}^I W \dot{W} \|\mathbf{U}_n\|)^2}, \quad (5.16)$$

$$C_{M_Z}^k = \frac{4}{\rho \pi D^2} \frac{\sum_{i=1}^I F_Z \dot{W} \sum_{i=1}^I W^2 \|\mathbf{U}_n\| - \sum_{i=1}^I F_Z W \|\mathbf{U}_n\| \sum_{i=1}^I W \|\mathbf{U}_n\| \dot{W}}{\sum_{i=1}^I \dot{W}^2 \sum_{i=1}^I W^2 \|\mathbf{U}_n\|^2 - (\sum_{i=1}^I W \dot{W} \|\mathbf{U}_n\|)^2} \quad (5.17)$$

5. C_{D_X} , C_{M_X} , C_{D_Z} and C_{M_Z} are averaged over the N_P periods in order to eliminate a potential variation of the numerical loads over the time:

$$C_{D_X} = \sum_{k=0}^{N_P} C_{D_X}^k \quad C_{M_X} = \sum_{k=0}^{N_P} C_{M_X}^k$$

$$C_{D_Z} = \sum_{k=0}^{N_P} C_{D_Z}^k \quad C_{M_Z} = \sum_{k=0}^{N_P} C_{M_Z}^k \quad (5.18)$$

Thus we obtain a set of coefficients C_{D_X} , C_{M_X} , C_{D_Z} and C_{M_Z} for each slice of each brace. We can then derive the mean coefficient for each brace.

These Morison coefficients are then imposed in Morison formula to compare the CFD loads to the theoretical ones. Thus the validity of our numerical slice methodology is checked and the application of Morison formula for the prediction of FOWT loads is investigated.

This is a brand new method that still may be improved and optimized. Nevertheless, as it will be detailed in Chapter 7, this numerical slice method has proved, several times during the thesis, its ability to derive consistent values of Morison coefficients.

Having defined the two-step methodology to investigate wave loads on a floater, the CFD model of a vertical surface-piercing cylinder subjected to waves is presented in the following chapter.

Chapter 6

Wave loads on a surface-piercing cylinder subjected to waves

We first investigate the wave loads on a simple structure: the vertical surface-piercing cylinder subjected to regular wave from Stansberg [1997] experiments. This first wave-structure interaction case is implemented in the CFD framework of OpenFOAM and validated against experimental data. Once the accuracy of the CFD model has been verified against experimental data, the wave loads on the cylinder are analysed. The cylinder diameter being negligible compared to the wavelength ($D = 0.2 \text{ m} \ll \lambda = 3.65 \text{ m}$), the Morison formula (section 2.3) is used to analytically predict the wave loads on the cylinder. Our numerical slice methodology to derive the hydrodynamic coefficients from CFD wave loads (section 5.2) is thus tested and validated in a first stage for a vertical cylinder.

This first step will then be used as a basis to perform the analysis of the wave loads on a more complex structure: the FOWT floater built as a set of cylinders of different orientations, positions, diameters and lengths that will be presented in the Chapter 7.

The present chapter is composed of three subsections.

The first one presents the study case and the validation of the CFD simulations against experiments. The second subsection deals with the application of the slice methodology to this vertical cylinder case; we first focus on velocity profiles, then on the hydrodynamic coefficient determination and finally on the analysis of the resulting loads on slices and over the cylinder. The third subsection presents a physical analysis of the influence of the interface on the wave loads.

6.1 Setup and validation of the CFD model

6.1.1 Physical case description

The surface-piercing cylinder CFD model is validated against experiments performed by Stansberg [1997] at the MARINTEK wave tank facility. During this test campaign,

regular and irregular deep-water waves were propagated along a basin (10m x 80m) and interact with cylinders of various diameters. These tests were intensively modelled in OC5 project in the framework of IEA Wind, where different engineering software were benchmarked (Robertson and Jonkman). Only one test of a regular wave interacting with a fixed vertical cylinder is selected for the present study. The reported wave characteristics are the following: a height H of 0.33 m, a period T of 1.53 s. Accordingly the wave can be classified as a Stokes 3^{rd} order deep water wave (cf. Fig. 5.1). The cylinder diameter is $D = 0.2$ m and located 38.6 m away from the wave paddles. Accordingly, the corresponding location in Chakrabarti classification (Fig. 5.4) shows that the wave loads should be correctly predicted by Morison formulation, with a small drag contribution and a large inertia term.

In experiments, the measured data are the free surface elevation at the centre of the cylinder when the latter is not present, as well as forces and moments applied to the cylinder. The test configuration is detailed in Fig. 6.1. The Reynolds number (Eq. 2.45) is equal to 1.4×10^5 , the flow is thus considered as turbulent.

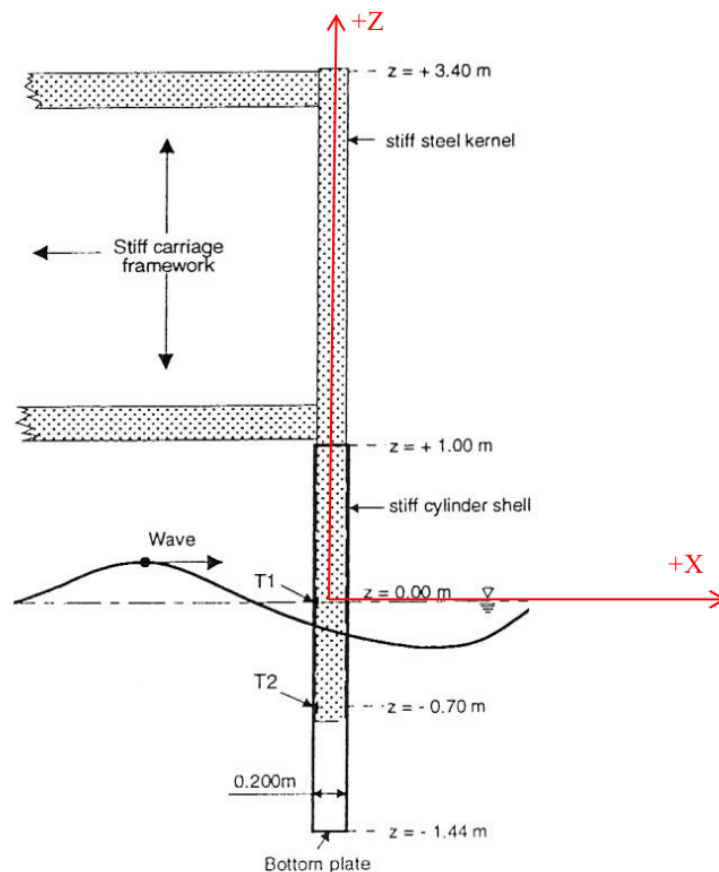


Figure 6.1: Cylinder test configuration from Stansberg [1997].

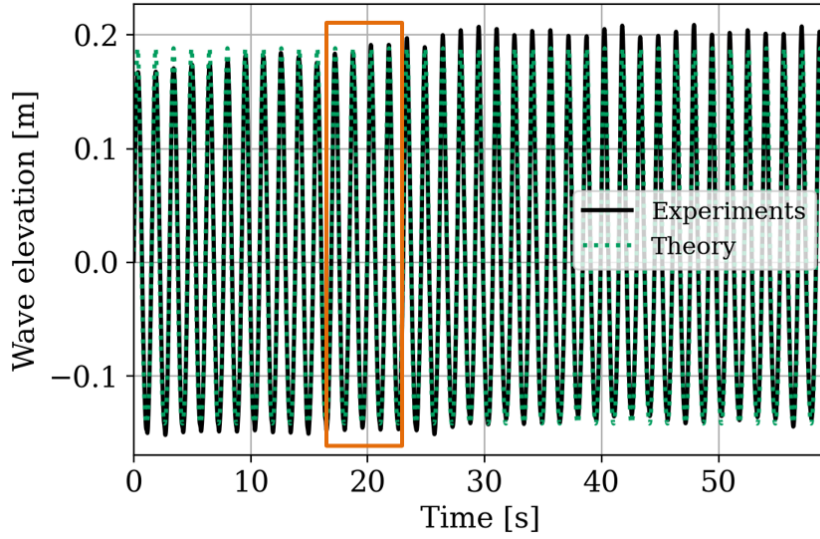


Figure 6.2: Wave elevation time series from Stansberg experiments.

Analysis method

Only the stable part of the experimental signal is kept for the analysis and to derive the statistics such as the wave height and the wave loads. Still, the wave elevation and load signals are rather dispersed (5%) as visible for the wave elevation in Fig. 6.2.

To compare plot shapes (amplitude, phase, crest and trough shape), the visualisation is restricted to four periods. To get a fair comparison, the starting time of this four-period zoom is chosen when experiments and theoretical elevation (based on 2nd order wave theory cf. section 5.1.1) match well enough, as represented in the rectangular zone of Fig. 6.2.

6.1.2 CFD Numerical model

The validation of the NWT without the cylinder is presented in Chapter 5.1. This is also precisely detailed in a paper submitted at the ASME 2020 39th International Conference on Ocean, Offshore and Arctic (Clément et al. [2020]).

The cylinder is then included into the mesh. An extra refinement level is imposed around the cylinder in order to get cells of $D/15$ size close to the structure. Though not presented in this study, we checked that the mesh was fine enough to well predict the wave forces.

We did not find in the literature a clear consensus on the boundary conditions for the velocity/pressure fields that should be applied on the cylinder wall for a wave/structure CFD case (section 4.3.1.1). For that reason three tests are performed and their impact on forces are analysed. A slip boundary condition (B.C.) on the cylinder (null velocity gradient) is compared to a no-slip B.C. (null velocity), both tests are performed without turbulence model. The third CFD simulation is run activating k-omegaSST stabRAS

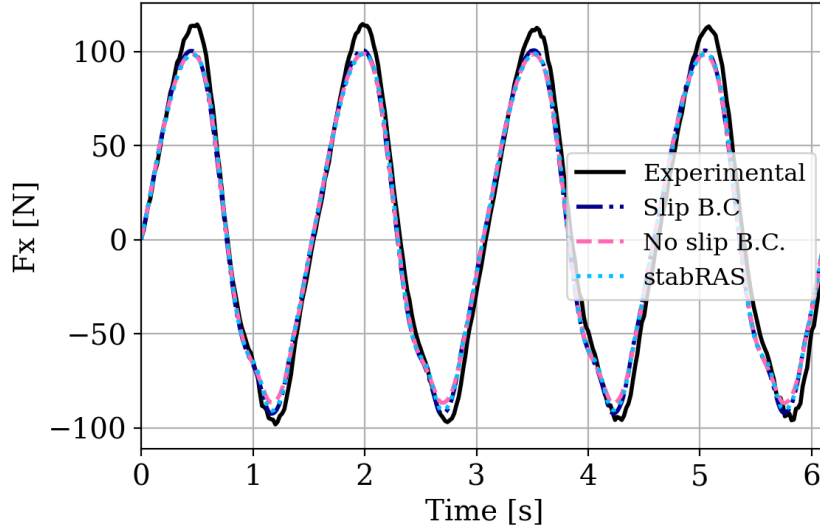


Figure 6.3: Horizontal wave loads (F_x) on the fixed cylinder.

turbulence model with no-slip B.C. For this case, the mesh refinement close to the cylinder satisfies wall functions requirements ($30 < y^+ < 300$).

With a configuration of a vertical cylinder, F_y and F_z are negligible, leading to only focus on the inline force F_x .

The CFD simulation duration is set to 120s, which corresponds to the time required to get a stabilized wave elevation time series with a dispersion of the maxima lower than 2.5%. Statistics and plots are computed from 80s to 120s.

Figure 6.3 represents horizontal forces (i.e. inline force F_x) over four periods. CFD loads are slightly underestimated compared to experiments. From Fig. 6.3, the difference with experiments has been found below 5% for each CFD case. Furthermore, force average value (shown in Tab. 6.1) and the small bump before the minimum are well predicted by each CFD simulation.

Viscous forces are negligible compared to pressure forces for the horizontal load. That explains why the three CFD results are very similar and implies that the turbulence model may not be necessary. In the end, we choose to impose a no-slip BC on the cylinder. The statistics obtained with this CFD model are shown in Tab. 6.1, F_x is the determined by Eq. 5.1. These observations assess the validity of the CFD model against the experimental data.

Case	F_x [N]	Error(CFD, Expe) [%]	NRMSE(CFD, Expe) [%]
Experiments	196.6	/	/
CFD	190.7	3%	5.62%

Table 6.1: CFD error relative to experimental results.

The CFD model of the cylinder in waves being validated against experimental data, the CFD wave loads are analyzed and the applicability of Morison approach for load prediction is investigated in the following section.

6.2 Application of the slice methodology

With this first wave/structure interaction CFD case, our numerical slice methodology is tested to derive Morison coefficients from CFD loads. Then, the variation of the wave loads along the cylinder axis is investigated. Finally, the influence of the interface on the wave loads and on the predicted Morison coefficient values is discussed.

6.2.1 Calculation of the wave velocity at the center of each slice

To derive Morison coefficients for each slice applying the numerical slice methodology, we need the undisturbed velocity time series at the center of each slice.

The velocity/acceleration time series at the center of each slice can be derived from CFD results but it implies complex post-processing. In CFD, the velocity time series are determined at the center of each mesh cell that makes the interpolation at the slice center difficult. Alternatively, we evaluate the wave velocity time series at the center of the slice using a Stokes 2^{nd} order wave model. However the theoretical model is only defined for $z < MSL$ (MSL standing for the Mean Sea water Level) as follows:

$$\begin{aligned} u(z, \theta) &= A\omega \frac{\cosh k(z+h)}{\sinh kh} \cos(\theta) + 3 \frac{A^2\omega k \cosh(2kz)}{4 \sinh^4(kh)} \cos(2\theta), \\ w(z, \theta) &= A\omega \frac{\sinh k(z+h)}{\sinh kh} \sin(k\theta) + 3 \frac{A^2\omega k \sinh(2kz)}{4 \sinh^4(kh)} \sin(2\theta), \end{aligned} \tag{6.1}$$

where $\theta = kx - \omega t + \Phi$ with Φ the wave phase.

In order to take into account the variation of the sea level with time, we need to evaluate the theoretical velocity for $z > MSL$. With that goal, we use a so-called stretching model to extrapolate the velocity profile between the MSL and the maximum wave elevation A_{max} .

Different stretching methods are tested as shown in Fig. 6.4:

- The vertical stretching model is based on Stokes 2^{nd} order wave theory for $z < MSL$. Between the MSL and A_{max} , the velocity is kept constant and equal to the velocity at the MSL (light blue dotted curve).
- The most commonly used model is the Wheeler stretching model (Wheeler et al. [1970]) and consists in stretching the vertical scale (dark blue dotted curve). Wheeler proposes to take the wave velocity/acceleration at $z = \eta$ (η the wave elevation) equal

to the velocity given by the linear theory at $z = MSL$. z is then changed in z' as in Eq. 6.2 (h the water depth):

$$z' + h = h\left(\frac{z + h}{h + \eta}\right). \quad (6.2)$$

- The extrapolated stretching model consists in extrapolating the Stokes 2nd order formula (Eq. 6.1) for $z > MSL$. The velocity is imposed null when the wave elevation is lower than z (green curve).

For comparison purposes, we extract the CFD wave velocity time series at the cell centres on a vertical line corresponding to the cylinder axis. This is done for the simulation without the cylinder. Based on these times series, we can determine the time averaged vertical profile for the CFD velocity field. In Fig. 6.4, the profiles obtained with the CFD model and with the different velocity theories are compared.

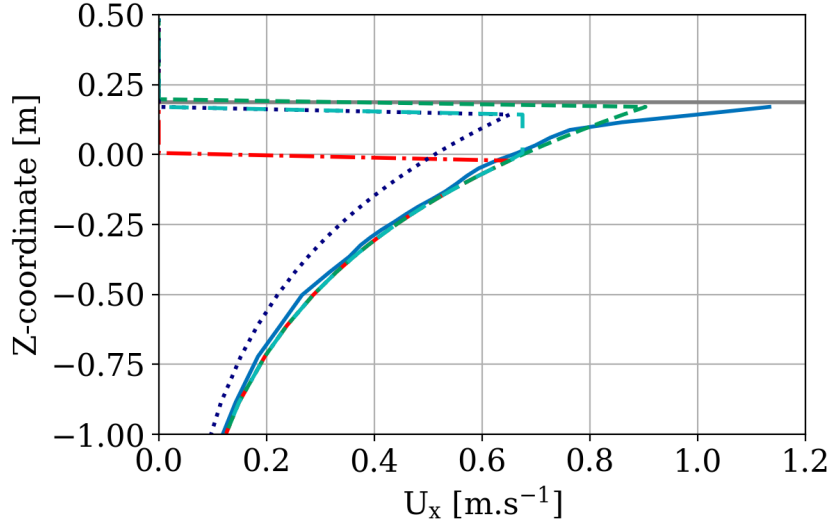


Figure 6.4: Velocity profile along water depth. CFD (—), Stokes 2nd order (—), Vertical stretching (—), Wheeler stretching (...), Stokes 2nd order extrapolated (—), A_{max} (—).

For water depth below the MSL, Stokes 2nd order wave theory (red curve) and CFD (blue curve) are in good agreement whereas Wheeler stretching model leads to lower velocities. Another major difference lies on the prediction of the velocity very close to the crest (A_{max}). CFD seems to overestimate the maximum velocity compared to Stokes 2nd order wave theory combined with extrapolated stretching model. This is also highlighted by Larsen et al. [2019] that demonstrate that crest velocities are very often overestimated with VOF methods.

To complete this comparison, the dispersion of the CFD velocity profile defined as the standard deviation (σ) of the maximum velocity (with a 95% range chosen i.e. $\pm 1.96\sigma$ on both sides of the maximum velocity) is plotted in Fig. 6.5.

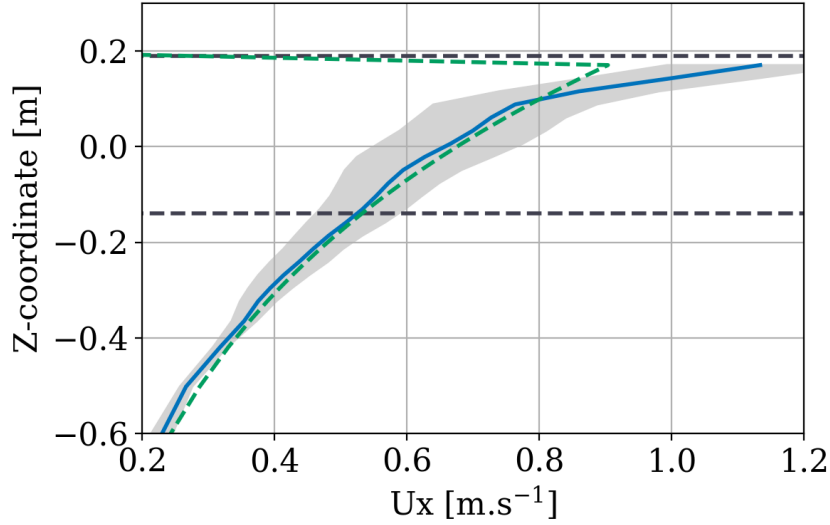


Figure 6.5: Velocity profile along water depth. CFD (—), Stokes 2nd order wave theory extrapolated (---), Standard deviation of CFD velocity (■), $A_{min}:A_{max}$ (---).

The dispersion of the CFD velocity is larger in the area between A_{max} and A_{min} (8.3% of the velocity at $z = 0.006$), than below the MSL (1.8% of the velocity at $z = -0.5$). This may be explained by the limits of the VOF MULES solver to reconstruct the interface or the existence of high air velocities on wave crests as detailed in the section 4.2.3.

Nevertheless, the agreement on the velocity profiles between the CFD and the wave theory with extrapolated stretching method is excellent. It is concluded that the theoretical formulation can be used in the Morison formulation to estimate the hydrodynamic coefficients for this cylinder case and the FOWT floater in Chapter 7. This is quite a valuable result since it avoids to run an additional simulation without the structure to extract the undisturbed velocity field.

6.2.2 Determination of Morison coefficients

For each slice, a set of Morison coefficients is derived from the inline CFD wave loads (F_x) applying the slice methodology detailed in the section 5.2. The coefficient formula to obtain C_D and C_M at the center of each slice are given by Eq. 5.14 and Eq. 5.15 replacing X by x , U and U_n by u . The undisturbed velocity/acceleration time series required in the equation at the center of each slice are determined applying the Stokes 2nd order wave theory and extrapolated stretching model as discussed previously. The last 26 periods of the CFD signal are used to carry out the slice methodology and so the coefficients are time-averaged over this duration (Eq. 5.18).

The resulting C_M and C_D values are plotted in Fig. 6.6 for each slice of the cylinder. The theoretical interface area, z between A_{max} and A_{min} , is also displayed on the graph.

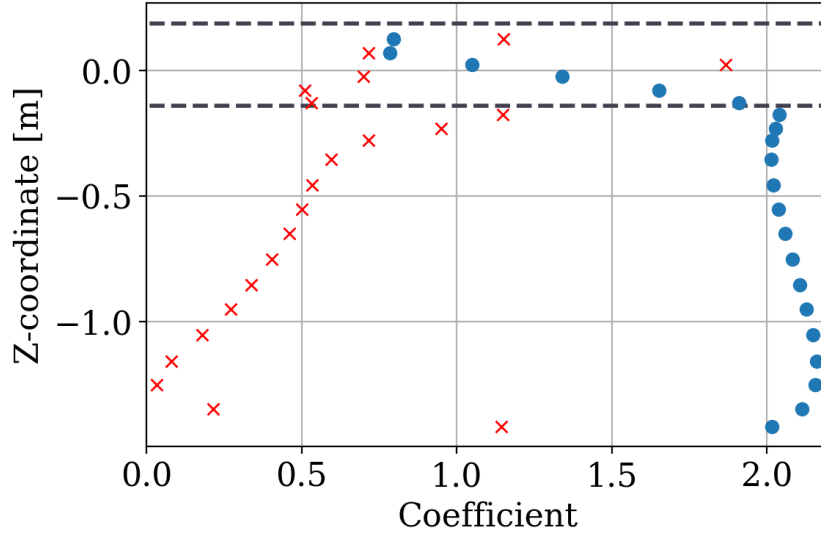


Figure 6.6: Morison drag and inertia coefficients for each slice along the cylinder. C_M (\bullet), C_D (\times), $A_{min}:A_{max}$ (—).

The inertia coefficient C_M varies slightly for submerged slices; a mean value of 2.08 with a standard deviation of 0.05 is obtained. The results are consistent with the values commonly defined in standards, such as the DNV-RP-C205 Veritas [2010]. In OC5 project, modelling this same cylinder with various design tools, participants came out with a value of 2 (Robertson and Jonkman).

The drag coefficient C_D varies a lot along the water depth, ranging from 0.03 to 1.87. As it will be explained in the section 6.2.4, the drag force being negligible compared to the inertia force, the determination of the drag coefficient is thus subject to high uncertainties, but anyway it does not modify the total force. In OC5 project, the drag coefficient value is between 1 and 1.2.

Regarding the zone located between A_{min} and A_{max} , the inertia coefficient strongly decreases. This is explained by the fact that this zone is outside the applicability range of Morison equation and the force cannot be predicted properly as discussed thereafter.

6.2.3 Analysis of CFD and Morison loads along the cylinder

The influence of the air/water interface on loads and the limitation of Morison theory to predict loads for slices located in the interface area is discussed below. We compare the loads computed from CFD pressure field and loads derived from Morison formulation. Four slices centred at different water depths, $z = -0.95$ m, $z = -0.35$ m, $z = -0.025$ m and $z = 0.025$ m, are considered for the analysis, as depicted in Fig. 6.7. The Morison load for a given slice can be obtained following two ways:

- Using the coefficient of the slice derived from CFD (C_D (slice) and C_M (slice))
- Using the mean value of the coefficient averaged on all the submerged slices, for $z < A_{min}$ (C_M (mean) and C_M (mean)).

The coefficients determined are indicated in Tab. 6.2.

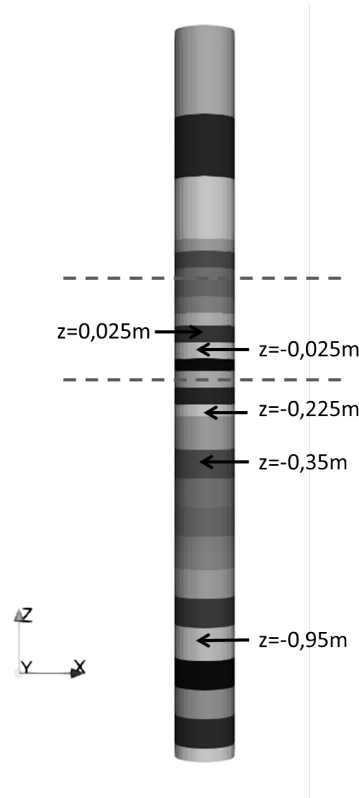


Figure 6.7: Location of the four cylinder slices. $A_{min}:A_{max}$ (---).

Coefficient	$z = -0.95$ m	$z = -0.35$ m	$z = -0.025$ m	$z = 0.025$ m
C_D (slice)	0.27	0.55	0.70	1.89
C_D (mean)	0.50	0.50	0.50	0.50
C_M (slice)	2.13	2.02	1.34	1.05
C_M (mean)	2.08	2.08	2.08	2.08

Table 6.2: Morison coefficients for the four slices from CFD.

For a slice deeply submerged, at $z = -0.95$ m

In Fig. 6.8, the CFD and Morison loads are plotted for the slice centred at $z = -0.95$ m, which is always submerged. Morison formulation, no matter which coefficient is used, leads to a prediction in excellent agreement with the reference loads provided by CFD.

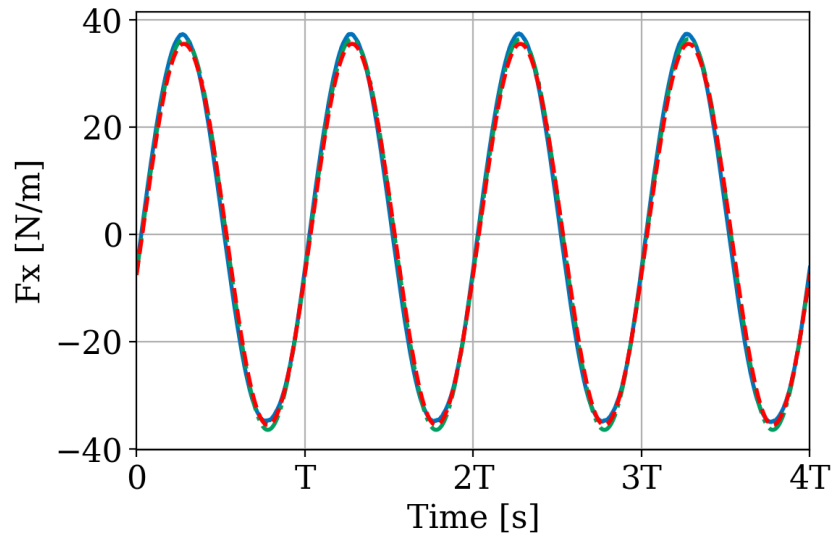


Figure 6.8: Loads on the slice centred at $z = -0.95$ m. CFD loads (—), Morison loads determined with the specific slice coefficient (---), Morison loads determined with the coefficients averaged over the water depth (-.-).

For a slice below the interface zone, at $z = -0.35$ m

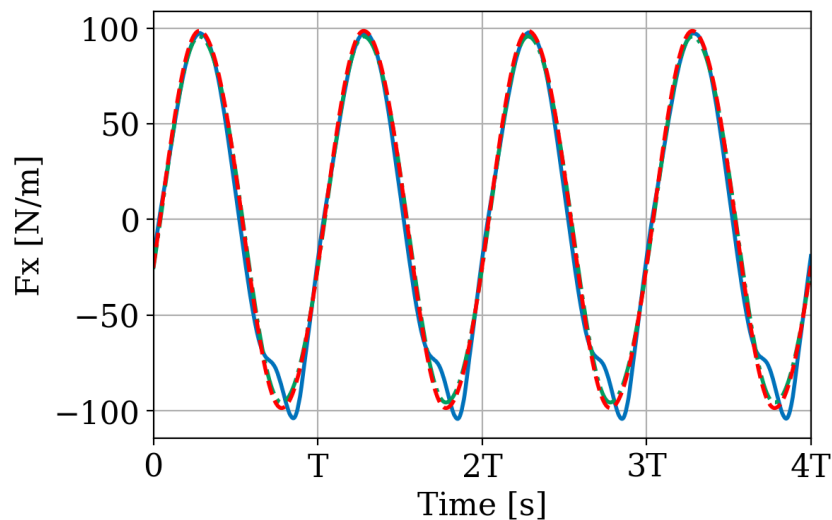


Figure 6.9: Loads on the slice centred at $z = -0.35$ m. CFD loads (—), Morison loads determined with the specific slice coefficient (---), Morison loads determined with the coefficients averaged over the water depth (-.-).

For a slice closer to the interface but below $z = A_{min}$, centred at $z = -0.95$ m, a bump occurs on the CFD force close to the trough. This phenomenon cannot be reproduced with Morison formulation as depicted in Fig. 6.9. This shape appears to be related to the interface influence on loads, which will be further investigated in the section 6.3. Despite this slight difference, the load variation and amplitude are quite well predicted by Morison formula and this whatever the coefficients.

For a slice within the interface zone, below the MSL, $z = -0.025$ m

CFD and the two Morison load predictions are plotted in Fig. 6.10 for a slice centred at $z = -0.025$ m.

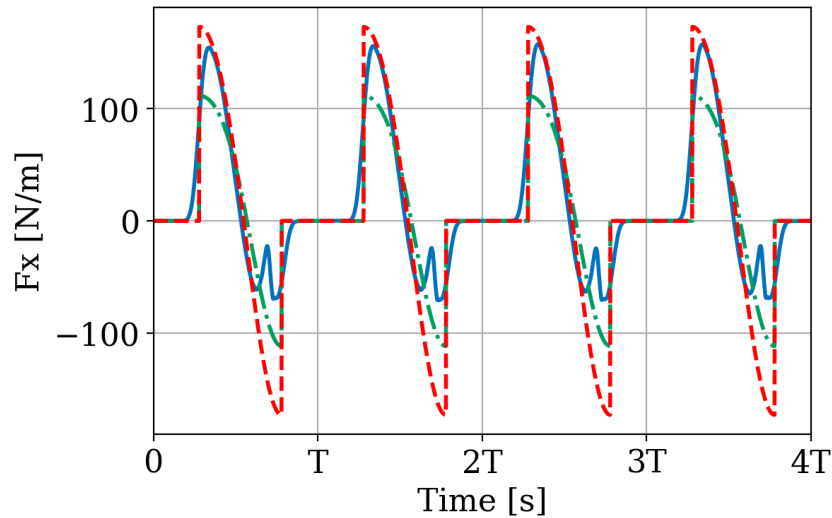


Figure 6.10: Loads on the slice centred at $z = -0.025$ m. CFD loads (—), Morison loads determined with the specific slice coefficient (-.-), Morison loads determined with the coefficients averaged over the water depth (- -).

The loads are null as long as the slice is in the air. When the slice is submerged by water, the loads are not well predicted by the Morison formulation; the Morison formulation was indeed developed for a completely submerged cylinder and is thus not suited for a surface-piercing cylinder. Regardless of the hydrodynamic coefficient chosen, the sinusoidal shape of Morison signal does not reproduce correctly the complex shape of the load on the slice.

Same conclusions are drawn for a slice above the MSL; see for example the results for the slice centred at $z = 0.025$ m in Fig. 6.11.

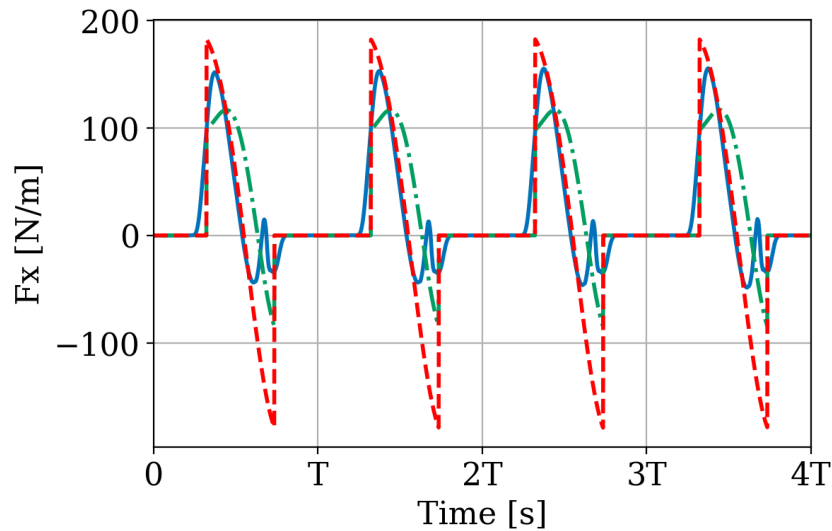


Figure 6.11: Loads on the slice centred at $z = 0.025$ m. CFD loads (—), Morison loads determined with the specific slice coefficient (-.-), Morison loads determined with the coefficients averaged over the water depth (- -).

Maximum load profile over the cylinder length

In Fig. 6.12 are plotted the maximum force profiles along the cylinder, obtained both from CFD and Morison theory (averaged hydrodynamic coefficients are used for Morison theory). The Morison theory correctly predicts maximum loads in the submerged part and over-predicts loads in the interface region, in agreement with observations from Fig. 6.10 and Fig. 6.11. The importance of this load prediction deviation or gap on the total load prediction is investigated in the following sub-section.

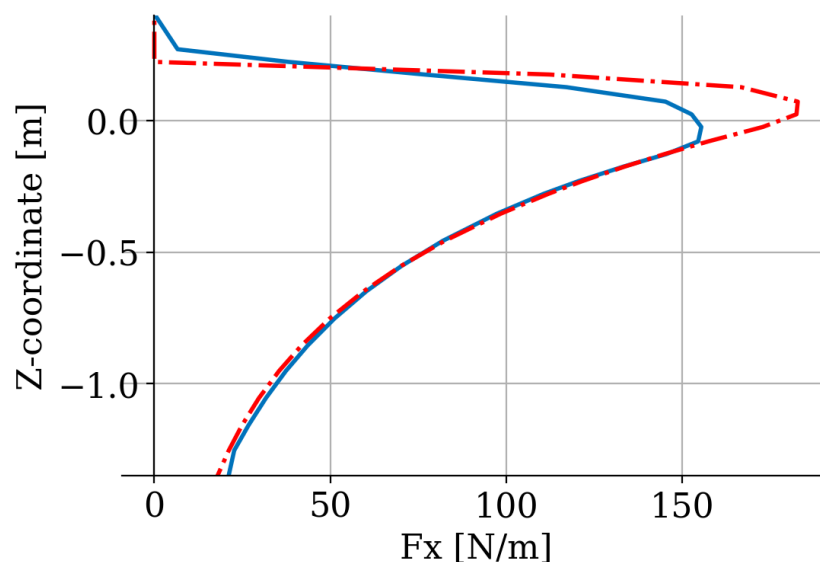


Figure 6.12: Maximum force profile along the cylinder length. CFD (—), Morison force with average coefficients determined in CFD (-.-).

6.2.4 Analysis of CFD and Morison loads for the entire cylinder

This sub-section deals with the total load prediction on the cylinder. Morison loads are derived by summing the loads on each slice. The Morison load on each slice is determined using the mean value for hydrodynamic coefficients, as detailed in the section 6.2.3. Thus, the total load, plotted in Fig. 6.13, is composed of an inertia term and a drag term depicted on the figure. We clearly evidence that the inertia term in Morison formula is preponderant compared to the drag term for this case as it was expected in the section 6.1.3; the value of C_D has a very weak impact on the total load.

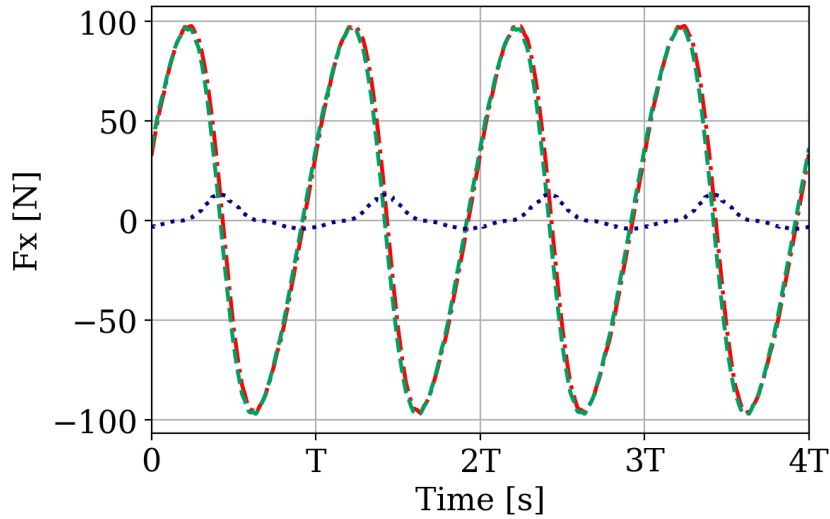


Figure 6.13: Total loads on the cylinder. Morison load (—), Inertia term (---), Drag term (...).

In Fig. 6.14, the time series of loads obtained from CFD simulation, Morison formula and experiments are compared. We first observe that the three signals have the same periods. The small bump just before the trough, related to the air/water interface behaviour as explained in the section 6.2.3, is visible on experiments and well predicted by CFD. However, the Morison empirical formula is not able to predict this bump as the interface influence is not taken into account in the Morison theory. The NRMSE between the CFD loads and Morison loads is 7.89%, that is small enough to ensure the accuracy of both models.

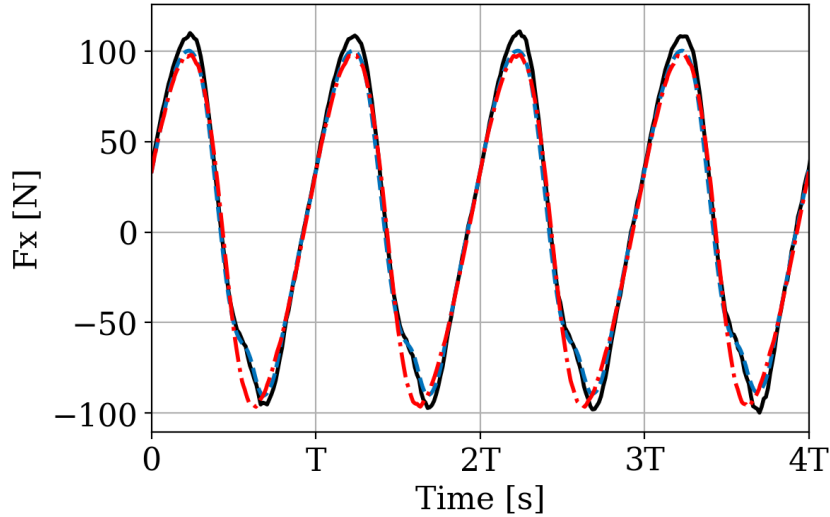


Figure 6.14: Total load on the cylinder. CFD (—), Morison formula with averaged coefficients (---), Experiments (· · ·).

It can be concluded that the interface does not impact significantly the total load in terms of amplitude and period, though it slightly modifies the signal shape and can be very important locally, as highlighted in the section 6.2.3.

The small bump noticed before the minimum in the load signal is investigated more precisely in the following subsection, confronting our results to past studies. Thanks to CFD, the direct impact of the interface on wave loads can be investigated by correlating wave load time series to the visualisation of the run-up around the cylinder.

6.3 Physical analysis of the influence of the interface on the wave loads

To analyse the influence of the interface on the wave loads for the surface-piercing cylinder, this section is composed of two parts. First we investigate the non-linear behaviour of the total inline force (cf. bump visible before the minimum on the wave load plot), by comparing the CFD loads with the ones obtained in past experimental and numerical studies. Then, we study the correlation between the wave loads and the interface behaviour using our CFD simulation.

6.3.1 Nonlinear diffraction load on the surface-piercing cylinder

The nonlinear effect visible in Fig. 6.14 has already been studied numerically and experimentally.

Indeed, Paulsen et al. [2012] studied, thanks to CFD, the wave forcing of a bottom mounted circular cylinder by steep regular waves at finite water depth, as presented in the section 4.3.1.3. The authors detail the appearance of an additional local peak during the time frame of minimum loading (T_2). This phenomenon known as secondary load

cycle is visible in Fig. 6.15.

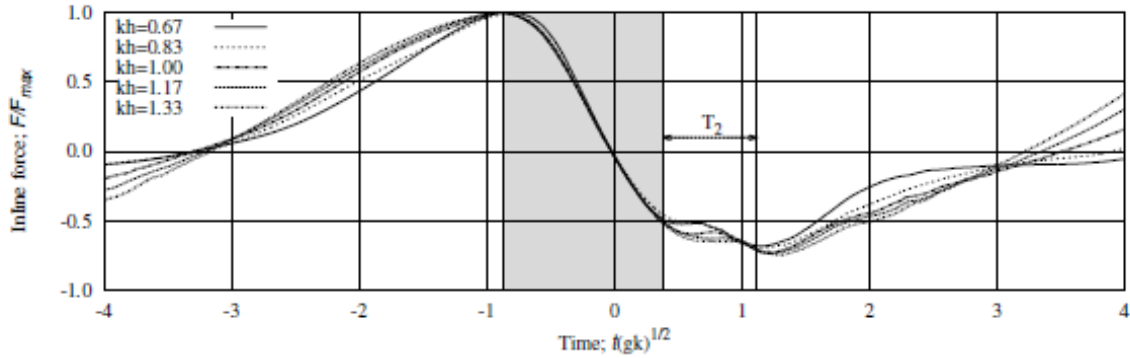


Figure 6.15: Time histories of the inline force on a vertical cylinder (Paulsen et al. [2012]).

Ferrant [1998] describes the nonlinear interaction between a regular wave and a surface-piercing-cylinder running simulations with ANSWAVE, a fully non linear Boundary Element Model. He reveals the existence of short diffraction waves around the cylinder (of second and third order) compared to the incident wave for the following simulation characteristics: $kR = 0.2$, $kA = 0.12$ and $kh = 8$ ($k = 2\pi/\lambda$ with λ the wavelength, R is the cylinder radius). These non linear diffraction forces may trigger ringing, a potentially dangerous nonlinear excitation of an elastic structure, with burst-like characteristics precisely described by Chaplin et al. [1997].

Huseby and Grue [2000] investigated experimentally first- and higher-harmonic wave loads on a vertical cylinder. A large set of waves with wave slope (kA) up to 0.24 was performed. Ferrant [1998] modelled numerically Huseby and Grue [2000] experiments for slope up to 0.145 ($kR = 0.245$). The harmonics derived numerically and experimentally are compared in Fig. 6.16. A good agreement between both models is obtained for the 3 – 5th harmonics but significant differences are visible for the 2nd harmonic. Globally, the force decreases as the wave slope kA becomes greater.

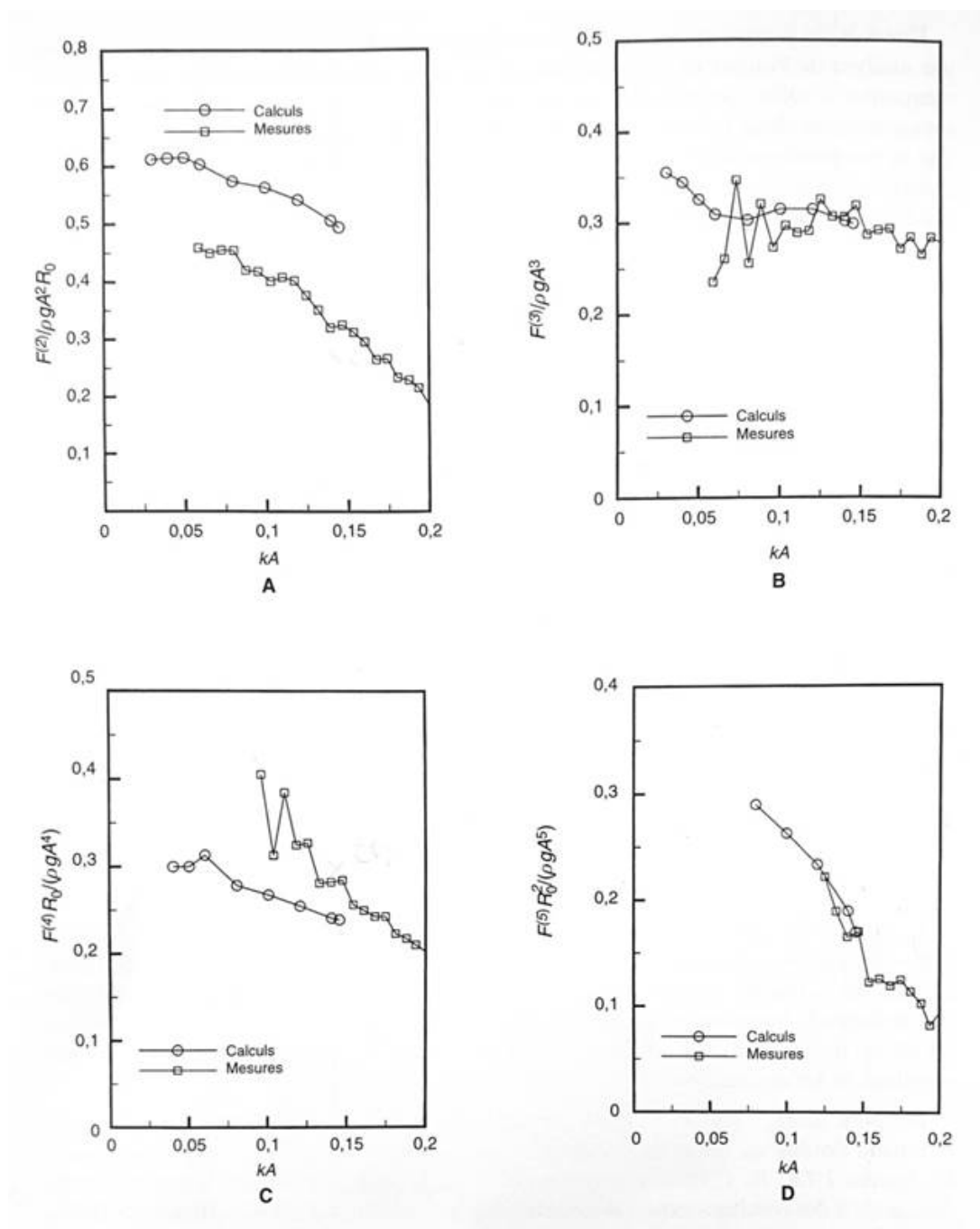


Figure 6.16: Inline force on a vertical cylinder. 2nd harmonic (Top left), 3rd harmonic (Top right), 4th harmonic (Bottom left) and 5th harmonic (Bottom right). Comparison between the values obtained experimentally by Huseby and Grue [2000] and numerically by Ferrant [1998].

The characteristics of Stansberg wave/cylinder case are $kR = 0.17$, $kh = 17$, $kA = 0.28$ and so the wave slope kA is larger than the maximum wave slope performed by Huseby and Grue [2000]. We compare in Tab. 6.3 the amplitudes of the first five harmonics derived by Huseby and Grue [2000] with the ones determined from Stansberg experiments and from the CFD model. The amplitude is made non-dimensional dividing the n th harmonic by $\rho g A^n R^{3-n}$.

Case	F_1 [-]	F_2/F_1	F_3/F_1	F_4/F_1	F_5/F_1
Huseby experiments ($kA=0.24$)	6.25	3.20%	3.52%	2.08%	0.80%
Stansberg experiments ($kA=0.28$)	6.01	6.35%	2.54%	1.16%	0.25%
CFD model of Stansberg experiments ($kA=0.28$)	5.57	4.66%	1.71%	0.53%	0.09%

Table 6.3: First normalised harmonic and ratio of second-and higher- harmonics relative to the first-harmonic from the inline load on a vertical cylinder from Huseby and Grue [2000] experiments, Stansberg [1997] experiments and the CFD model of Stansberg experiments.

Tab. 6.3 indicates that the harmonics derived from Stansberg experiments and the CFD model are in good agreement with slightly larger harmonics for the experiments. The harmonics derived from Huseby experiments are of the same order than the ones derived from Stansberg cases. From the 3rd order, Stansberg harmonics (CFD and experiments) are lower than Huseby ones. This is consistent with the decreasing trend in the 2nd – 5th forces as the wave slope becomes greater (cf. Fig.6.16), the 1st harmonic varying little with the wave slope.

The non-linearities visible on the experimental and numerical load signals (especially the slope break before the minimum) may thus be related to the diffraction loads associated with the harmonics of order greater than 2. Molin [2002] details that for $kR < 0.5$, the diffraction loads are well predicted by the inertia term in Morison formula. Indeed, this assertion is confirmed for Stansberg cylinder ($kR = 0.17$) as visible in Fig. 6.14.

All the studies mentioned previously deal with the total load on the cylinder. Thanks to CFD, we can precisely analyse the load evolution with water depth as detailed in the following section, an information difficult to obtain experimentally.

6.3.2 Physical analysis of the influence of the interface on two slices

In the section 6.2.3, we showed that the closer to the interface the slice is, the more important the bump before the wave load trough is. We focus this study on two slices: the submerged slice centred at $z = -0.225m$ and the slice in the interface region centred at $z = -0.025m$ (Fig. 6.7) for trying to explain the physical origin of the bump.

We divide each slice into two parts to evaluate the distribution of the loads on it: an upstream one and a downstream one as presented in Fig. 6.17.

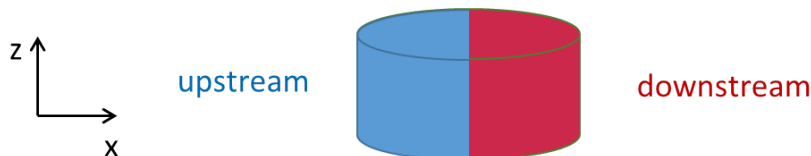


Figure 6.17: Slice split into an upstream and a downstream part.

The inline force F_x along (Ox) direction is reported on each part, as well as the total

inline force (F_x) on the entire slice. Also, the transverse force along (Oy) is plotted. These forces are plotted over one wave period. During this same period, the wave run-up around the cylinder is visualized using the 0.5 iso-surface of the VOF volume fraction. For the sake of clearness, only half of the NWT is displayed, being cut at its center by the plane (xOz). Key moments over one period (between $0s$ and T_p) are described in the two following subsections.

6.3.2.1 Slice fully submerged in water ($z = -0.225m$)

First, we investigate the impact of the wave run-up for the load on the submerged slice located at $z = -0.225m$. Four remarkable moments (t_1 , t_2 , t_3 and t_4) are described below and reported in Fig. 6.18 and Fig. 6.19.

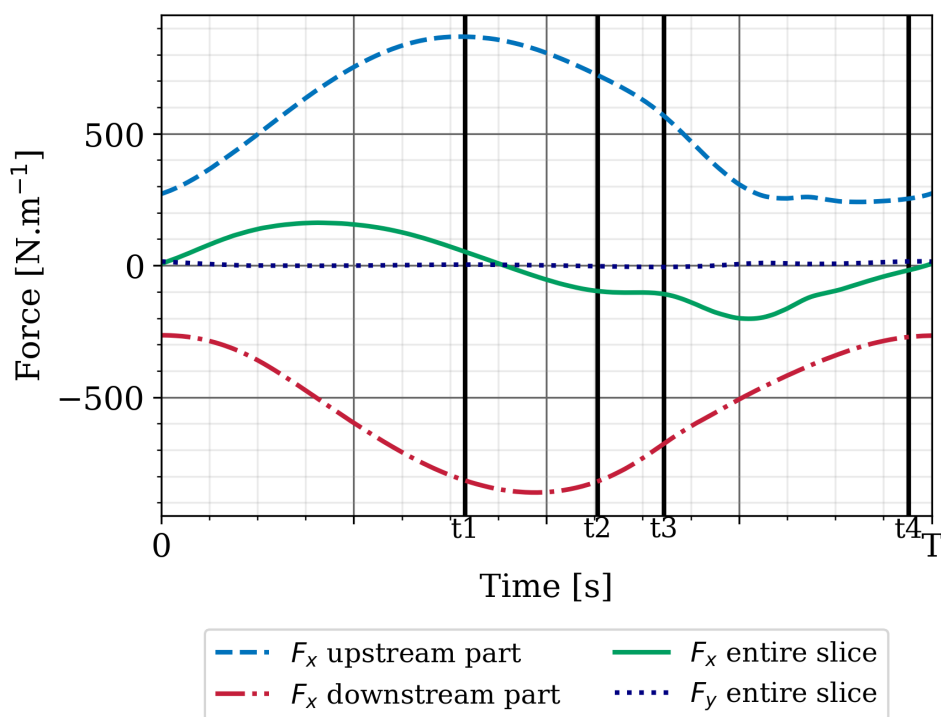


Figure 6.18: Wave loads on the slice centred at $z=-0.225$ m.

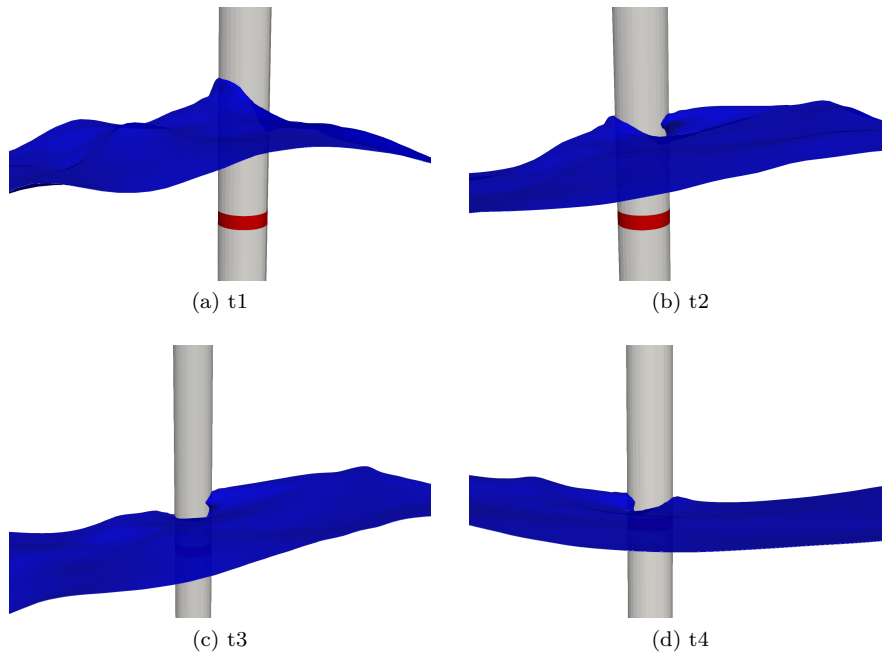


Figure 6.19: Visualisation of the air/water interface at four key moments for slice $z = -0.225m$.

- **t1**: Maximum of the upstream inline force. The maximum inline load on the upstream side of the cylinder is reached exactly at the time when the wave run-up on the upstream part is maximum. We observe a roll shape of the upstream wave run-up. For Paulsen et al. [2012], it is due to the stagnation pressure that accelerates a sheet of water upwards.
- **t2**: First slope change of the total inline force. At this moment, the wave goes back from the downstream to the upstream side of the cylinder. According to Paulsen et al. [2012], this corresponds to the beginning of the secondary load cycle. Like Paulsen et al. [2012], we note that the maximum wave run-up at the downstream side occurs prior (t1) to the secondary load cycle (t2).
- **t3**: Second slope change of the total inline force. It corresponds to a slope change of the upstream force and to the transition between a small roll to a linear shape of the wave run-up on the upstream side. From this moment, on the upstream part, the wave runs down faster corresponding to a faster decrease of the upstream force (higher slope). This is the end of the secondary load cycle.
- **t4**: At the end of the period, the absolute value of the upstream and downstream forces are equal, resulting in a null total force on the cylinder. The free-surface is almost flat and barely disturbed by the cylinder.

From these observations, a clear relation exists between the wave run-up and the slope change of the inline load signals: the wave return from the downstream part to the upstream part seems to be responsible for the slope break on the total load.

In the following subsection, the physical analysis of loads on a slice located in the interface area will be performed to check if similar conclusions can be drawn.

6.3.2.2 Slice close to the interface ($z = -0.025m$)

Over one wave period, height remarkable key moments are described for analysing wave loads on a slice located close to the interface region. Loads are plotted in Fig. 6.20 and the air/water interface visible in Fig. 6.21.

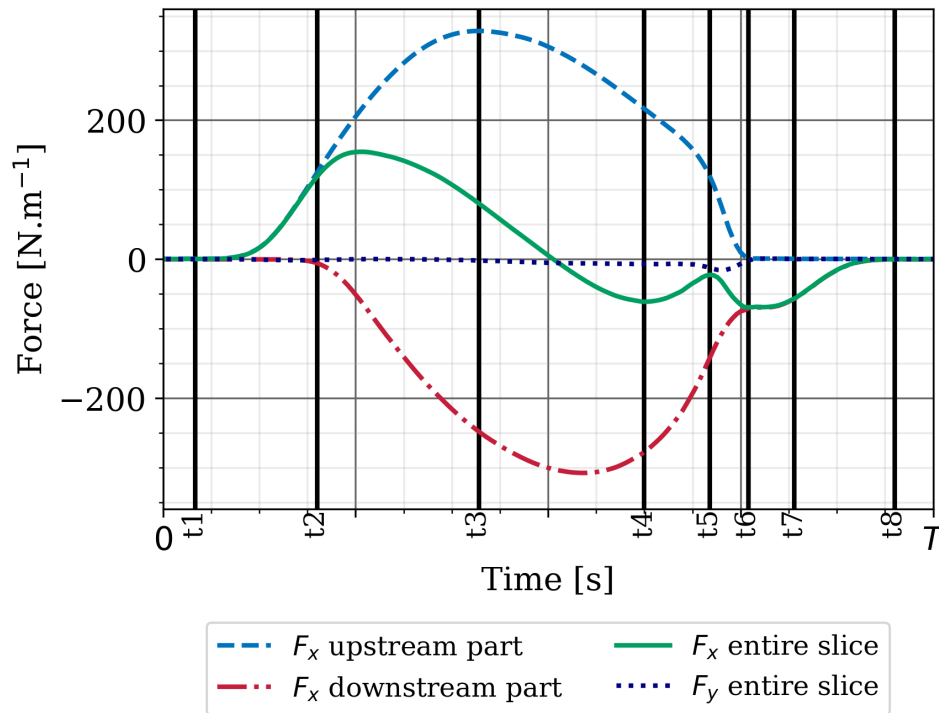


Figure 6.20: Wave loads on the slice centred at $z=-0.025$ m.

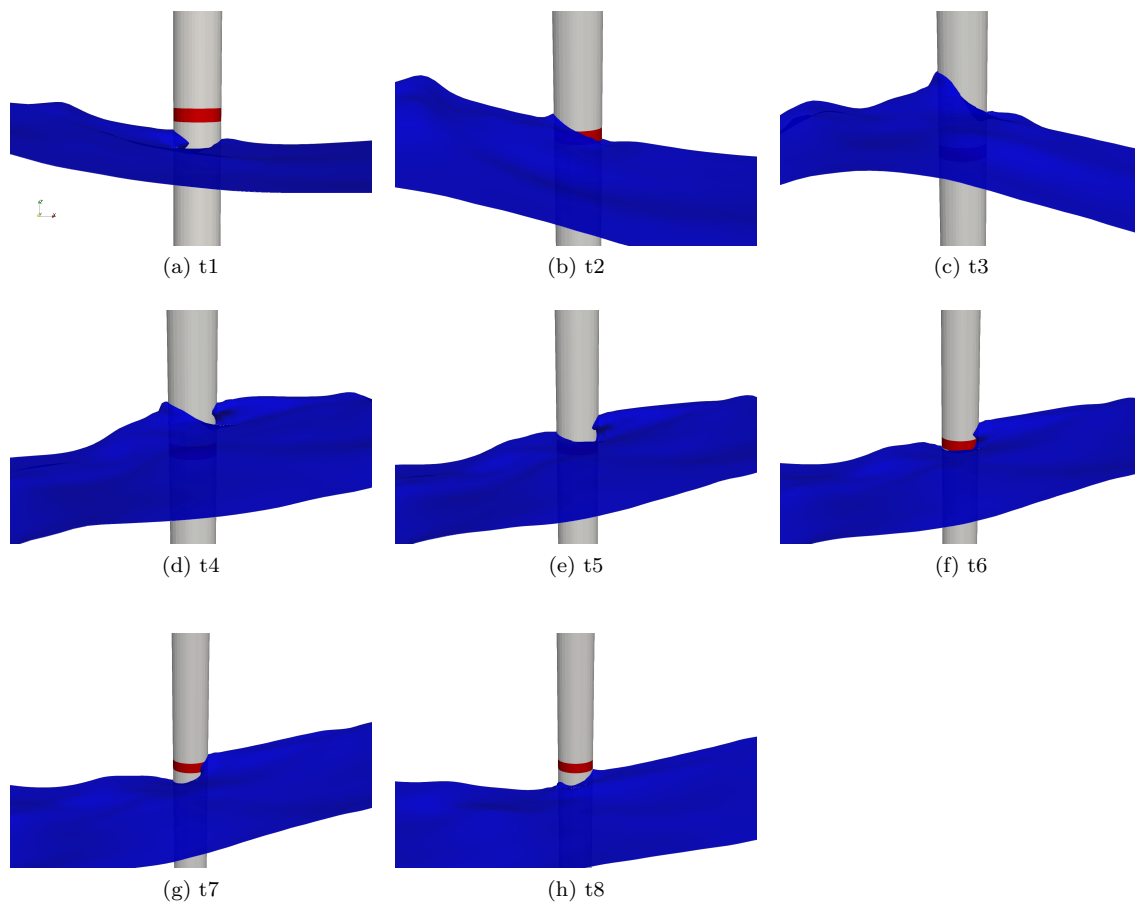


Figure 6.21: Visualisation of the air/water interface at height key moments for slice $z = -0.025m$.

- **t1**: At the beginning of the period, all forces are null because the slice is not immersed in water yet.
- **t2**: The wave reaches the upstream part of the cylinder which in turn increases the upstream inline force. The downstream inline force remains null since the downstream part of the cylinder is still in the air.
- **t3**: Maximum of the upstream force. The wave run-up is maximum on the upstream part as observed for the slice centred at $z = -0.225m$ when the maximum inline force on the upstream part is reached (Fig. 6.19a). A slight change of the total force slope is observed.
- **t4**: First local minimum of the total inline force. We observe a slope inversion of the total inline force when the wave starts flowing back from the downstream to the upstream side of the cylinder. This was also noticed for the submerged slice at t2, resulting in a slope change of the total inline force. This phenomenon is greatly emphasised here, for a slice closer to the interface. This is the beginning of the secondary load cycle.
- **t5**: Local maximum of the total inline force. This peak occurs simultaneously with

a strong slope change on the upstream inline force. It corresponds to the transition between the roll to the linear shape of the wave run-up on the upstream side, as noticed for the submerged slice (at time t_3). Besides, a small transverse force is noticeable whereas it was negligible until now. This might be explained by the asymmetry of the flow around the cylinder when the wave flows back.

- **t6**: From t_6 , the upstream part is not immersed anymore, the corresponding force is null.
- **t7**: Decrease of the downstream inline force. The wave runs down and finally comes under the slice leading to a total null force on the slice.
- **t8**: The total inline load is null again when the slice is not immersed in water anymore.

In conclusion, the specific variation of wave loads (slope change or inversion) is strongly connected to the wave run-up. Specific times are determined to identify precisely the secondary load cycle. The latter is explained by the wave flowing back from the downstream to the upstream part. This phenomenon impacts more the upstream part of the cylinder compared to the downstream one.

6.4 Conclusion

With this first study, we set up, validated and analysed a CFD model for a simple wave/structure interaction case, by modelling in the CFD framework of OpenFOAM the Stansberg [1997] experiments.

Though the flow is turbulent ($Re = 10^5$), we demonstrated that a no-slip boundary condition and no turbulence model were sufficient to reproduce the experimental load for this constrained cylinder in waves.

We demonstrated the validity of our numerical slice methodology to determine Morison coefficients from CFD loads, on the simple case of a vertical cylinder. For this case, the drag term of Morison formula is found negligible, that makes the inertia term enough to determine the wave load. The inertia coefficient varies slightly along the submerged part of the cylinder ($C_M = 2.08 + -0.05$). The total load obtained applying Morison formula for each slice with $C_M = 2.08$ (and $C_D = 0.5$) is in good agreement with the experimental and numerical loads. Only the non-linear behaviour before the minimum of the load signal, caused by the air/water interface behaviour, is not captured by Morison formula. Indeed, this interface strongly impacts the loads in the air/water area, where Morison approach cannot be applied, but its influence remains negligible for the total load.

Finally, we confronted our results to past hydrodynamic studies that also focused on surface-piercing cylinders and highlighted the non-linear effect of the interface on the total

load. This non linearity is called secondary-load cycle. Thanks to CFD, we were able to detail this specific cycle highlighting key moments and correlating the wave run-up to the load on the upstream and downstream parts of the cylinder. A wave backflow from the downstream to the upstream part of the cylinder was evidenced, responsible for the non-linear shape of the total wave load.

We have thus set up an accurate CFD model of a surface-piercing cylinder in waves and proposed a first hydrodynamic study of the wave loads. In particular, Morison coefficients were determined from CFD results, to then check the validity of Morison approach for predicting the wave loads. With this bench of skills acquired, we will study in the following chapter the hydrodynamic behaviour of the constrained FOWT floater in waves, composed by multiple inclined submerged and surface-piercing cylinders.

Chapter 7

Investigation of FOWT hydrodynamics

In this chapter, we investigate the hydrodynamics of a FOWT floater.

Having defined some guidelines in order to propagate regular waves along a NWT in a controlled way minimising any reflection or damping phenomena (section 5.1), we can now include the TLP floater in the NWT.

The section 1 presents the understudy case: the TLP floater in a constrained configuration subjected to regular waves. The corresponding experimental tests, so-called captive tests, are detailed. The modelling of the captive test with DeepLinesWind™ and with CFD is then presented. Both models are validated against the experimental data. The distribution of the forces on the floater can be investigated as illustrated in the section 2 and thus the weight of the potential theory/Morison formula in the total load prediction is precised. That notably highlights why it is important to specify Morison load prediction accuracy for FOWT loads using CFD.

The three following sections (section 7.4, 7.5 and 7.7) study the applicability of Morison approach for the prediction of FOWT loads. Three main limitations of Morison formula, that may impact the wave loads, are investigated: the presence of the whole structure (versus an isolated cylinder), the vicinity of the air/water interface and the brace orientation. From the CFD results, we derive Morison coefficients applying the numerical slice methodology detailed previously (cf. section 5.2) and we check the agreement between the Morison prediction and the CFD results.

Finally, we propose in the section 7.9 some advice to improve Morison prediction for FOWT floater loads.

7.1 Captive test description and simulation

7.1.1 Experiments

Basin model tests were performed in 2015 at the MARIN wave tank facility (the Netherlands) to validate and ensure the proper behaviour of the TLP floater concept and also to validate the design tools, such as DeepLinesWind™. Several captive tests, consisting in the propagation of waves on the constrained floater, were performed as shown in Fig. 7.1. The TLP floater was represented by a newly built model at a geometrical scale of 1:40.

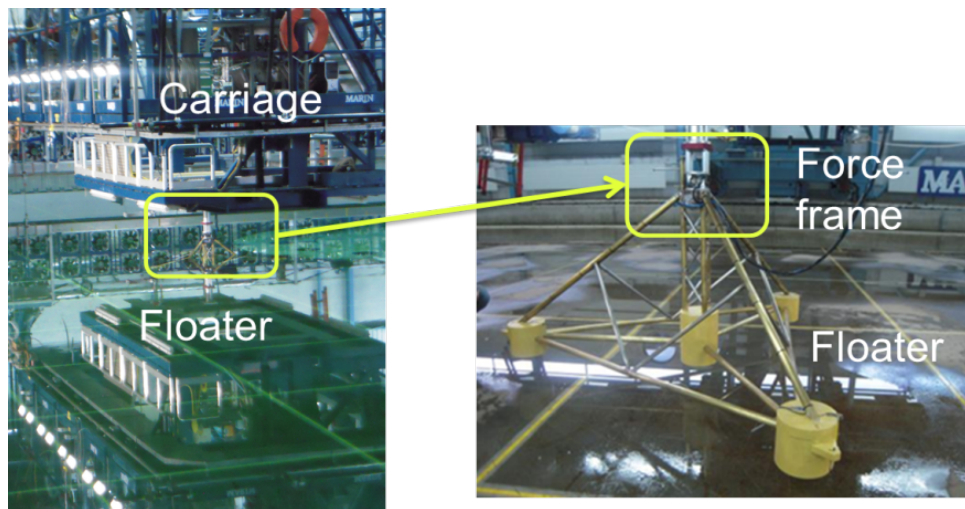


Figure 7.1: Photos of the captive tests performed at MARIN (the Netherlands).

The wave elevation is measured with resistance type wave probes, at several places in the tank without the floater presence. The wave loads and moments on the floater are also measured with gauge force transducers (force frame depicted in Fig. 7.1). All the data are provided by MARIN at full scale (a common practice in hydrodynamics). That is why the results (from experiments and CFD) are post-treated at full scale in this chapter, applying Froude similitude with a scale ratio of 40 (Annexe 9.1). It is important to underline that Froude's similitude does not maintain the Reynolds number between the model and the full scale device. As a consequence the viscous forces may not be properly evaluated.

In the present study, three different regular waves are modelled in CFD. Their characteristics at full scale are detailed in Tab. 7.1 and reported in Méhauté [1976] classification in Fig. 5.1:

Case	H [m]	T [s]	h [m]	λ [m]	kA (steepness) [-]
w1	0.984	8.039	100	100	0.031
w2	4.92	8.039	100	100	0.155
w3	9	14	100	297	0.095

Table 7.1: Wave characteristics (full scale).

Wave w1, consisting in operational wind turbine sea condition, was performed at MARIN. w2 was not performed experimentally and is similar to w1 with a height five times larger. w3 is an irregular wave performed at MARIN, it is a design wave for turbine parked conditions. Due to the complexity of modelling irregular waves in CFD, we simplify w3 as a regular wave whose period and height are taken from the Jonswap spectra characteristics of the irregular wave w3. As indicated in the section 5.1.1, these waves allow us to review different ranges of inertia/drag Morison contribution.

For wave w1, the experimental surge load F_x is stabilized over time but the heave load F_z and the sway F_y are more dispersed as shown in Fig. 7.2 and quantified in Tab. 7.2.

In Tab. 7.2, the surge, sway and heave force values are detailed. Similarly to the wave height, the load value is determined by $F = 2\sqrt{2\text{var}(F(t))}$. The dispersion of the time signal corresponds to the standard deviation of the series of the maxima minus the minima.

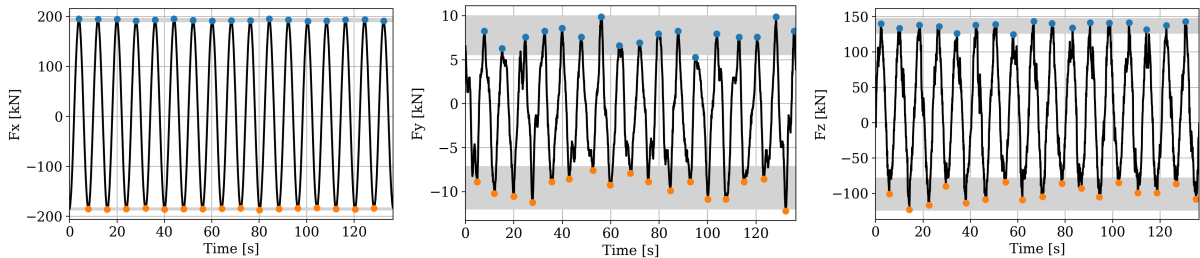


Figure 7.2: Experimental loads on the TLP (wave w1).

Wave w1	Surge (F_x) [kN]	Sway (F_y) [kN]	Heave (F_z) [kN]
Experimental data	377.20 ± 2.22	15.39 ± 1.57	211.57 ± 11.07

Table 7.2: Forces amplitudes and variation.

No information is reported concerning the experimental uncertainty.

7.1.2 Modelling of the captive test in DeepLinesWind™

In design tools, we commonly apply the same Morison coefficients C_D and C_M for each brace throughout the whole structure. Calibration procedure aims to determine the best set of coefficients that enables Morison theory, combined with the potential theory, to

fit as close as possible the experimental data (here, heave, sway and surge forces on the TLP floater). From a parametric study, $C_D = 0.8$ and $C_M = 2.5$ appears to be the best set of coefficients for load prediction: the difference relative to the experiments for F_x is -1.1% and for F_z is 26.1% as visible in Fig. 7.3. C_M can be decreased to 1.5 to better predict F_z (error of 8.25%) but this leads to a significant underestimation of F_x by -21.09% . Because of the important dispersion of the experimental data for F_z , we chose to calibrate DeepLinesWind™ model by favouring the prediction of F_x over F_z .

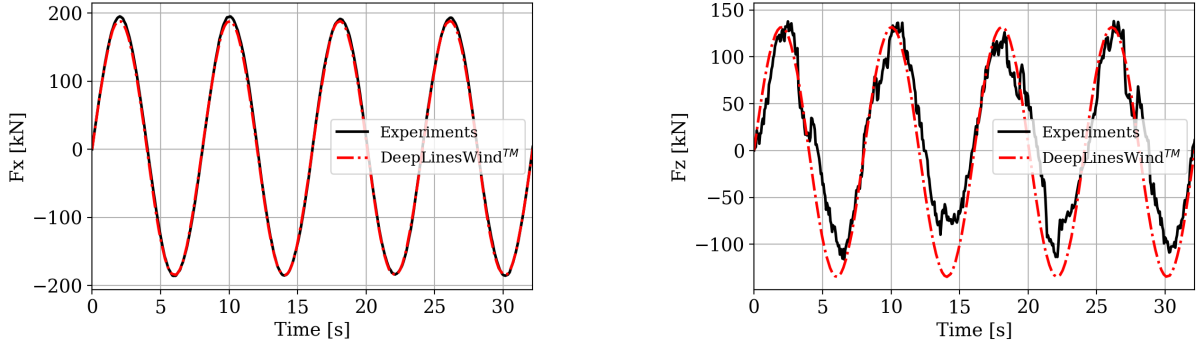


Figure 7.3: Calibration of DeepLinesWind™ on experiments (wave w1).

→ Thus we have to make a compromise between the heave and surge prediction in DeepLinesWind™. It seems that imposing the same coefficients for every brace makes the predictions of the wave loads on the whole structure difficult. Maybe the differences between the experiments and the theoretical prediction could be decreased adapting Morison formula for FOWT load prediction. That is why we use CFD in order to investigate the hydrodynamics of FOWT and the applicability of Morison formula for FOWT load prediction.

7.1.3 Setup and validation of the CFD model

7.1.3.1 Setup of the CFD model with the TLP floater

The wave-only case is detailed and validated in section 5.1. The TLP floater is then included in the NWT.

The boundary conditions on the floater are of no-slip type, based on the conclusions drawn for the Stansberg surface-piercing cylinder (Chapter 6). The cells next to the floater are cubic and their size is comprised between $D/10 - D/13$. Here we can point out the complexity of correctly meshing the connection between the refined zone around the interface and the refined zone required around the structure. A system of superimposed refinement boxes is implemented in the meshing file *snappyHexMeshDict*. The final mesh is shown in Fig. 7.4 and Fig. 7.5.

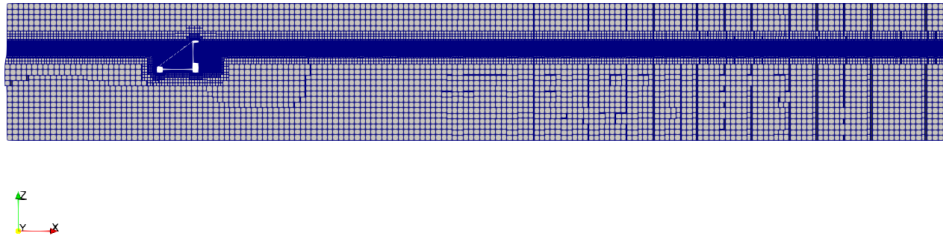


Figure 7.4: Inclusion of the TLP floater in the NWT mesh.

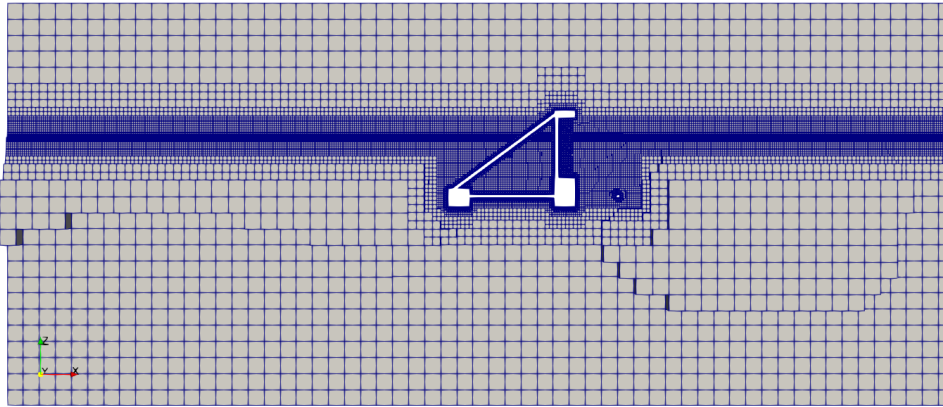


Figure 7.5: Inclusion of the TLP floater in the NWT mesh (zoom).

The simulations of the TLP floater subjected to waves are run with adjustable time step as it is detailed in the following section.

7.1.3.2 Sensitivity study to the CFL number

The wave-only NWT cases are run with a fixed time step. The combination of the time step (Tab. 5.4) with the mesh refinement (section 5.1.5) leads to a maximum CFL below 0.2, necessary to get a proper resolution of the interface with the VOF MULES method implemented in waveFoam solver.

With the TLP included in the NWT, for wave w2 and w3, the cells next to the floater in the interface area are smaller than the smallest cells of the mesh without the floater. So the time step has to be reduced compared to the wave only cases, in order to ensure at least a CFL number below 1, ensuring the numerical stability of the solver. That is why we perform a convergence study, with adjustable time step, varying the condition on the maximum CFL imposed in the simulation. This aims at getting an optimal CFL number that enables to generate correctly the waves and at the same time correctly model the wave interaction with the floater.

Three maximum CFL numbers are tested with wave w2: $\max\text{CFL} = 0.9$, $\max\text{CFL} = 0.75$ and $\max\text{CFL} = 0.5$. The total loads on the floater in (Ox) and (Oz) direction are plotted in Fig. 7.6. Tab. 7.3 details the load amplitudes and the time step obtained during the simulation.

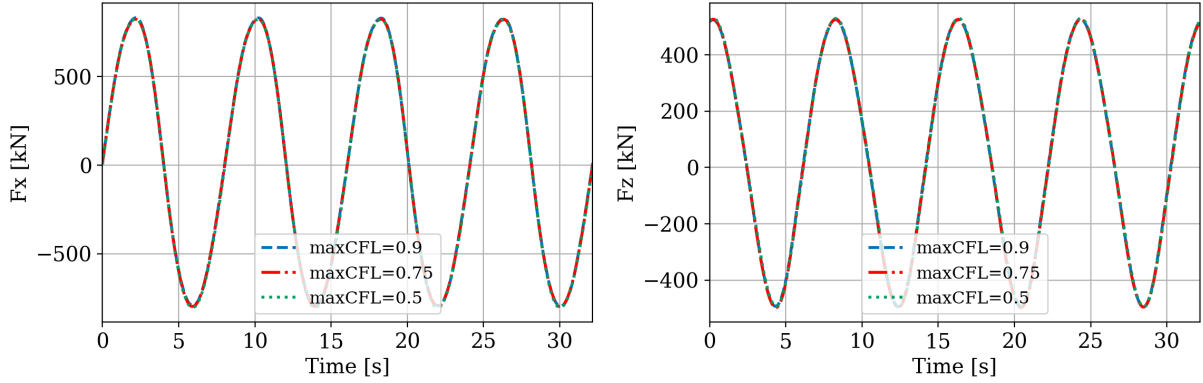


Figure 7.6: Surge (F_x) and heave (F_z) forces for the convergence study in CFL number (wave w2).

max CFL imposed	F_x [kN]	F_z [kN]	time step [s]
0.9	1645.95	999.34	0.0009-0.0018
0.75	1642.91	1000.78	0.0008-0.0018
0.5	1647.93	1000.81	0.0003-0.0015

Table 7.3: Wave loads statistics for the convergence study in CFL (wave w2).

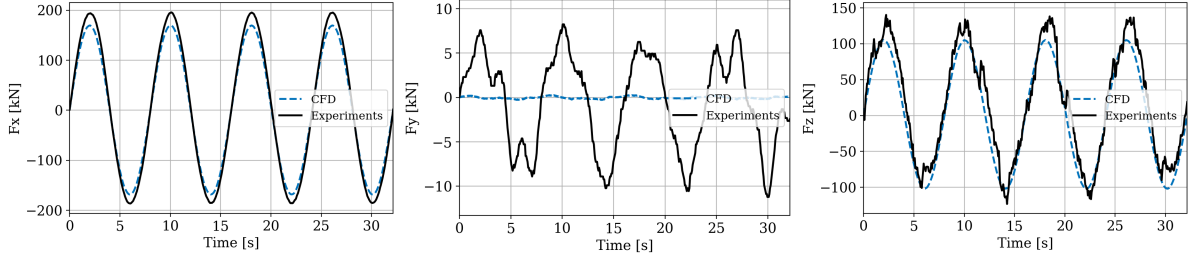
Wave load differences between the three simulations are negligible and so the three CFL numbers seem to be suitable to correctly model wave/floater interaction.

We choose to set a maximum CFL number to 0.75 for wave w2 (and w3). With this imposed maximum CFL number, the time step obtained is within the range of the requirements to get a proper wave propagation (for wave w2, 0.008 – 0.0018 s obtained in the TLP simulation against 0.002 s recommended for the wave-only case).

7.1.3.3 Validation of the CFD model against experiments (wave w1)

Only the CFD model of the floater with wave w1 can be validated against experimental data. For wave w1, the cells next to the floater have the same size as those in the free surface zone. So we decided to run the CFD model of the TLP floater with wave w1 with the fixed-time step determined for the w1 wave-only case ($dt = 0.002$ s). For wave w2 and w3, the simulation is run with adjustable time step with a maximum imposed CFL number of 0.75 as explained in the section 7.1.3.2.

Applying the mesh recommendations as previously discussed, the CFD wave loads are compared to the experimental ones for wave w1 in Fig. 7.7. The statistics obtained from CFD and experiments are detailed in Tab. 7.4.

Figure 7.7: Surge (F_x), sway (F_y) and heave (F_z) forces from CFD and experiments (wave w1).

Wave w1	Surge (F_x) [kN]	Sway (F_y) [kN]	Heave (F_z) [kN]
Experiments	377.20 ± 2.22	15.39 ± 1.57	211.57 ± 11.07
CFD	337.76 ± 0.05	0.45 ± 0.53	206.13 ± 0.12
Difference(CFD,Experiments)	-10.46%	-97%	-2.57%

Table 7.4: Statistics for CFD and experimental forces (wave w1).

The heave loads F_z from CFD and experiments are in good agreement. A difference of 10.46% is highlighted concerning the surge force (F_x), the CFD underestimates F_x compared to the experiments. This gap may decrease by further improving the mesh (complexity to control the mesh around the floater in the interface area). The sway force predicted by the CFD model is negligible compared to the experiments, this may be explained by the high dispersion for F_y in experiments and the very low amplitude compared to F_x and F_z . We choose to carry on the hydrodynamic analysis of the CFD wave loads on the floater, keeping in mind this under-prediction of the surge force.

7.1.3.4 Wave loads derived from the three CFD models

The simulations of waves w2 and w3 are run imposing a maximum CFL number of 0.75.

The wave loads derived for these two waves are detailed in Tab. 7.5. Wave loads are much stronger than for w1, as expected because of the increased wave height.

Wave	F_x [kN]	F_y [kN]	F_z [kN]
w1	337.76	0.45	206.13
w2	1642.91	18.98	1000.78
w3	3878.04	23.25	2803.15

Table 7.5: Surge (F_x) and heave (F_z) forces derived from the CFD model of the TLP for the three waves.

→ For the three waves, the heave force accounts for about 60% of the total load and the surge force accounts for 40% of the total load. The contribution of the sway force to the total loads remains negligible (< 1%). This is expected as the wave propagates along

the (Ox) axis. In the following section, the load distribution is precisely analysed.

7.2 Distribution of the forces on the floater

To study the floater load distribution, the braces are gathered in groups (Braci, Brac1i, Centi, Transi, Interi and Renforti) as detailed in the section 5.2.1 and shown in Fig. 7.8. Buoyi corresponds to the group formed by the three side buoys and the central buoy (coloured in red).

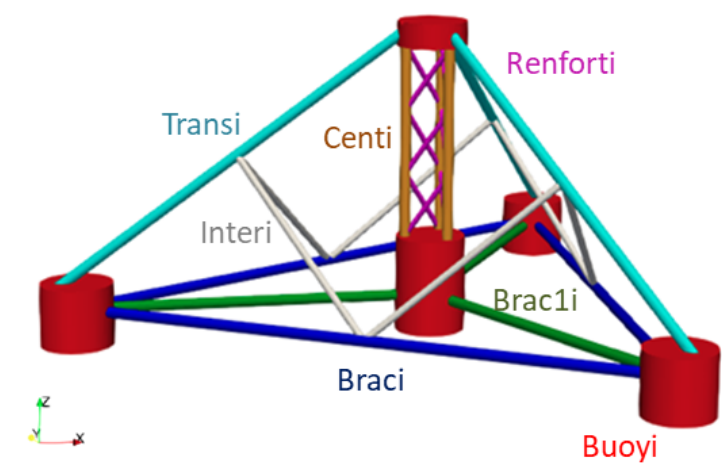


Figure 7.8: Typical groups of braces and buoys.

For each group, the load time series is derived as the sum of load time series for each brace (possible because of the floater symmetry). A load value is determined in (Ox), (Oy) and (Oz) directions for each group (global frame shown in Fig. 7.8).

The load distribution among the groups for wave w1, w2 and w3 are respectively shown in Fig. 7.9, Fig. 7.10 and Fig. 7.11.

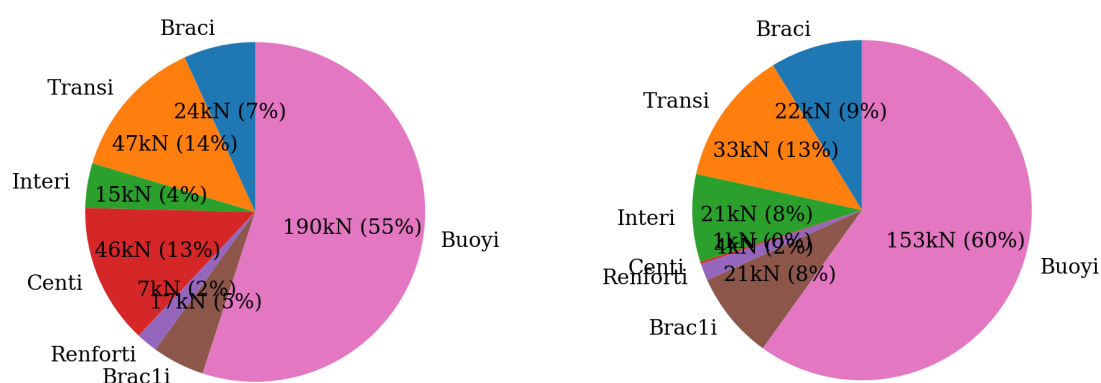


Figure 7.9: Surge (F_x) and heave (F_z) force distribution from CFD (wave w1).

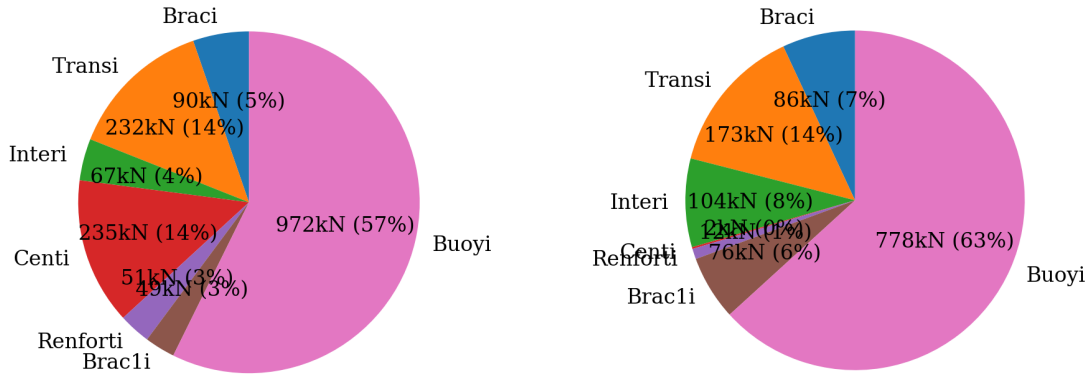


Figure 7.10: Surge (F_x) and heave (F_z) force distribution from CFD (wave w2).

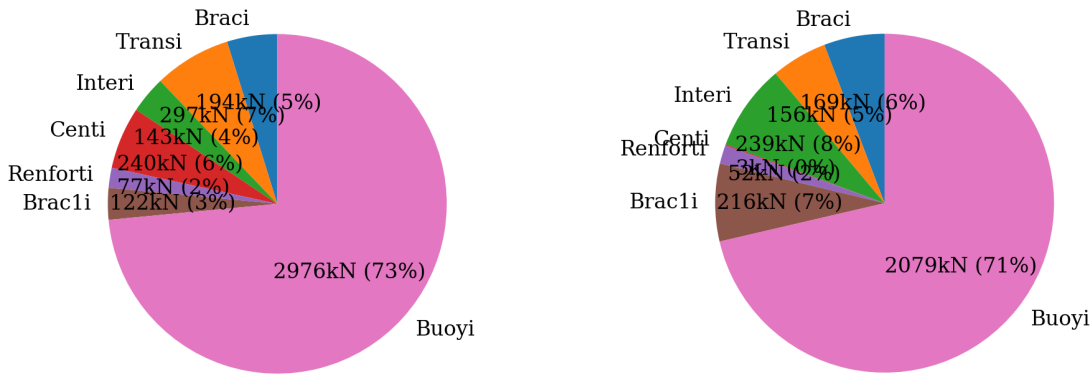


Figure 7.11: Surge (F_x) and heave (F_z) force distribution from CFD (wave w3).

For wave w1 and w2, the loads on the braces account for about half of the total load. For wave w3, the braces account for about 30% of the total load. Although this contribution is smaller than the one for wave w1 and w2, it remains significant.

The similar total load distribution is obtained for the three waves from DeepLinesWind™ models but not presented here. The wave loads on the four buoys in red in Fig. 7.13 are commonly predicted applying the potential flow theory (cf. section 2.4). Some uncertainties concerning second-order wave load prediction on the larger buoys of FOWT floaters (cf. section 4.1.3) are currently investigated in the OC6 project performing in CFD bichromatic waves on the OC5-DeepCWind semisubmersible floater (cf. section 4.3.2.1). This will not be investigated in the PhD thesis. Here we only focus on Morison’s prediction applied for brace loading.

Focusing now on the braces: the contribution of each group of braces is compared for the three waves. For each wave, the load value for each group (F_{group}) is normalized by the sum of the load values of all the groups: $F_{group,normalized} = F_{group}/F_{sum}$ where $F_{sum} = F_{Braci} + F_{Brac1i} + F_{Centi} + F_{Transi} + F_{Interi} + F_{Renforti}$. Fig. 7.12 shows the results in (Ox), (Oy) and (Oz) directions.

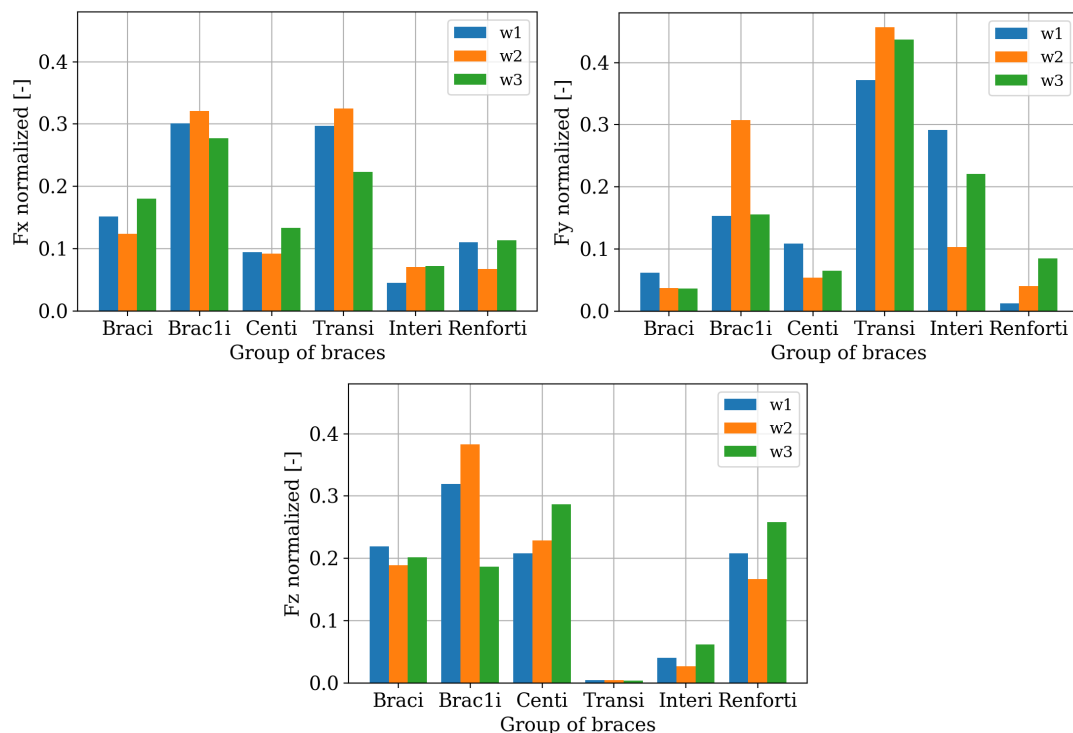


Figure 7.12: Surge, sway and heave force distribution for the groups of braces for the three waves.

Fig. 7.12 shows significant differences between the three waves for Brac1i and Transi. Here it is complex to conclude about the impact of the wave characteristics on the brace loads. That is why in the following sections, we precisely investigate the load dependency on the wave characteristics (amplitude and period) and the brace specifics (position in the floater, vicinity of the interface, orientation).

→ The wave loads on the braces, that are determined with Morison approach, account for an important part of the total loads (30-50%). Thus it makes sense to investigate Morison applicability for FOWT load prediction. Also, the distribution of the wave loads on the floater depends on the imposed wave. Therefore we will investigate the applicability of Morison approach for FOWT load prediction with the three different waves.

When applying Morison empirical approach for FOWT design, we do not take into account some aspects and may wonder about the applicability of such a theory for FOWT: Does the whole structure impact the wave loads on the braces, supposed as isolated in Morison formulation (section 7.4)? Does the interface strongly influence the wave load on the surface-piercing braces (section 7.5)? Can Morison formula predict wave loads on oriented braces (section 7.7)? In the following sections, we will investigate these three questions. The final aim is to propose advice when applying Morison empirical approach to predict the wave loads on the FOWT floater.

7.3 Two methods to determine Morison coefficients for brace load prediction

We investigate Morison applicability for the brace load prediction. The braces studied in the following sections are indicated in Fig. 7.13.

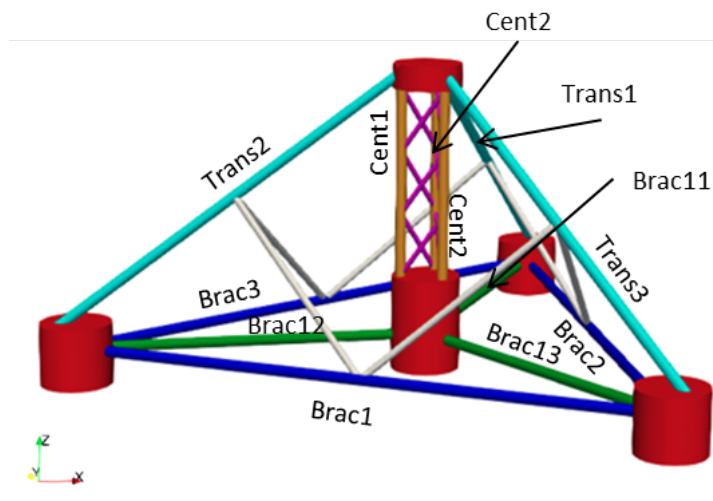


Figure 7.13: Detail of the brace names in the TLP floater.

From the CFD loads, we determine the Morison coefficients along the brace applying the numerical slice methodology presented in the section 5.2. For each slice, a set of four directional coefficients is derived in the local frame of the brace (ΩXYZ): C_{D_x} , C_{M_x} , C_{D_z} and C_{M_z} .

To determine the Morison load on the entire brace, the theoretical slice loads are summed. We have two methods to determine the Morison coefficients for the load prediction on a slice:

- Variable coefficients: we take the slice coefficients determined from the CFD loads on the slice. Thus we impose one set of coefficients per slice. This solution is the most precised one but too advanced to be implemented in design tools.
- Constant averaged coefficients: we take the average of all the slice coefficients derived from CFD. Thus we impose the same set of coefficients for every slice. For the brace crossing the interface, the coefficients are averaged over the slices that are always submerged, as concluded in Stansberg cylinder study (cf. section 6.2.3).

The Morison force on the brace is then compared to CFD.

We study locally the wave loads on the braces and the load prediction applying Morison formula to then conclude at the level of the group of the braces and finally at the floater level. We define four main levels of study: the floater level, the group of braces level, the brace level and the slice level.

7.4 Impact of the structure

First we investigate the impact of the structure on the loads with wave w1.

7.4.1 Impact of the TLP floater on all the braces

To evaluate the impact of the structure, we compare loads on a specific brace when it is placed alone in the NWT (Fig. 7.14a), or when the whole structure is in the NWT (Fig. 7.14b).

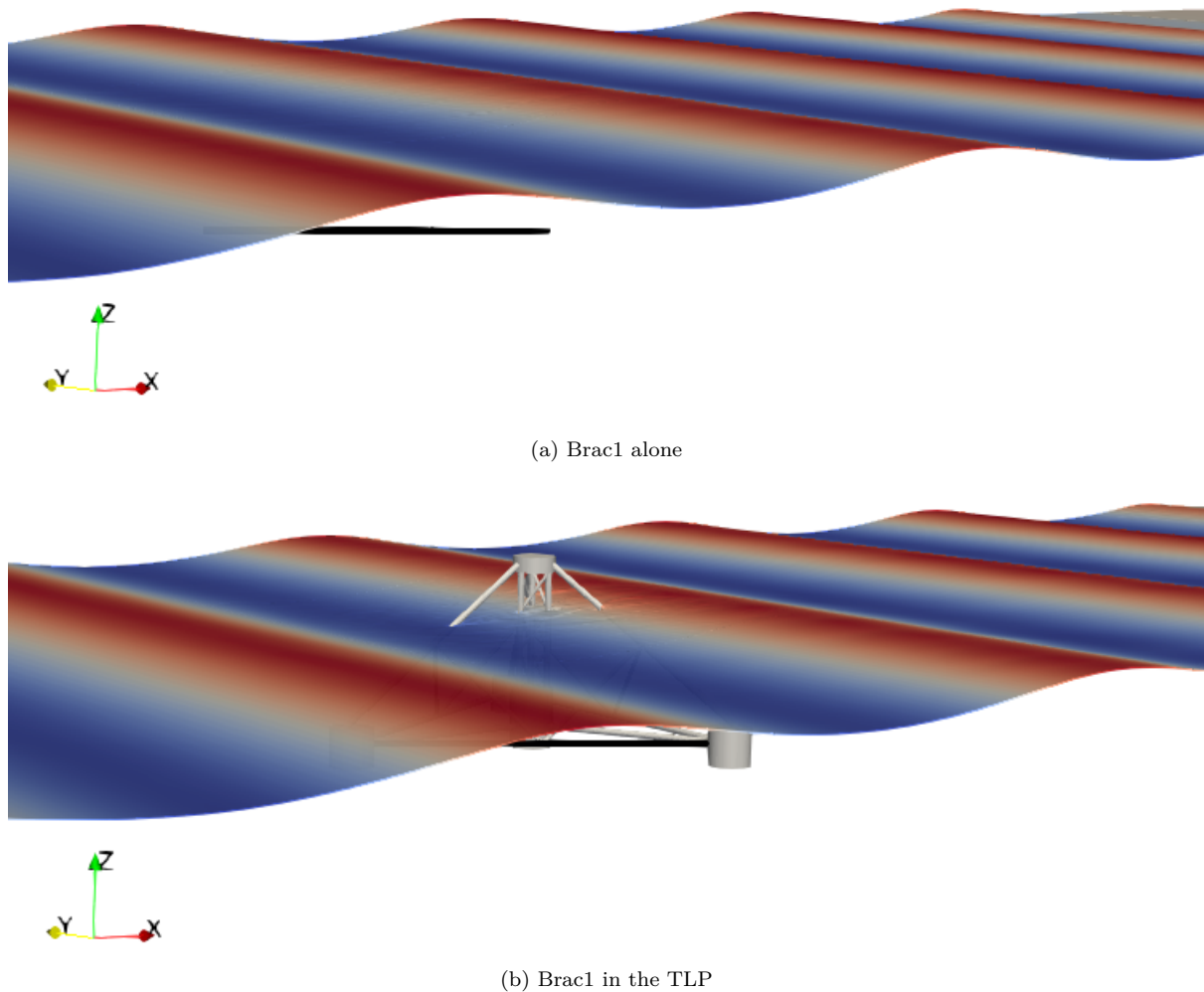


Figure 7.14: Visualisation of the two configurations of Brac1 in the NWT (the free surface is coloured with the dynamics pressure field)

The loads obtained from the isolated brace and from the configuration with the brace included in the TLP are compared in Tab. 7.6. The relative differences between the two models are detailed.

	Fx [kN]	Fy [kN]	Fz [kN]
Brac1 alone	3.22	5.46	13.39
Brac1 TLP	3.35	5.62	9.80
Difference Brac1(alone,TLP)	-3.8 %	-2.9 %	36.7 %
Brac2 alone	20.90	0.00	20.86
Brac2 TLP	21.84	0.01	18.06
Difference Brac2(alone,TLP)	-4.3 %	/	15.5 %
Brac12 alone	0.13	0.00	9.64
Brac12 TLP	0.12	0.01	10.33
Difference Brac12(alone,TLP)	12 %	/	-6.7 %
Cent1 alone	13.77	0.09	0.19
Cent1 TLP	18.33	1.08	0.18
Difference Cent1(alone,TLP)	-24.9 %	-91.9 %	10.1 %
Trans2 alone	17.05	0.15	22.51
Trans2 TLP	17.75	0.14	23.50
Difference Trans2(alone,TLP)	-4 %	10.2 %	-4.2 %
Trans3 alone	21.50	3.47	14.70
Trans3 TLP	22.85	6.77	16.46
Difference Trans3(alone,TLP)	-6 %	-48.7 %	-10.7 %

Table 7.6: Surge, sway and heave loads on the braces alone and in the TLP.

Major differences are highlighted in Tab. 7.6. The heave force for the isolated Brac1 and Brac2 is much bigger than the brace force in the TLP (respectively +36.72% and +15.48%). So the TLP floater severely impacts the forces in (Oz) direction on the horizontal braces located at the bottom of the structure (Braci).

The surge force for Cent1 is also impacted by the structure: the force for the isolated brace is much smaller than the brace force in the TLP (-24.89%).

The heave force on the isolated Trans3 is smaller than within the TLP (-10.72%). The sway force is doubled when the brace is included in the TLP compared to the isolated brace.

→ From these observations, we can assert that the TLP floater does modify the flow in a manner that significantly impacts the wave loads on the braces. Except for the brace at the centre of the floater, the inline force is slightly impacted. On the contrary, the vertical loads are more prone to differences. However, checking only the brace load amplitudes is not sufficient to understand how the floater impacts the loads on the brace.

Does these load differences between the isolated brace and the configuration with the

brace included the TLP floater come from the disturbance of the flow by the structure? Is it explained by the interconnections between the braces? In order to answer to these questions, we will investigate the load distribution along two horizontal braces (Brac1 and Brac12) in the following two subsections.

7.4.2 Impact of the floater presence on a horizontal and deeply submerged brace, intercepted by other braces, Brac1

First we focus on Brac1, which is coloured in Fig. 7.15.

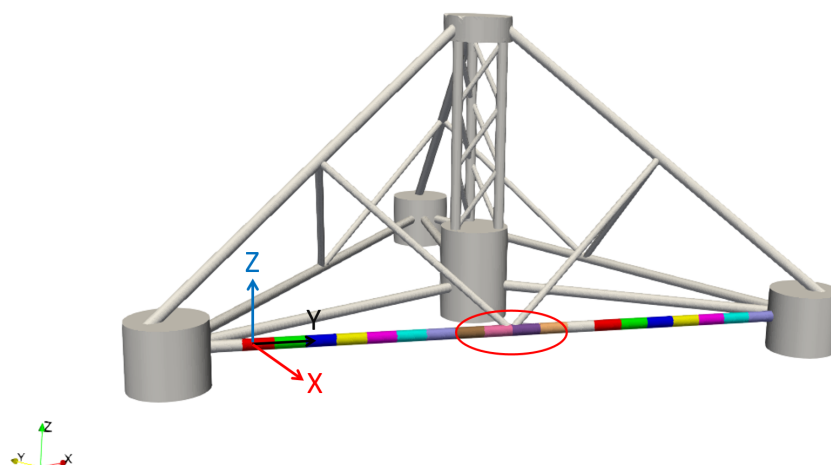


Figure 7.15: Brac1 in TLP

The impact of the TLP floater on the heave force is illustrated on the loads in the global frame ($Oxyz$) for the isolated Brac1 and in the configuration within the TLP floater as shown in Fig. 7.16 (in agreement with the data presented in Tab. 7.6).

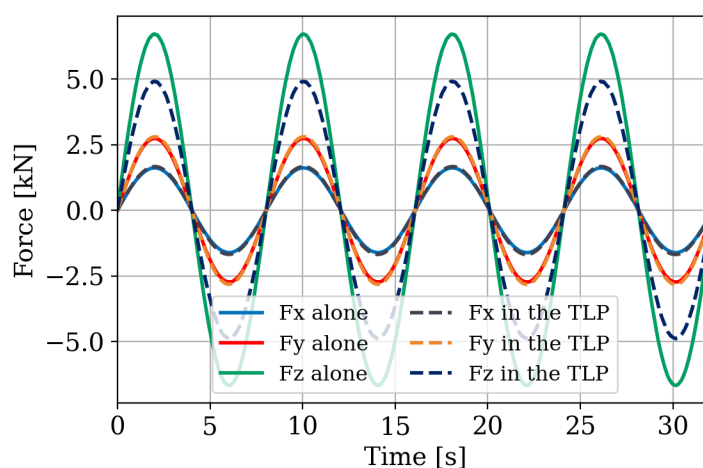


Figure 7.16: Surge, sway and heave forces for Brac1 alone and in the TLP.

In order to investigate how the floater impacts the loads, we analyse the loads along the brace by cutting it into slices (Fig. 7.15) for both configurations.

We focus first on the not-pierced slices by the interconnections between the braces.

The interconnection area encircled in red in Fig. 7.15 is shown in Fig. 7.17 to visualise the pierced slices and two not-pierced slices on both sides.

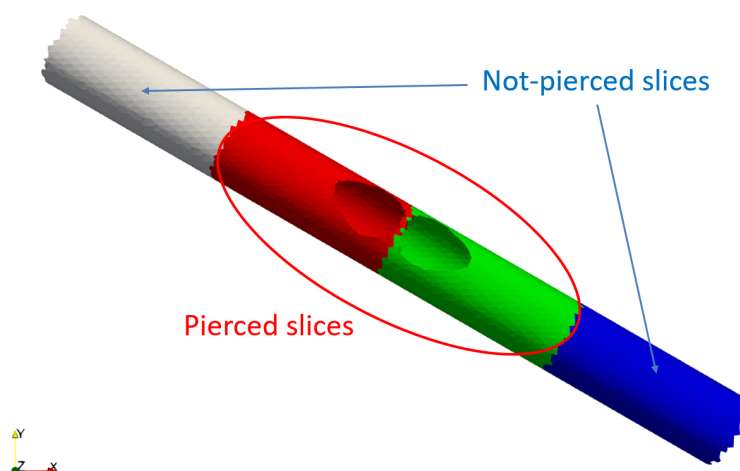


Figure 7.17: Visualisation of the pierced slices and two not-pierced slices on both sides for Brac1.

The sum of loads derived for the not-pierced slices in the isolated brace and in the TLP floater are plotted in Fig. 7.18.

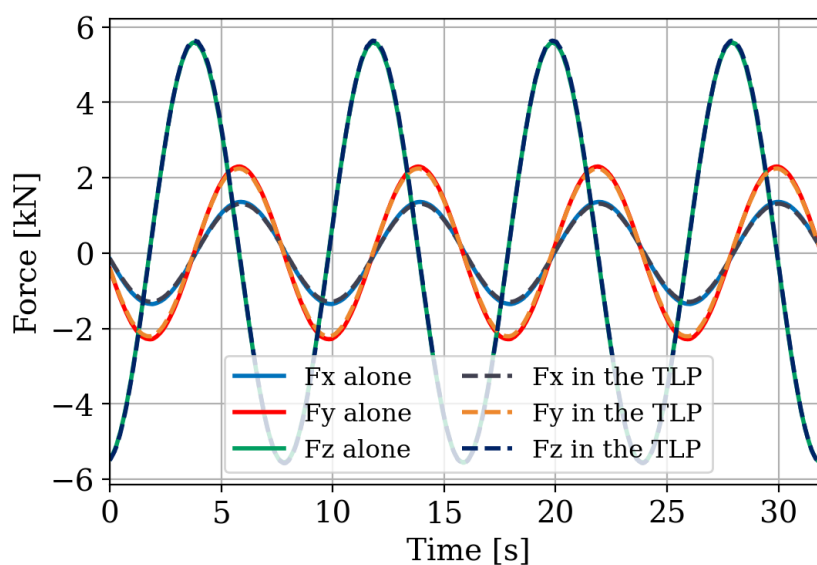


Figure 7.18: Forces on the not-pierced slices of Brac1 alone and in the TLP.

Fig. 7.18 shows that the loads are identical for the two different configurations. The floater does not disturb the flow perceived by the not-pierced slices (9/10th of the brace) in a manner that significantly affects the loads.

However, we demonstrated the floater does significantly impact the heave load for Brac1. So the impact of the floater seems to occur at the interconnections.

When applying Morison formula to predict wave loads on the braces in the design tools, the impact of the interconnections are not taken into account (same coefficient all

along the braces). We now analyse how the interconnections influence the coefficients and the force predicted applying Morison formula.

The coefficients are derived along the brace following the method explained in the section 5.2.

The coefficients derived from the loads with brace included in the TLP are plotted in Fig. 7.19.

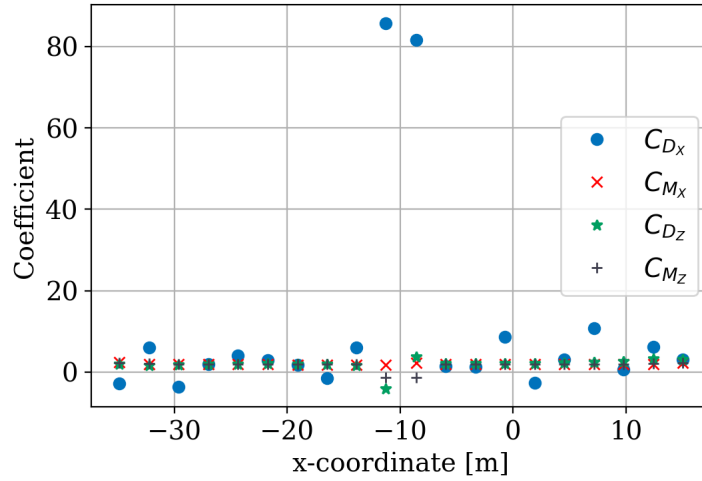


Figure 7.19: Morison coefficients derived from CFD for Brac1 in TLP.

Fig. 7.19 highlights that the coefficients determined for the pierced slices are rather extreme ($C_{D_X} = 86$ and $C_{M_X} = -1.38$ for one of the two pierced slices). Indeed, in the local frame (ΩXYZ), the phase shift between F_X and F_Z for the pierced slice differs from the one for the whole slices as visible in Fig. 7.20 (3.8 s against 2.5 s).

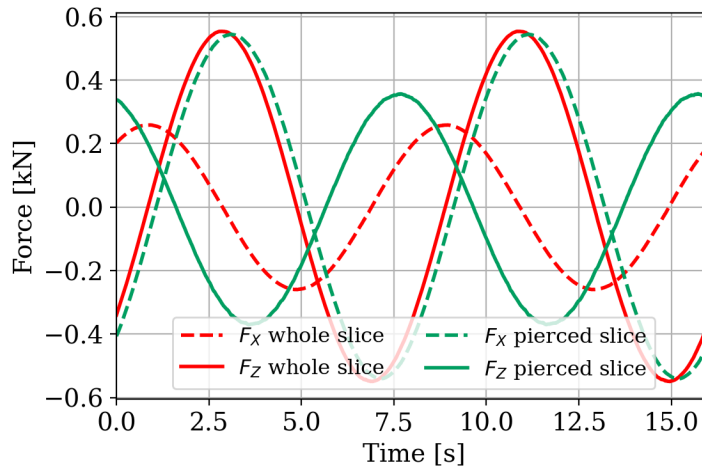


Figure 7.20: F_X and F_Z CFD forces on a whole slice and a pierced slice in the brace local frame.

Nevertheless, we show in Fig. 7.21 that Morison prediction for the pierced slice loads using these extreme values is quite close to the CFD loads. Only non-linearities on the extrema of F_X derived with Morison formula are visible.

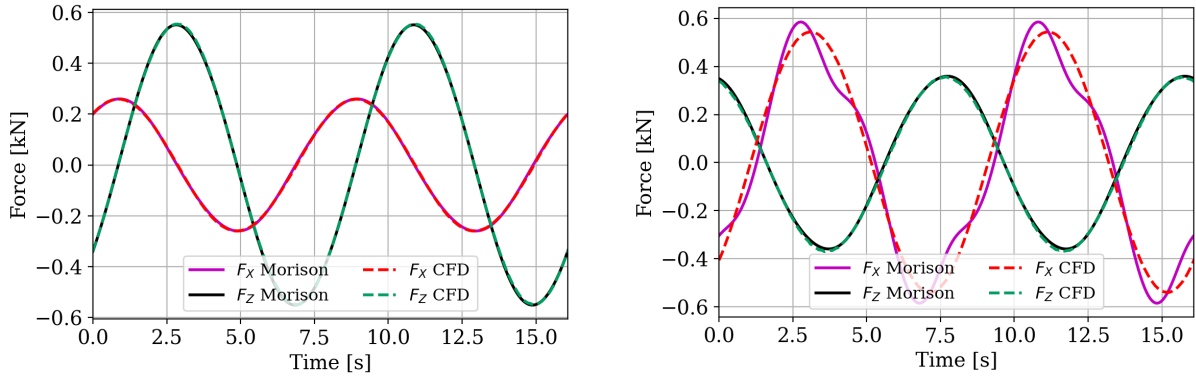


Figure 7.21: F_X and F_Z forces from CFD and Morison for a whole slice ($C_{D_X} = 2.9$, $C_{M_X} = 1.85$, $C_{D_Z} = 2.05$ and $C_{M_Z} = 1.97$) and for a pierced slice ($C_{D_X} = 82$, $C_{M_X} = 2.23$, $C_{D_Z} = 3.7$ and $C_{M_Z} = -1.38$).

These non-linearities on the extrema of Morison F_X for the pierced slice are probably due to the unexpected drag term in Morison force as shown in Fig. 7.22. Such extreme drag force for the pierced slices are necessary to minimize the phase shift and the load differences between Morison and CFD loads for the pierced slices. They may not have a physical meaning but they are a way to fit CFD with Morison formulation that was not developed for such geometries.

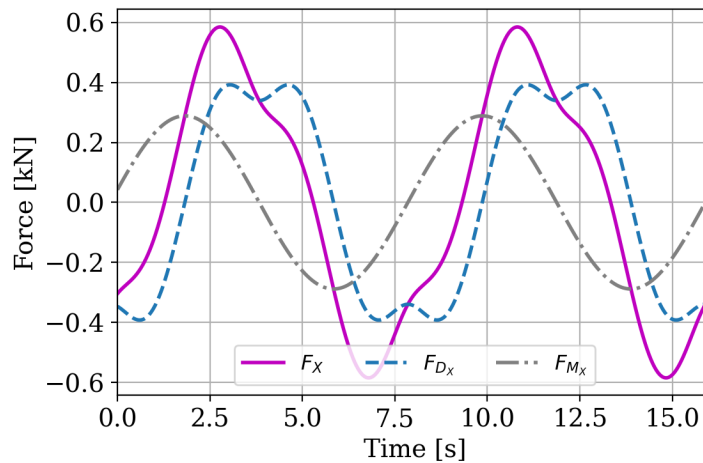


Figure 7.22: Morison prediction for a pierced slice.

In the following paragraph, we focus on the not-pierced slices: the coefficients are plotted in Fig. 7.23.

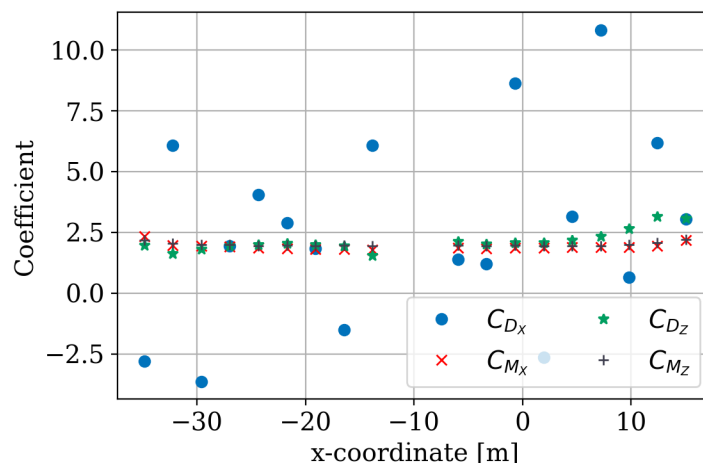


Figure 7.23: Morison coefficients derived from CFD for Brac1 in TLP without the pierced slices.

Fig. 7.23 indicates an important dispersion of C_{Dx} along the brace. This is due to the negligible value of the Morison drag term for the not-pierced slice loads.

We now focus on the inertia coefficients in Fig. 7.24.

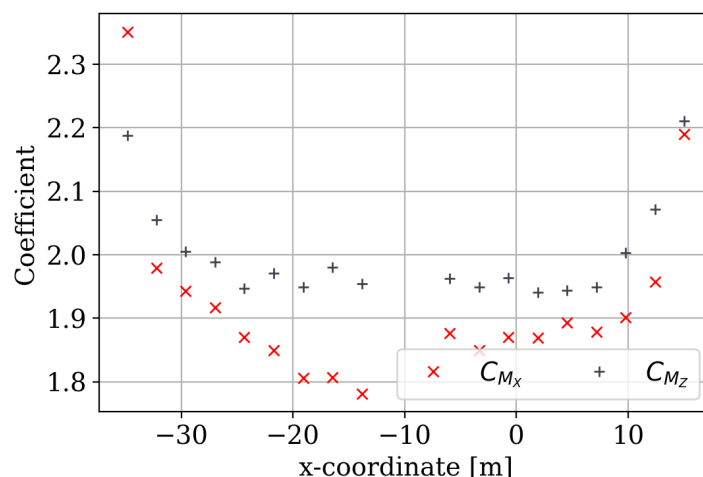


Figure 7.24: Inertia Morison coefficients derived from CFD for Brac1 in TLP without the pierced slices.

Fig. 7.24 shows that the inertia coefficients slightly vary along the brace (variation smaller than 10%) and increase at the extremities, certainly explained by the presence of the buoys at the brace edges.

The two methods (cf. section 7.3) determining the Morison coefficients to impose in the load formula for each slice are tested. For this horizontal pierced brace Brac1, a third method determining the Morison coefficients is tested: we average the slice coefficients only considering the not-pierced slices (the constant coefficient averaged over not-pierced slices).

- The brace loads obtained with variable coefficients for each slice are shown in Fig. 7.25.

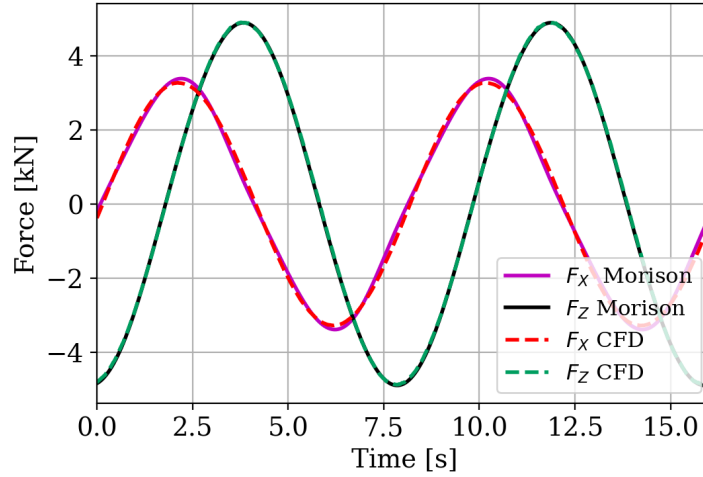


Figure 7.25: Morison prediction with variable coefficients for Brac1.

This method allows Morison formula to get predictions close to the CFD wave loads. So our numerical slice methodology, already validated with Stansbserg vertical cylinder in the section 6.3, also works for the horizontal brace Brac1. However, this method is not easy to apply in design tools.

- The brace loads determined with constant averaged coefficients ($C_{D_X} = 10.75$, $C_{M_X} = 1.92$ $C_{D_Z} = 1.91$ and $C_{M_Z} = 1.67$) are shown in Fig. 7.26.

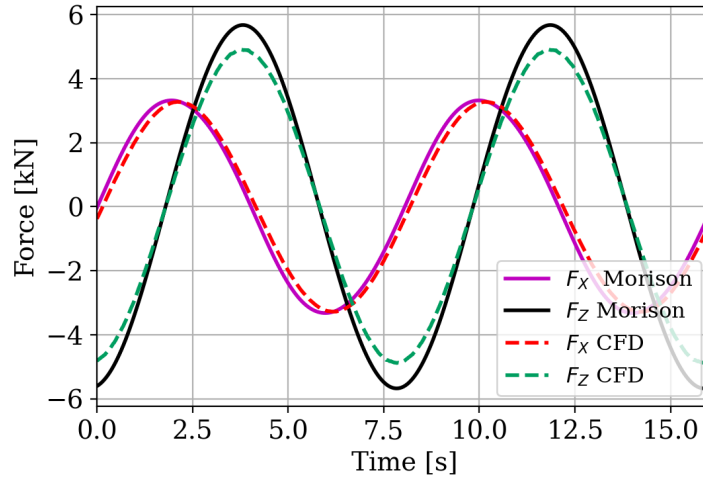


Figure 7.26: Morison prediction with constant averaged coefficients for Brac1.

The F_X forces obtained in CFD and predicted by Morison are in good agreement. The CFD heave force F_Z is 13% smaller than Morison heave force, certainly due to C_{M_Z} too low for the whole slices (1.67 against 1.97 to correctly predict F_Z on a whole slice as shown in Fig. 7.21).

- The brace load obtained with constant coefficients averaged over not-pierced slices ($C_{D_X} = 2.64$, $C_{M_X} = 1.92$ $C_{D_Z} = 2.14$ and $C_{M_Z} = 2$) are shown in Fig. 7.27. These

coefficients are within the range of the standards commonly used in the design tool ($C_D = 0.8$ and $C_M = 2.5$ for the model of the TLP in wave w1 in DeepLinesWind™). This method is close to the common application of Morison in design tools that do not take into account the interconnections.

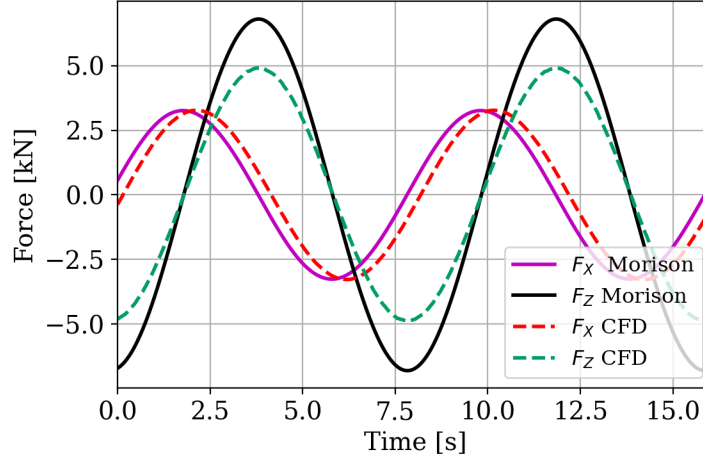


Figure 7.27: Morison prediction with constant coefficients averaged over not-pierced slices for Brac1.

With this method, F_Z derived with Morison is 39% higher than the CFD force. Also, a phase shift is noticed between the two F_X forces. In fact, this application of Morison predicts well the load on the isolated Brac1 (load difference of 1.2%). The difference is only attributed to the load difference on the pierced slices.

→ To conclude, we proved that neglecting the interconnections in Morison coefficients lead to an error of 39% in heave (F_Z) and a phase shift for F_X in the brace local frame. Using the average coefficients over the entire brace decreases the error to 13% in heave and leads to a negligible phase shift between Morison and CFD F_X force.

Similar conclusions are obtained for Brac2 also pierced at its centre but perpendicular to (Ox). Morison load prediction with the coefficients using the constant average coefficients leads to an error of 0.13% for F_X and -1.5% for F_Z .

To complete the analysis of the impact of the TLP on the wave loads, we study the hydrodynamics of a horizontal brace aligned with the flow direction (Ox) and not-pierced, Brac12.

7.4.3 Impact of the floater presence on a horizontal and deeply submerged brace, between two large buoys, Brac12

Brac12 is coloured in Fig. 7.28.

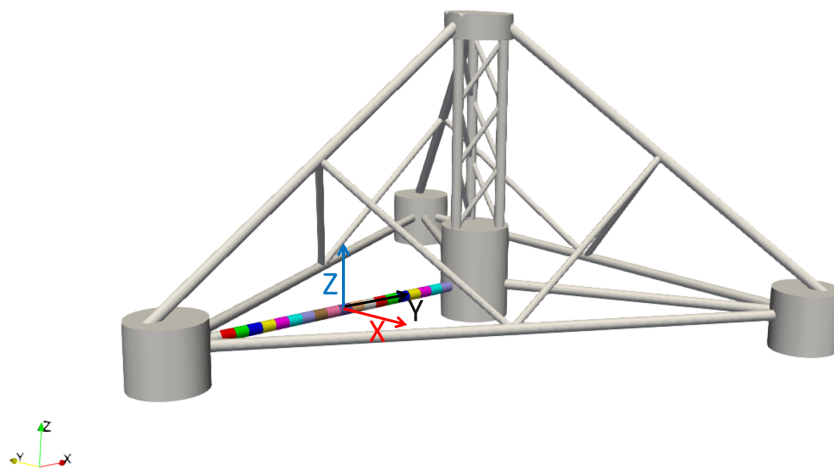


Figure 7.28: Brac12 in TLP

At the beginning of this section, Tab. 7.6 showed that the heave force F_z was 6.7% smaller for the brace alone than the brace in the TLP. The CFD loads in the global frame ($Oxyz$) for Brac12 alone and in the TLP are plotted in Fig. 7.29.

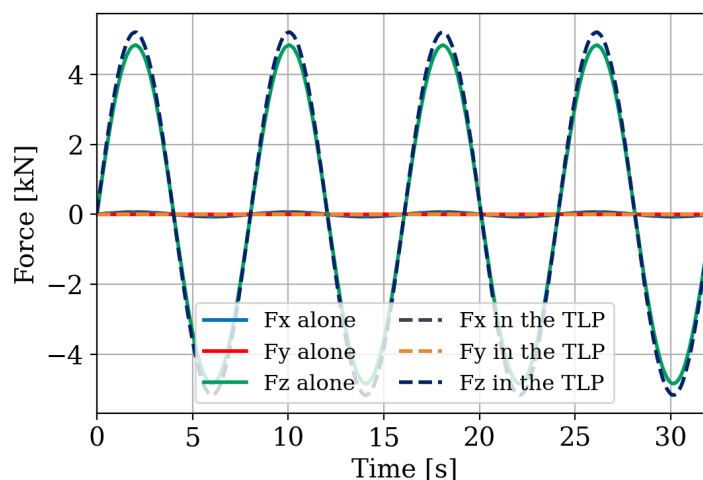


Figure 7.29: Surge, sway and heave forces for Brac12 isolated or in the TLP.

Contrary to Brac1, Brac12 is not intercepted by any brace. The structure impact on Brac12 cannot be explained by the interconnections like for Brac1. To investigate the impact of the TLP structure on Brac12, we analyse the variation of the coefficients derived from the CFD loads for the brace alone and within the TLP.

For Brac12, which is aligned with the wave direction, F_x (the axial force) and F_y (the transverse force) are negligible compared to F_z (Fig. 7.29 and Tab. 7.6). Only C_{D_z} and C_{M_z} are determined. Like for Brac1, C_{D_z} is rather dispersed along the brace because of the negligible contribution of the drag term in the total force. The variation of C_{M_z} along the Brac12, alone and in the TLP is plotted in Fig. 7.30.

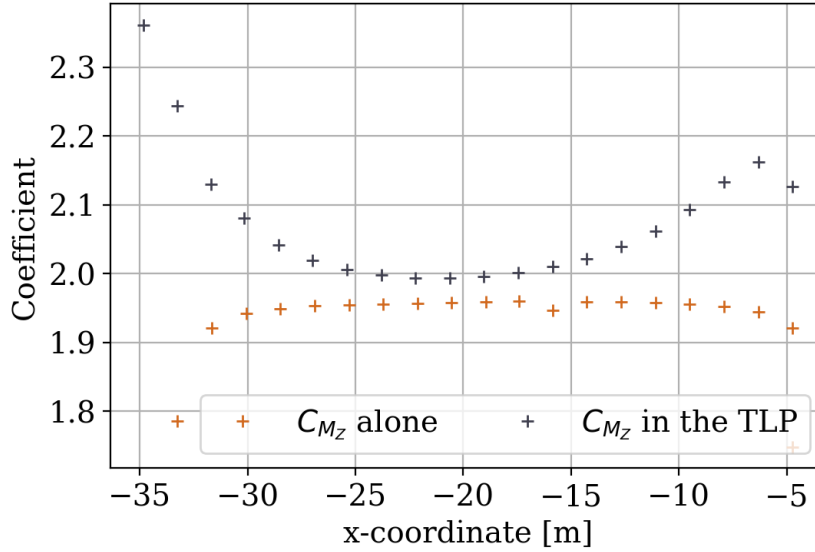


Figure 7.30: Morison C_{M_x} and C_{M_z} derived from CFD loads on Brac12 alone and in the TLP.

The coefficients for the brace in the TLP varies a little bit more than the coefficients derived for Brac12 alone (10% against 4%). For Brac12 in the TLP, the coefficients increase by 0.2 at the extremities whereas for Brac12 alone, they decrease by 0.08. This might be explained by the presence of large buoys at both extremities that can strongly disturb the flow field.

The average of C_{D_z} and C_{M_z} for the two configurations are given in Tab. 7.7. C_{M_z} is 7.2% smaller for the brace alone than in the floater.

Brac12	C_{D_z}	C_{M_z}
Alone	-1.74	1.93
In the TLP	1.24	2.08

Table 7.7: Morison coefficients derived for Brac12 averaging the coefficients all over the brace.

The two Morison coefficient methods to determine the loads on Brac12 in the brace local frame are tested:

- The brace loads obtained with variable coefficients per slice are shown in Fig. 7.31.

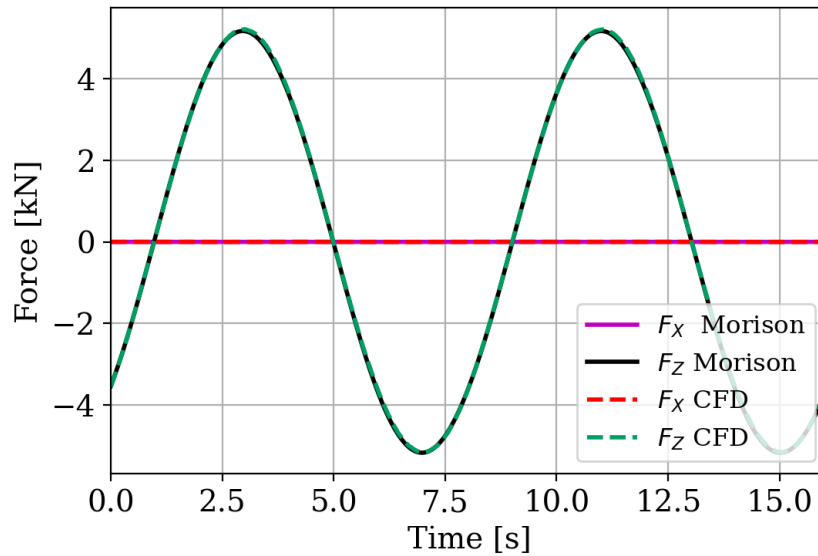


Figure 7.31: Morison prediction with variable coefficients for Brac12.

With these coefficients, Morison exactly predicts the CFD. Here our numerical slice methodology proves again its ability to determine consistent coefficients. Still, as mentioned for Brac1, taking one coefficient per slice is not applicable in the design process.

- The brace loads determined with constant averaged coefficients ($C_{Dz} = 1.24$ and $C_{Mz} = 2.08$) are shown in Fig. 7.32.

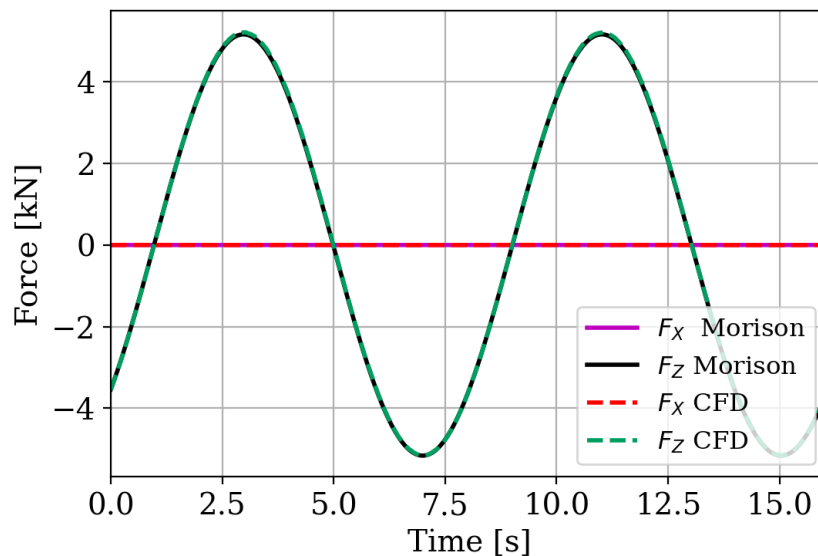


Figure 7.32: Morison prediction with constant averaged coefficients for Brac12.

Morison prediction perfectly fits with CFD. The effect of the extremities on the total load are correctly predicted by taking the average of the coefficients for all the slices. In addition, if we use the constant averaged coefficients in Morison prediction for

Brac12 alone, Morison also predicts exactly the CFD loads.

Thus the impact of the structure is taken into account in the constant averaged coefficients with a difference of 7% between Brac12 alone and Brac12 in the TLP. To conclude, if there is a substantial structure in the vicinity of the brace, the loads in the vicinity of that structure may be affected and impact the total loading on the brace. But the differences are such that averaging the coefficients gives a good prediction.

7.5 Impact of the air/water interface vicinity

Several braces in the TLP floater cross the air/water interface. In the practical application of Morison formulation for design purposes, the interface presence is taken into account through the velocity/acceleration imposed in the formula. Still, Morison formula cannot predict well the loads at the interface as explained for Stansberg surface-piercing cylinder (cf. section 6.3). However the interface influence remains negligible when considering the total load on Stansberg cylinder.

Is this observation still valid for the surface-piercing braces within the TLP floater? Are the interface effects negligible on Morison coefficients imposed for the prediction of the CFD wave loads for the FOWT floater? The influence of the interface on the brace is successively investigated for two braces: a vertical brace Cent1 and an oriented brace Trans2. In this section, we only study braces included in the TLP structure with wave w1.

7.5.1 Impact of the interface vicinity on a vertical surface-piercing brace at the centre of the floater, Cent1

Cent1 is coloured in Fig. 7.33. It consists of a vertical surface-piercing cylinder, like Stansberg's cylinder (Chapter 6), intercepted by several small braces. Since it is a vertical brace, F_z (the axial force) is null.

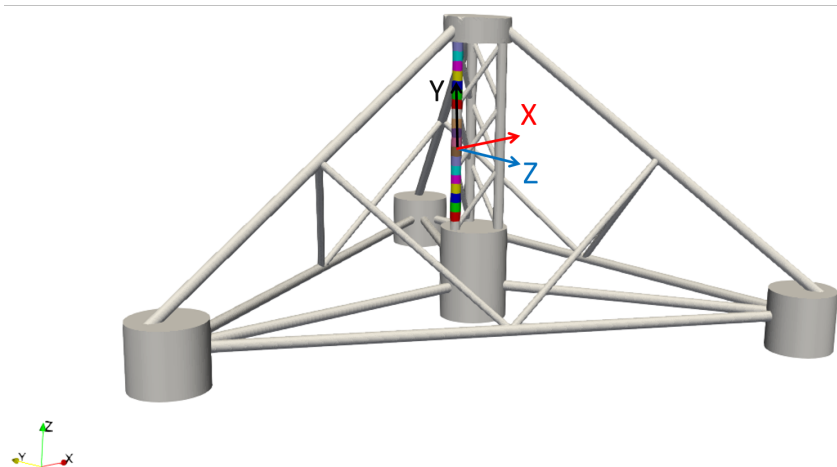


Figure 7.33: Cent1 in TLP

First the influence of the interface is analysed at the brace level.

The CFD loads in the global frame ($Oxyz$) on the entire brace or only for the submerged part of the brace are compared in Fig. 7.34. The submerged part of the brace is defined using slices always submerged by water.

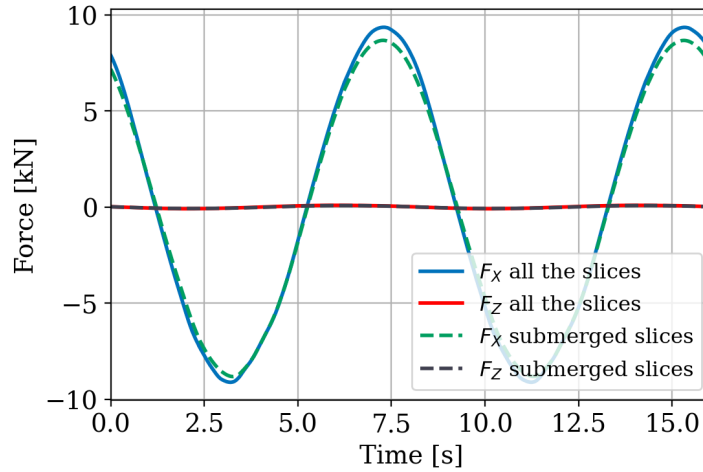


Figure 7.34: Influence of the interface on Cent1 at the brace level.

F_x for the submerged part of the brace is 5.2% smaller than the total brace load, thus the interface slightly influences the load amplitude.

The coefficients obtained along Cent1 applying the numerical slice methodology are plotted in Fig. 7.35. In the brace local frame, F_Z being negligible compared to F_X for the vertical brace Cent1, only the coefficients for F_X are plotted. The null coefficients obtained for the slices in air are not plotted.

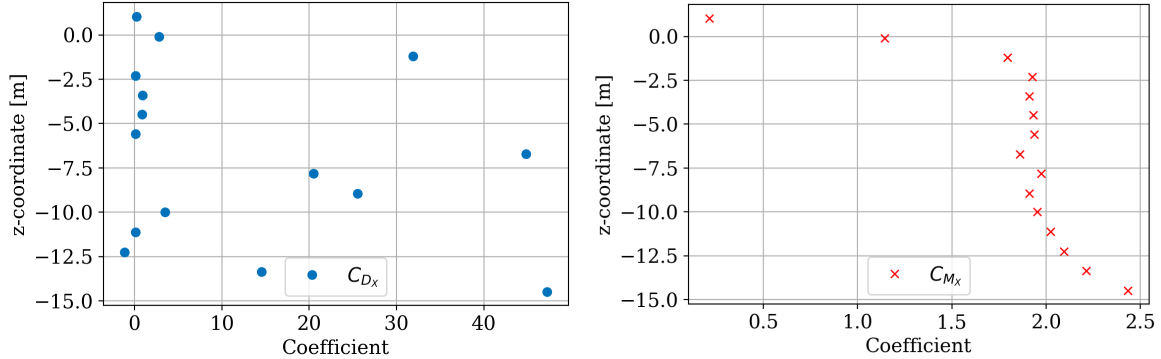

 Figure 7.35: Morison coefficients derived from CFD for Cent1 (C_{D_x} on the left, C_{M_x} on the right).

Fig. 7.35 shows that C_{D_x} is dispersed because of the small drag contribution ($-1.1 < C_{D_x} < 47.24$). C_{M_x} decreases approaching the interface: from 2.44 to 1.78 for submerged slices. This variation was not observed for Stansberg cylinder. It might be explained by the impact of the central buoy on the bottom of the brace. The C_{M_x} for the two interface slices ($C_{M_x} = 1.14$ and $C_{M_x} = 0.21$) are much smaller than for the submerged slices.

In Fig. 7.36 are plotted the Morison and CFD loads for one fully submerged slice (Fig. 7.36a) and one in the interface (Fig. 7.36b), the z -coordinates of the slice centres are indicated in the captions.

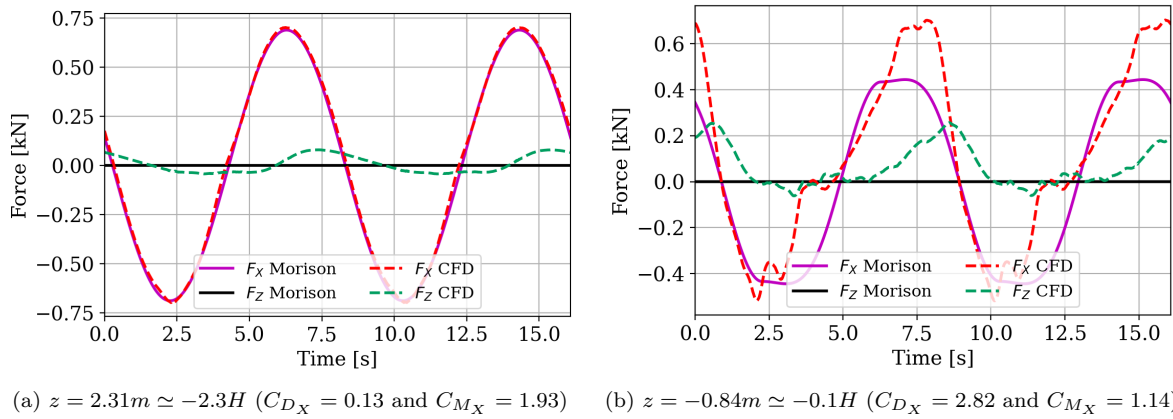


Figure 7.36: Morison and CFD loads for a submerged slice (on the left) and a slice in the interface (on the right).

C_{D_X} and C_{M_X} can be derived from the loads over a submerged slice and lead to a perfect prediction (cf. Fig. 7.36a). For the slice in the interface, the loads are rather non-linear and asymmetrical and fitting Morison with CFD is more complex (cf. Fig. 7.36b). Nevertheless, a difference for F_X of 7.8% between the Morison and CFD loads is obtained.

Again, the two different ways to derive Morison loads in the brace local frame are tested. A third method averages the slice coefficients over all the slices, including the ones in the interface.

- The wave loads on the brace using variable coefficients per slice are shown in Fig. 7.37.

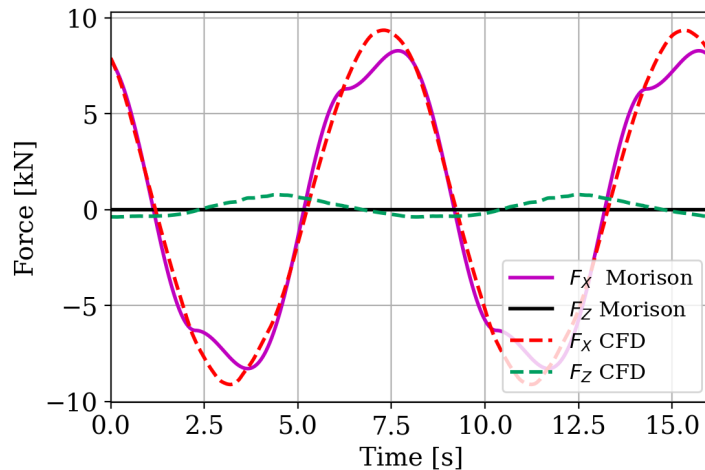
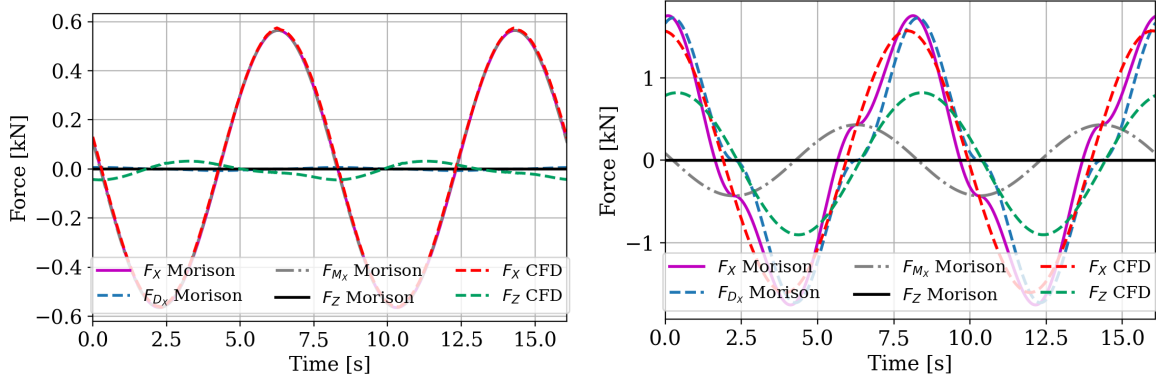


Figure 7.37: Morison prediction with variable coefficients for Cent1.

Morison formulation rather well predicts the total CFD load.

A small non-linear effect is visible around the crests and troughs of the force based on Morison coefficients. This non-linear effect is attributed to the pierced slices where there are interconnections with other braces, as observed for the horizontal

oriented brace Brac1 (cf. section 7.4.2). Fig. 7.38 presents loads for a not-pierced slice and a pierced slice, both submerged.



(a) $z = -5.59m \simeq -5.6H$ ($C_{D_X} = 0.13$ and $C_{M_X} = 1.94$) (b) $z = -6.71m \simeq -6.7H$ ($C_{D_X} = 44.8$ and $C_{M_X} = 1.87$)

Figure 7.38: Morison and CFD loads for a not-pierced slice (on the left) and for a pierced slice (on the right).

There is a good agreement between Morison and CFD loads on the entire slice (cf. Fig. 7.38a). For the pierced slice (cf. Fig. 7.38b), the non-linear effect is visible on F_X . It is explained by the extreme C_{D_X} value (44.8) that leads to a significant drag term in F_{D_X} .

We also observe from the CFD results that for the pierced slice, F_Z is significant compared to F_X as visible in Fig. 7.38b. This transverse force F_Z may be explained by the presence of the structure surrounding Cent1. This cannot be predicted by Morison formulation which only accounts for loads in line with the wave direction.

- The brace loads determined with the constant averaged coefficient (over only the submerged slices) ($C_{D_X} = 14.53$ and $C_{M_X} = 2$) are shown in Fig. 7.39.

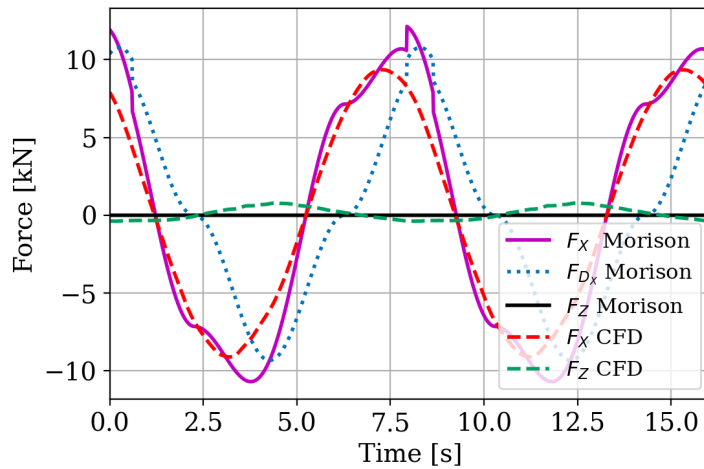


Figure 7.39: Morison prediction with constant averaged coefficients for Cent1.

A relative difference with CFD of 19.7% for F_X is obtained. This rather significant difference is explained by the discrepancies at the extrema as visible in Fig. 7.40. The large C_{D_X} value (to account for the interconnection effect) leads again to a significant drag term.

- The brace loads determined with the constant average coefficients over all the slices (including the slices in the interface) ($C_{D_X} = 12.8$ and $C_{M_X} = 1.82$) are shown in Fig. 7.40.

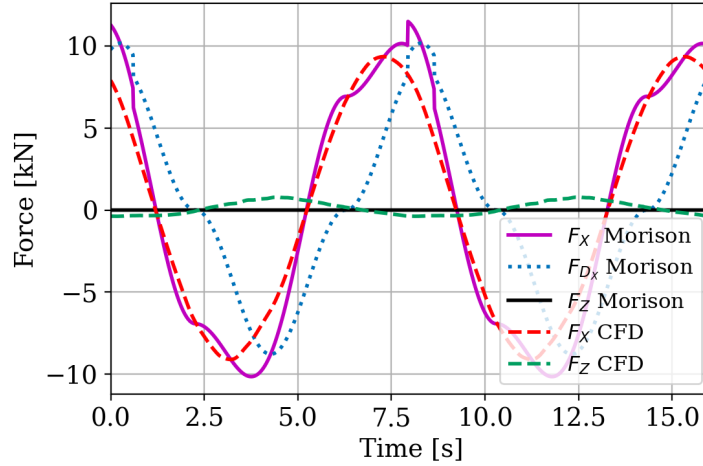


Figure 7.40: Morison prediction with constant averaged coefficients (including the slices in the interface) for Cent1.

Morison formula rather correctly predicts the phase and the load, with a relative difference of 14.2% compared to CFD. Thus including the coefficients for the slices in the interface in the average improves very slightly Morison prediction.

→ For Cent1, in agreement with the results on Stansberg cylinder, the interface has a very slight influence on the total load. We proved that Morison formula with the constant average coefficient (over the submerged slices) leads to a rather valid prediction of the CFD loads. For this particular brace, the interconnections with other braces have a strong influence, in agreement with previous observations.

Having analysed the interface influence on wave loads for Cent1, the wave loads on Trans2, also crossing the interface but inclined contrary to Cent1, are analysed in the following section.

7.5.2 Impact of the interface vicinity on an inclined vertical surface-piercing cylinder at the upstream of the floater, Trans2

Trans2 is an inclined brace, crossing the free-surface and located at the upstream part of the floater. It is coloured in Fig. 7.41.

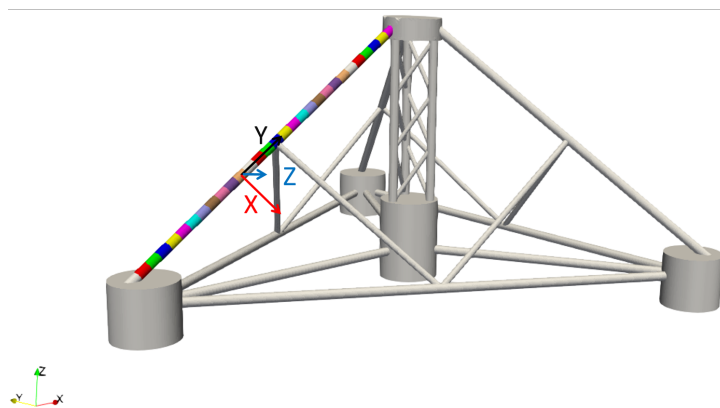


Figure 7.41: Trans2 in TLP

Fig. 7.42 compares the total load with the load of the submerged part of the brace in the global frame ($Oxyz$).

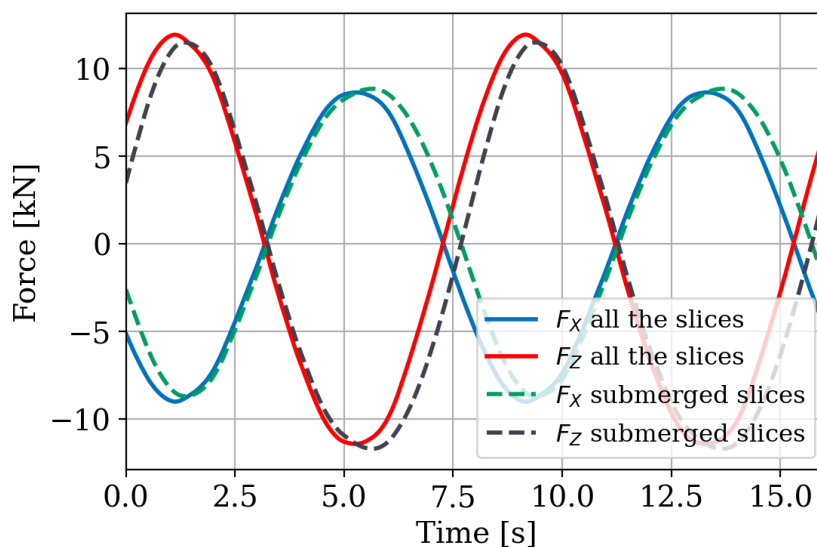


Figure 7.42: Influence of the interface on Trans2 at the brace level.

As observed for the vertical brace Cent1, the interface slightly influences the load amplitudes. However, the plots exhibit a slight difference on the shape of the load cycles that was not observed for Cent1. We will investigate further these differences at the slice level and by determining the coefficients and Morison loads.

In Trans2 local frame, F_Z is negligible compared to F_X because the brace is aligned with wave direction. Consequently, only C_{D_X} and C_{M_X} are derived for each slice and are shown in Fig. 7.43. The coefficients for the pierced slice and the extreme bottom slice are not plotted due to their outlying values (for the pierced slice at the centre of Trans2: $C_{D_X} = 31.59$ and $C_{M_X} = 8.37$, for the bottom slice: $C_{D_X} = 265.98$ and $C_{M_X} = 26.45$).

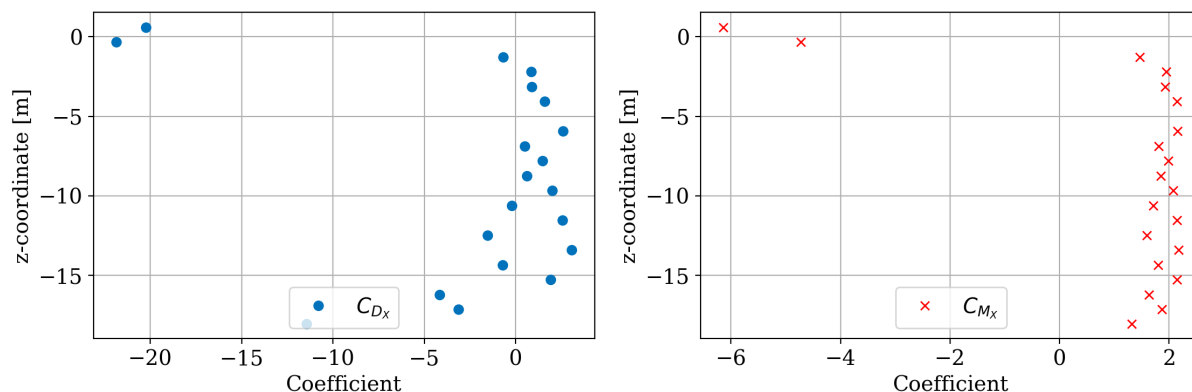


Figure 7.43: Morison coefficients derived from CFD for Trans2 (C_{D_x} on the left, C_{M_x} on the right).

Like the other braces, C_{D_x} is very dispersed along the brace due to the small contribution of the drag term. Fig. 7.43 highlights that C_{M_x} spreads on a wide range from 1.31 to 2.18. Trans2 seems to disturb locally the incoming flow. The coefficients obtained for the slices in the interface strongly differ compared to the submerged slices.

Indeed, for the three slices in the interface, the CFD loads F_x are highly non-linear and asymmetrical that leads to a rather rough fitting by Morison as shown in Fig. 7.44.

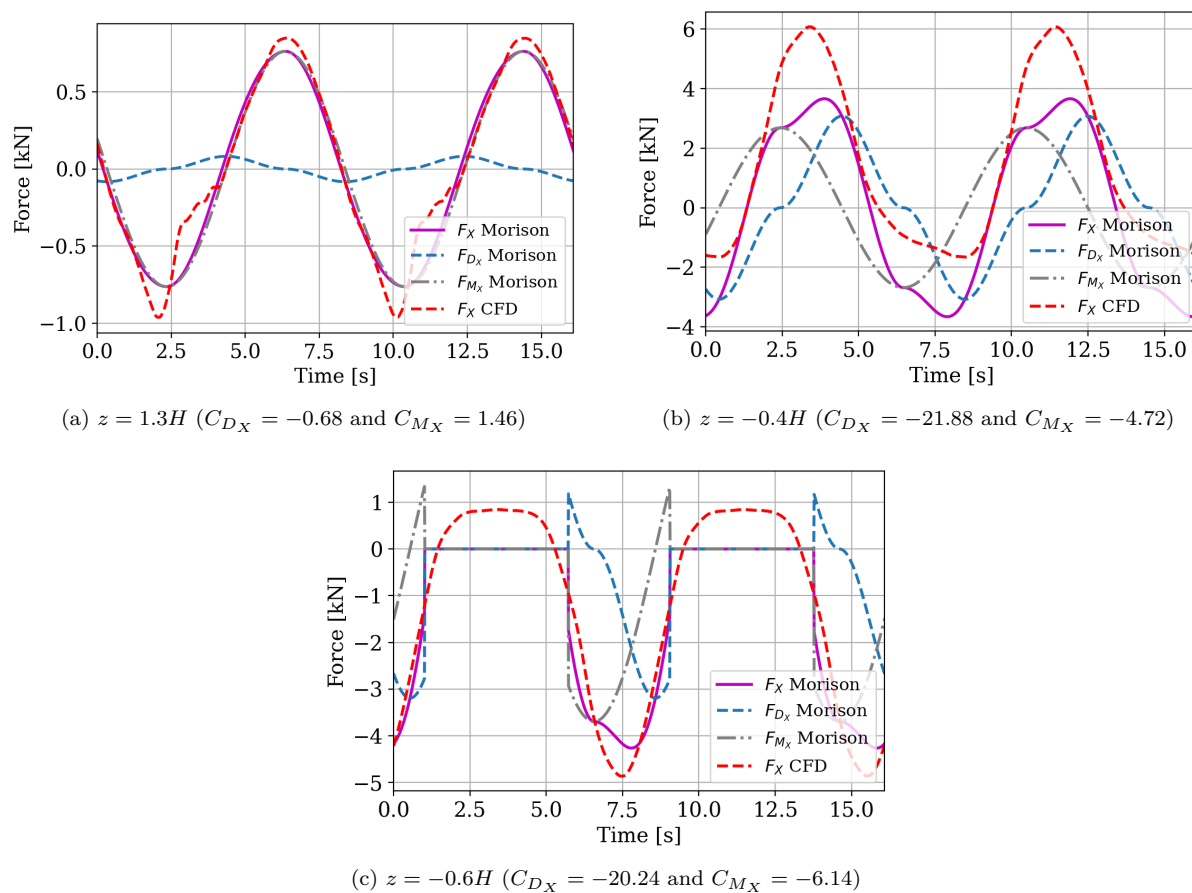


Figure 7.44: CFD and Morison F_x forces for the three slices in the interface for the oriented vertical surface-piercing brace Trans2.

Again, the two different ways to derive Morison loads in the brace local frame are tested. The third method averaging all the slice coefficients, including the slices in the interface is also tested. The results are presented in the brace local frame.

- The brace loads derived with Morison variable coefficients are shown in Fig. 7.45.

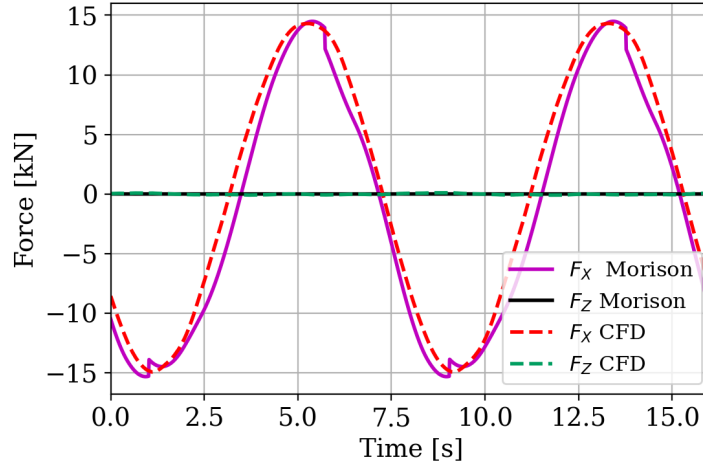


Figure 7.45: Morison prediction with variable coefficients for Trans2.

The amplitude of F_X determined by Morison equation only differs from CFD by -1% . Contrary to Brac1, the non-linear effects on the extrema, due to the interconnections, are negligible because Trans2 has only one pierced slices contrary to Brac1 pierced all along its length.

A difference in the shape of the load cycles between both models is observed, as it was observed on the CFD loads when comparing the total load and the submerged brace load (cf. Fig. 7.42). This is explained by the influence of the interface that is complex to predict applying Morison formula, originally developed for submerged cylinder.

- The brace loads determined with the constant averaged coefficient ($C_{D_X} = 1.46$, $C_{M_X} = 2.21$) are shown in Fig. 7.46.

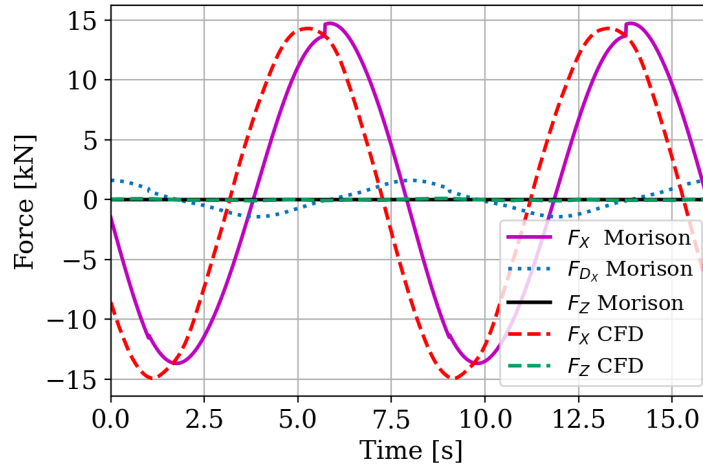


Figure 7.46: Morison prediction with constant averaged coefficients for Trans2.

Morison only underestimates the CFD F_X by -4.5% . However, a phase shift is observed between Morison and CFD forces.

- The brace loads determined with the constant coefficients averaged over all the slices ($C_{D_X} = -0.68$, $C_{M_X} = 1.49$) are shown in Fig. 7.47

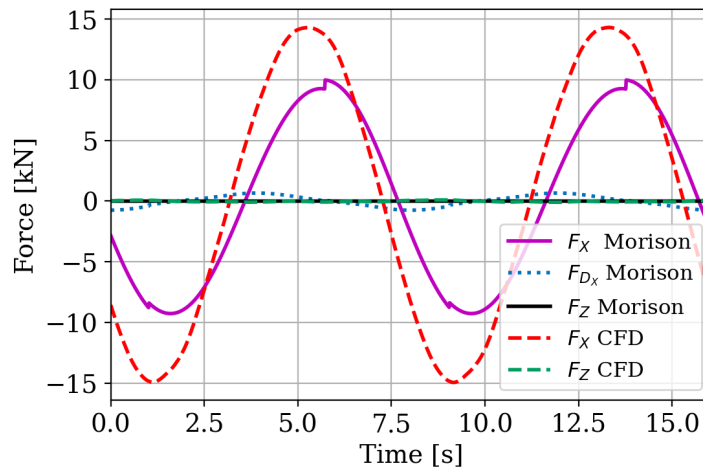


Figure 7.47: Morison prediction with constant averaged coefficients (including the slices in the interface) for Trans2.

With this coefficient setting, Morison approach underestimates F_X by 34.7% compared to the CFD and a phase shift is observed between Morison and the CFD loads. So taking into account in the average the coefficients derived for the slices in the interface leads to an inaccurate load prediction. This differs from the vertical brace Cent1 for which no significant differences were observed between the two constant averaged coefficients.

In conclusion, the interface slightly impacts wave load amplitude ($\simeq 3\%$). However, the interface impacts the CFD force period that cannot be correctly predicted applying Morison. Consequently, Morison prediction leads to a phase shift with CFD. This

is explained by the significant non-linear slice loads in the interface for the vertical and oriented brace Trans2, contrary to the vertical brace Cent1. From Cent1 and Trans2 analysis, we choose to only keep the submerged slices for the constant averaged coefficients, as for Stansberg cylinder case (cf. section 6.2.3).

7.5.2.1 Impact of the interface vicinity on an inclined vertical surface-piercing cylinder at the downstream part of the floater, Trans3

Similar results are obtained for Trans3, an inclined surface-piercing brace like Trans2 but on the lateral side of the TLP, as visible in Fig. 7.13. The loads determined in the brace local frame from Morison formulation with the constant averaged coefficient (over submerged slices only, ($C_{D_X} = 1.56$, $C_{M_X} = 2.09$, $C_{D_Z} = 0.71$ and $C_{M_Z} = 1.84$)) are compared to the CFD results in Fig. 7.48 .

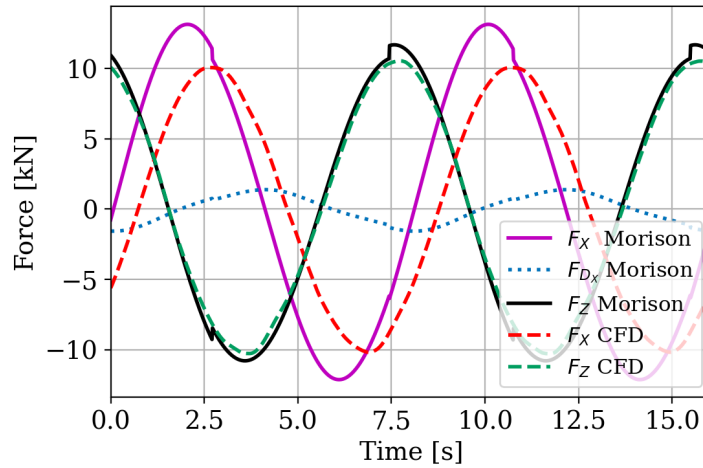


Figure 7.48: Morison prediction with constant averaged coefficients for Trans3.

As for Trans2, a phase shift caused by the interface prevents from correctly fitting in time F_X . Also a difference of 24% is observed on F_X amplitude. On the contrary, Morison correctly perfectly predicts F_Z (relative difference with CFD of 7%) with non-linearities on the extrema explained by the interconnections.

→ As for the Stansberg case, Morison formulation can hardly predict local load within the free-surface area. But since this contribution remains small compared to the total load, using average coefficients over the submerged part of the brace in the Morison formulation provide rather good load amplitude predictions. Deviations from the Stansberg case are observed, either due to the structure complexity (pierced slices) or to the brace orientation. The latter is investigated further in the section 7.6.

⇒ We have seen at the brace and at the slice scales the impact of the interconnections (Brac1, Cent1), of the vicinity with large structure (Brac12) and with the interface (Cent1, Trans2) on loads and on their prediction with Morison formulation. In the following section, we will compare the Morison prediction to the CFD loads at the scale of groups of braces.

7.6 Impact of the structure and the free-surface at the brace group level

Here we investigate the impact of the interconnections and the interface at the brace group level for the three waves w1, w2 and w3. The brace groups that are considered are: Braci, Brac1i, Centi and Transi represented in Fig. 7.8. The loads are given in the global frame ($Oxyz$)

The brace loads are predicted using the variable coefficients or the constant averaged coefficients (cf. section 7.3).

Regarding the loads on the braces that have not been investigated before (Brac3, Cent2, Trans1 cf. Fig. 7.13), the Morison coefficients are the same as the ones for their symmetric counterparts (Brac1, Cent3, Trans3).

7.6.1 Analysis for the small wave w1

First, we focus on the results obtained with wave w1 for which the hydrodynamic analysis at the brace/slice level was previously conducted. Tab. 7.49 presents the predicted loads, using the variable coefficients or constant averaged coefficients, for the brace groups: Braci, Brac1i, Centi and Transi. The constant averaged coefficients are detailed in Tab. 7.8.

7.6. IMPACT OF THE STRUCTURE AND THE FREE-SURFACE AT THE BRACE GROUP LEVEL

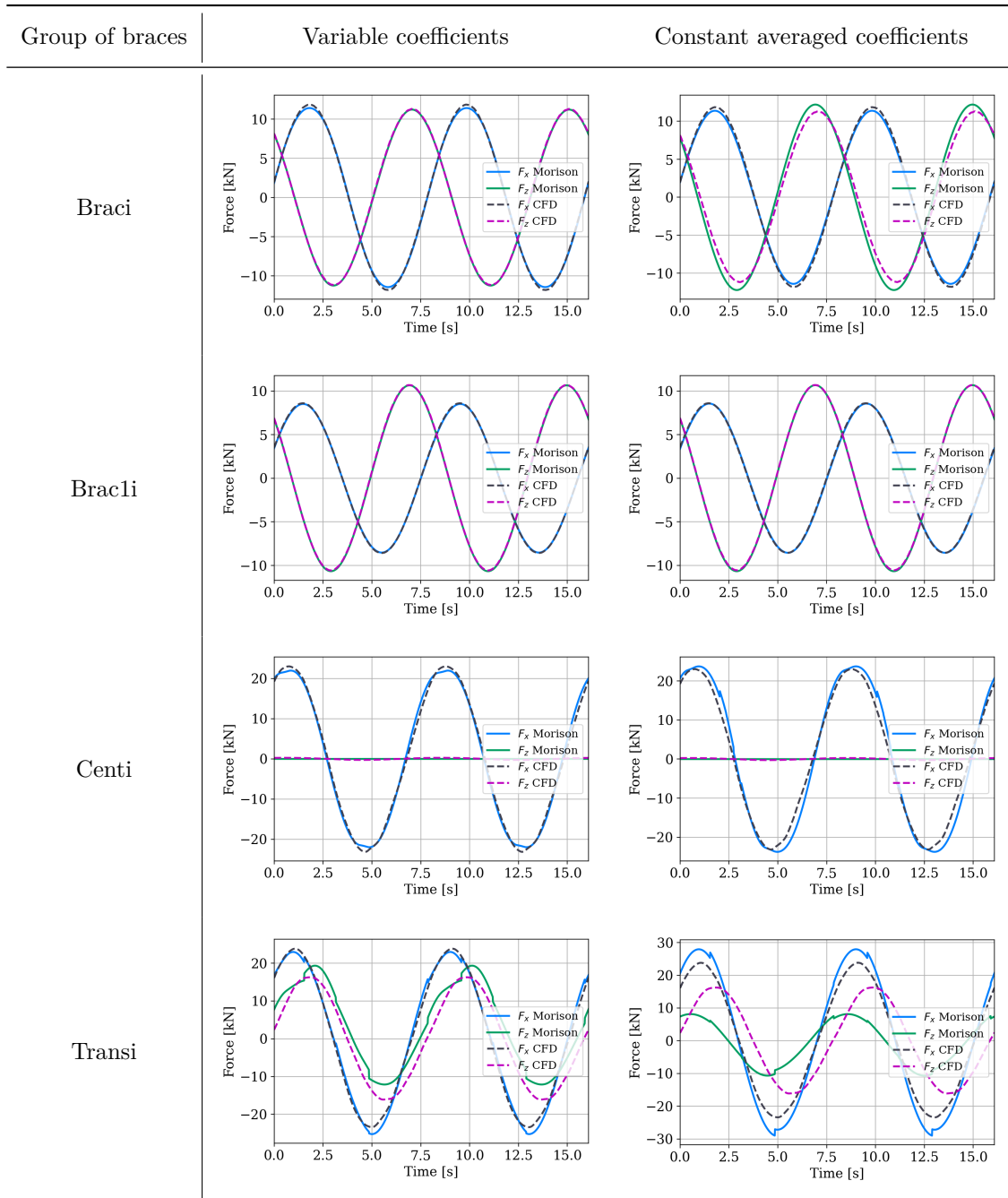


Figure 7.49: Morison and CFD forces at the brace group level (wave w1).

Brace	C_{D_x}	C_{M_x}	C_{D_z}	C_{M_z}
Brac1	10.74	1.93	1.91	1.67
Brac2	-0.64	1.95	2.16	1.59
Brac12	0.00	0.00	1.24	2.08
Brac13	2.45	2.02	2.47	1.96
Cent1	14.53	2.00	0.00	0.00
Cent2	-24.33	2.07	3.68	2.25
Trans2	1.46	2.21	0.00	0.00
Trans3	1.56	2.09	0.74	1.84

Table 7.8: Constant averaged coefficients (wave w1).

For Braci, results are in good agreement with the observations on Brac1. Match is very good with the variable coefficients. The forces derived with the constant averaged coefficients differ by -3.9% for F_x and by 8.8% for F_z relative to CFD.

For Brac1i, the two coefficient methods leads to a perfect load prediction applying Morison formula. This was expected because we observed, at the brace level, that the influence of the buoys at the extremities of the braces was correctly predicted using the constant averaged coefficients.

For Centi, the two methods lead to similar loads between Morison and CFD. At the brace level, we observed non-linear effects on the crests and troughs of the force predicted by Morison in the brace local frame. They were attributed to the pierced slices. Here, at the brace group level in the global frame, it seems that these non-linear effects are cancelled, maybe due to the symmetry of the braces.

For horizontal loads on Transi, using the constant averaged coefficients overestimates F_x by 21% and underestimates F_z by 46% . A phase shift between Morison and CFD loads is also observed for F_z . This is explained by the strong non-linear effects observed on CFD loads at the interface (as illustrated in Fig. 7.44) that impact the total load amplitude and phase and that cannot be correctly predicted by Morison.

⇒ From these results, we conclude that the constant averaged coefficients enable Morison formula to correctly predict the wave loads. Some difficulties remain when applying Morison formulation to predict the loads on the group Transi (inclined braces crossing the free surface).

This analysis is extended to wave w2, which has the same period as wave w1 but a five time larger height.

Are these observations also noticed for wave w2?

7.6.2 Analysis for the higher wave w2

Tab. 7.50 presents the predicted group loads for wave w2 using variable coefficients or constant averaged coefficients detailed in Tab. 7.9.

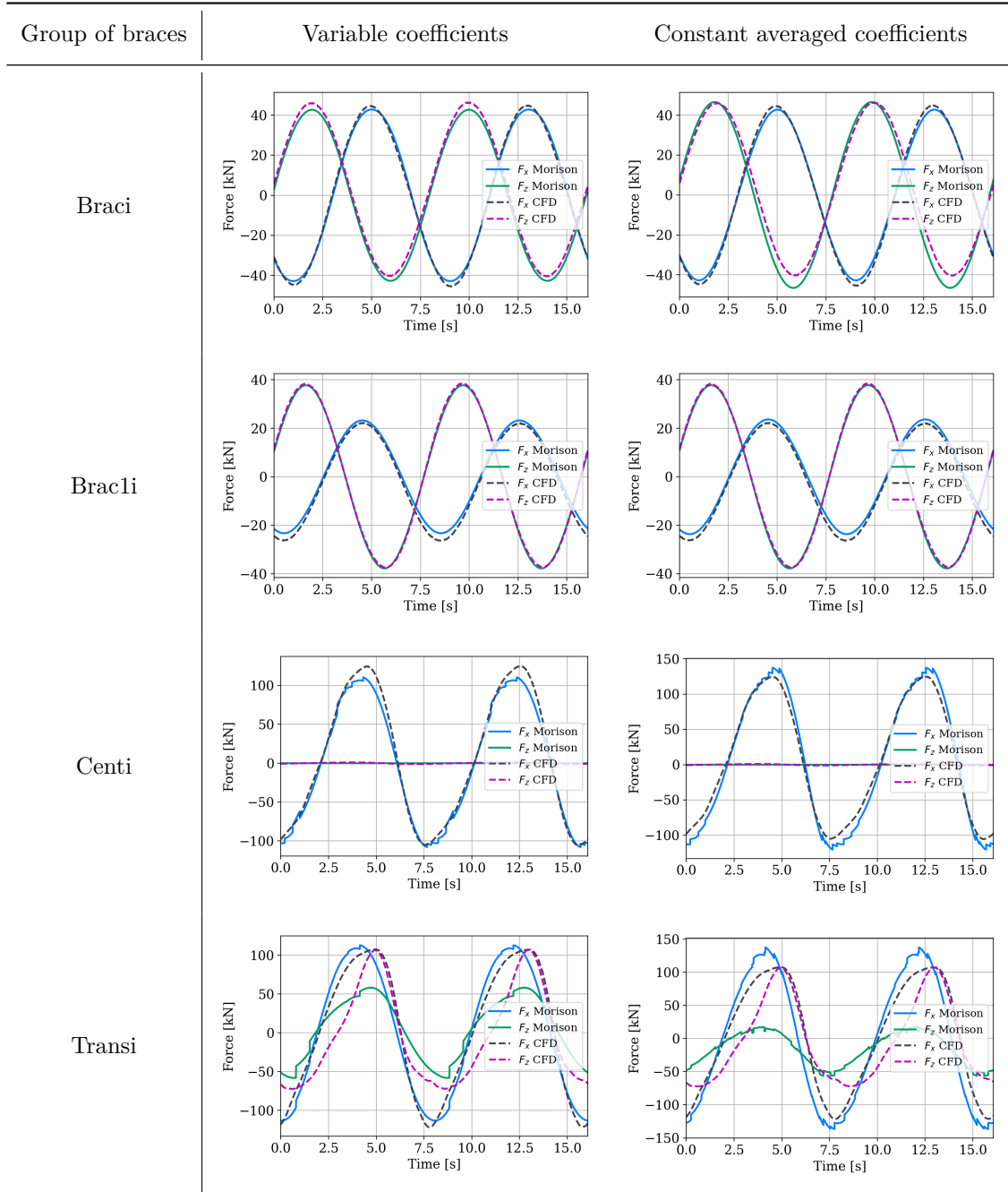


Figure 7.50: Morison and CFD forces at the brace group level (wave w2).

Brace	C_{D_x}	C_{M_x}	C_{D_z}	C_{M_z}
Brac1	1.74	0.65	-0.27	1.35
Brac2	-0.84	1.39	-0.13	1.04
Brac12	0.00	0.00	-0.76	2.07
Brac13	-0.28	1.11	-0.29	1.29
Cent1	2.78	2.30	0.00	0.00
Cent2	-4.40	1.17	1.19	2.35
Trans2	0.03	2.30	0.00	0.00
Trans3	0.03	1.87	-0.46	1.51

Table 7.9: Constant averaged coefficients (wave w2).

Similarly to wave w1, for Braci the constant averaged coefficients enable a good prediction of the loads with a relative difference of only 8% for F_z .

The two coefficient methods lead to a good fitting between Morison and CFD for Brac1i. As observed for w1, the effects of the side buoys on the extremities of the braces Brac1i is included in the constant average coefficients and thus in Morison prediction.

For Centi, Morison fits rather well with the CFD though the braces are pierced and crossed by the interface. Non-linear effects are visible on Morison peaks and troughs contrary to wave w1. This is attributed to the complex fitting of Morison with CFD for the loads in the interface. This interface has a stronger influence on the force prediction for wave w2 than wave w1 on Centi, w2 having a five time larger height. Also, the CFD F_x is no longer symmetrical, again explained by the loads in the interface that are asymmetrical.

For Transi, similar conclusions are obtained with wave w2 than wave w1. F_x is rather well predicted by Morison but important differences remain between Morison and CFD for F_z . Thus the difficulty to fit Morison with CFD for the vertical load does not depend on the wave height. It seems that Morison formula cannot correctly predict the vertical load on the vertical and oriented braces Transi, independently of the wave conditions.

7.6.3 Analysis for the design wave for turbine park conditions w3

Tab. 7.51 presents the predicted group loads for wave w3 using variable coefficients or constant averaged coefficients detailed in Tab. 7.10.

7.6. IMPACT OF THE STRUCTURE AND THE FREE-SURFACE AT THE BRACE GROUP LEVEL

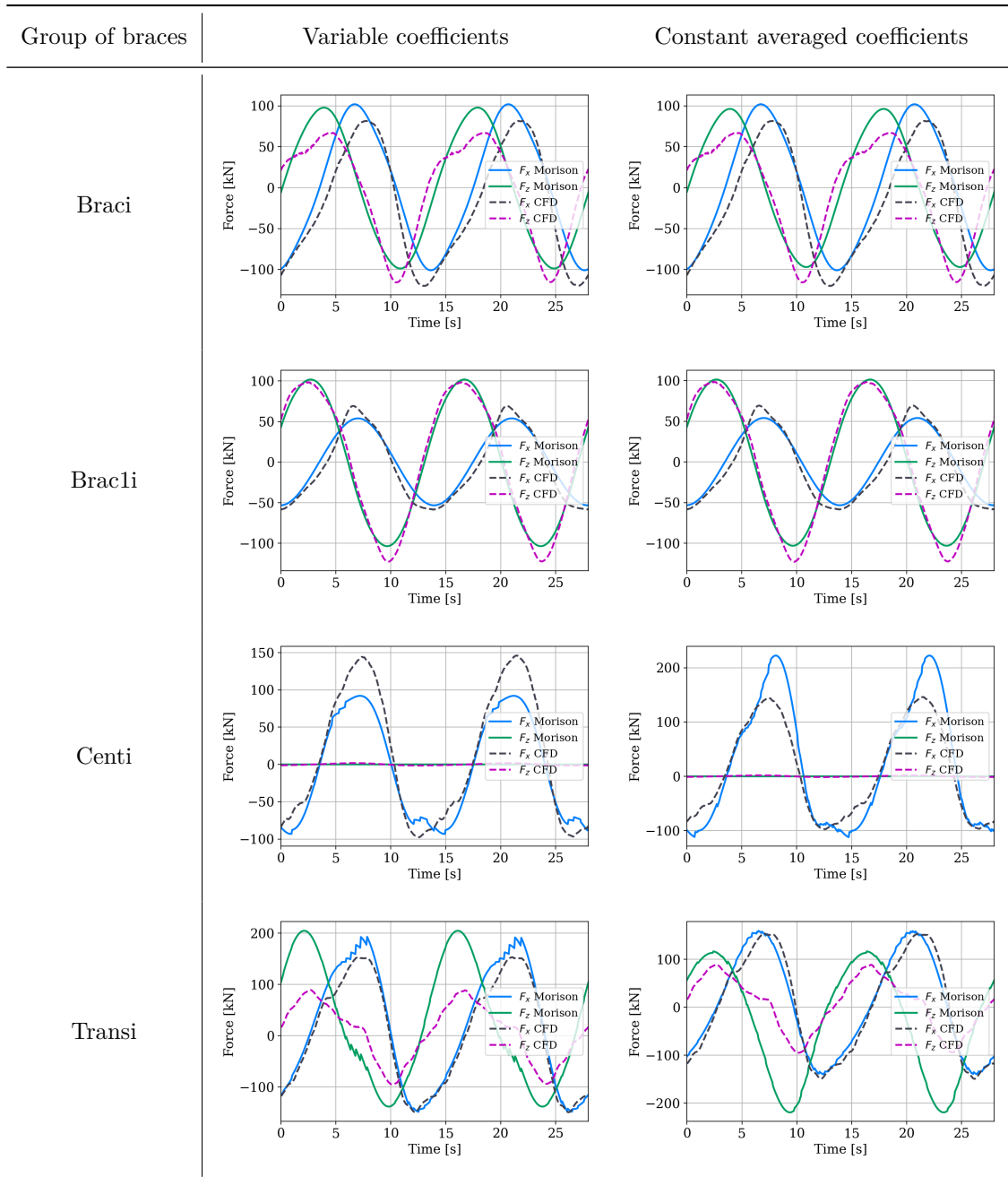


Figure 7.51: Morison and CFD forces at the brace group level (wave w3).

Brace	C_{D_x}	C_{M_x}	C_{D_z}	C_{M_z}
Brac1	1.70	0.83	0.38	0.63
Brac2	0.11	1.42	0.59	0.68
Brac12	0.00	0.00	0.45	2.12
Brac13	0.54	1.37	0.46	1.42
Cent1	4.17	2.04	0.00	0.00
Cent2	-5.38	1.62	1.97	2.15
Trans2	0.77	3.31	0.00	0.00
Trans3	0.11	3.28	0.31	1.40

Table 7.10: Constant averaged coefficients (wave w3).

For Braci, the CFD loads are asymmetrical and the signal has no longer a perfect sinusoidal shape as for wave w1 and w2. We notably observe that the loads on Brac2, the upstream horizontal brace perpendicular to the flow direction (cf. Fig. 7.13), are highly non linear. This can be explained by the significant impact of the structure on the incoming flow on Brac2. Still, Morison formula predicts rather well the loads on Braci. Similar conclusions are obtained for Brac1i.

For Centi, significant differences on F_x force exist between CFD and Morison. This can be attributed to the impact on the loads of the interconnections and the interface, much stronger with wave w3 than with wave w1 and w2.

Surprisingly, Morison horizontal loads on Transi fit rather well with CFD but the vertical CFD load is not accurately predicted as we observed for wave w2 and w3.

To conclude, for wave w3, the impact of the structure (interconnections and local flow disturbance by buoys and braces) combined with the influence of the interface makes Morison fitting rather complex with CFD, particularly for the brace crossing the interface.

⇒ The constant averaged coefficients enable Morison to correctly fit the CFD for Braci, Brac1i and Centi with wave w1 and w2. We highlighted some limitations of Morison formula to predict the vertical loads on the Transi braces, strongly influenced by the air/water interface. With wave w3, we stand at the limit of the applicability of Morison formula because of the complex combination of the impact of the structure and the interface on the wave loads.

The following section focuses on the impact of the brace orientations on the wave loads.

7.7 Impact of the brace orientations varying the wave characteristics

The idealised conditions in which Morison coefficients were derived (isolated and submerged cylinder with a cross flow orientation in an oscillating and uniform velocity field) are quite far from realistic conditions: interaction with other cylinders and the free-surface, inclined orientation, moving structure within a complex wave field. The present study investigates the effect on the loads of a few of these realistic conditions.

In the proposed numerical slice methodology, we take into account the orientation of the braces. Two force components in the plane perpendicular to the brace axis are considered. Consequently four coefficients, C_{Dx} , C_{Mx} , C_{Dz} and C_{Mz} , are determined. Such a calculation is uncommon, Morison approach was originally developed for horizontal/vertical cylinders with only one force component.

To investigate the influence of the brace orientation, we focus on two slices in two oriented braces: Brac1 located in a horizontal plane and Trans2 included in a vertical plane parallel to the flow direction. The selected slices are always submerged, not-pierced and not located at the brace extremity in order to ease the analysis. Morison coefficients are derived from the CFD loads for the three waves w1, w2 and w3. The loads are always plotted in the brace local frame in this section.

The KC number for wave w3 (a design wave for a turbine parked) is much larger than for wave w1 and w2 (cf. Tab. 7.11) and the contribution of the Morison inertia and drag terms may significantly differ from wave w1 and w2. The KC for the two slices are determined based on the maximum velocity at the centre of the slice and provided in Tab. 7.11.

Wave	KC (slice 3 of Brac1)	KC (slice 5 of Trans2)
w1	0.63	1.02
w2	3.17	5.09
w3	15.16	17.65

Table 7.11: KC number for the two slices and the three wave conditions.

7.7.1 Impact of the brace orientation on the loads for an oriented horizontal submerged brace, Brac1

First we focus on the slice number 3 in the oriented horizontal submerged Brac1 highlighted in Fig. 7.52.

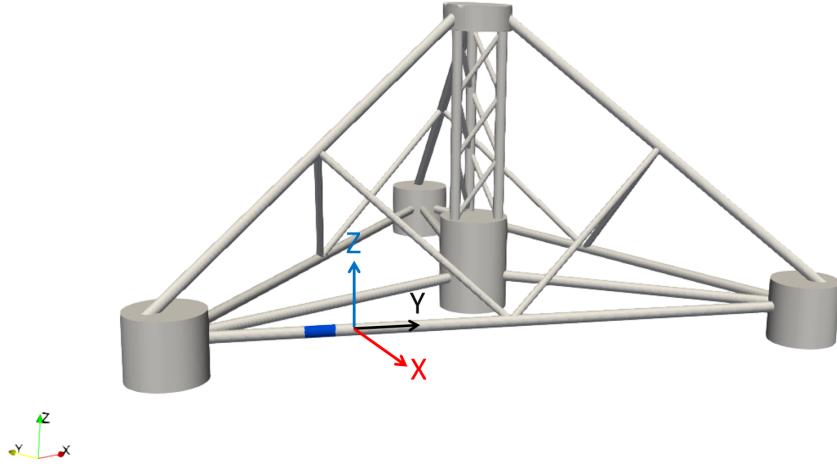


Figure 7.52: Slice 3 in Brac1 in TLP

The directional coefficients are derived from the CFD loads for the 3 waves and listed in Tab. 7.12. The Reynolds number is determined at model scale.

Wave	C_{D_x}	C_{M_x}	C_{D_z}	C_{M_z}	KC	Re (MS)
w1	1.93	1.92	1.94	1.99	0.63	5×10^2
w2	-0.53	0.32	-0.37	1.67	3.17	3×10^3
w3	0.56	0.91	0.34	1.51	15.16	7×10^3

Table 7.12: Morison coefficients derived from CFD for slice 3 in Brac1 for the three waves.

Boccotti [2014] determined Morison coefficients from experimental loads on a submerged horizontal cylinder for a wide range of KC values between 3 and 30 ($2.5 \times 10^4 < Re < 2 \times 10^5$). The Reynolds number for the CFD cases are 10-100 times smaller than in Boccotti's experiments. We first investigate this difference focusing on Brac12. Brac12 is a submerged horizontal brace and inline with the wave direction, like the cylinder in Boccotti's experiments. The constant averaged coefficients for Brac12 are added to Boccotti's plots in Fig. 7.53.

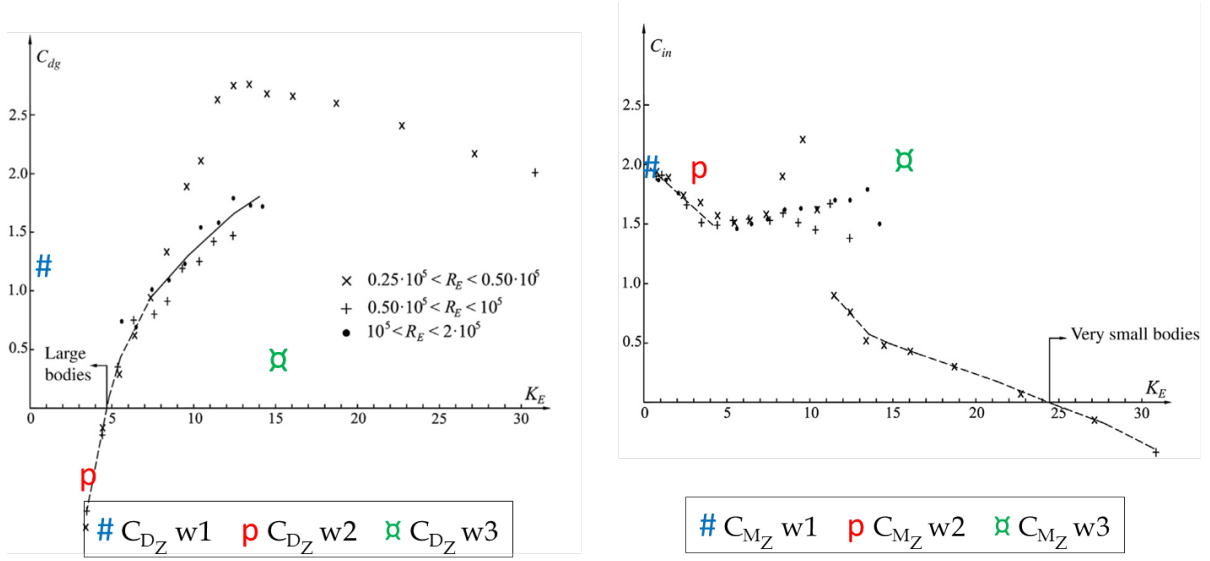


Figure 7.53: C_{D_Z} (left side) and C_{M_Z} (right side) for the horizontal and submerged Brac12 added on Boccotti's plots.

The inertia coefficient for the three waves fit well with Boccotti's coefficients. The differences for the drag coefficients are explained studying the oriented braces but are not attributed to the Reynolds differences. Thus for the following analyses, the coefficient differences between CFD and Boccotti's cases cannot be explained by the different Reynolds numbers.

We add on Boccotti's plots C_{D_X} , C_{M_X} , C_{D_Z} and C_{M_Z} derived from the CFD loads on slice 3 in Brac1 (Fig. 7.54).

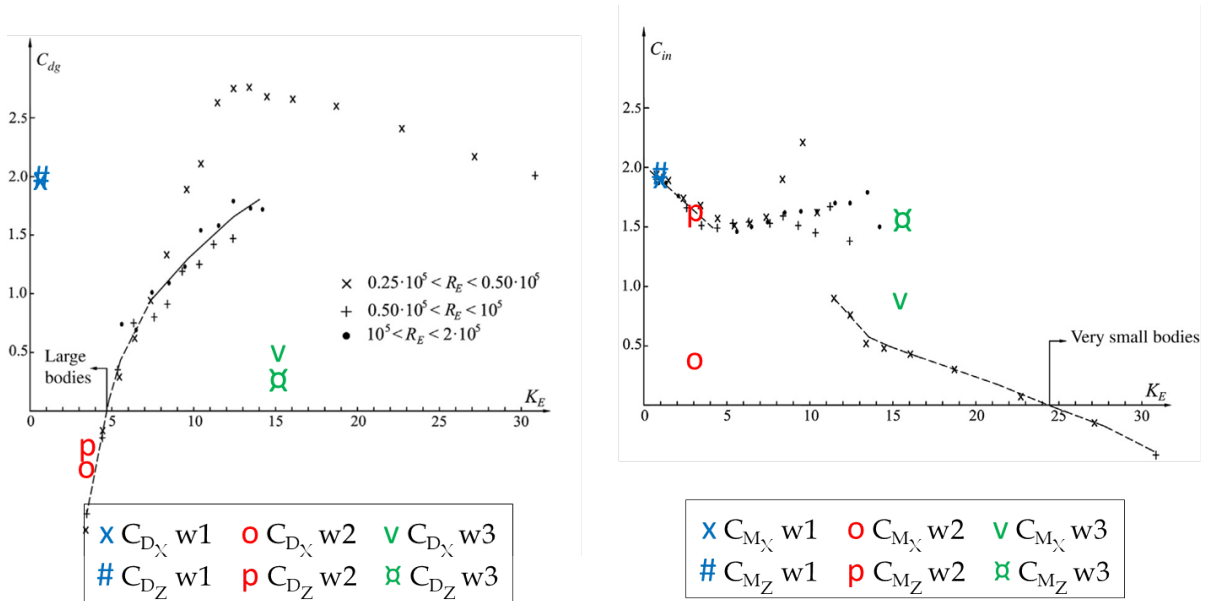


Figure 7.54: C_{D_X} , C_{D_Z} (left side), C_{M_X} and C_{M_Z} (right side) for slice 3 in the oriented horizontal submerged Brac1 added on Boccotti's plots.

We observe that the predicted C_{M_Z} are consistent with C_M Boccotti's values maybe

due to the fact that both are derived from vertical loads. The C_{M_X} values fit worse with Boccotti's C_M , especially for the C_{M_X} obtained for wave w2. C_{M_X} is derived on the extended direction of Morison formula ΩX that might explain the differences between Boccotti and CFD results.

On the contrary, C_{D_X} and C_{D_Z} both differ from Boccotti results apart from the coefficients for wave w2. For wave w1, it may be explained by the negligible drag term in Morison force leading to high uncertainties in the estimation of the drag coefficients (cf. section 7.4.2).

Here we can notice that negative values of C_{D_X} and C_{D_Z} can be obtained for wave w2, but are consistent with Boccotti's results. According to Boccotti, for KC smaller than 5, the drag term is negligible and that can explain the negative values of C_D . Indeed, for wave w2, we observe in the local frame (ΩXYZ) in Fig. 7.55 that F_{D_X} and F_{D_Z} have a negligible impact on F_X and F_Z amplitude.

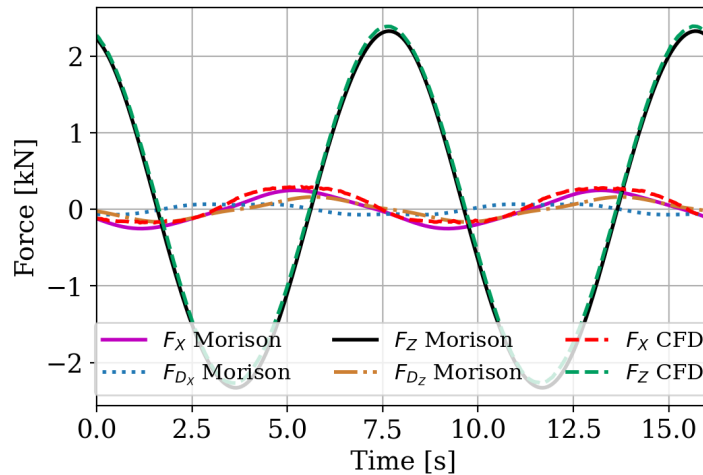
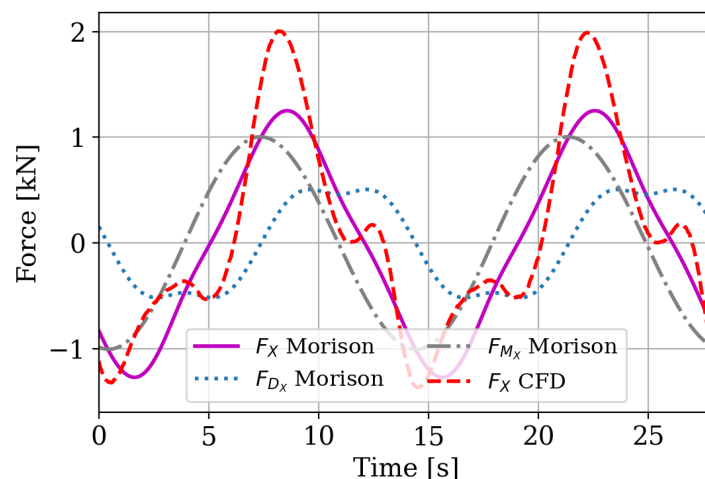
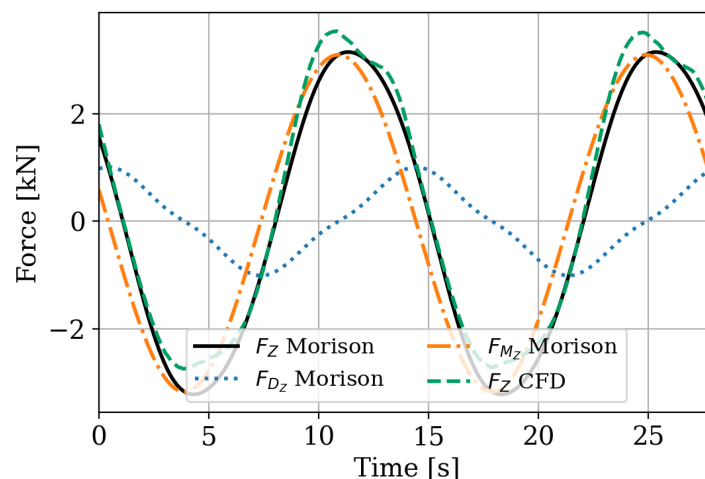


Figure 7.55: CFD and Morison loads on slice 3 in Brac1 (wave w2).

Regarding wave w3, in the local frame (ΩXYZ), F_X derived from CFD is highly non-linear and asymmetrical (contrary to F_Z) as visible in Fig. 7.56. Morison forces are generally symmetrical because they depend on symmetrical Stokes velocity/acceleration signals. Thus Morison prediction of asymmetrical load is subjected to high uncertainties.

Figure 7.56: F_X force on slice 3 in Brac1 (wave w3).

Regarding F_Z for wave w3, Morison prediction seems rather consistent with CFD results as visible in Fig. 7.57. F_{D_Z} amplitude is not negligible anymore, like F_{D_X} , compared to wave w1.

Figure 7.57: F_Z force on slice 3 in Brac1 (wave w3).

→ The coefficients derived with the three waves does not always follow the trend of Boccotti [2014] coefficient variations with the KC. It seems complex to predict the adapted coefficients for the oriented braces with experiments commonly used in standards for offshore design.

7.7.2 Impact of the brace orientation on the loads determined on a slice within an oriented vertical surface-piercing brace, Trans2

We now focus on the slice 5 in Trans2, located in a vertical plane parallel to the flow direction and highlighted in Fig. 7.58.

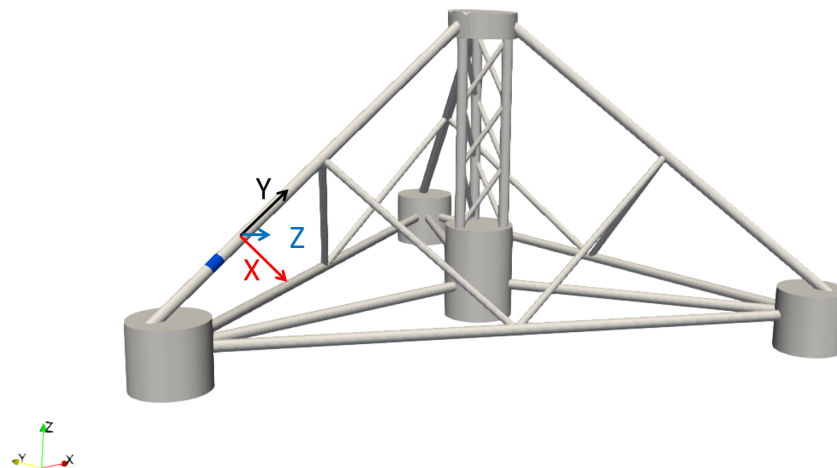


Figure 7.58: Slice 5 in Trans2 in TLP

The directional coefficients are determined from the CFD loads for the three different waves (Tab. 7.13). For all the waves, F_Z is negligible compared to F_X , so only C_{D_X} and C_{M_X} are determined.

Wave	C_{D_X}	C_{M_X}	KC	Re (MS)
w1	-0.72	1.8	1.02	8×10^2
w2	-0.77	1.52	5.09	4×10^3
w3	0.46	2.33	17.65	8×10^3

Table 7.13: C_{D_X} and C_{M_X} derived from CFD loads for slice 5 in Trans2.

To compare with experiments generally used in standard for design, the Morison directional coefficients derived from CFD are compared with Chakrabarti et al. [1976] results who determine Morison coefficients from experimental loads on a vertical submerged cylinder in waves ($Re = 2.8 \times 10^4$, $D = 76$ mm). The coefficients derived from CFD are included into Chakrabarti's graph in Fig. 7.59. The Reynolds number derived for the three waves is 10 times smaller than Chakrabarti's Reynolds.

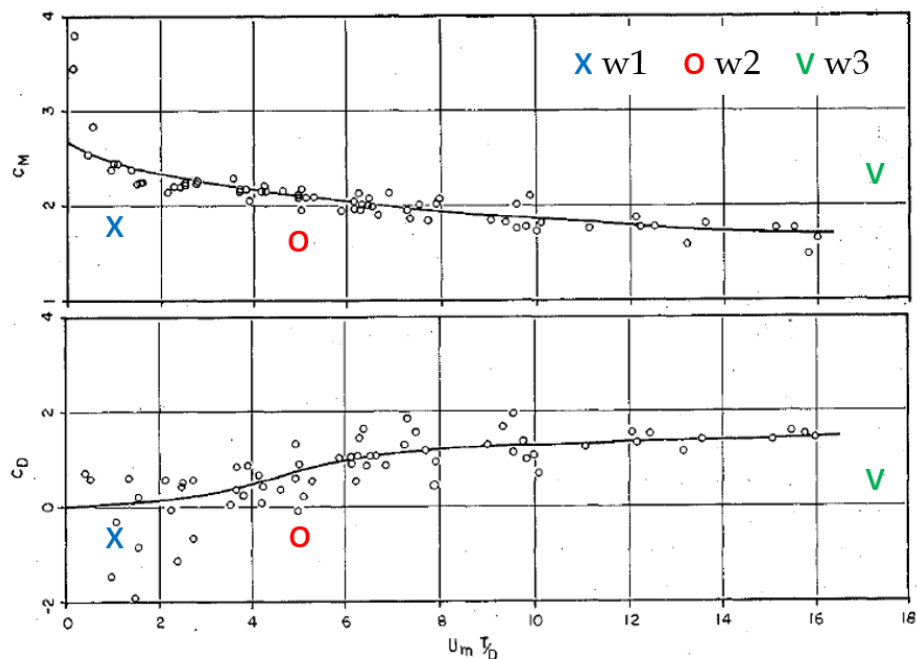


Figure 7.59: C_{M_X} (at the top) and C_{D_X} (at the bottom) derived from CFD loads on slice 5 in Trans2 reported in Chakrabarti et al. [1976].

For the three waves, the CFD coefficients significantly differ from Chakrabarti et al. [1976] coefficients. Such differences may be explained by the orientation of the brace Trans2. Though they differ from Chakrabarti's results, the determined C_{D_X} and C_{M_X} lead to a good agreement between Morison prediction and the CFD results. For instance, dealing with wave w3, the Morison and the CFD loads slightly differ as shown in Fig. 7.60.

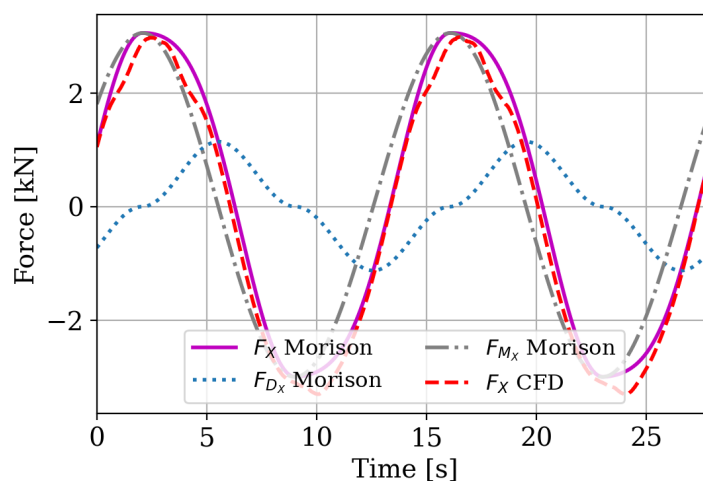


Figure 7.60: F_X derived from Morison ($C_{D_X} = 0.51$ and $C_{M_X} = 2.32$) and CFD for slice 5 in Trans2 (wave w3).

→ We have seen that the directional coefficients derived from CFD are consistent with the experimental standards on horizontal cylinders that are commonly used during design process to set the Morison coefficients. The inconsistency can come from the inclined position of the brace in the present study, the wave field represented on two

directions (versus inline oscillating flow).

Imposing directional coefficient seems to be necessary to correctly predict the wave loads on the oriented brace. However, in design tools, only one drag and one inertia coefficients are commonly applied to calculate the directional forces. So is it possible to consider the brace orientation in the definition of Morison coefficients used in design tools?

7.7.3 A attempt to consider brace orientation in the determination of Morison coefficients used for design purposes

Here we investigate how we can apply Morison formula with one identical set of coefficients (C_D, C_M) whatever the brace orientation. $C_{D_x}, C_{M_x}, C_{D_z}$ and C_{M_z} are the constant averaged coefficients. We proved several times in the past sections that imposing such directional coefficients in Morison formula leads to a correct prediction of the CFD loads. We test different methods to determine C_D and C_M :

- The simple average as (Eq. 7.1):

$$C_D = \frac{C_{D_x} + C_{D_z}}{2} \quad C_M = \frac{C_{M_x} + C_{M_z}}{2} \quad (7.1)$$

- The magnitude as (Eq. 7.2):

$$C_D = \sqrt{C_{D_x}^2 + C_{D_z}^2} \quad C_M = \sqrt{C_{M_x}^2 + C_{M_z}^2} \quad (7.2)$$

- The weighted average as (Eq. 7.3):

$$C_D = \frac{C_{D_x} F_{D_x} + C_{D_z} F_{D_z}}{F_{D_x} + F_{D_z}} \quad C_M = \frac{C_{M_x} F_{D_x} + C_{M_z} F_{D_z}}{F_{M_x} + F_{D_z}} \quad (7.3)$$

where $F_{D_x}, F_{D_z}, F_{M_x}, F_{M_z}$ are the predicted Morison inertia and drag load amplitudes on the brace.

The three methods are tested on Brac1 for wave w1, w2 and w3. The corresponding coefficients are detailed in Tab. 7.14. The constant averaged coefficients $C_{D_x}, C_{M_x}, C_{D_z}$ and C_{M_z} are indicated in Tab. 7.8, Tab. 7.9 and Tab. 7.10 for respectively wave w1, w2 and w3

Wave	Simple average		Magnitude		Weighted Average	
	C_D	C_M	C_D	C_M	C_D	C_M
w1	6.31	1.8	10.9	2.55	7.83	1.76
w2	0.74	1	1.76	1.5	1.14	1.22
w3	1.04	0.73	1.74	1.05	1.23	0.71

Table 7.14: C_D and C_M derived from the constant directional averaged coefficients C_{D_x} , C_{M_x} , C_{D_z} and C_{M_z} with three methods for the three waves w1,w2 and w3.

C_M s obtained with the simple average or weighted average are similar apart for wave w2 (difference of 20%). This difference was expected because C_{M_z} is the double of C_{M_x} for wave w2. The coefficients determined with the magnitude are larger compared to the simple and weighted averages.

The forces derived in the brace local frame for wave w1, w2 and w3 using the three coefficient methods are shown respectively in Fig. 7.61, Fig. 7.62 and Fig. 7.63. The force derived with the four directional constant averaged coefficients is added for comparison.

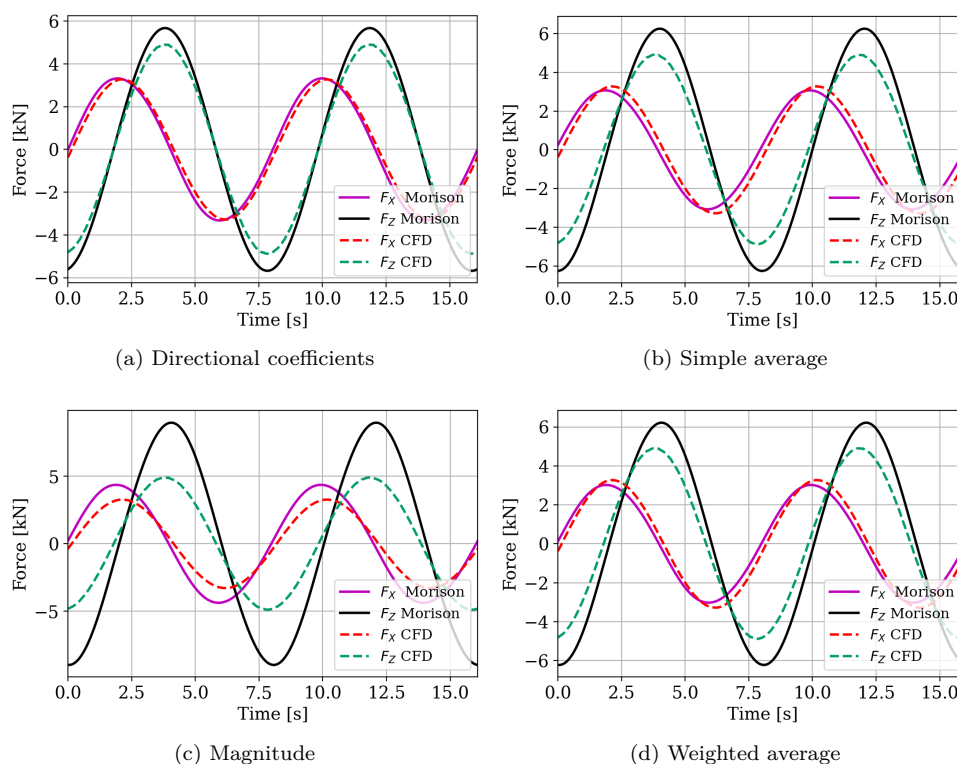


Figure 7.61: Morison prediction with C_D and C_M determined with the three methods for Bracl1 (wave w1).

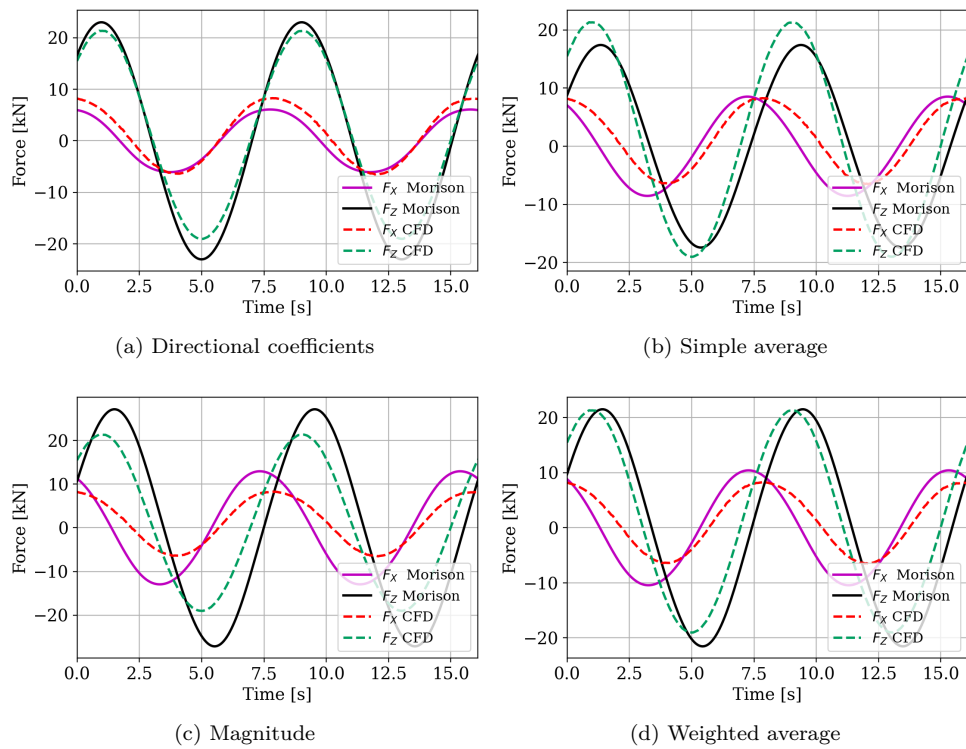


Figure 7.62: Morison prediction with C_D and C_M determined with the three methods for Brac1 (wave w2).

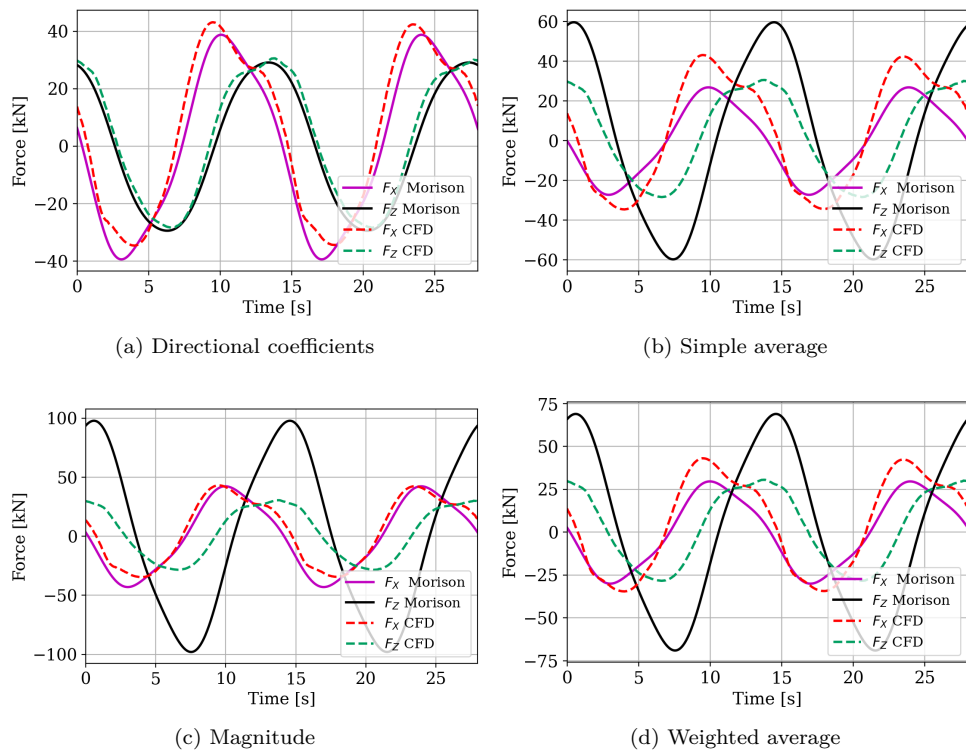


Figure 7.63: Morison prediction with C_D and C_M determined with the three methods for Brac1 (wave w3).

For wave w1, we observe that F_Z predicted here, whatever the method, is overestimated compared to the CFD by about 26% with the averages and 82% with the magnitude. Whereas using the four directional constant averaged coefficients enable a proper prediction of the vertical CFD loads with a difference smaller than 13%. F_X is rather well predicted with the simple or weighted averages C_D and C_M .

Similarly for wave w2, Morison loads obtained with the three methods differ from the CFD loads in amplitude and in phase as shown in Fig. 7.62. The weighted average method leads to the smallest difference for F_Z between Morison and CFD (5.5%) but F_X is overestimated by 47%. Again, using one C_D and C_M prevents from correctly fitting Morison to CFD.

For wave w3, F_Z is strongly overestimated by Morison compared to CFD. The magnitude method enables Morison to rather well predict F_X .

→ Thus we did not find a proper method to estimate C_D and C_M from the constant averaged coefficients C_{D_x} , C_{M_x} , C_{D_z} and C_{M_z} . Other methods should be investigated to correctly predict wave loading on oriented braces. Maybe Morison formula could be modified to include directional forces to correctly predict wave loading on oriented braces. This implementation makes the design model more complex including beforehand a prediction of the directional coefficients.

7.8 Distribution of the coefficients through the TLP floater

The four directional coefficients, at the brace level, are presented for the three wave cases in Fig. 7.64

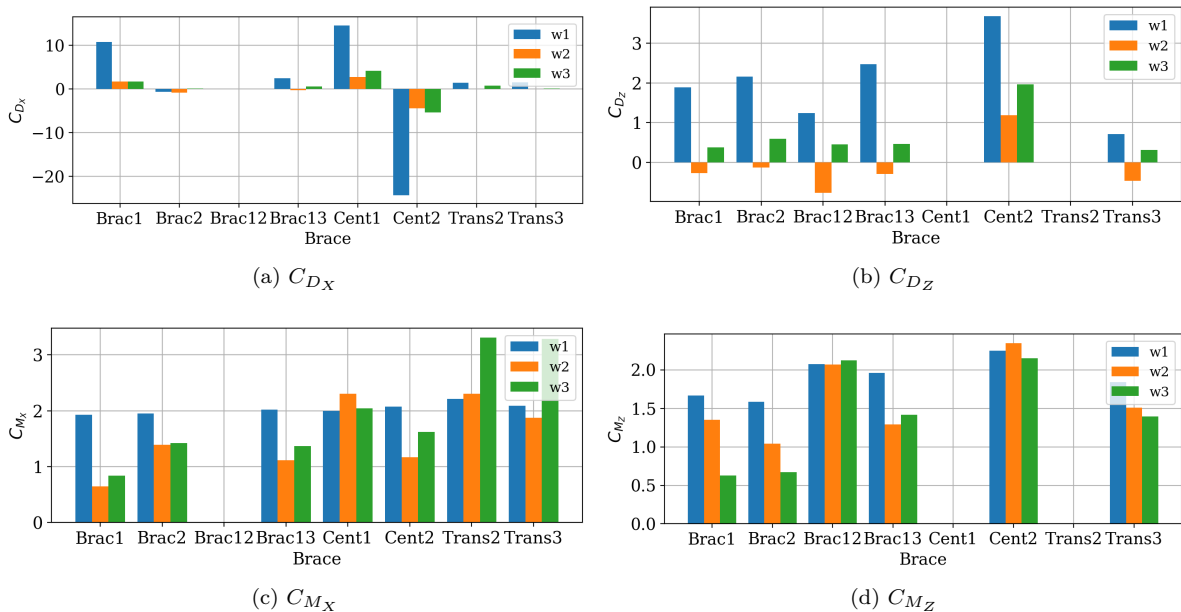


Figure 7.64: Directional coefficients for each brace derived from the CFD modelling of the TLP subjected to the three different waves w1, w2 and w3.

- For the operational wave w1, C_{M_X} varies slightly from one brace to another within the TLP structure ($< 14\%$). As observed in the section 7.4, such a variation has a slight impact on the wave load prediction. Thus, using the same inertia coefficient C_{M_X} for all the braces to calculate the load components on (ΩX) should be a fair assumption. However, C_{M_Z} coefficient varies more within the TLP (about 34%). Imposing the same C_{M_Z} for all the horizontal braces would lead to a significant error on the heave force. C_{D_X} strongly varies within the floater, from -24.3 to 14.53 . As already observed, drag coefficients are subjected to a high level of uncertainty due to the negligible drag term for wave w1.
- For the steeper wave w2, the variations of C_{M_X} within the TLP are larger (107%) than for wave w1, in particular for vertical braces. Also, the variations of C_{M_Z} are smaller than C_{M_X} ones (82%). Thus increasing the wave height impacts a little more C_{M_X} than C_{M_Z} . For wave w2, most of C_{D_X} and C_{D_Z} coefficients are negative compared to wave w1.
- C_{M_X} coefficients obtained for wave w3, as well as their variations within the floater are close to the wave w2 ones for the horizontal brace. However, strong variations are observed for the surface-piercing cylinders apart from Cent1. Such variations might be explained by the influence of the interface observed on the Transi that varies with the wave. C_{M_Z} coefficients obtained for wave w3, as well as their variations within the floater are close to the wave w2 ones, except for Brac1 and Brac2.

7.9 Towards a few advice to improve Morison formula predictions

To conclude, we propose some advice to improve the use of Morison formula for FOWT load prediction from the conclusions drawn above.

- We observed that the impact of the floater has to be included in Morison prediction. For horizontal braces, we highlighted that the impact of the TLP floater could be up to 37% on the heave loads in operating wave conditions. To include the effect of the floater, mainly due to the interconnections between braces, we propose to use Morison coefficients for each brace calculated from the average of the slice coefficients derived for the submerged and pierced slices.
- The effect of the interface cannot be taken into account applying Morison formula. In particular, a phase shift is observed between the CFD forces and the Morison forces for the oriented surface-piercing braces at the scale of the brace. Strongly non linear loads are locally observed and make the determination of Morison coefficients difficult.

- We demonstrated that for braces with complex orientation, Morison formula can be extended with two force components in the perpendicular plan to the brace axis. Thus a set of four coefficients C_{D_x} , C_{M_x} , C_{D_z} and C_{M_z} is determined per brace and enables a correct prediction of wave loads applying the extended Morison formula. We proved that these coefficients cannot be averaged in order to get one set of C_D and C_M per brace. Thus to improve Morison prediction in design tools, the Morison formula should be extended to take into account directional coefficients.
- We observed variations of the Morison coefficient from one brace to another within the floater for the three waves. These variations can be explained by the impact of the interconnections, the interface vicinity and the brace orientation. As a result, we advise taking one set of coefficients per brace or per type of brace, and not the same set of coefficients for the whole structure, in order to improve the predictions of the floater loads.

All the analysis conducted in this work bring some information to improve the use of Morison formula for the prediction for FOWT loads. However, the generalisation of these recommendations should be followed carefully for the following reasons:

- We base our conclusions on the CFD results derived from only three different waves. We should extend our analysis to other wave characteristics in order to supply the database of Morison coefficients to the whole range of waves encountered by a floater. For instance, this study only deals with regular waves. It should be extended to bi-chromatic waves to get closer to real wave conditions.
- The floater is constrained, its motion is not modelled. In reality, the flow field perceived by a brace is the combination of the wave field and of the floater motion. This leads too much more complex oscillations that may impact the Morison coefficient values.
- Scaling problems exist. The Reynolds number is not conserved when upscaling from the basin test to real sea condition. This can notably impact the viscous load prediction. This uncertainty could be investigated modelling directly the TLP at full scale with the three waves w1, w2 and w3. Morison coefficients could thus be derived from the CFD model at full scale and compared to the model scale results.

Chapter 8

Conclusion and perspectives

Two theories are commonly implemented in design solvers to model the hydrodynamic loads on FOWT: the linear potential flow theory and the Morison empirical formula. Historically developed for offshore oil and gas systems, using these theories with the same standard practices may be questionable or too conservative when applied to FOWT. This PhD thesis objective is to contribute to the following problematic: How can we evaluate, improve and adapt the commonly used hydrodynamic theories to FOWT design, thanks to CFD?

To address this research question, we first implement a Numerical Wave Tank with the aim of propagating regular waves in a controlled way. The solver `waveFoam` in the CFD framework of `OpenFOAM` is chosen to perform the simulations. This method applies relaxation zones at both extremities of the tank: at the inlet to generate the waves and at the outlet to absorb them. The air/water interface is solved by the VOF MULES method. We propose a methodology to verify the proper wave propagation and assess its validity against experimental data.

Then the floater is included in the Numerical Wave Tank. Due to the complexity of the FOWT floater, we firstly choose to model the vertical surface-piercing cylinder case of Stansberg [1997]. Then, a realistic FOWT floater (Caillé et al. [2017]) is included in the NWT. Both structures are constrained and subjected to regular waves. Once the wave/structure interaction validated against experimental data, the wave loads are analysed: we notably derive Morison coefficients from the CFD wave loads on the complex structure plunged in a wave field and discuss the validity of Morison prediction at different scales within the structure.

The two main outputs of this PhD work are first the development of a methodology to carefully setup a NWT, and then the development of a slice method to derive Morison coefficients for a complex floater.

To setup a Numerical Wave Tank, we strongly recommend checking the temporal evolution of the wave elevation at a position in the NWT, as commonly done in the

literature, but also the spatial variation of the wave height along the tank. Thanks to a parametric study on mesh refinement, time step convergence, and also on relaxation zone lengths, we provide general guidelines to set-up a NWT for various ranges of waves:

- The generation zone length must be around 1λ
- An absorption zone length of 6λ is necessary to correctly absorb the wave and avoid reflection phenomenon.
- The free surface must evolve in a $2H$ -height refinement box, centred around the mean sea water level. The box dimensions on (Ox) and (Oy) directions are the same as the ones of the background grid. The ratio r relating the cell size dz and dx , on (Oz) and (Ox) directions respectively, to the wave steepness ($dz/dx = r * H/L$) has to be around 10, while keeping the maximum number of points per wave height on (Oz) direction between 10 and 20.
- The time step should be smaller than $T/700$ to minimise the wave height damping along the tank and higher than $T/900$ to avoid numerical reflection along the tank.
- To ensure numerical stability of the VOF MULES method, the maximum CFL in the interface zone should not be higher than 0.2.

Once we have validated the NWT, we applied the numerical slice methodology to derive Morison coefficients for the complex floater. Various test campaigns were conducted in the 80s to determine database of hydrodynamic coefficients commonly used for offshore design. Based on the literature, we propose in this PhD thesis a methodology to derive Morison coefficients from the CFD wave loads for slender cylinders, whose diameter is much lower than the wavelength.

We slice the cylinder along its axis and determine Morison coefficients for each slice. Thus, the load variation along the cylinder is taken into account, while these complex information are impossible to obtain in experiments. Using this numerical methodology, a complex set of two directional wave velocity/acceleration field is taken into account contrary to the experiments for which only a unidirectional oscillating velocity field is considered.

The main interest of the methodology lies on the possibility to be applied to any type of cylinder whatever its orientation such as the braces of a realistic and complex FOWT floater. Thus, the Morison coefficients obtained for an actual FOWT floater take into account the brace orientation, the position in the structure, the distance to the interface and the interaction between the braces, as well as the wave characteristics imposed in the NWT.

FOWT Hydrodynamics is investigated for two structures: we first model Stansberg vertical surface-piercing cylinder to then model a FOWT floater in regular waves.

This first simple case enables us to draw recommendations regarding mesh and numerical characteristics to perform a valid CFD wave/structure model. We demonstrate that the CFD wave loads on vertical, free-surface piercing cylinder are in good agreement with experimental ones without activating any turbulence model though the flow is turbulent ($Re = 1.4 \times 10^5$). Imposing a no-slip boundary condition on the cylinder wall with cells of $D/15$ -size near the structure is enough to capture the wave loads.

We apply the numerical slice methodology to derive Morison coefficients from the CFD wave loads on the cylinder. In this methodology, the velocity/acceleration at each slice centre has to be determined. We demonstrate that the CFD velocity field can be well predicted, and thus used for the coefficient calculation, by Stokes 2nd order theory and extrapolated stretching model.

For this case, the drag term of Morison formula is found to be negligible. The inertia Morison coefficients appear to be constant along the water depth. We show that the loads in the air/water area are highly non-linear and cannot be correctly predicted by Morison formula originally developed for submerged cylinder only. Still, the average of the coefficients over all the submerged slices leads to an inertia coefficient that provides a good agreement between Morison forces and the CFD loads. Thus, though the interface strongly impacts the loads in the air/water area, its influence remains negligible for the total load.

We also observe a small bump close to the minimum of the wave loads attributed to the air/water interface impact. This non-linear effect has already been studied in the literature and corresponds to a secondary-load cycle occurring for surface-piercing cylinder subjected to steep waves. This non-linear effect can be related to load harmonics up to the fourth order. Thanks to CFD, we are able to detail this specific cycle highlighting key moments and correlating the wave run-up to the load variation on the upstream and downstream parts of the cylinder.

With this bench of skills acquired from Stansberg cylinder study case, we then investigate the hydrodynamic behaviour of the constrained FOWT floater in waves, composed by multiple inclined submerged and surface-piercing cylinders.

The TLP floater is included in the NWT. Three different regular waves are modelled to scan the range of waves that can be encountered by a FOWT floater installed in the open sea. The waves are also chosen to review different ranges of inertia/drag Morison contribution. The three main limitations of Morison formula expected for the prediction of FOWT loads, that may impact the wave forces, are investigated: the presence of the whole structure (versus an isolated cylinder), the vicinity with the air/water interface and the brace orientation. We demonstrate that different levels of study have to be considered for this analysis, from the largest to the finest level: the floater, the brace and the slice level.

First, we observe that the impact of the floater has to be included in Morison prediction: for horizontal braces, we highlight that the impact of the TLP floater can be

up to 37% on the heave loads in operating wave conditions. To include the effect of the floater, mainly due to the interconnections between braces, we propose to use Morison coefficients for each brace calculated from the average of the slice coefficients derived for the submerged and pierced slices.

At the air/water interface, as for Stansberg cylinder study, non-linear loads are observed locally making the determination of Morison coefficients difficult. That is why we average only the submerged slice coefficients to derive the constant coefficient imposed in Morison formula. For the vertical surface-piercing braces perpendicular to the flow direction, wave loads can be correctly predicted when excluding the effect of the interface for operation sea condition. Nevertheless, the accuracy of load prediction degrades for more extreme waves. For vertical and oriented braces, independently of the wave conditions, the effect of the interface leads to a wrong load prediction contrary to vertical braces. In particular, a phase shift is observed between CFD forces and Morison forces for oriented surface-piercing braces at the scale of the brace.

We demonstrate that for braces with complex orientation, Morison formula can be extended with two force components in the perpendicular plan to the brace axis. Thus a set of four coefficients C_{DX} , C_{MX} , C_{DZ} and C_{MZ} is determined per brace and enables a correct prediction of wave loads applying the extended Morison formula. We prove that these coefficients cannot be averaged in order to get one set of C_D and C_M per brace. Thus to improve Morison prediction in design tools, the Morison formula should be extended to take into account directional coefficients.

We observe variations of the Morison coefficients from one brace to another within the floater for the three waves. These variations can be explained by the impact of the interconnections, the interface vicinity and the brace orientation. As a result, we advise taking one set of four directional coefficients per brace or per type of brace, and not the same set of coefficients for the whole structure in order to improve the predictions of the floater loads. For the moment, such databases of coefficients per brace does not exist and seem very complex to be included in the design process. Still, this PhD thesis work provides methods and recommendations to derive coefficients per brace using CFD modelling and determining these databases may be possible in the next few years with the exponential deployment of CFD.

Several proposals for future work can be mentioned:

- In addition to the force study conducted in this PhD, the pitch moment could also be analysed. The experimental moment could be compared to the CFD moment to specify the load distribution on the TLP floater.
- Other regular waves with small amplitudes and different periods were performed at the MARIN wave tank facility. They could be modelled to complete the PhD results and make the methodology more robust.

-
- The TLP FOWT floater could be modelled under bichromatic wave loading. The numerical slice methodology should be extended to this case. Thus, Morison coefficients could be derived for cases close to more realistic conditions. Also, as it currently investigated in the OC6 project for the OC5-DeepCWind semisubmersible floater, the inaccurate second-order wave load prediction in design tools could be investigated with the TLP floater.
 - Scaling relative problems exist due to the difficulty of maintaining relevant all dimensionless parameters between the scaled model in a wave tank and the full-scale floater in open-sea (namely a choice has to be made between Froude and Reynolds similarities, Froude similarity is selected most of the time for wave tank tests). The FOWT floater could be modelled in CFD at full scale to investigate this scaling issue. A comparison between the wave loads both derived from the model scale and full scale models could be achieved. Also, Morison coefficients could be determined and compared with model scale ones. However modelling at full scale may imply to model the turbulence, that makes the CFD model more complex than without activating turbulence modelling as in the present work.
 - Upgrades of the CFD model could be tested. Indeed, meshing could be improved trying other mesh strategies.

We demonstrated that deep-water waves cannot be correctly absorbed with active solver whereas the relaxation zone solver implies high computational time. New methods for wave generation/absorption could be investigated.

- To better predict the loads on the TLP floater and notably on oriented braces, directional coefficients should be implemented in DeepLinesWind™. This could improve the assessment of the total TLP loads derived from DeepLinesWind™ when compared to experimental data (relative difference observed of 20%).
- Other non-linear numerical models, naming weakly non-linear approaches or fully non-linear potential-flow codes, could be tested to predict the loads on the complex TLP floater.
- Finally, the models and methodology developed through this PhD work combined with CFD models currently used for specific cases of decay test/forced oscillations could model the free motion of the TLP floater in waves.

However, such simulations point out difficulties to derive complex hydrodynamic coefficients and post-process the results. Still this combination of models could be used to provide information for non-linear wave load models applied in design tools.

Bibliography

- M. A. Afshar. Numerical wave generation in openfoam®. 2010.
- J. Azcona, F. Bouchotrouch, and F. Vittori. Low-frequency dynamics of a floating wind turbine in wave tank-scaled experiments with sil hybrid method. *Wind Energy*, 22(10): 1402–1413, 2019.
- E. E. Bachynski and T. Moan. Ringing loads on tension leg platform wind turbines. *Ocean engineering*, 84:237–248, 2014.
- I. Bayati, J. Jonkman, A. Robertson, and A. Platt. The effects of second-order hydrodynamics on a semisubmersible floating offshore wind turbine. *Journal of Physics: Conference Series*, 524:012094, jun 2014. doi: 10.1088/1742-6596/524/1/012094.
- M. A. Benitz, D. P. Schmidt, M. A. Lackner, G. M. Stewart, J. Jonkman, and A. Robertson. Validation of hydrodynamic load models using cfd for the oc4-deepcwind semisubmersible. In *International Conference on Offshore Mechanics and Arctic Engineering*, volume 56574, page V009T09A037. American Society of Mechanical Engineers, 2015.
- P. Boccotti. *Wave mechanics and wave loads on marine structures*. Butterworth-Heinemann, 2014.
- L. Borgman. Computation of the ocean-wave forces on inclined cylinders. *Eos, Transactions American Geophysical Union*, 39(5):885–888, 1958.
- A. Borràs Nadal and P. Bozonnet. Surge decay cfd simulations of a tension leg platform floating wind turbine. 2020. doi: 10.13140/RG.2.2.14518.24641.
- P. Bozonnet, A. Emery, et al. Cfd simulations for the design of offshore floating wind platforms encompassing heave plates. In *The Twenty-fifth International Ocean and Polar Engineering Conference*. International Society of Offshore and Polar Engineers, 2015.
- N. Bruinsma. Validation and application of a fully nonlinear numerical wave tank. 2016.
- S. Burmester, S. Gueydon, G. Vaz, and B. el Moctar. Surge decay simulations of a semisubmersible floating offshore wind turbine. In *Proceedings of the 20th numerical towing tank symposium*, pages 2–3, 2017.

- S. Burmester, G. Vaz, S. Gueydon, and O. el Moctar. Investigation of a semi-submersible floating wind turbine in surge decay using CFD. *Ship Technology Research*, 67(1):2–14, dec 2018. doi: 10.1080/09377255.2018.1555987.
- F. Caillé, P. Bozonnet, T. Perdrizet, Y. Poirette, and C. Melis. Model test and simulation comparison for an inclined-leg tlp dedicated to floating wind. In *ASME 2017 36th International Conference on Ocean, Offshore and Arctic Engineering*. American Society of Mechanical Engineers Digital Collection, 2017.
- S. Chakrabarti. Wave forces on vertical array of tubes. In *Proc. Civil Eng. Ocean*, pages 241–259, 1979.
- S. Chakrabarti. *Handbook of Offshore Engineering (2-volume set)*. Elsevier, 2005.
- S. Chakrabarti, W. Tam, and A. Wolbert. Wave forces on a randomly oriented tube. In *Offshore Technology Conference*. Offshore Technology Conference, 1975. doi: 10.4043/2190-ms.
- S. K. Chakrabarti. Hydrodynamic coefficients for a vertical tube in an array. *Applied Ocean Research*, 3(1):2–12, jan 1981. doi: 10.1016/0141-1187(81)90080-8.
- S. K. Chakrabarti, W. A. Tam, and A. L. Wolbert. Wave forces on vertical circular cylinder. *Journal of the Waterways, Harbors and Coastal Engineering Division*, 102(2): 203–221, 1976.
- S. K. Chakrabarti, A. L. Wolbert, and W. A. Tam. Wave forces on inclined tubes. *Coastal Engineering*, 1:149–165, jan 1977. doi: 10.1016/0378-3839(77)90012-6.
- J. Chaplin, R. Rainey, and R. Yemm. Ringing of a vertical cylinder in waves. *Journal of Fluid Mechanics*, 350:119–147, 1997.
- L. Chen, D. Stagonas, H. Santo, E. Buldakov, R. Simons, P. Taylor, and J. Zang. Numerical modelling of interactions of waves and sheared currents with a surface piercing vertical cylinder. *Coastal Engineering*, 145:65–83, mar 2019. doi: 10.1016/j.coastaleng.2019.01.001.
- C. Clément. Cfd simulation of waves in openfoam for floating wind turbines. Master’s thesis, 2018.
- C. Clément, P. Bozonnet, G. Vinay, A. B. Nadal, P. Pagnier, and J. Réveillon. Numerical wave tank including a fixed vertical cylinder subjected to waves, towards the investigation of floating offshore wind turbine hydrodynamics. In *Volume 6A: Ocean Engineering*. American Society of Mechanical Engineers, aug 2020. doi: 10.1115/omae2020-18797.
- A. J. Coulling, A. J. Goupee, A. N. Robertson, and J. M. Jonkman. Importance of second-order difference-frequency wave-diffraction forces in the validation of a FAST

- semi-submersible floating wind turbine model. In *Volume 8: Ocean Renewable Energy*. American Society of Mechanical Engineers, jun 2013. doi: 10.1115/omae2013-10308.
- J. Davidson, M. Cathelain, L. Guillemet, T. Le Huec, and J. Ringwood. Implementation of an openfoam numerical wave tank for wave energy experiments. In *Proceedings of the 11th European wave and tidal energy conference*. European Wave and Tidal Energy Conference 2015, 2015.
- R. G. Dean. Methodology for evaluating suitability of wave and wave force data for determining drag and inertia coefficients. In *University of Delaware, Department of Civil Engineering, Newark DE 19711, USA, Presented at the Conference on Behaviour of Offshore Structures, BOSS'76, The Norwegian Institute of Technology, Papers: P1976-7 Proceedings*, 1976.
- R. G. Dean, R. A. Dalrymple, and R. T. Hudspeth. Force coefficients from wave project I and II data including free surface effects. *Society of Petroleum Engineers Journal*, 21(06):779–786, dec 1981. doi: 10.2118/9103-pa.
- S. S. Deshpande, L. Anumolu, and M. F. Trujillo. Evaluating the performance of the two-phase flow solver interfoam. *Computational science & discovery*, 5(1):014016, 2012.
- B. Devolder, P. Rauwoens, and P. Troch. Application of a buoyancy-modified $k-\omega$ SST turbulence model to simulate wave run-up around a monopile subjected to regular waves using OpenFOAM®. *Coastal Engineering*, 125:81–94, jul 2017. doi: 10.1016/j.coastaleng.2017.04.004.
- G. Diz-Lois Palomares. Cfd simulations on a partially submerged cylinder under regular waves using openfoam. Master’s thesis, University of Stavanger, Norway, 2015.
- A. J. Dunbar, B. A. Craven, and E. G. Paterson. Development and validation of a tightly coupled CFD/6-DOF solver for simulating floating offshore wind turbine platforms. *Ocean Engineering*, 110:98–105, dec 2015. doi: 10.1016/j.oceaneng.2015.08.066.
- L. Eça and M. Hoekstra. Evaluation of numerical error estimation based on grid refinement studies with the method of the manufactured solutions. *Computers & Fluids*, 38(8):1580–1591, sep 2009. doi: 10.1016/j.compfluid.2009.01.003.
- L. Eça and M. Hoekstra. A procedure for the estimation of the numerical uncertainty of CFD calculations based on grid refinement studies. *Journal of Computational Physics*, 262:104–130, apr 2014. doi: 10.1016/j.jcp.2014.01.006.
- L. Eça, G. Vaz, S. Toxopeus, and M. Hoekstra. Numerical errors in unsteady flow simulations. *Journal of Verification, Validation and Uncertainty Quantification*, 4(2), 2019.
- D. Faltinsen. Wave loads on offshore structures. *Annual Review of Fluid Mechanics;(USA)*, 22, 1990.

- O. M. Faltinsen, J. N. Newman, and T. Vinje. Nonlinear wave loads on a slender vertical cylinder. *Journal of Fluid Mechanics*, 289:179–198, apr 1995. doi: 10.1017/s0022112095001297.
- P. Ferrant. Fully nonlinear interactions of long-crested wave packets with a three dimensional body. In *Proc. 22nd ONR Symposium on Naval Hydrodynamics*, pages 403–415, 1998.
- C. J. Greenshields. Programmer’s guide. *OpeFOAM Foundation Ltd*, 2015.
- C. J. Greenshields. Openfoam user guide. *OpenFOAM Foundation Ltd, version*, 3(1): e2888, 2020.
- J. Grue. On four highly nonlinear phenomena in wave theory and marine hydrodynamics. *Applied ocean research*, 24(5):261–274, 2002.
- K. W. Gueydon S. *Hydrodynamics of fixed and floating offshore wind turbine foundations*. MaRINET2, MARIN, 2018.
- GWEC. Global wind report 2021. *Global Wind Energy Council*, 2021.
- W. Heronemus. Power from the offshore winds. In *University of Massachusetts, Department of Civil Engineering, 8th Annual Conference and Exposition Marine Technology Society, Washington DC, USA*, 1972.
- P. Higuera. Application of computational fluid dynamics to wave action on structures. *PhD. Universidade de Cantabria*, 2015.
- P. Higuera. Enhancing active wave absorption in rans models. *Applied Ocean Research*, 94:102000, 2020.
- P. Higuera, I. J. Losada, and J. L. Lara. Three-dimensional numerical wave generation with moving boundaries. *Coastal Engineering*, 101:35–47, jul 2015. doi: 10.1016/j.coastaleng.2015.04.003.
- M. Huseby and J. Grue. An experimental investigation of higher-harmonic wave forces on a vertical cylinder. *Journal of fluid Mechanics*, 414:75–103, 2000.
- N. Jacobsen. waves2foam manual. *Deltares, The Netherlands*, 2017.
- H. Jasak. Error analysis and estimation for the finite volume method with applications to fluid flows. 1996.
- J. M. Jonkman, M. L. Buhl Jr, et al. Fast user’s guide. *Golden, CO: National Renewable Energy Laboratory*, 365:366, 2005.
- G. H. Keulegan, L. H. Carpenter, et al. Forces on cylinders and plates in an oscillating fluid. *Journal of research of the National Bureau of Standards*, 60(5):423–440, 1958.

- D. Kristiansen and O. Faltinsen. A study of wave loads on fixed horizontal cylinders in the free surface. In *Proceedings of the 8th International Conference on Hydrodynamics*, pages 1–9, 2008.
- B. E. Larsen and D. R. Fuhrman. On the over-production of turbulence beneath surface waves in reynolds-averaged navier–stokes models. *Journal of Fluid Mechanics*, 853: 419–460, aug 2018. doi: 10.1017/jfm.2018.577.
- B. E. Larsen, D. R. Fuhrman, and J. Roenby. Performance of interFoam on the simulation of progressive waves. *Coastal Engineering Journal*, 61(3):380–400, may 2019. doi: 10.1080/21664250.2019.1609713.
- C. Le Cunff, J.-M. Heurtier, L. Piriou, C. Berhault, T. Perdrizet, D. Teixeira, G. Ferrer, and J.-C. Gilloteaux. Fully coupled floating wind turbine simulator based on nonlinear finite element method: Part i—methodology. In *International Conference on Offshore Mechanics and Arctic Engineering*, volume 55423, page V008T09A050. American Society of Mechanical Engineers, 2013.
- H. Lewy, K. Friedrichs, and R. Courant. Über die partiellen differenzgleichungen der mathematischen physik. *Mathematische Annalen*, 100:32–74, 1928.
- Y. Liu, Q. Xiao, A. Incecik, C. Peyrard, and D. Wan. Establishing a fully coupled cfd analysis tool for floating offshore wind turbines. *Renewable Energy*, 112:280–301, 2017.
- W. Massie and J. Journée. Offshore hydromechanics. *Delft University of Technology: Delft, The Netherlands*, 2001.
- B. L. Méhauté. Similitude in coastal engineering. *Journal of the waterways, harbors and coastal engineering division*, 102(3):317–335, 1976.
- F. Menter and Y. Egorov. The scale-adaptive simulation method for unsteady turbulent flow predictions. part 1: theory and model description. *Flow, Turbulence and Combustion*, 85(1):113–138, 2010.
- F. R. Menter. Two-equation eddy-viscosity turbulence models for engineering applications. *AIAA journal*, 32(8):1598–1605, 1994.
- A. Miquel, A. Kamath, M. A. Chella, R. Archetti, and H. Bihs. Analysis of different methods for wave generation and absorption in a CFD-based numerical wave tank. *Journal of Marine Science and Engineering*, 6(2):73, jun 2018. doi: 10.3390/jmse6020073.
- B. Molin. *Hydrodynamique des structures offshore*. Edition TECHNIP, 2002.
- J. Morison, J. Johnson, S. Schaaf, et al. The force exerted by surface waves on piles. *Journal of Petroleum Technology*, 2(05):149–154, 1950.

- J. Palm, C. Eskilsson, G. M. Paredes, and L. Bergdahl. Coupled mooring analysis for floating wave energy converters using CFD: Formulation and validation. *International Journal of Marine Energy*, 16:83–99, dec 2016. doi: 10.1016/j.ijome.2016.05.003.
- J. Pan and T. Ishihara. Numerical prediction of hydrodynamic coefficients for a semi-sub platform by using large eddy simulation with volume of fluid method and richardson extrapolation. *Journal of Physics: Conference Series*, 1356:012034, oct 2019. doi: 10.1088/1742-6596/1356/1/012034.
- E. Paterson. Multiphase and free surface flow simulations. In *Third OpenFOAM workshop, Politecnico di Milano, Milan, Italy*, 2008.
- B. Paulsen, H. Bredmose, and H. Bingham. Accurate computation of wave loads on a bottom fixed circular cylinder. 01 2012.
- B. T. Paulsen. *Efficient computations of wave loads on offshore structures*. PhD thesis, Technical University of Denmark, 2013.
- B. T. Paulsen, H. Bredmose, and H. B. Bingham. An efficient domain decomposition strategy for wave loads on surface piercing circular cylinders. *Coastal Engineering*, 86: 57–76, apr 2014. doi: 10.1016/j.coastaleng.2014.01.006.
- J. R. Pedersen, B. E. Larsen, H. Bredmose, and H. Jasak. A new volume-of-fluid method in openfoam. In *7th International Conference on Computational Methods in Marine Engineering*, pages 266–278. International Center for Numerical Methods in Engineering, 2017.
- A. Pegalajar-Jurado and H. Bredmose. Reproduction of slow-drift motions of a floating wind turbine using second-order hydrodynamics and operational modal analysis. *Marine Structures*, 66:178–196, jul 2019. doi: 10.1016/j.marstruc.2019.02.008.
- R. Pinguet, S. kanner, M. Benoit, and B. Molin. Modeling the dynamics of freely-floating offshore wind turbine subjected to waves with an open-source overset mesh method. 02 2021.
- D. Quarton. Float - technical and economic feasibility of a floating wind turbine. In *Deep water wind energy research and development planning workshop, Washington DC*, 2004.
- Rainey. Slender-body expressions for the wave load on offshore structures. *Proceedings of the Royal Society of London. Series A: Mathematical and Physical Sciences*, 450(1939): 391–416, aug 1995. doi: 10.1098/rspa.1995.0091.
- R. Rainey. A new equation for calculating wave loads on offshore structures. *Journal of Fluid Mechanics*, 204:295–324, 1989.
- R. Rainey. Weak or strong nonlinearity: the vital issue. *Journal of Engineering Mathematics*, 58(1):229–249, 2007.

- L. Ramírez, D. Fraile, and G. Brindley. Offshore wind in europe: Key trends and statistics 2019. 2020.
- N. Ren, Y. Li, and J. Ou. Coupled wind-wave time domain analysis of floating offshore wind turbine based on computational fluid dynamics method. *Journal of Renewable and Sustainable Energy*, 6(2):023106, 2014.
- I. Rivera Arreba. Computation of nonlinear wave loads on floating structures. Master’s thesis, NTNU, 2017.
- I. Rivera-Arreba, N. Bruinsma, E. E. Bachynski, A. Viré, B. T. Paulsen, and N. G. Jacobsen. Modeling of a semisubmersible floating wind platform in severe waves. In *International Conference on Offshore Mechanics and Arctic Engineering*, volume 51302, page V009T13A002. American Society of Mechanical Engineers, 2019.
- L. Roald, J. Jonkman, A. Robertson, and N. Chokani. The effect of second-order hydrodynamics on floating offshore wind turbines. *Energy Procedia*, 35:253–264, 2013. doi: 10.1016/j.egypro.2013.07.178.
- A. Robertson and J. Jonkman. Oc5 phase i: Definition of marintek cylinder dataset.
- A. Robertson, J. Jonkman, M. Masciola, H. Song, A. Goupee, A. Coulling, and C. Luan. Definition of the semisubmersible floating system for phase ii of oc4. Technical report, National Renewable Energy Lab.(NREL), Golden, CO (United States), 2014. URL <https://www.nrel.gov/docs/fy14osti/60601.pdf>.
- A. N. Robertson, F. Wendt, J. M. Jonkman, W. Popko, H. Dagher, S. Gueydon, J. Qvist, F. Vittori, J. Azcona, E. Uzunoglu, C. G. Soares, R. Harries, A. Yde, C. Galinos, K. Hermans, J. B. de Vaal, P. Bozonnet, L. Bouy, I. Bayati, R. Bergua, J. Galvan, I. Mendikoa, C. B. Sanchez, H. Shin, S. Oh, C. Molins, and Y. Debruyne. OC5 project phase II: Validation of global loads of the DeepCwind floating semisubmersible wind turbine. *Energy Procedia*, 137:38–57, oct 2017. doi: 10.1016/j.egypro.2017.10.333.
- A. N. Robertson, S. Gueydon, E. Bachynski, L. Wang, J. Jonkman, D. Alarcón, E. Amet, A. Beardsell, P. Bonnet, B. Boudet, et al. Oc6 phase i: Investigating the underprediction of low-frequency hydrodynamic loads and responses of a floating wind turbine. In *Journal of Physics: Conference Series*, volume 1618, page 032033. IOP Publishing, 2020. URL <https://iopscience.iop.org/article/10.1088/1742-6596/1618/3/032033/pdf>.
- J. Roenby, H. Bredmose, and H. Jasak. A computational method for sharp interface advection. *Royal Society Open Science*, 3(11):160405, nov 2016. doi: 10.1098/rsos.160405.
- š. Malenica and B. Molin. Third-harmonic wave diffraction by a vertical cylinder. *Journal of Fluid Mechanics*, 302:203–229, nov 1995. doi: 10.1017/s0022112095004071.

- H. Sarlak, A. Pegalajar-Jurado, and H. Bredmose. Cfd simulations of a newly developed floating offshore wind turbine platform using openfoam. 12 2018.
- G. R. Sarmiento J. *Introduction to offshore wind fixed structures*. Environmental Hydraulics Institute Universidad de Cantabria, 2018.
- T. Sarpkaya. In-line and transverse forces on cylinders in oscillatory flow at high reynolds numbers. *Journal of ship Research*, 21(04):200–216, 1977.
- H. A. Schäffer and G. Klopman. Review of multidirectional active wave absorption methods. *Journal of waterway, port, coastal, and ocean engineering*, 126(2):88–97, 2000.
- P. Schmitt, C. Windt, J. Davidson, J. V. Ringwood, and T. Whittaker. The efficient application of an impulse source wavemaker to CFD simulations. *Journal of Marine Science and Engineering*, 7(3):71, mar 2019. doi: 10.3390/jmse7030071.
- C. Stansberg. Comparing ringing loads from experiments with cylinders of different diameters—an empirical study. In *BOSS '97 Conference*, 1997.
- B. M. Sumer et al. *Hydrodynamics around cylindrical structures*, volume 26. World scientific, 2006.
- G. Susbielles, C. Bratu, and A. Cavanié. *Vagues et ouvrages pétroliers en mer*, volume 23. Editions Technip, 1981.
- L. Tao and S. Cai. Heave motion suppression of a spar with a heave plate. *Ocean Engineering*, 31(5-6):669–692, apr 2004. doi: 10.1016/j.oceaneng.2003.05.005.
- L. Tao, K. Y. Lim, and K. Thiagarajan. Heave response of classic spar with variable geometry. *Journal of Offshore Mechanics and Arctic Engineering*, 126(1):90–95, feb 2004. doi: 10.1115/1.1643085.
- L. Tao, B. Molin, Y.-M. Scolan, and K. Thiagarajan. Spacing effects on hydrodynamics of heave plates on offshore structures. *Journal of Fluids and Structures*, 23(8):1119–1136, nov 2007. doi: 10.1016/j.jfluidstructs.2007.03.004.
- T. T. Tran and D.-H. Kim. The coupled dynamic response computation for a semi-submersible platform of floating offshore wind turbine. *Journal of wind engineering and industrial aerodynamics*, 147:104–119, 2015.
- J. Van der Vegt. Slinger gedrag van schepen. *KIVI-Lecture on Seakeeping*, 1984.
- V. Venugopal, K. S. Varyani, and N. D. Barltrop. Wave force coefficients for horizontally submerged rectangular cylinders. *Ocean Engineering*, 33(11-12):1669–1704, aug 2006. doi: 10.1016/j.oceaneng.2005.09.007.

- D. N. Veritas. Dnv-rp-c205 environmental conditions and environmental loads. *Det Norske Veritas: Oslo, Norway*, 2010.
- L. Wang, A. Robertson, J. Jonkman, Y.-H. Yu, et al. Uncertainty assessment of cfd investigation of the nonlinear difference-frequency wave loads on a semisubmersible fowt platform. *Sustainability*, 13(1):1–1, 2020a.
- L. Wang, A. Robertson, J. Jonkman, Y.-H. Yu, A. Koop, A. Borràs Nadal, H. Li, W. Shi, R. Pinguet, Y. Zhou, et al. Investigation of nonlinear difference-frequency wave excitation on a semisubmersible offshore-wind platform with bichromatic-wave cfd simulations. In *International Conference on Offshore Mechanics and Arctic Engineering*, volume 84768, page V001T01A009. American Society of Mechanical Engineers, 2021.
- Y. Wang, H.-C. Chen, G. Vaz, and S. Burmester. CFD simulation of semi-submersible floating offshore wind turbine under pitch decay motion. In *ASME 2019 2nd International Offshore Wind Technical Conference*. American Society of Mechanical Engineers, nov 2019. doi: 10.1115/iowtc2019-7515.
- Y. Wang, H.-C. Chen, G. Vaz, S. Burmester, et al. Cfd simulation of semi-submersible floating offshore wind turbine under regular waves. In *The 30th International Ocean and Polar Engineering Conference*. International Society of Offshore and Polar Engineers, 2020b.
- J. Wheeler et al. Method for calculating forces produced by irregular waves. *Journal of petroleum technology*, 22(03):359–367, 1970.
- C. Windt, J. Davidson, P. Schmitt, and J. Ringwood. On the assessment of numerical wave makers in CFD simulations. *Journal of Marine Science and Engineering*, 7(2):47, feb 2019. doi: 10.3390/jmse7020047.
- J. Wolfram and M. Naghipour. On the estimation of morison force coefficients and their predictive accuracy for very rough circular cylinders. *Applied Ocean Research*, 21(6): 311–328, dec 1999. doi: 10.1016/s0141-1187(99)00018-8.
- M. Yan, X. Ma, W. Bai, Z. Lin, and Y. Li. Numerical simulation of wave interaction with payloads of different postures using OpenFOAM. *Journal of Marine Science and Engineering*, 8(6):433, jun 2020. doi: 10.3390/jmse8060433.
- S. Zhang and T. Ishihara. Numerical study of hydrodynamic coefficients of multiple heave plates by large eddy simulations with volume of fluid method. *Ocean Engineering*, 163: 583–598, sep 2018. doi: 10.1016/j.oceaneng.2018.03.060.
- S. Zhang and T. Ishihara. Numerical study of distributed hydrodynamic forces on a circular heave plate by large-eddy simulations with volume of fluid method. *Ships and Offshore Structures*, 15(6):574–586, sep 2019. doi: 10.1080/17445302.2019.1661630.

Y. Zhou, Q. Xiao, Y. Liu, A. Incecik, C. Peyrard, D. Wan, and S. Li. A cfd study for floating offshore wind turbine aerodynamics in turbulent wind field. In *ASME 2020 3rd International Offshore Wind Technical Conference*, 2020.

Chapter 9

Annexes

9.1 Froude scale

Froude similitude is commonly used in Hydrodynamics for offshore structures, for instance to downscale the floating wind turbine for the model test campaign at MARIN (Caillé et al. [2017]). It allows to downscale dimensions while maintaining hydrodynamic forces.

The scale is noted e , the tank dimensions are linked to the realistic ones by the relation $d = eD$, for surfaces by $s = e^2S$ and volumes by $v = e^3V$. The other relations are described in the following Tab. 9.1. Most of the time for the offshore sector, e is included between 1/40 and 1/80.

μ is also defined as:

$$\mu = \frac{\rho_d}{\rho_s} \quad (9.1)$$

ρ_d is the real basin density (pure water, $1\,000\text{ kg} \cdot \text{m}^{-3}$) and ρ_s is the density of sea water ($1\,025\text{ kg} \cdot \text{m}^{-3}$).

Time	Velocity	Acceleration	Mass	Pressure	Force	Moment
e	\sqrt{e}	\sqrt{e}	μe^3	μe	μe^3	μe^4

Table 9.1: Froude scale

Froude similitude leads to changes for phenomena related to water viscosity described by the Reynolds Number:

$$Re = \frac{UD}{\nu} \quad (9.2)$$

Assuming that the cinematic viscosity ν is the same in pure water and seawater, the Reynolds Number on Froude scale is:

$$Re = e^{\frac{3}{2}} Re \quad (9.3)$$

9.2 Numerical Wave Tank with olaFlow

At the beginning of the PhD thesis, the solver olaFlow developed by Higuera [2015] was tested for different sea states. A comparison between olaFlow and waveFoam was achieved to determine which solver should be kept to model the FOWT floater in deep-water waves. From the results, we concluded that waveFoam was more adapted for the PhD thesis purposes.

Here we present the results obtained with olaFlow and why we chose waveFoam for the PhD thesis.

Simulations were run in 2D to minimize computation costs. In each case, wave elevation time series at different probes in the NWT were analysed in order to check the stability of the simulation. Also, the envelop of amplitude along the tank was analysed to get information about damping and reflection in the tank. Minimizing both phenomena in the NWT with wave only cases is primordial to generate controlled waves to then model the flow around an offshore structure.

9.2.1 Physical problem

Firstly, three different waves were tested with the shallow water library (SW-AWA) which is the library Higuera developed olaFlow with. Then, the recent Extend-Range library (ER-AWA,(June, 2019)) was used to run two simulations with deep water waves. On Fig. 9.1, the tested waves are represented with a cross, their characteristics are detailed in Tab. 9.2.

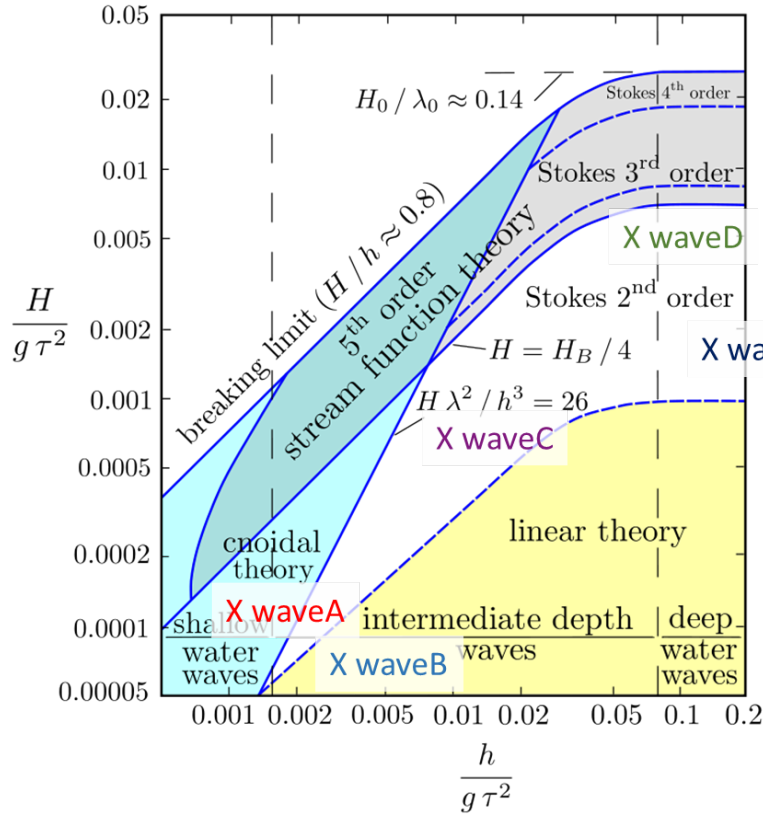


Figure 9.1: Cases run with olaFlow solver.

Case name	Water Depth	Wave order	T (period), H (height), h (depth)
waveA	Shallow water	Cnoidal theory	T= 4 s, H=0,02 m, h=0,2 m
waveB	Intermediate depth	Linear theory	T= 3 s, H=0,007 m, h=0,2 m
waveC	Intermediate depth	Stokes 2nd order	T= 3 s, H=0,05 m, h=0,4 m
waveD	Deep water	Stokes 2nd order	T=1 s, H=0,06 m, h=0,45 m
waveE	Deep water	Stokes 2nd order	T=1,265 s, H=0,025 m, h=2,5 m

Table 9.2: Tested waves with olaFlow solver.

waveA and waveB are chosen to test olaFlow solver in shallow water conditions using SW-AWA library. waveC characteristics come from Higuera’s PhD to compare the wave elevation analysed in his PhD report to the one obtained in our tests. waveD aims at testing the new ER-AWA library imposing wave characteristics corresponding to deep water waves. waveE belongs to the set of wave tested by Caillé et al. [2017] during the 2015 test campaign for the SBM Offshore/IFPEN TLP floater. The wave is modelled at model scale in CFD. waveE is the wave 201018 detailed in Chapter5. Wave elevation is then converted to full scale dimensions to be validated against experiments, reported at

full scale by MARIN applying Froude similitude (Annexe 9.1).

9.2.2 Set up of OpenFOAM model

9.2.2.1 Control Volume

The main difference with the NWT implemented with waveFoam (Fig. 5.5) is the absence of relaxation zones with olaFlow thus the length of the tank is much smaller than with the waveFoam solver. This reduced mesh size, associated to smaller computational time, is the main advantage of this active method for wave generation.

The length of the tank is typically 3-4 wavelength. The height of the tank depends on the depth of the wave simulated.

9.2.2.2 Mesh

The following mesh characteristics were implemented before precisely investing the methodology to set up a NWT with waveFoam solver (Section 5.1.7).

This bench of tests is performed in 2D so the width of the domain is equal to one cell. The free surface elevation is refined i.e. the cells get smaller around the interface and become bigger approaching walls. The minimum cell height is $H/8$ and the maximum is $2H$ (or $4H$). It was also obtained in the internship before the PhD thesis that 100 points per wave length in (Ox) direction should at least be respected. The cell dimensions are chosen in order to avoid a too important aspect ratio at the air/water interface. Cell dimensions in (Ox) direction (dx) depends one the cell dimension along (Oz) axis (dz) respecting a maximum aspect ratio (dx/dz) of 2.

9.2.2.3 Boundary conditions

On each of the 6 boundary faces (also called patch) of the tank, a boundary condition is imposed. In Tab. 9.3, the BC on each patch are detailed for the velocity, pressure and phase fraction variable.

Patch	Velocity	Pressure	Phase fraction
Inlet	waveVelocity	fixedFluxPressure	waveAlpha
Outlet	waveAbsorption2DVelocity	fixedFluxPressure	zeroGradient
Bottom	fixedValue 0	fixedFluxPressure	zeroGradient
Atmosphere	pressureInletOutletVelocity	totalPressure	inletOutlet
Front and Back	empty	empty	empty

Table 9.3: Boundary conditions

Boundary conditions at the inlet and outlet for velocity and phase fraction are specific to olaFlow generation and absorption libraries. They are defined based on the active

numerical wave tank theory defined in section 3.3.2.2. Other boundary conditions are standards. The atmosphere behave like an open face. The front and back walls are similar to symmetry walls to represent the flow as infinite in (Oy) direction.

During this bench of CFD simulations, no turbulence model is implemented.

9.2.2.4 Time step control

This time step control was defined before precisely investing the methodology to set up a NWT with waveFoam solver (Section 5.1.7).

It was determined that a maximum time step of 0.005s, corresponding to around $T/250$, should be imposed in simulation parameters, as well as a maximum CFL of 0.5. The duration of the simulation is between 120-200s, depending of the wave period. The numerical stability of the wave elevation time series is generally from 80 s.

The dimension of the tank and characteristics of simulations having been detailed, the CFD results are analysed in the following sections. In each case, wave amplitude time series and the mean amplitude along the tank were checked.

9.2.3 Numerical results

9.2.3.1 SW-AWA results

First, shallow water active wave absorption library (SW-AWA) was tested with three waves, as detailed in Tab. 9.2.

waveA

A shallow water and cnoidal wave is propagated in the NWT. The free surface elevation time trace at the center of the tank is shown on graph 9.2.

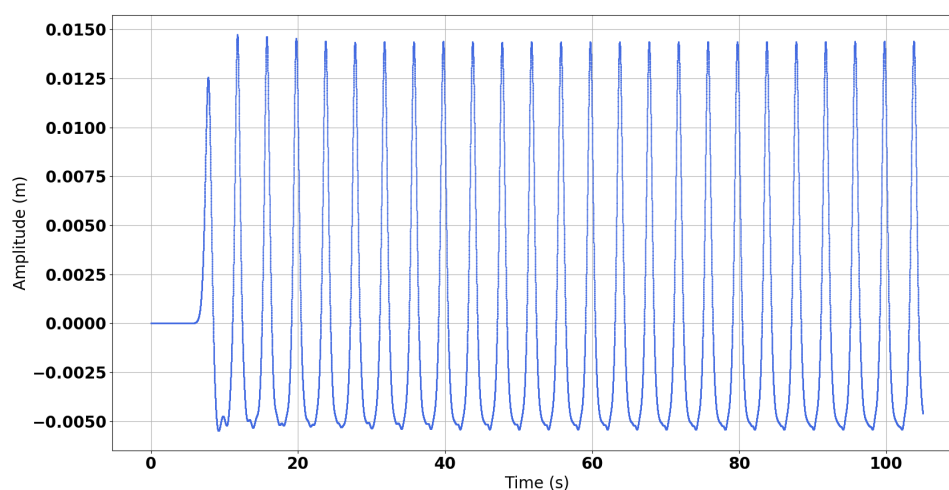


Figure 9.2: Wave elevation time series at the center of the tank (waveA).

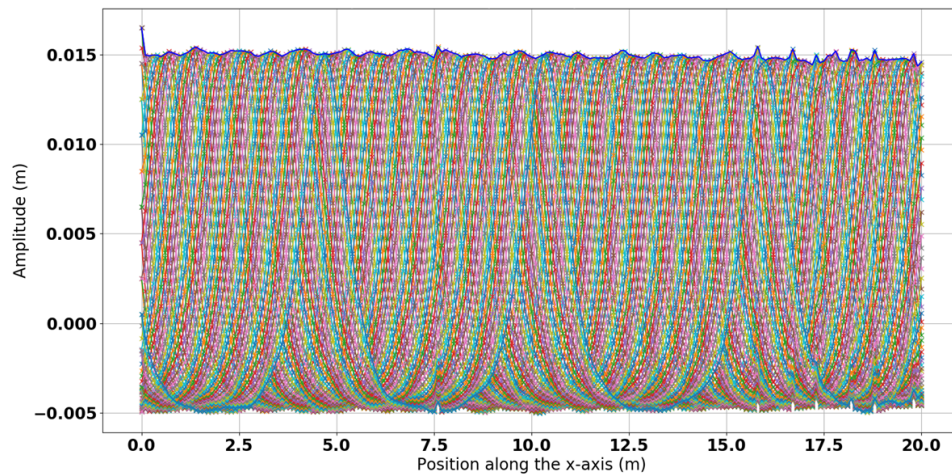


Figure 9.3: Amplitude envelop during one period (waveA).

The signal is stabilized after 10 periods as visible on the graph 9.2.

The amplitude envelop is drawn on Fig. 9.3. To get this plot, the amplitude at gauges every $L/10$ in the tank along (Ox) is drawn during one period starting at $t = 80$ s.

This plot indicates that the mean amplitude is rather constant along the tank. A little instability is visible but can be neglected compare to the wave height (less than 1%).

olaFlow thus propagates shallow water and cnoidal waves in a controlled way as expected.

In the following subsection, linear and intermediate water depth waves are tested, sea conditions encountered for FOWT.

waveB

Wave amplitude time evolution at 5 different gauges spaced by 1.7 m ($2L/5$) at the center of the tank is plotted on Fig. 9.4. The evolution of the amplitude over two wave lengths ($\lambda = 4.14$) is analysed.

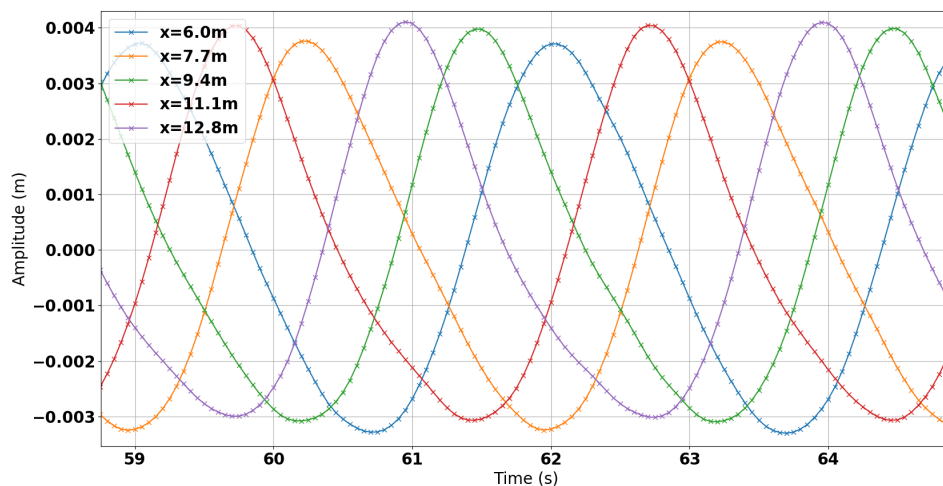


Figure 9.4: Wave elevation time series at 5 probes (waveB).

Over time, free surface elevation seems rather stable. However, a difference of height is observed at the different gauges. The difference between the biggest and smallest peak amplitude of two probes (spaced by two wave lengths) over the theoretical height is 5.6%. This increase of height along the tank is investigated in the following Fig. 9.5.

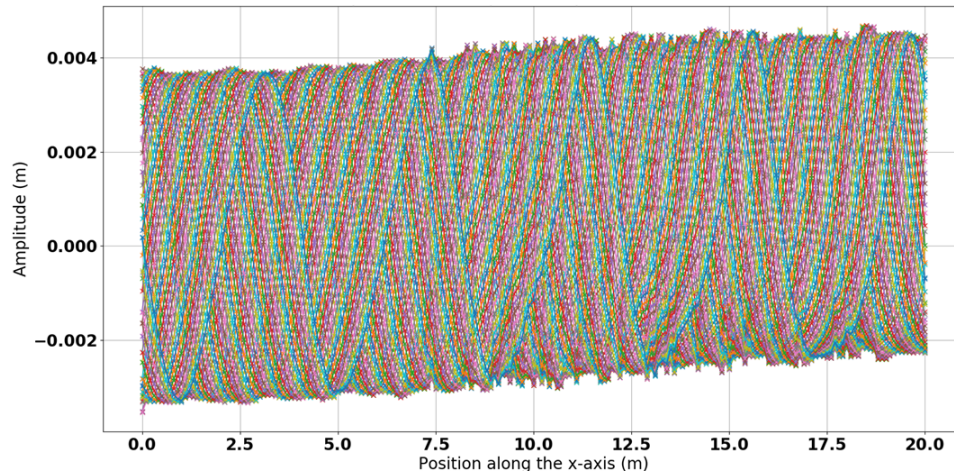


Figure 9.5: Amplitude envelop at $t=80$ s over one period along the tank (waveB).

The amplitude envelop plotted the same way than previously (9.3) indicates an increase of the mean value of the amplitude along the NWT but conserving the same peak to peak amplitude.

This test showed that intermediate and linear waves may lead to a non-physical behaviour of the amplitude along the propagation axes.

waveC

In the PhD thesis, the TLP floater needs to be modelled under Stokes 2nd order and intermediate/deep water wave conditions. That is why, firstly, intermediate depth and 2nd order waves were tested. Figure 9.6 representing free surface time trace at the center of the tank evidences a proper evolution.

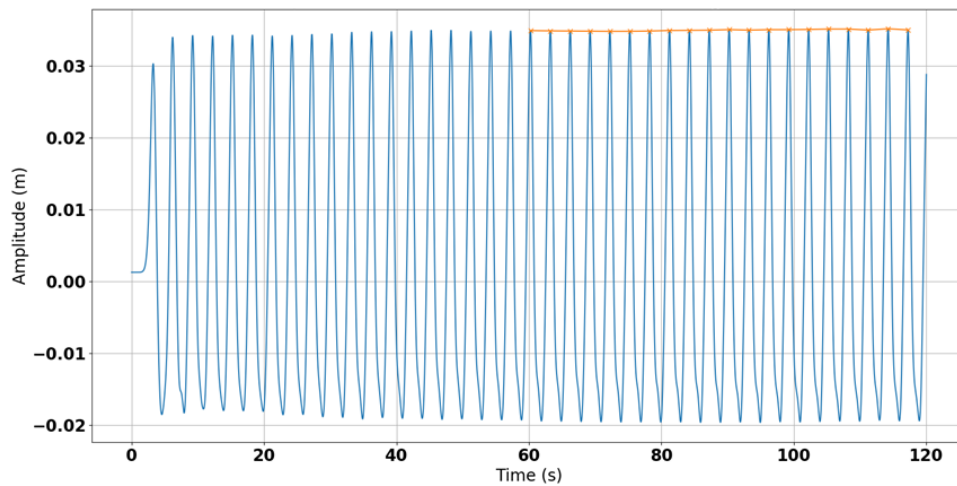
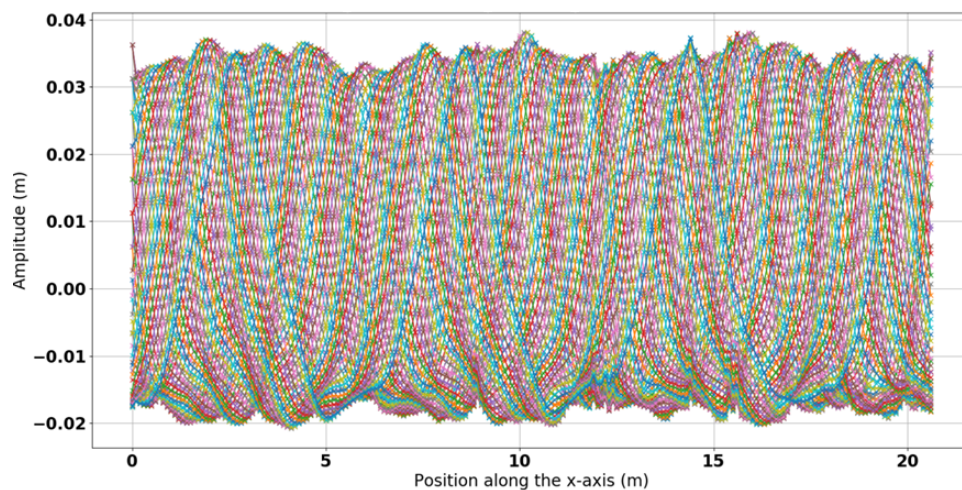


Figure 9.6: Wave elevation time series (waveC).

Figure 9.7: Amplitude envelop at $t=80$ s over one period along the tank (waveC).

However, the envelop amplitude underlines an important reflection phenomena in the tank as seen in Fig. 9.7.

This shows that, as expected, SW-AWA may not be suited for intermediate water depth waves due to the absorption strategy, based on shallow water wave theory (cf. paragraph 3.3.2.2). In the following section, the ER-AWA library is tested in order to check its capacity to propagate intermediate and deep water waves.

9.2.3.2 ER-AWA results

In this subsection, results obtained with simulations using the recent ER-AWA are presented. Deep water and Stokes 2nd order waves are propagated, characterized by different periods and heights. In each case, wave elevation time series and the evolution of the amplitude envelop along the tank were analysed.

waveD

This test should help to prove the correctness of this new library for deep water and second order waves. The short wave length of the waveD understudy, 1 m, induces a short length of the domain compared to other simulations (8 m for 20 m lengths). Free surface time trace at the center of the NWT indicates a correct behaviour of the signal as seen in Fig. 9.8.

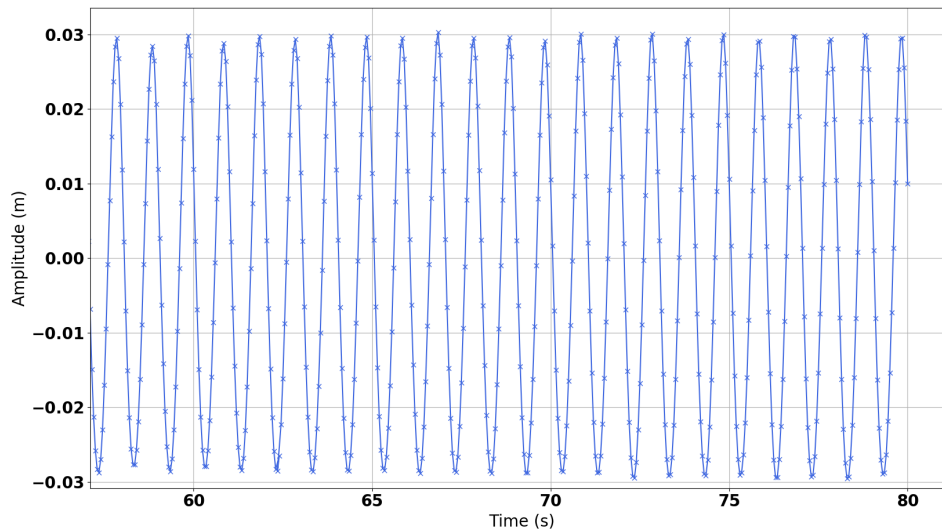


Figure 9.8: Free surface elevation time series at the center of the tank ($x=4$ m).

Comparing the envelop of amplitudes selected at the same time ($T=93$ s) along the tank with SW-AWA library and ER-AWA library, crucial differences appear as it is observed one the two figures 9.9 and 9.10.

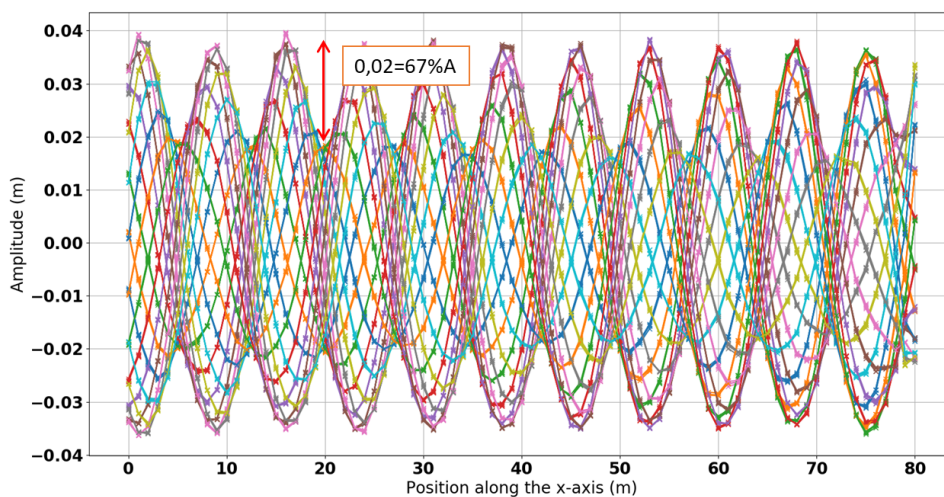


Figure 9.9: SW-AWA library for 2nd order and deep water waves.

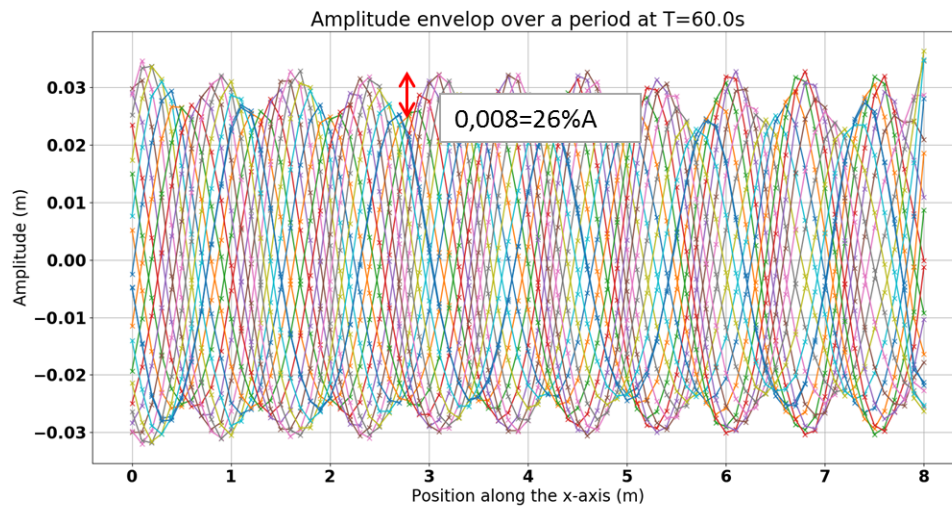


Figure 9.10: ER-AWA library for 2nd order and deep water waves.

Various conclusions can be drawn from the comparison of these graphs:

- SW-AWA strategy does not lead to correct results for second order and deep water waves propagation in the NWT. This was expected due to the specificity of this library for shallow waters only. The amplitude along the NWT varies by 67%.
- With ER-AWA, the amplitude envelop presents less reflection and the amplitude along the propagation axis varies only by 26% A. It still remains significant.

9.2.3.3 waveE: comparison of olaFlow and waveFoam

This test also deals with deep water and 2nd order waves, typical of FOWT sea conditions. The results are compared with experiments performed at MARIN, Netherlands, for the development of the SBM Offshore/IFPEN TLP floater. This case is run with olaFlow (ER-AWA library) and waveFoam solvers for comparison purposes.

The same mesh is used for both simulations (same refinement in the free surface area), with relaxation zones added for the passive solver waveFoam. CFD parameters are also the same (resolution time step, numerical schemes). For each solver, the wave height along the propagation zone is plotted on Fig. 9.11 . This propagation zone is the zone between the inlet and outlet patch for olaFlow and the zone between each relaxation zone for waveFoam.

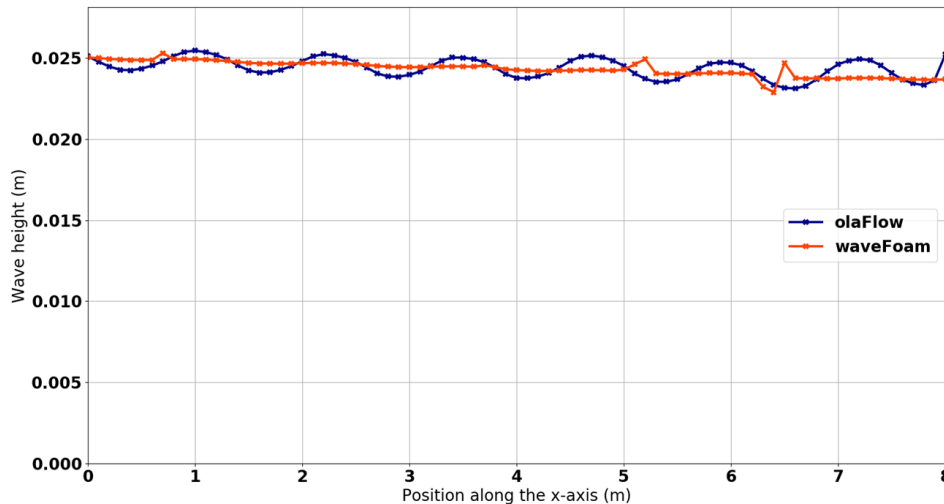


Figure 9.11: Wave height along the NWT obtained with olaFlow and waveFoam runs.

The plot obtained with olaFlow shows an important reflection in the tank. However, waveFoam results seems more constant and less impacted by reflection. A slight decrease of height along the tank is observed with the passive code. As concluded in Windt et al. [2019], the active method olaFlow comes at lower computational cost due to smaller mesh size required than the passive method waveFoam (3.5h for olaFlow, 7h for waveFoam on 72 processors).

9.2.3.4 Conclusions

This bench of tests first aims at assessing the validity of olaFlow in different wave conditions. This active solver seems rather promising, notably on computation time. The following conclusions are obtained from the analysis of CFD simulations:

- Using olaFlow library to propagate cnoidal and shallow water waves is coherent. A proper wave elevation time series and amplitude envelop was achieved. This was expected because the wave condition imposed is in the validity range of the solver.
- For 2nd order and deep water waves, a reflection phenomena occurs for every simulation cases. Though an improvement was observed with the use of ER-AWA instead of the SW-AWA, the reflection still remains significant and too important for the purpose of our study. For the same wave imposed in CFD, results obtained with waveFoam solver show less reflection than with olaFlow runs. That is why waveFoam solver was chosen to perform the CFD simulations during the PhD thesis.

9.3 Scalability study for OpenFOAM

A scalability study performed at the VKI (Von Karman Institute), shows that 30 000 cells par core is an optimal distribution for an OpenFOAM case, regardless of the processor used. Fig. 9.12 shows a satisfactory scalability of OpenFOAM for simulations run with the interFoam solver.

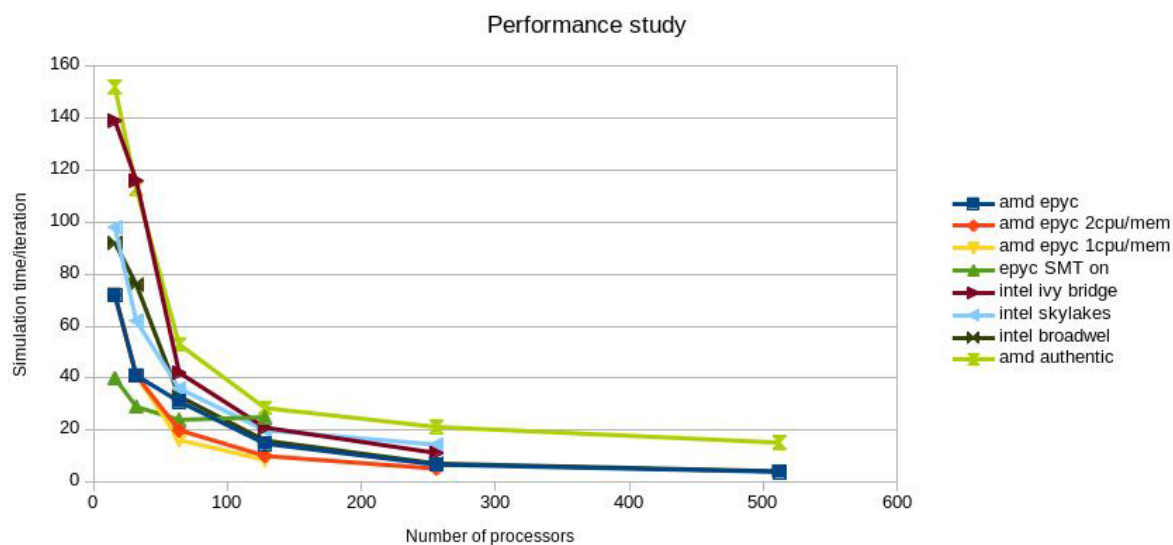


Figure 9.12: Scalability study with interFoam solver.

During the PhD thesis, CFD simulations are run with the IFPEN High Performance Computer and the CEA Cobalt High Performance Computer.

For a wave-only NWT case run with waveFoam (11 768 659 cells), it takes 46h42mn to run 140s of physical time using 108 cores (memory of the core 2.7 Go). For a simulation of the TLP floater included in the NWT (18 460 592 cells), it takes 47h30mn to run 92s of physical time using 170 cores. So we chose to keep the number of cells per core between 50 000 and 100 000.

9.4 Numerical schemes used in the CFD simulations

Tab.9.4 details the numerical schemes chosen in the CFD simulation to solve the Navier-Stokes equations (continuity and momentum equations) and the interface advection equation with VOF MULES method. These numerical schemes are implemented in the *fvSchemes* file.

Detail	Term	Numerical scheme
Time derivative terms	ddt(U),ddt(alpha)	Euler
Continuity equation	grad(U)	Gauss linear
Convection term in the momentum equation	div(rhoPhi,U)	Gauss limitedLinearV 1
Diffusion term in the momentum equation	laplacian(gamma,phi)	Gauss linear corrected
Convection term in the VOF equation	div(phi,alpha)	Gauss vanLeer
Compression term in the VOF equation	div(phirb,alpha)	Gauss interfaceCompression

Table 9.4: Numerical schemes used for the CFD model.

Investigation of Floating Offshore Wind Turbine Hydrodynamics with Computational Fluid Dynamics

Résumé

Afin d'accéder à un vent plus fort et plus régulier loin des côtes, et de s'affranchir des contraintes liées à la profondeur, de nombreux projets sont en cours pour développer l'éolien flottant. Dans les logiciels de dimensionnement, deux théories hydrodynamiques sont imposées pour prédire les chargements dus à la houle : la théorie linéaire potentielle et la formule empirique de Morison. Historiquement utilisées dans le secteur pétrolier, l'applicabilité de ces théories dans le cadre de l'éolien flottant peut être questionnée. La formule de Morison initialement établie pour un cylindre infini, immergé, perpendiculaire à l'écoulement, est désormais appliquée à un flotteur de forme complexe. Les coefficients de Morison sont extraits de bases de données expérimentales et certaines simplifications sont réalisées comme utiliser un seul jeu de coefficients pour toute la structure et pour des états de mer différents. C'est pourquoi, l'hydrodynamique d'un flotteur d'éolienne est étudiée dans cette thèse avec un outil complémentaire : la mécanique des fluides numérique (ou CFD, Computational Fluid Dynamics). L'objectif est d'évaluer, améliorer et adapter la formule de Morison pour la prédiction des chargements hydrodynamiques dans le cadre de l'éolien flottant.

En premier lieu un bassin à houle numérique est défini, avec le code libre de CFD OpenFOAM, dans lequel des houles régulières sont générées, propagées et absorbées. L'élévation de la houle à la future position du flotteur ainsi que la variation de la hauteur de houle le long du bassin sont analysées afin d'éviter tout phénomène de réflexion ou d'amortissement. Des critères adimensionnels sont établis pour définir un bassin numérique pour différents types de houles régulières. Par la suite, le flotteur est inclus dans le bassin numérique et trois différentes houles régulières sont modélisées : une opérationnelle, une intermédiaire et une extrême. Nous développons une méthode des tranches pour déterminer les coefficients de Morison pour chaque bracon à partir des forces issues des simulations numériques, données non accessibles expérimentalement. Cette méthode évalue précisément les forces et les coefficients directionnels associés en prenant en compte la variation des forces le long du bracon et au sein du flotteur. L'impact de la structure et l'orientation complexe du bracon sont inclus dans le calcul des coefficients de Morison. Cependant, la forte influence de l'interface sur les forces des bracons inclinés et perçant l'interface ne peut pas être correctement prédite en appliquant la formule de Morison. Enfin, des variations importantes des coefficients de Morison pour les trois houles au sein de la structure sont observées.

Mots clés: Eolien flottant, Hydrodynamique, Mécanique des fluides numérique.

Abstract

Floating Offshore Wind Turbines (FOWT) offer the possibility to harvest wind energy far offshore and thus considerably extend the potential of offshore wind energy. In the engineering tools used to design FOWT, two theories are implemented to model the hydrodynamic loads: the potential flow theory and the Morison empirical formula. Often used for offshore oil and gas systems, applying these theories to FOWT may be questionable. Since Morison formula was determined for an infinite cross-flow oriented submerged cylinder, its extension to a complex FOWT floater may trigger some uncertainties. Also, Morison coefficients come from standards obtained with various test campaigns and some simplifications are sometimes applied such as using one set of coefficients whatever the sea state. That is why, FOWT hydrodynamics is studied in this PhD thesis with a complementary tool: Computational Fluid Dynamics (CFD). The aim is to evaluate, improve and adapt the Morison formula to FOWT load prediction with CFD modelling.

First, a Numerical Wave Tank (NWT) is implemented in the open-source CFD tool OpenFOAM, in which regular waves are generated, propagated and absorbed. The wave elevation at the future position of the floater and the wave height along the tank are checked to avoid any damping or reflection phenomena. Dimensionless criteria are obtained to set-up a controlled NWT for different types of waves. Secondly, the FOWT floater is included in the NWT and three different regular waves are modelled: an operational, an intermediate and an extreme wave. We develop a slice methodology to determine Morison coefficients from CFD loads locally on each brace of the floater, such data cannot be accessed in experiments. This methodology provides an accurate and detailed determination of loads, like the load variation along each brace and within the complex structure, and associated directional Morison coefficients. We demonstrate that the impact of the structure and the brace orientation can be included in Morison coefficients. However, the significant influence of the free-surface on inclined surface-piercing brace loads cannot be correctly predicted using the Morison formula. Finally, we observe significant variations of the Morison coefficients throughout the structure for the three waves.

Keywords: Floating Offshore Wind Turbines, Hydrodynamics, Computational Fluid Dynamics.